Title
Exploiting Diffusional Constraints in Microporous Materials for Methane Reforming Reactions with Insights from Isotopic Exchange Experiments

Author
Leung, Samuel Lin

Publication Date
2021

Peer reviewed|Thesis/dissertation

Exploiting Diffusional Constraints in Microporous Materials for Methane Reforming Reactions with Insights from Isotopic Exchange Experiments

By

Samuel Lin Tin Chee Leung

A dissertation submitted in partial satisfaction of the

requirements for the degree of

Doctor of Philosophy

in

Chemical Engineering

in the

Graduate Division

of the

University of California, Berkeley

Committee in charge:

Professor Enrique Iglesia, Chair
Professor Alexander Katz
Professor John Arnold

Summer 2021

Exploiting Diffusional Constraints in Microporous Materials
for Methane Reforming Reactions
with Insights from Isotopic Exchange Experiments

by

Samuel Lin Tin Chee Leung

Abstract

Exploiting Diffusional Constraints in Microporous Materials
for Methane Reforming Reactions
with Insights from Isotopic Exchange Experiments

by

Samuel Lin Tin Chee Leung

Doctor of Philosophy in Chemical Engineering

University of California, Berkeley

Professor Enrique Iglesia, Chair

Steam methane reforming (CH_4-H_2O) is the most widely used process for the production of H_2 and is also a key reaction in the production of a wide variety of value-added chemicals and products derived from natural gas resources. Ni-based materials are the most commonly used catalysts in these processes but suffer from the undesired formation of carbonaceous deposits, most often in the form of filaments that can lead not only to deactivation but also catalyst disintegration. Low CH_4/H_2O feed ratios are frequently used to mitigate such carbon formation. These strategies reflect the wider effects and consequences of the thermodynamic activity of carbon on the catalyst surface during steady-state catalysis. The dynamics of carbon deposition during CH_4-H_2O and CH_4-CO_2 reactions (800-1000 K) on Ni-based catalysts and kinetic treatments show that carbon activities and thus carbon formation rates are uniquely determined by a ratio of pressures ψ $\left(\frac{(CH_4)(H_2)}{(H_2O)}\right)$ for a given temperature. These carbon activities provide the thermodynamic driving force for the diffusion of carbon through Ni nanoparticles and subsequent formation of filaments. The diameters of carbon filaments are correlated with the diameters of the Ni particles (5-11 nm). Smaller filaments are less stable and exhibit higher thermodynamic carbon activities, rendering their formation more difficult and decreasing the thermodynamic driving force for their formation, thus decreasing also rates of carbon deposition. The conclusions from these carbon formation studies inform subsequent strategies for encapsulating metal (Pt) clusters in microporous materials.

The encapsulation of metals in zeolites provides many advantages over conventional metal-oxide supported metal nanoparticles, including the retention of small nanoparticles even at high temperatures. Such microporous materials are frequently used in catalytic applications to selectively sieve molecules based on their size and shape and can therefore be used to selectively impose intracrystalline concentration gradients, leading to changes in reactant ratios within the channels of molecular dimensions. These properties can be exploited for CH_4-H_2O reactions, where the diffusivity of smaller H_2O molecules is expected to be much greater than for CH_4 in these intracrystalline pores. The extrapolation of diffusion data to reaction temperatures, however, can involve significant error. Furthermore, the measurement of H_2O and CH_4 diffusion time constants $\left(\frac{R^2}{D_e}\right)$ at reaction temperatures by conventional methods such as transient uptake measurements is not feasible because of the extremely short timescales of these processes and low

uptakes at such temperatures. The measurement of diffusion time constants $\left(\frac{R^2}{D_e}\right)$ at reaction temperatures is accomplished here by analyzing effective reaction rates, specifically isotopic exchange rates, in mass transport limited systems using reaction-diffusion models.

The extraction of diffusion time constants $\left(\frac{R^2}{D_e}\right)$ from reaction-diffusion models can only be rigorously performed with accurate kinetic models. The kinetics of H_2O-D_2 and H_2-D_2 exchange and their mechanistic interpretations are therefore addressed here to allow for such calculations. H_2-D_2 isotopic exchange rates (5-80 kPa H_2, 5-80 kPa D_2; 383 K; H_2/D_2 = 0.0625-16) on Pt-based catalysts show monotonic increases in rate with H_2 and D_2 pressures, in contrast with the kinetics expected from the commonly-cited recombinative desorption (H* + D*) pathway. Such recombination events only become significant at temperatures greater than 700 K and at low combined pressures (<10 kPa) of H_2 and D_2. The kinetics at lower temperatures are instead consistent with the reaction of H_2 with D* and D_2 with H* in a single-site mechanism that does not exhibit a kinetic isotope effect. These exchange events are shown, using theoretical calculations, to occur via the dissociative adsorption of H_2 (or D_2) at vacancies that arise from fluctuations in mobile H*/D*-adlayers. These reaction pathways circumvent desorption/recombination reactions; such exchange reactions therefore cannot be used to demonstrate reversibility of H_2 adsorption on catalytic surfaces at conditions of practice for hydrogenation/dehydrogenation reactions. The kinetics of H_2O-D_2 isotopic exchange reactions (473 K, 5-80 kPa D_2, 2.5-40 kPa H_2O) are consistent with the reaction between D_2 and molecularly adsorbed H_2O*. This reaction pathway remains the predominant pathway for temperatures below 900 K, at which point the dissociation of H_2O (to form OH* and H*) and recombination of OH* and D* likely becomes the primary pathway for exchange. These kinetic studies also show that H_2O irreversibly titrates Pt surface sites by forming OH* species that can only be fully removed by reductive treatments at temperatures greater than 700 K.

The kinetics of exchange inform the rigorous calculation of diffusion time constants from isotopic exchange rates in mass transport limited materials. CH_4-D_2 (5-35 kPa CH_4, 5-30 kPa D_2) H_2O-D_2 (5-30 kPa H_2O, 5-30 D_2), and H_2-D_2 (10 kPa H_2, 10 kPa D_2) isotopic exchange rates are measured here on Pt/SiO_2, Pt/γ-Al_2O_3, Pt/Na-LTA, and Pt/Ca-LTA samples at temperatures (573-900 K) relevant for CH_4-H_2O reforming reactions. Effectiveness factors for CH_4-D_2 and H_2O-D_2 exchange on Pt/Na-LTA and Pt/Ca-LTA are used to extract diffusion time constants $\left(\frac{R^2}{D_e}\right)$ for CH_4 and H_2O using classical reaction-diffusion models. CH_4 exhibits significantly larger diffusion time constants (by factors of more than 10^2) than H_2O in both Pt/Na-LTA and Pt/Ca-LTA throughout this temperature range (573-900 K), indicating that H_2O diffuses more readily in these materials, as required for elevated intracrystalline H_2O/CH_4 ratios during CH_4-H_2O reactions. H_2-D_2 exchange reactions do not exhibit mass transport limitations in these materials at these conditions.

The measured CH_4 and H_2O diffusion time constants are used in the interpretation of deactivation rates during CH_4-H_2O reactions at 873 K on Pt/γ-Al_2O_3, Pt/Na-LTA, and Pt/Ca-LTA samples. Deactivation rates on Pt/γ-Al_2O_3 are linearly dependent on a ψ $\left(\frac{(CH_4)(H_2)}{(H_2O)}\right)$, as expected from carbon formation studies on Ni. Deactivation rates on Pt/Na-LTA and Pt/Ca-LTA are undetectable for ψ $\left(\frac{(CH_4)(H_2)}{(H_2O)}\right)$ values below 10 (including stoichiometric CH_4/H_2O ratios) and are 3-8 times slower than on Pt/γ-Al_2O_3 for ψ values between 10 and 40. These improvements reflect the high H_2O/CH_4 ratios within the zeolite pores, as indicated by extensive numerical models.

Simulations of deactivation behavior are also used to provide additional insight into further optimizing these materials. The strategies for exploiting differences in diffusivity in microporous materials, demonstrated here for CH_4-H_2O reforming reactions, are generally applicable to reactions where selective access of smaller reactants is desirable.

Dedication

I dedicate this dissertation to my parents, Christopher and Helen, who have been supportive of every step along my journey to where I am today. They inspired me to pursue a career in the sciences and gave me strength to continue whenever I thought of giving up.

Thank you Mom and Dad.

Table of Contents

Acknowledgements

I would like to thank Professor Enrique Iglesia for his patience and persistence in teaching me to become a better critical thinker in all aspects of life and for inspiring a sense of curiosity and rigor in my work. This dissertation would not have been possible without his tireless hours in guiding me towards becoming a better scientist. I learned more than I could have imagined during my time in LSAC.

I would like to thank all my collaborators: Junmei Wei, Bill Holstein, Miguel Avalos-Borja, and David Hibbitts. Their work and extensive contributions were key in making my project a success.

I would also like to thank the other "triplets" of LSAC, Ari and Haefa, who completed this journey with me. They provided incredible support for both personal and technical issues during our time together and are two of the best friends I could have asked for.

Finally, I would like to thank all of my family and friends in the Bay Area, who helped make this place feel like home, even though I lived 2000 miles away from my parents.

Chapter 1

Introduction to Steam Methane Reforming and Mass Transport Limitations in Microporous Materials

Methane is an important feedstock in the production of many value-added chemicals, including ammonia, methanol, and liquid hydrocarbons.[1] It is also one of the most common sources of hydrogen.[1-2] Recent increases in the production of CH_4 have driven the need to develop and improve methane conversion processes.[2] While there is considerable research interest in the direct conversion of methane to high-value liquids,[2-4] steam methane reforming remains the most common pathway for the production of value-added chemicals via synthesis gas. Steam reforming reactions, however, suffer from mass and heat transfer issues and from the formation of inactive carbon deposits. The most common catalysts for these reactions are based on Ni, which tend to form carbon filaments[5-6] that, in the long term, lead to significant pressures drops in the reactor and to disintegration of catalytic particles and their subsequent elution. Suprastoichiometric H_2O/CH_4 ratios are used in practice to prevent the formation of these carbon residues, leading to significant energy inefficiencies.[7] As discussed in Chapter 2, these strategies address the formation of carbon by altering the prevalent thermodynamic activity of carbon on catalytic surfaces, which are set by a ratio of pressures $\left(\psi = \frac{(CH_4)(H_2)}{(H_2O)}\right)$ (800-1000 K) that reflects the pseudo-steady-state carbon concentration, as mediated by elementary steps previously reported for CH_4-CO_2 and CH_4-H_2O reactions on metal catalysts.[8] These carbon activities provide the thermodynamic driving force for the diffusion of carbon through Ni nanoparticles and subsequent formation of filaments, leading to carbon deposition rates that are linearly dependent on ψ. Such mechanistic interpretations inform the subsequent strategies for encapsulating metal clusters in microporous materials.

Zeolites are crystalline microporous materials with well-defined pore and cage structures[9] that exhibit desirable sieving and adsorptive properties. These materials are frequently used as solid-acid catalysts[10-11] but have found increasing use in metal-catalyzed chemistries by placing metal nanoparticles within voids in the framework.[12] This encapsulation of metal clusters provides distinct advantages over conventionally supported metal nanoparticles,[12] including the protection of encapsulated metal nanoparticles from contact with bulky catalytic poisons,[13-14] the selective retention of bulky products until they fragment or isomerize to form species that diffuse more readily through the channels of the framework,[15] and the stabilization of transition states via van der Waals interactions with the walls of intracrystalline channels and cages.[16] The framework surrounding metal clusters also provides significant resistance against sintering, allowing clusters to retain their small size even at temperatures that would lead to agglomeration of metal particles on conventional metal-oxide supports.[13-14] Molecular motion within the channels and voids of zeolites is strongly influenced by interactions between guest molecules and the host framework.[17] These interactions can decrease catalytic productivity in certain applications,[10, 17-19] but can also be exploited to provide selective access to the active sites contained within the pores of molecular dimensions.

H_2O molecules exhibit a smaller kinetic diameter (0.264 nm) than for CH_4 (0.376 nm),[20] leading to diffusivities that are much greater for H_2O than CH_4 in LTA zeolites.[20-22] Such

differences in diffusivity can be exploited during mass-transport-limited reactions of CH_4 and H_2O to increase H_2O/CH_4 ratios at the catalyst level rather than at the process level, in strategies that lead to the suppression of carbon activities and thus carbon formation rates at active sites located within LTA crystallites, as shown in Scheme 1.

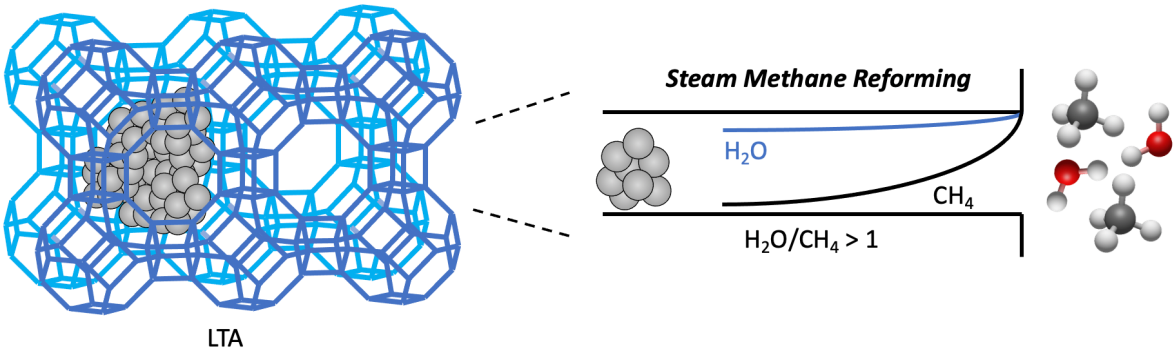

Scheme 1. Approach for exploiting differences in CH_4 and H_2O diffusivities to increase H_2O/CH_4 ratios and suppress carbon formation within zeolite micropores.

The accurate prediction and modelling of concentration profiles within the pores of zeolites require accurate molecular diffusivities and effective diffusion lengths at reaction temperatures. Conventional methods for measuring diffusion (e.g., transient uptake experiments), however, are often infeasible at reaction temperatures because the diffusive processes occur on timescales that are too fast to be measured accurately. These measurements are therefore typically performed near ambient temperatures. The extrapolation of diffusion data collected at such conditions to methane reforming reaction temperatures (800-1000 K), however, can involve significant error; the accuracy of such extrapolations is highly dependent on estimates of the activation energy for diffusion.[17] An alternative strategy for measuring diffusion time constants at reaction temperatures is presented in this work. The reaction-diffusion models and formalisms typically used to calculate effective reaction rates from diffusion data can also be used to obtain diffusion time constants $\left(\frac{R^2}{D_e}\right)$ from measured effective reaction rates, including isotopic exchange rates, in mass-transport-limited systems. Such methodologies require accurate kinetic models to interpret these rates.

The kinetics of H_2-D_2 (Chapter 3), H_2O-D_2 (Chapter 4), and CH_4-D_2 (Chapter 5) isotopic exchange on Pt-based catalysts and their mechanistic consequences for measuring and interpreting effective reaction rates (Chapter 5) are addressed in this work. H_2-D_2 isotopic exchange is frequently used also to probe the reversibility of H_2 dissociative adsorption events on surfaces as such molecules participate in catalytic hydrogenation-dehydrogenation reactions. These experiments and interpretations implicitly assume that isotopic scrambling can only occur via the aforementioned dissociative adsorption and recombinative desorption reactions. The observed kinetics of H_2-D_2 and monotonic increases with rate with H_2 and D_2 pressure (5-80 kPa H_2, 5-80 kPa D_2; 383 K; H_2/D_2 = 0.0625-16), however, are inconsistent with such pathways and instead implicate reactions of H_2 with D* and D_2 with H*, in a single-site mechanism that does not exhibit a kinetic isotope effect. Such reactions remain the primary pathway for exchange at temperatures

below 700 K. Theoretical calculations (DFT) indicate that these reactions likely proceed via the dissociative adsorption of H_2 (or D_2) at vacancies that arise from fluctuations in mobile H*/D*-adlayers. Such pathways circumvent desorption/recombination reactions; H_2-D_2 exchange reactions therefore cannot be used to conclusively demonstrate reversibility of H_2 adsorption on catalytic surfaces at temperatures of common practice.

Condensed H_2O has been previously shown to destabilize H* adatoms at Pt surfaces using inferences from isotopic exchange rate data and kinetic isotope effects.[23] The kinetics of H_2O-D_2 and H_2O-H_2-D_2 reactions carried out on Pt catalysts (323-473 K) in the present work (Chapter 4), however, provides a different interpretation of the kinetic data. The presence of even gas-phase H_2O during H_2-D_2 reactions results in an irreversible decrease in H_2-D_2 exchange rates, consistent with the partial titration of Pt surfaces by OH* or O* species formed from the dissociation of H_2O. These species cannot be removed except by high temperature treatments (> 700 K) in H_2. Surface-bound molecular H_2O species are also present and compete with H* and D* during these isotopic exchange reactions. These combined effects lead to an apparent decrease in the amount of dissociatively adsorbed hydrogen during such exchange reactions. The kinetics of H_2O-D_2 isotopic exchange (473 K, 5-80 kPa D_2, 2.5-40 kPa H_2O) are also shown to be inconsistent with previously proposed mechanisms;[23-29] they are consistent instead with reactions between D_2 and molecularly adsorbed H_2O*. These reactions are reminiscent of H_2-D_2 reaction pathways (Chapter 3); the rate constants for H_2-D* and H_2O-D* reactions are also similar, suggesting that H_2O-D* reactions may initially proceed via the same dissociative adsorption of D_2 at vacancies that form in the D*-H_2O*-adlayer. These reactions remain the predominant pathway for temperatures below 900 K, at which point the rates of H_2O dissociation and recombination become significant.

The kinetics of CH_4-D_2 isotopic exchange reactions (873 K), as shown in Chapter 5, are consistent with CH_4 dissociation and recombination; these reactions involve breaking C-H bonds and thus share a common rate limiting step with CH_4-H_2O reforming reactions on metal surfaces.[30] CH_4-D_2 isotopic exchange rates are therefore nearly identical to CH_4 turnover rates during steam methane reforming. The mechanistic interpretations from H_2-D_2, H_2O-D_2, and CH_4-D_2 kinetic studies (Chapters 3-5) inform the rigorous calculation of diffusion time constants $\left(\frac{R^2}{D_e}\right)$ from isotopic exchange events in mass transport limited materials, as discussed in Chapter 5. Effectiveness factors for CH_4-D_2 and H_2O-D_2 reactions on Pt/Na-LTA and Pt/Ca-LTA, derived from isotopic exchange rates, are used in reaction-diffusion models[31-32] to calculate diffusion time constants for CH_4 and H_2O, respectively. CH_4 exhibits significantly larger diffusion time constants than H_2O in both Pt/Na-LTA and Pt/Ca-LTA (by a factors of 1200 and 46, respectively; 873 K), as required for elevating intracrystalline H_2O/CH_4 ratios during CH_4-H_2O reactions on these materials. H_2-D_2 exchange rates on Pt/Na-LTA and Pt/Ca-LTA are identical to those on unencapsulated samples (Pt/SiO_2), reflecting the absence of mass transport limitations and concentration gradients for H_2 (or D_2) molecules.

CH_4-H_2O reactions on Pt proceed via the same elementary steps as for Ni.[8, 30] Surface carbon activities are therefore set by the same ratio of pressures $\left(\psi = \frac{(CH_4)(H_2)}{(H_2O)}\right)$. Carbon residues on Pt, however, tend to form graphite-like layers that block access to the surface over time, leading to deactivation of the catalyst;[33] these differences in carbon morphology reflect the much lower solubility of carbon in Pt (4×10^{-12} wt. %, 873 K; extrapolated from 1473-1773 K)[34] than in Ni (0.04 wt. %, 873 K).[35] Deactivation rates on Pt/γ-Al_2O_3 are therefore linearly dependent on ψ (873 K), as shown in Chapter 6. Deactivation rates on Pt/Na-LTA and Pt/Ca-LTA are undetectable for

ψ values below 10 (including stoichiometric H_2O/CH_4 ratios) and exhibit deactivation rates that are 3-8 times lower than on Pt/γ-Al_2O_3 for ψ values between 10 and 40. These deactivation rates are in agreement with numerical models and simulations that utilize the CH_4 and H_2O diffusion time constants derived from isotopic exchange methods (Chapter 5). The improvements in stability thus reflect the high H_2O/CH_4 ratios within the zeolite pores, in accordance with Scheme 1. The numerical simulations are used to provide further guidance in the selection and design of more stable catalysts.

This dissertation provides a framework for exploiting diffusive constraints in microporous materials to alter reactant ratios at the locations of active sites. The insights provided from carbon formation studies (Chapter 2) are used to design a solution that addresses a process design problem at the catalytic level (Chapter 6). Such strategies for exploiting diffusion are applicable to a wide variety of reactions and can be employed even for the complete exclusion of molecules. A method for deriving diffusion time constants from effectiveness factors at temperatures relevant for catalytic reactions is also presented in this work (Chapter 5). These methods are used with rigorous interpretations of kinetic data from isotopic exchange reactions (Chapter 3-5). This work also resolves some of the conflicting data in the literature on isotopic exchange mechanisms and demonstrates the importance of having accurate mechanistic understandings of these exchange reactions.

References

1. Basile, A.; Liguori, S.; Iulianelli, A., 2 - Membrane reactors for methane steam reforming (MSR). In *Membrane Reactors for Energy Applications and Basic Chemical Production*, Basile, A.; Di Paola, L.; Hai, F. l.; Piemonte, V., Eds. Woodhead Publishing: 2015; pp 31-59.
2. Anabtawi, J. A.; Aitani, A. M.; Siddiqui, M. A. B., Prospects for Direct Natural Gas Conversion to Petrochemical Feedstocks. *Journal of King Saud University - Engineering Sciences* **1995**, *7*, 191-206.
3. Spitz, P. H., [23]4 Technology Trends in Petrochemicals Manufacture. 1987.
4. Park, M. B.; Park, E. D.; Ahn, W. S., Recent Progress in Direct Conversion of Methane to Methanol Over Copper-Exchanged Zeolites. *Frontiers in Chemistry* **2019**, *7*.
5. Snoeck, J. W.; Froment, G. F.; Fowles, M., Steam/CO_2 Reforming of Methane. Carbon Filament Formation by the Boudouard Reaction and Gasification by CO_2, by H_2, and by Steam: Kinetic Study. *Ind. Eng. Chem. Res.* **2002**, *41*, 4252-4265.
6. Leung, S. L.; Wei, J. M.; Holstein, W. L.; Avalos-Borja, M.; Iglesia, E., Dynamics and Mechanism of Carbon Filament Formation during Methane Reforming on Supported Nickel Clusters. *J. Phys. Chem. C* **2020**, *124*, 20143-20160.
7. Rostrup-Nielsen, J. R., Catalytic Steam Reforming. In *Catalysis: Science and Technology*, Anderson, J. R.; Boudart, M., Eds. Springer Berlin Heidelberg: Berlin, Heidelberg, 1984; Vol. 5, pp 1-117.
8. Wei, J.; Iglesia, E., Isotopic and Kinetic Assessment of the Mechanism of Reactions of CH_4 with CO_2 or H_2O to Form Synthesis Gas and Carbon on Nickel Catalysts. *J. Catal.* **2004**, *224*, 370-383.
9. Breck, D. W., *Zeolite molecular sieves: structure, chemistry, and use*; New York, Wiley [1973, c1974], 1973.
10. Corma, A., From microporous to mesoporous molecular sieve materials and their use in catalysis. *Chem. Rev.* **1997**, *97*, 2373-2419.
11. Verdoliva, V.; Saviano, M.; De Luca, S., Zeolites as Acid/Basic Solid Catalysts: Recent Synthetic Developments. *Catalysts* **2019**, *9*.
12. Farrusseng, D.; Tuel, A., Perspectives on zeolite-encapsulated metal nanoparticles and their applications in catalysis. *New J. Chem.* **2016**, *40*, 3933-3949.
13. Sachtler, W. M. H., Metal-Clusters in Zeolites - an Intriguing Class of Catalysts. *Acc. Chem. Res.* **1993**, *26*, 383-387.
14. Goel, S.; Wu, Z. J.; Zones, S. I.; Iglesia, E., Synthesis and Catalytic Properties of Metal Clusters Encapsulated within Small-Pore (SOD, GIS, ANA) Zeolites. *Journal of the American Chemical Society* **2012**, *134*, 17688-17695.
15. Teketel, S.; Erichsen, M. W.; Bleken, F. L.; Svelle, S.; Lillerud, K. P.; Olsbye, U., Shape selectivity in zeolite catalysis. The Methanol to Hydrocarbons (MTH) reaction. *Catalysis, Vol 26* **2014**, *26*, 179-217.
16. Csicsery, S. M., Catalysis by Shape Selective Zeolites - Science and Technology. *Pure Appl. Chem.* **1986**, *58*, 841-856.
17. Kärger, J.; Vasenkov, S.; Auerbach, S., Diffusion in Zeolites. In *Handbook of Zeolite Science and Technology*, CRC Press: 2003; pp 446-548.
18. Karger, J.; Valiullin, R.; Enke, D.; Glaser, R., Measuring Mass Transport in Hierarchical Pore Systems. *Mesoporous Zeolites: Preparation, Characterization and Applications* **2015**, 385-423.

19. Maxwell, I. E., Shape-Selective Catalysis and Process Technology Via Molecular Inclusion in Zeolites. *Journal of Inclusion Phenomena* **1986**, *4*, 1-29.
20. Sircar, S.; Myers, A., Gas Separation by Zeolites. In *Handbook of Zeolite Science and Technology*, CRC Press: 2003.
21. Haq, N.; Ruthven, D. M., Chromatographic Study of Sorption and Diffusion in 4a Zeolite. *J. Colloid Interface Sci.* **1986**, *112*, 154-163.
22. Karger, J.; Pfeifer, H.; Rosemann, M.; Feokistova, N. N.; Zdanov, S. P., Intracrystalline Self-Diffusion of Water and Short-Chain-Length Paraffins in a-Type Zeolites. *Zeolites* **1989**, *9*, 247-249.
23. Yang, G. J.; Akhade, S. A.; Chen, X.; Liu, Y.; Lee, M. S.; Glezakou, V. A.; Rousseau, R.; Lercher, J. A., The Nature of Hydrogen Adsorption on Platinum in the Aqueous Phase. *Angewandte Chemie-International Edition* **2019**, *58*, 3527-3532.
24. Gupta, N. M.; Mishra, K.; Belapurkar, A. D.; Rao, K. V. S. R.; Iyer, R. M., Deuterium-Isotope Exchange-Reaction between Hydrogen and Water over Polyester-Supported Platinum Catalysts. *J. C*
o, Y.; Kusunoki, K., Kinetics of Isotopic Exchange-Reaction between Hydrogen and Water-Vapor over Platinum Supported on a Hydrophobic Carrier. *Can. J. Chem. Eng.* **1986**, *64*, 432-439. *atal.* **1990**, *121*, 386-395.
25. Halpern, J.; James, B. R., Homogeneous Catalysis of D2-H2O Exchange by Ruthenium (III) Chloride: Evidence for the Heterolytic Splitting of Hydrogen. *Can. J. Chem.* **1966**, *44*, 671-675.
26. Kawakami, K.; Taka
27. Rolston, J. H.; Goodale, J. W., Isotopic-Exchange between Hydrogen and Water Vapor over Supported Metal Catalysts .1. Kinetics of Exchange. *Can. J. Chem.* **1972**, *50*, 1900-1906.
28. Borstad, G. M.; Yoo, C. S., H2O and D2 mixtures under pressure: Spectroscopy and proton exchange kinetics. *J. Chem. Phys.* **2011**, *135*.
29. Miyamoto, S.; Sakka, T.; Iwasaki, M., Hydrogen Isotope Exchange between D2 and H2o Catalyzed by Platinum Plate. *Canadian Journal of Chemistry-Revue Canadienne De Chimie* **1989**, *67*, 857-861.
30. Wei, J.; Iglesia, E., Mechanism and Site Requirements for Activation and Chemical Conversion of Methane on Supported Pt Clusters and Turnover Rate Comparisons among Noble Metals. *J. Phys. Chem. B* **2004**, *108*, 4094-4103.
31. Fogler, H. S., *Elements of Chemical Reaction Engineering*; Prentice Hall PTR, 2006.
32. Thiele, E. W., Relation between Catalytic Activity and Size of Particle. *Industrial & Engineering Chemistry* **1939**, *31*, 916-920.
33. Schulz, L. A.; Kahle, L. C. S.; Delgado, K. H.; Schunk, S. A.; Jentys, A.; Deutschmann, O.; Lercher, J. A., On the coke deposition in dry reforming of methane at elevated pressures. *Appl. Catal., A* **2015**, *504*, 599-607.
34. Watson, E. B., Diffusion and Solubility of C in Pt. *Am. Mineral.* **1987**, *72*, 487-490.
35. Lander, J. J.; Kern, H. E.; Beach, A. L., Solubility and Diffusion Coefficient of Carbon in Nickel: Reaction Rates of Nickel-Carbon Alloys with Barium Oxide. *J. Appl. Phys.* **1952**, *23*, 1305-1309.

Chapter 2

Dynamics and Mechanism of Carbon Filament Formation during Methane Reforming on Supported Nickel Clusters

Abstract

CH_4-CO_2 and CH_4-H_2O reforming on Ni-based catalysts can lead to the undesired formation of carbonaceous residues. The dynamics of the formation of carbon filaments and encapsulating layers on dispersed Ni nanoparticles (5-11 nm diameter) are determined here using an inertial microbalance to measure mass changes and mass spectrometry to concurrently assess turnover rates at conditions of reforming practice (800-1000 K). The morphology and rate of formation of carbonaceous species were controlled by a ratio of pressures ($\chi = P_{CH4}P_{CO}/P_{CO2}$) that uniquely determines the thermodynamic activity of carbon at the metal surface ($(a_{C^*})_s$) and the thermodynamic driving force for carbon diffusion and filament formation, based on a reaction-transport model derived from the elementary steps that mediate CH_4 reforming. Each sample exhibited three distinct kinetic regimes for carbon formation, which evolved with increasing χ values from undetectable carbon deposition (I), to a constant rate of carbon filament growth without detectable changes in CH_4 reforming rates (II), and ultimately to the formation of carbon overlayers with a concurrent decrease in CH_4 reforming and carbon formation rates (III). Rates of filament growth in regime II were proportional to χ values, consistent with a filament growth mechanism limited by carbon diffusion. Such carbon filaments were similar in diameter to the attached Ni nanoparticles. In regime III, the high prevalent carbon activities led to the simultaneous nucleation of several carbon patches, thus precluding the directional diffusion imposed by a single filament and leading to the encapsulation and loss of accessible surface for CH_4 turnovers. Filaments formed in regime II were removed when placed at the conditions of regime I via the microscopic reverse of their formation processes. Threshold carbon activities required for the incipient formation of filaments are higher and filament formation rates are lower (for a given χ) on smaller nanoparticles because of the less stable nature (higher thermodynamic carbon activity) of filaments with smaller diameters. Carbon deposition rates decreased with increasing temperature (for a given χ) because of a corresponding decrease in the lumped kinetic and thermodynamic parameters that relate the surface carbon activity to χ. The formalism used to describe carbon formation rates, in this study for CH_4 reforming rates far from equilibrium and for carbon formation and removal rates that do not disturb the carbon activity set by CH_4 reforming turnovers at steady-state, also inform the testing of these assumptions, while providing also a framework for the rigorous extension of these reaction-diffusion constructs to more practical conditions, for which these assumptions may no longer apply.

2.1 Introduction

CH_4 reacts with CO_2 or H_2O to form synthesis gas, an important intermediate in the production of many valuable fuels and chemicals. Industrial processes predominantly use Ni-based catalysts that tend to form filamentous carbon deposits when using stoichiometric CH_4-CO_2 or CH_4-H_2O reactant mixtures.[1] Other materials such as noble metals and recently developed bimetallic alloys have demonstrated lower tendencies to form such deposits.[2-5] Such materials, however, have not found widespread use at this time. The formation of carbonaceous residues hinders catalysis by blocking pores, active sites, and even interpellet voids in packed catalyst beds; in extreme cases, these residues lead to catalyst disintegration, elution as fines, and reactor plugging.

CO_2/CH_4 and H_2O/CH_4 ratios significantly larger than unity are used in practice in order to prevent the formation of these carbon residues, in strategies that lead to significant recycle and separation costs and energy inefficiencies.[1] The accurate prediction and selection of conditions at which carbon deposition on metal catalysts can be prevented or minimized remain essential in efforts to improve process efficiency; this topic has been addressed in several previous studies[6-38] and reviewed by Trimm,[7] Rostrup-Nielsen and Trimm,[8] Baker and Harris,[9] Rodriguez,[10] de Jong and Geus,[11] Liu et al.,[12] Lobo et al.,[13] and Sperle et al.[14] The unique morphology and properties of carbon nanotubes[15, 39-41] have driven parallel studies in efforts to optimize their purposeful synthesis by elucidating the pathways required for the formation of single-walled or multi-walled carbon nanotubes on catalytic metal particles.[16-22, 42-51]

It is generally accepted that the formation of carbon filaments from hydrocarbons on Ni crystallites proceeds via: (a) the dissociative chemisorption of the hydrocarbon on metal surfaces to form carbon atoms, (b) the dissolution of carbon atoms into the metal, (c) the bulk diffusion of the carbon atoms through the metal, and (d) the nucleation of filaments and the precipitation of carbon atoms at the metal-filament interface at the location on the crystallite surface where filament nucleation initially occurred.[13, 23-26] The diffusion of carbon atoms through the catalyst particle (step (c)) is typically considered to limit filament growth rates, while the dissolution of carbon atoms into the metal and their deposition at the growing filament are thought to be fast quasi-equilibrated processes. The diffusion of carbon though metal particles is driven by gradients in carbon concentration[8, 26-27, 29, 31] or more precisely in carbon chemical potentials, and temperature.[23-24, 28-29] Holstein showed that temperature gradients could not be responsible for filamentous carbon growth.[25]

Holstein[25] and Lund and Yang[30] indicated that the true driving force for diffusion is a gradient in the chemical potential of dissolved carbon (μ_c), defined by:

$$\mu_c = \mu_c^* + RT \ln a_c \qquad (1)$$

where μ_c* is the chemical potential of the reference state and a_c is the thermodynamic activity of the carbon dissolved within the metal particle. The chemical potential of carbon is proportional to its thermodynamic activity in dilute solutions of C-atoms within Ni, such as those encountered here (< 0.01 mole fraction C in Ni),[52] because activity coefficients become independent of the concentration of the carbon solute. In this limiting case and for isothermal particles, the gradient in thermodynamic activity of dissolved carbon between the part of the Ni surface exposed to gas-phase reactants and that in contact with the growing carbon filament drives the diffusion of carbon through the metal particle toward the filament and determines the formation rates of such filaments.

Most carbon deposition processes of industrial relevance occur during the steady-state catalytic reactions of multi-component gas mixtures. Yet, most previous studies measured the dynamics of carbon formation using equilibrated binary mixtures, such as CO-CO_2 [31, 41, 53-54] or CH_4-H_2 [44-45, 53-56]. For these quasi-equilibrated mixtures, the thermodynamic activity of carbon (a_C) is set by the gas-phase composition and given by thermodynamic relations:[31, 55]

$$2CO \overset{K_{CO}}{\rightleftharpoons} C + CO_2 \qquad (a_C) = \frac{K_{CO}(CO)^2}{(CO_2)} \tag{2}$$

$$CH_4 \overset{K_{CH4}}{\rightleftharpoons} C + 2H_2 \qquad (a_C) = \frac{K_{CH4}(CH_4)}{(H_2)^2} \tag{3}$$

Carbon formation rates depend linearly on the carbon activity (a_C) for these equilibrated mixtures,[31, 55] consistent with a diffusion-limited filament growth mechanism. A few studies have addressed the formation rates and morphology of carbon filaments during CO-H_2-H_2O-CO_2-CH_4 reactions,[14, 57-60] but without accurate mechanism-based frameworks, which are required to relate the prevalent carbon activity at catalytic surfaces to the dynamics of filament formation for different reaction conditions. The information available about the effects of Ni crystallite size on growth rates and morphology of carbon deposits remains largely anecdotal.[57, 61] Moreover, the effects of H_2 on carbon deposition rates remain contradictory, with some studies[57-58] reporting that H_2 increases carbon formation rates and others[14, 60] demonstrating the opposite trend. The effect of H_2 on the thermodynamic carbon activity prevalent during reactions of CO-H_2-H_2O-CO_2-CH_4 mixtures remains largely unexplored at this time.

The mechanistic details of carbon deposition and its dynamics are explored here through measurements of carbon formation rates during steady-state CH_4 reforming catalysis at conditions far away from the chemical equilibrium of this reaction on supported Ni-based catalysts with different nanoparticle diameters, as these reforming reactions occur under strict kinetic control. Carbon formation rates are shown to depend solely on χ and ψ ratios of pressures ($P_{CO}P_{CH4}/P_{CO2}$ and $P_{H2}P_{CH4}/P_{H2O}$, respectively), which are proportional to each other through the water-gas shift equilibrium constant. These ratios are shown to set the thermodynamic activity of carbon at Ni surfaces via elementary steps previously reported for CH_4-CO_2 and CH_4-H_2O reactions on metal catalysts at similar conditions.[62] These carbon thermodynamic activities are used within a diffusion-reaction framework to relate the dynamics of filament growth and their morphology to the prevalent conditions of reforming catalysis.

The morphology of carbon structures formed during reactions of CO-CO_2-H_2 and CO-H_2-H_2O-CO_2-CH_4 mixtures on Ni catalysts depends on temperature and on the composition of the contacting gaseous mixtures.[37-38, 59, 63] CO-CO_2 binary mixtures lead to filaments and onion-like carbon structures on Ni, while CO-CO_2-H_2 mixtures form only filamentous carbon,[38] perhaps because H_2 preserves unblocked active surfaces that can continue to supply the C-atoms required to form filaments in such mixtures. CO-H_2-H_2O-CO_2-CH_4 mixtures also tend to form filamentous forms of carbon, though "platelet" carbon structures are also observed at higher O/H ratios in such mixtures.[59] These previous studies fail to provide clear mechanistic connections between the composition of the CO-H_2-H_2O-CO_2-CH_4 mixtures, the rate of their interconversions at surfaces, the surface carbon activity, and the structure of the carbon deposits formed.

The present study addresses such connections. The evidence provided here shows how the nature of the carbon structures (filamentous or encapsulating) is determined by the surface carbon activity, which is related to the reaction environment through the elementary steps of CH_4 reforming catalysis. Such carbon activities are set by the prevalent χ (or ψ) values. The morphology of the deposited carbon reflects nucleation and growth processes directly related to well-known effects of supersaturation on the nucleation and growth of solid phases.[64]

2.2 Experimental Methods

Supported Ni catalysts with 7% wt. and 15% wt. Ni content were prepared by incipient wetness impregnation of MgO powders, prepared for this study (MgO-A) or obtained from commercial sources (MgO-B; Alfa, CAS# 1309-48-4), with aqueous solutions of $Ni(NO_3)_2 \cdot 6H_2O$ (Alfa, 99.9%). MgO-A powders were prepared by sol-gel methods using supercritical drying.[62] The impregnated powders were treated overnight in stagnant ambient air at 393 K and then in flowing dry air (Airgas, UHP, 1.2 $cm^3\ g^{-1}\ s^{-1}$) at 923 K (0.167 K s^{-1}) for 5 h. Samples were then treated in H_2 (Airgas, UHP, 50 $cm^3\ g^{-1}\ s^{-1}$) by heating to 1123 K (0.167 K s^{-1}) and holding for 3 h.

The metal dispersion of fresh Ni catalysts was determined from the uptake of strongly chemisorbed H_2 at 313 K (3-50 kPa) using a Quantasorb chemisorption analyzer (Quantachrome Corporation Model 05-10). Samples were treated in H_2 at 873 K for 0.5 h within the adsorption cell before uptake measurements. A backsorption isotherm was measured by repeating this procedure after evacuation for 0.5 h at 313 K. Strongly chemisorbed hydrogen uptakes were obtained from the difference between chemisorption and backsorption uptakes using a 1:1 $H:Ni_{surf}$ stoichiometry.[65] The extent of Ni reduction in these samples was measured from temperature-programmed reduction (TPR) using a Quantasorb analyzer (Quantachrome Corporation Model 05-10), using procedures reported previously,[62] from the amount of H_2 consumed during temperature ramping to 1123 K (at 0.167 K s^{-1}) in a flowing 20% H_2/Ar mixture (6.7 $cm^3\ g^{-1}\ s^{-1}$).

Catalyst samples (0.030 g) were treated again within the balance chamber in flowing H_2 at reaction temperature (843-973 K) for 0.5 h before reaction. Carbon formation rates were measured during CH_4 reforming reactions at 843-973 K using a tapered-element oscillating quartz microbalance (TEOM; Ruprecht and Patashnick, Series 1500 PMA) in a flow-through sample holder that ensured plug-flow hydrodynamics at all inlet CH_4 (50% CH_4/Ar, Matheson, UHP, certified mixture), CO_2 (50% CO_2/Ar, Matheson UHP, certified mixture), CO (Matheson, 99.9%), H_2 (Airgas, 99.999%), and H_2O (>17.9 MΩ-cm resistivity; introduced by syringe pump, ISCO Model 500D) pressures and residence times (and chemical conversion). These TEOM systems measure the mass of samples placed at the tip of a quartz element using changes in its oscillation frequency, thus avoiding the corrections for buoyancy typically required for gravimetric data.

The composition of effluent streams was continuously monitored by on-line mass spectrometry (Leybold Inficon Transpector). Forward CH_4 reforming rates (r_f), normalized per initially exposed Ni atom measured from H_2 uptakes, were calculated by correcting measured rates (r_n) for approach to equilibrium (η) using:

$$r_n = r_f\,(1 - \eta) \tag{4}$$

The approaches to equilibrium for CH_4-CO_2 (Eq. 5) and CH_4-H_2O (Eq. 6) reforming reactions are defined as:

$$\eta_{\mathrm{DRM}} = \frac{(\mathrm{CO})^2(\mathrm{H_2})^2}{(\mathrm{CH_4})(\mathrm{CO_2})} \times \frac{1}{\mathrm{K_{DRM}}} \quad (5)$$

$$\eta_{\mathrm{SRM}} = \frac{(\mathrm{CO})(\mathrm{H_2})^3}{(\mathrm{CH_4})(\mathrm{H_2O})} \times \frac{1}{\mathrm{K_{SRM}}} \quad (6)$$

where K_{DRM} and K_{SRM} are the equilibrium constants for the respective CH_4 reforming reaction at a given temperature.[66] The absence of interparticle and intraparticle mass transport artifacts was confirmed by turnover rates that were independent of the extent of interparticle and intraparticle dilution with an inert material.[62]

Transmission electron micrographs (TEM) of fresh and spent catalyst samples were obtained using a JEOL 2010 electron microscope at accelerating voltages of 200 keV. TEM samples were prepared by crushing powder samples in an agate mortar, suspending the fine powders in isopropanol, placing a drop of the suspension on a porous carbon copper grid, and allowing the liquid to evaporate in ambient air. Micrographs were obtained from regions of the sample that minimized interference with the porous carbon copper grid. Ni crystallites were identified by contrast differences arising from the stronger electron scattering of Ni atoms relative to the Mg and O atoms in the support. Ni crystallite size distributions were measured manually from enlarged prints made from digitized negatives by counting more than 400 crystallites for each sample. Carbon filaments and encapsulating deposits were identified by repeating layered patterns of strong and weak electron scattering, representing the layered structure of such carbon deposits, which are absent from the support material and Ni crystallites. The spacing of these layers and filament diameters were measured from enlarged prints.

2.3 Results and Discussion

2.3.1 Catalyst Characterization

The size distribution of supported Ni nanoparticles was measured by transmission electron microscopy (TEM). Surface-averaged Ni cluster diameters $< d_s >$ were calculated from:[34]

$$< d_s >= \frac{\sum(n_i d_i^3)}{\sum(n_i d_i^2)} \quad (7)$$

where n_i is the number of clusters with diameter d_i. These values were 5.4, 11.1, and 11.0 nm for 7% wt., 15% wt. Ni/MgO-A and 7% wt. Ni/MgO-B, respectively. The respective extents of Ni reduction (from TPR, reported previously for these catalysts)[62] were 28%, 46%, and 43%. The remaining refractory Ni^{2+} species are likely present in a solid-solution with the MgO support, the formation of which has been observed at such high temperature treatments.[67] Such compounds are unlikely to catalyze CH_4-CO_2 and CH_4-H_2O reactions or the formation of carbon deposits. The fractional dispersions of Ni, defined as the number of exposed Ni atoms measured from H_2 chemisorption divided by the number of reduced Ni metal atoms, as determined from reduction measurements, were 0.14, 0.10, and 0.09, respectively. These dispersions were also used to estimate average crystallite diameters by assuming spherical Ni particle geometries using:[68]

$$D = 1/d \quad (8)$$

where D is the fractional dispersion and d is the crystallite diameter (in *nm*). These fractional Ni dispersion values led to average cluster diameters of 6.7, 10.4 and 10.8 nm for 7%, 15% wt. Ni/MgO-A and 7% wt. Ni/MgO-B samples, respectively, which agree well with TEM-derived $\langle d_s \rangle$ values. Such agreement also provides additional evidence that the remaining refractory Ni^{2+} species are not present within the Ni nanoparticles.

2.3.2 Mathematical Descriptions of Carbon Diffusion Through Ni Nanoparticles and of Carbon Filament Formation

The rate of filament growth on Ni catalysts is limited by the rate of carbon diffusion (normalized by the particle surface area; J_C) through the Ni particles.[13, 23-26] A one-dimensional diffusion model (in z) gives J_C in terms of the gradient in chemical potential of dissolved carbon, referenced to graphite:[25]

$$J_C = -\frac{D_C c_C}{RT}\frac{d\mu_C}{dz} \tag{9}$$

Here, D_C is the diffusion coefficient of carbon within Ni, c_C is the concentration of carbon, R is the ideal gas constant, and T is the absolute temperature. Substituting the definition of chemical potential (Eq. 1) into Equation 9 yields:

$$J_C = -\frac{D_C}{\gamma_C}\frac{da_c}{dz} \tag{10}$$

where γ_C is the activity coefficient of dissolved carbon within Ni. The activity coefficient is independent of concentration (and therefore position) for low solute concentrations. Equation 10 can therefore be integrated to give:

$$J_C = \frac{D_C^*}{d_p}\left[\left(a_{C,Ni}\right)_{\mathrm{s}} - \left(a_{C,Ni}\right)_{\mathrm{fil}}\right] \tag{11}$$

$$D_C^* = \frac{D_C}{\gamma_C} \tag{12}$$

where d_p is the particle diameter.

Dissolved carbon atoms at the surface-bulk interface are in equilibrium with those at the surfaces.[25-26, 30, 33] The thermodynamic activity at the free surface $(a_{C^*})_{\mathrm{s}}$ and at the filament $(a_{C^*})_{\mathrm{fil}}$ can therefore be related to the activity of dissolved carbon at each of these interfaces through a factor c^0 representing the proportionality between the reference states of dissolved carbon (in equilibrium with graphite) and surface carbon (a Henry's law constant), such that:

$$\left(a_{C,Ni}\right)_{\mathrm{s}} = c^0(a_{C^*})_{\mathrm{s}} \tag{13}$$

$$\left(a_{C,Ni}\right)_{\mathrm{fil}} = c^0(a_{C^*})_{\mathrm{fil}} \tag{14}$$

Equation 11 can then be written as:

$$J_C = \frac{D_C^* c^0}{d_p}[(a_{C^*})_s - (a_{C^*})_{fil}] \quad (15)$$

Figure 1 shows a graphical representation of this diffusion and filament formation process depicted as a one-dimensional process. The carbon diffusion rates that govern filament growth are thus proportional to $(a_{C^*})_s$, the value of which is set by the elementary steps that mediate CH_4-H_2O and CH_4-CO_2 reactions at the Ni catalyst surfaces.[62]

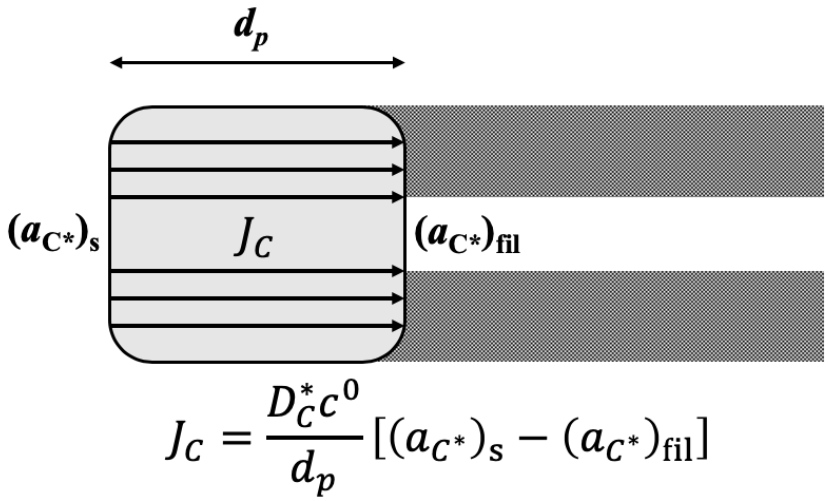

Figure 1. Carbon diffusion and filament formation model for Ni particles. D_C^* is the diffusivity of carbon in Ni, c^0 is the Henry's law constant relating the surface carbon and dissolved carbon phases, d_p is the diameter of the Ni particle, $(a_{C^*})_s$ is the thermodynamic carbon activity at the free metal surface, and $(a_{C^*})_{fil}$ is the thermodynamic carbon activity at the metal-filament interface.

2.3.3 Mechanism-Based Surface Carbon Activities and their Implications for Carbon Formation during CH_4 Reforming

A sequence of elementary steps for CH_4-CO_2 and CH_4-H_2O reactions was previously shown to accurately describe measured reaction rates on Ru,[69] Rh,[70] Ir,[71-72] Pt, [73] and Ni[62] catalysts (Scheme 1). These steps also include implicitly those required for chemical reactions typically denoted as CH_4 decomposition, Boudouard, and water-gas shift. Previous isotopic tracing experiments showed that CH_4 chemical conversion rates were much faster than isotopic cross-exchange rates ($CH_{4-x}D_x$ formation rates) for $CH_4/CD_4/CO_2$ or $CH_4/CD_4/H_2O$ (1:1:2) mixtures at 823-973 K on all catalysts (Ru, Rh, Ni, Ir and Pt), reflecting the irreversibility of C-H bond activation (Scheme 1, step 1.1) during CH_4 reforming reactions.[62, 69-73] The quasi-equilibrated nature of CO_2 dissociation (Scheme 1, step 1.5) and CO desorption (Scheme 1, step 1.7) was confirmed by the identical ^{13}C contents observed in CO and CO_2 molecules during reactions of $^{13}CO/^{12}CO_2/^{12}CH_4$ (0.4:1:1) mixtures at 823-973 K on all metal catalysts.[62, 69-73] $CH_4/CO_2/D_2$ (1:1:0.2) mixtures led to binomial distributions of deuterium isotopologs of dihydrogen and water at all reactant conversions on these catalysts.[62, 69-73] Thus, the recombinative desorption of H-atoms and OH-groups to form H_2 or H_2O (Scheme 1, steps 1.8-1.10) must also be quasi-equilibrated during CH_4 reforming catalysis. These mechanistic conclusions and the application of the pseudo-steady-state approximation (PSSA) for all surface intermediates give an expression that relates the

prevalent concentration of carbon at surfaces ($C*$) during steady-state CH_4-H_2O and CH_4-CO_2 reactions to the prevalent contacting pressures of reactants and products, as described below.

$$CH_4 + 2* \underset{k_{-1}}{\overset{k_1}{\rightleftharpoons}} CH_3* + H* \quad [1.1]$$

$$CH_3* + * \underset{k_{-2}}{\overset{k_2}{\rightleftharpoons}} CH_2* + H* \quad [1.2]$$

$$CH_2* + * \underset{k_{-3}}{\overset{k_3}{\rightleftharpoons}} CH* + H* \quad [1.3]$$

$$CH* + * \underset{k_{-4}}{\overset{k_4}{\rightleftharpoons}} C* + H* \quad [1.4]$$

$$CO_2 + 2* \overset{K_5}{\rightleftharpoons} CO* + O* \quad [1.5]$$

$$C* + O* \underset{k_{-6}}{\overset{k_6}{\rightleftharpoons}} CO* + * \quad [1.6]$$

$$CO* \overset{K_7}{\rightleftharpoons} CO + * \quad [1.7]$$

$$H_2 + 2* \overset{K_8}{\rightleftharpoons} 2H* \quad [1.8]$$

$$H_2O + 2* \overset{K_9}{\rightleftharpoons} OH* + H* \quad [1.9]$$

$$OH* + * \overset{K_{10}}{\rightleftharpoons} O* + H* \quad [1.10]$$

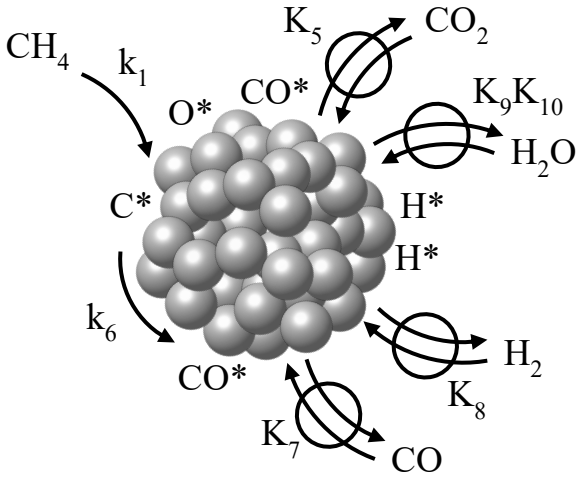

Scheme 1. Identity and reversibility of elementary steps for CH_4 reforming catalytic sequences on Ni catalysts

The application of the PSSA to C* during CH_4-CO_2 and CH_4-H_2O reforming at conditions far from equilibrium of this reaction leads to $(a_{C^*})_s$ values (details in Section 2.6.1) given by:

$$\frac{(a_{C^*})_s}{(L)} = \alpha\chi\frac{(1+\omega(a_{C^*})_{fil})}{(1+\omega\alpha\chi(L))} = \beta\psi\frac{(1+\omega(a_{C^*})_{fil})}{(1+\omega\beta\psi(L))} \tag{16}$$

$$\alpha = \frac{k_1}{k_6 K_5 K_7} \tag{17}$$

$$\beta = \frac{k_1 K_8}{k_6 K_9 K_{10}} \tag{18}$$

$$\omega = \frac{D_C^* c^0}{d_p(L)}\frac{1}{k_1(CH_4)} \tag{19}$$

Here, χ and ψ represent the $\frac{(CH_4)(CO)}{(CO_2)}$ and $\frac{(CH_4)(H_2)}{(H_2O)}$ pressure ratio, respectively, and (L) is the concentration of exposed surface metal atoms. This equation was derived by assuming, as evidenced from experiments, that CH_4 dissociative adsorption (Scheme 1, steps 1.1-1.4) and the reaction of C*-O* (Scheme 1, step 1.6) are irreversible at reaction conditions far from CH_4 reforming equilibrium (except by the extent required by microscopic reversibility) and there are no significant coverages of intermediates during steady-state CH_4 reforming catalysis. The parameters, α and β, are proportional to each other through the equilibrium constant for water-gas shift (K_{WGS}) at a given temperature because this reaction was equilibrated at all reforming conditions in this study:

$$\alpha = K_{WGS}\beta \tag{20}$$

The surface concentration of carbon ($C*$) is equivalent to its thermodynamic activity $(a_{C^*})_s$ here. Equation 15 can therefore be rewritten to obtain an expression for the rate of carbon formation (per surface Ni; r_C):

$$\begin{aligned} r_C = \frac{J_C}{(L)} &= \frac{D_C^* c^0}{d_p(L)}\left[\alpha\chi(L)\frac{(1+\omega(a_{C^*})_{fil})}{(1+\omega\alpha\chi(L))} - (a_{C^*})_{fil}\right] \\ &= \frac{D_C^* c^0}{d_p(L)}\left[\beta\psi(L)\frac{(1+\omega(a_{C^*})_{fil})}{(1+\omega\beta\psi(L))} - (a_{C^*})_{fil}\right] \end{aligned} \tag{21}$$

An additional assumption, relaxed later for experiments where it is inaccurate, that the rates of carbon transport into the Ni-C solid solution are much smaller than the rates of C* formation from CH_4 decomposition (Scheme 1, steps 1.1-1.4) and C* removal by reaction between C* and O* (Scheme 1, step 1.6) leads to:

$$r_C = \frac{J_C}{(L)} = \frac{D_C^* c^0}{d_p(L)}[\alpha\chi(L) - (a_{C^*})_{fil}] = \frac{D_C^* c^0}{d_p(L)}[\beta\psi(L) - (a_{C^*})_{fil}] \tag{22}$$

The mechanism-based model represented by Equations 21 and 22 thus relates the carbon diffusion and filament formation rate to the prevalent gas phase composition at steady-state conditions away

from chemical equilibrium of CH_4 reforming reactions. When reforming turnover rates are much larger than filament growth rates, it leads to values of the latter that are single-valued functions of χ (or ψ) (Eq. 22).

2.3.4 Measured Effects of χ and ψ on Carbon Deposition Rates

Carbon formation rates were measured at different inlet CH_4, CO_2, CO, H_2, and H_2O concentrations and residence times, resulting in a broad range of χ and ψ values (0-10 kPa and 0-24 kPa, respectively) during catalytic reactions of CH_4-CO_2 and CH_4-H_2O reforming. These χ and ψ ratios are calculated from the mean pressures for all chemical species along the reactor.

Figure 2 shows CH_4-CO_2 turnover rates (normalized per initially exposed Ni atom), carbon formation rates (at near the detection limit), and the cumulative amount of carbon formed on 7% Ni/MgO-A as a function of the time elapsed since its initial contact with the reacting stream for a χ value of 1.01 kPa (ψ = 2.47 kPa; 22.5 kPa CH_4, 27.5 kPa CO_2 feed) at 873 K. Carbon formation rates were nearly undetectable (< 0.05 C Ni_{surf}^{-1} s^{-1}; Fig. 2b) because the prevalent surface carbon activity $(a_{C^*})_s$ was insufficient to nucleate carbon filaments. CH_4-CO_2 turnover rates did not change with time (Fig. 2a) because the $(a_{C^*})_s$ value did not lead to kinetically-detectable C* coverages on Ni surfaces, consistent with the small amounts of carbon deposited on Ni particles, as observed in TEM images of this sample (Fig. 3a). Such behavior is characteristic of CH_4-CO_2 and CH_4-H_2O reactions on this catalyst at χ values below 1.1 kPa (or ψ < 2.7 kPa; 873 K); this range of values defines what is denoted here as regime I.

Figure 4 shows CH_4-CO_2 turnover rates (normalized per initially exposed Ni atom), carbon deposition rates, and the cumulative amount of carbon deposited as a function of the time elapsed on 7% Ni/MgO-A since its initial contact with the CH_4-CO_2 stream at χ values of 2.16 kPa (ψ = 5.29 kPa; 25 kPa CH_4, 15 kPa CO_2 feed) and 3.74 kPa (ψ = 9.16 kPa; 25 kPa CH_4, 10 kPa CO_2 feed) at 873 K. CH_4 reforming turnover rates remained essentially constant with time (Fig. 4a), even after the deposition of carbon quantities corresponding to very large C/Ni_{surf} ratios (~800; Fig. 4c). Such large extents of carbon deposition are consistent with the presence of filamentous carbon structures affixed to nearly all nanoparticles, as evident in TEM images of samples exposed to these environments (Fig. 3b). The rate of carbon formation (Fig. 4b) shows an initial increase upon contact with the reacting mixture, consistent with an induction period associated with the stochastic assembly of the number of C-atoms required to nucleate the filamentous carbon phase. This process becomes more probable as the activity of the carbon species at the surface of Ni nanoparticles increases with increasing χ or ψ values.[9, 56] Consequently, larger values of χ or ψ (and of carbon activity) lead to shorter induction periods (Fig. 4b). Carbon deposition rates ultimately reached a near constant value with time. These nearly constant carbon deposition and CH_4 turnover rates indicate that Ni surfaces remain accessible for C-H activation events (Scheme 1, step 1.1), in spite of the prevalence of affixed filamentous carbon structures, and that C* surface coverages do not change with time. C* species formed from CH_4 are removed via reactions with either H* (Scheme 1, step 1.4) or O* (Scheme 1, step 1.6), or via diffusion through the particle and deposition at the carbon filament. The low steady-state C* coverages (and $(a_{C^*})_s$ values) here require that the rates of removal be sufficient to maintain such low coverages even as the activity of C* increases with increasing χ values between 1.1 and 4.2 kPa (ψ = 2.7-10.3 kPa; 873 K), a range of carbon activity that we denote here as regime II.

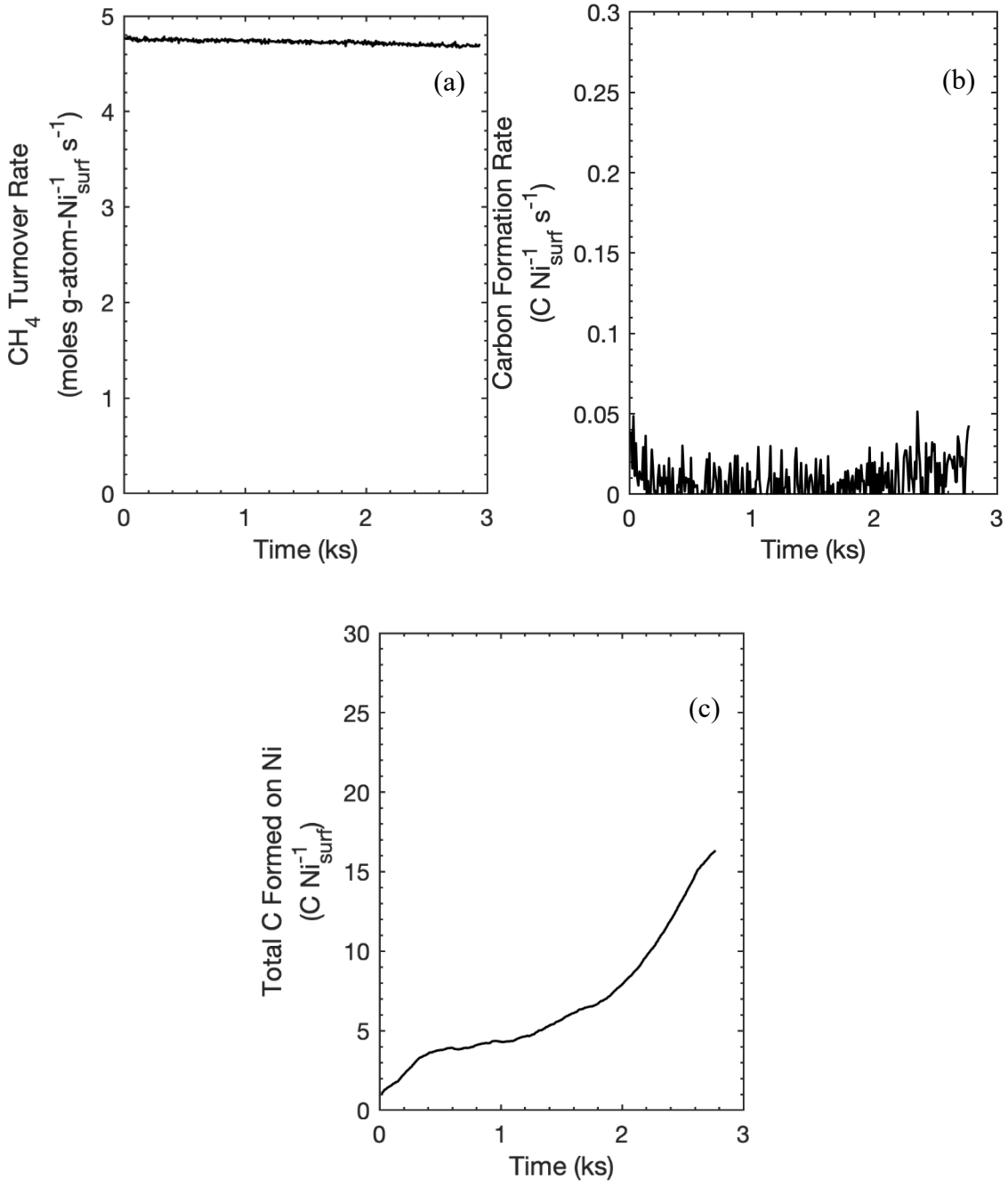

Figure 2. CH_4 reforming turnover rate (a), carbon formation rate (per surface Ni) (b), and total carbon accumulated on Ni surface (c) as functions of time on stream on 7 % wt. Ni/MgO-A at χ = 1.01 kPa (ψ = 2.47 kPa; 22.5 kPa CH_4, 27.5 kPa CO_2 feed) during CH_4-CO_2 reaction at 873 K (regime I). Reaction conditions were far from CH_4 reforming equilibrium.

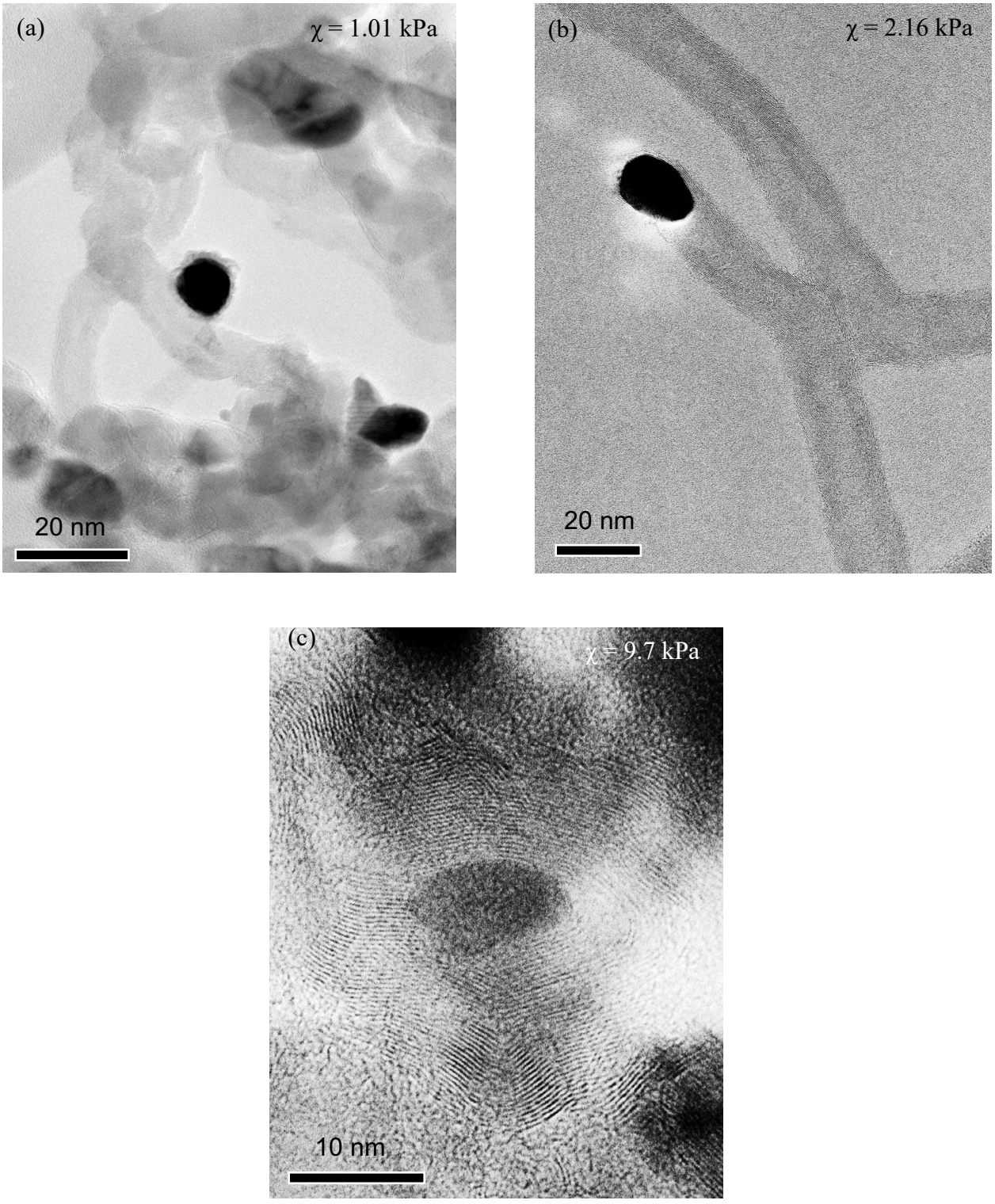

Figure 3. Transmission electron micrographs of carbon morphology after CH_4-CO_2 reaction on 7 % wt. Ni/MgO-A at 873 K and (a) χ = 1.01 kPa (ψ = 2.47 kPa) (b) χ = 2.16 kPa (ψ = 5.29 kPa) and (c) χ = 9.7 kPa (ψ = 23.8 kPa).

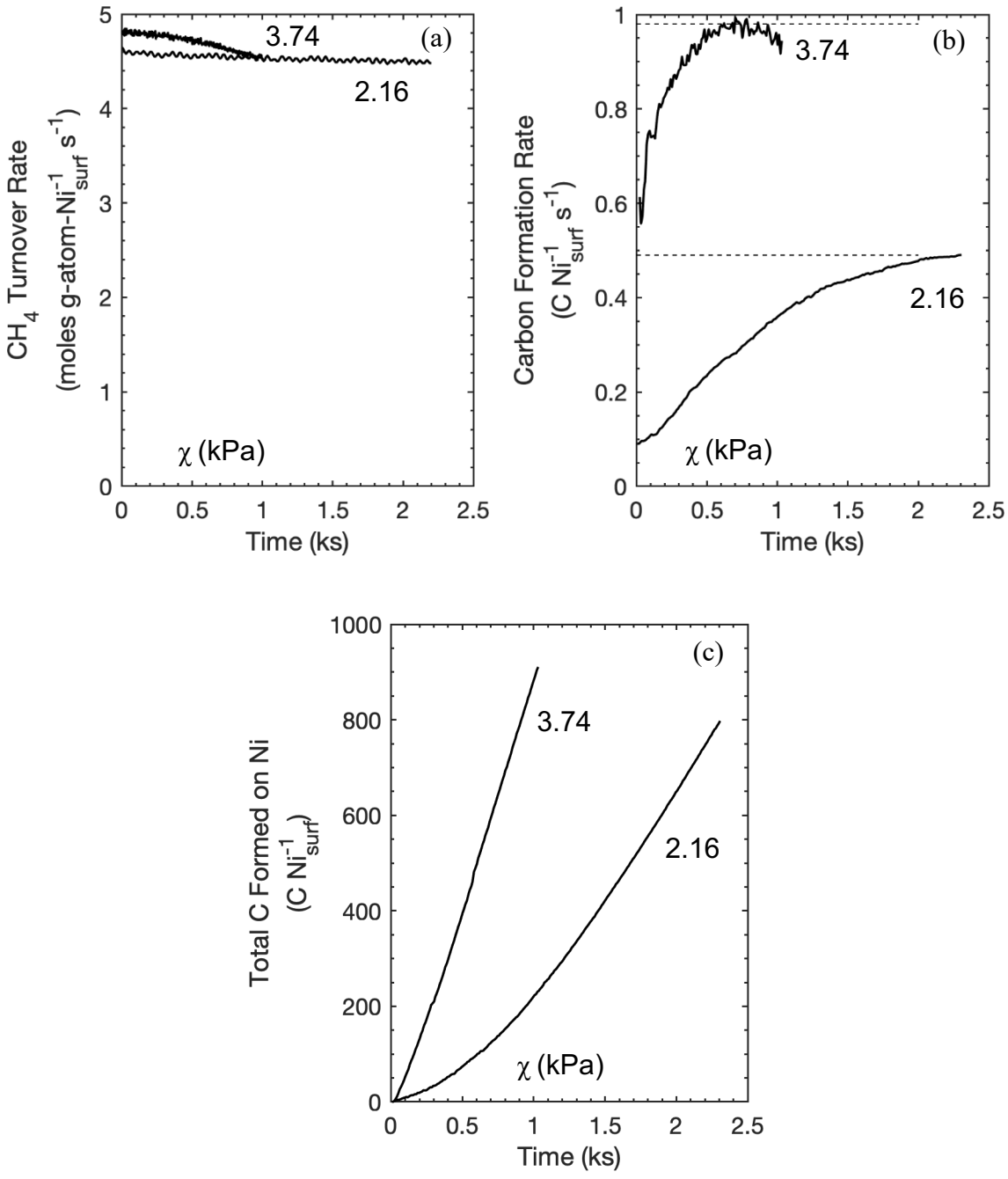

Figure 4. CH_4 reforming turnover rate (a), carbon formation rate (per surface Ni) (b), and total carbon accumulated on Ni surface (c) as functions of time on stream on 7 % wt. Ni/MgO-A at χ = 2.16 kPa (ψ = 5.29 kPa; 25 kPa CH_4, 15 kPa CO_2 feed) and 3.74 kPa (ψ = 9.16 kPa; 25 kPa CH_4, 10 kPa CO_2 feed) during CH_4-CO_2 reaction at 873 K (regime II). Dotted lines added to guide the eye. Reaction conditions were far from CH_4 reforming equilibrium.

Figure 5 shows CH_4-CO_2 turnover rates (normalized per initially exposed Ni atom), rates of formation of carbon filaments, and the total amount of carbon deposited on 7% Ni/MgO-A as a function of the time elapsed since initial contact with the CH_4-CO_2 stream for a χ value of 5.3 kPa (ψ = 13 kPa; 873 K; 25 kPa CH_4, 5 kPa CO_2 feed). CH_4 reforming rates decreased monotonically with time (Fig. 5a), while carbon formation rates (Fig. 5b) showed a brief induction period (100 seconds), during which rates initially increased as carbon supersaturation and nucleation processes occurred, followed by a relatively constant carbon deposition rate, and ultimately a gradual decrease in rate with time. At these high χ and ψ values, the concomitant high carbon activity leads to the simultaneous incipient nucleation of filament precursors at several locations on a given nanoparticle and to their ultimate coalescence to form carbon layer structures that block active surfaces for C-H activation reactions (Fig. 3c). These processes lead to a concurrent decrease in CH_4 reforming and carbon formation rates with time for such χ and ψ values (Fig. 5a and 5b, respectively). This behavior was observed on 7% Ni/MgO-A samples at χ values above 4.2 kPa (ψ > 10.3 kPa; 873 K), which is denoted here as regime III.

Carbon formation rates increased monotonically with increasing χ and ψ values in regimes II and III during steady-state catalytic reactions of CH_4-CO_2 and CH_4-H_2O. Figure 6 shows steady-state carbon formation rates at 873 K as a function of χ and ψ ratios on 7% Ni/MgO-A. At the intermediate values of χ (or ψ) corresponding to regime II, steady-state carbon formation rates are proportional to χ or ψ values and reflect rates predicted by the functional form of Equation 22 for diffusion-limited filament growth.

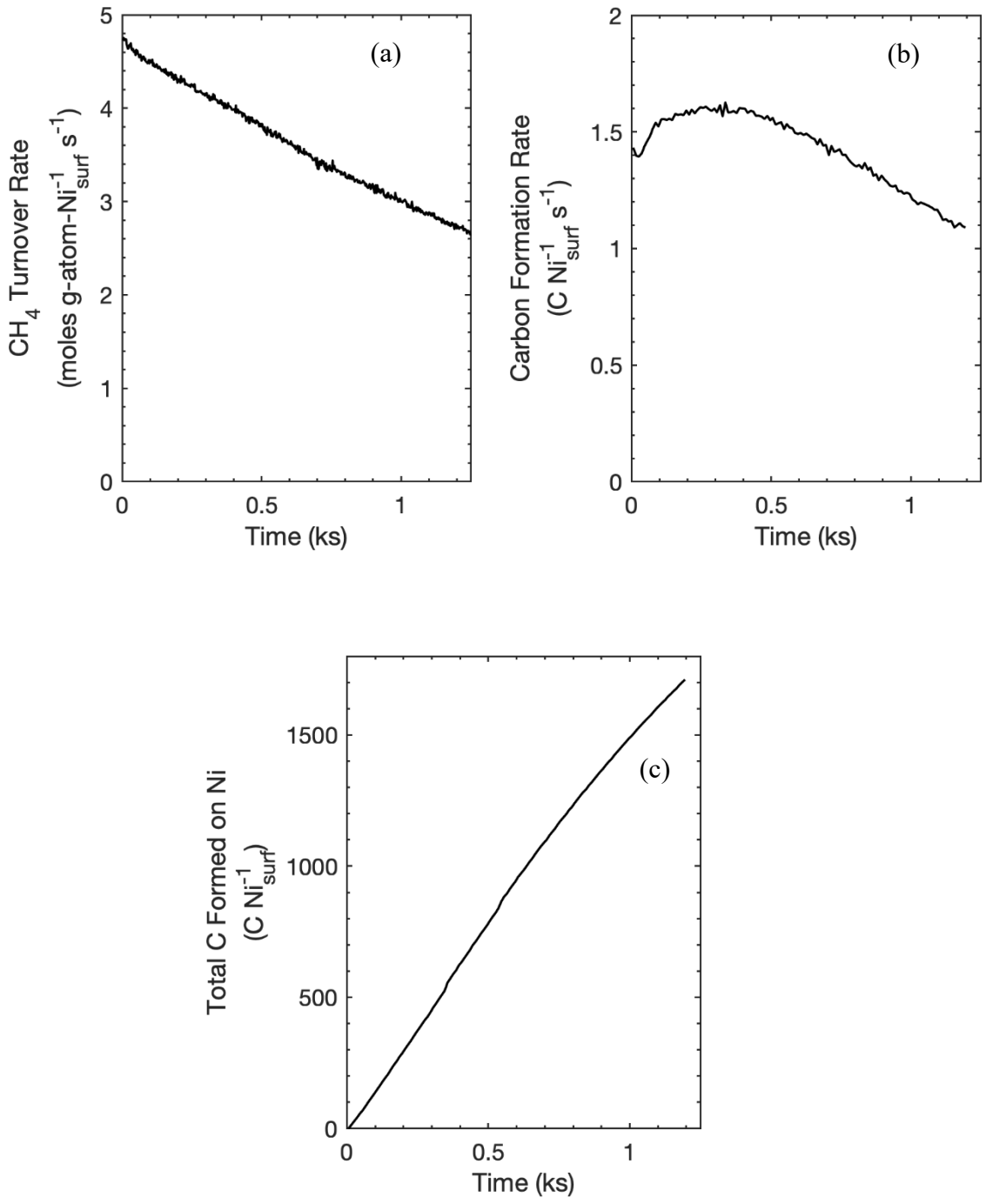

Figure 5. CH_4 reforming turnover rate (a), carbon formation rate (per surface Ni), (b) and carbon accumulated on Ni surface (c) as functions of time on stream on 7 % wt. Ni/MgO-A at χ = 5.3 kPa (ψ = 13 kPa; 25 kPa CH_4, 5 kPa CO_2 feed) during CH_4-CO_2 reaction at 873 K (regime III). Reaction conditions were far from CH_4 reforming equilibrium.

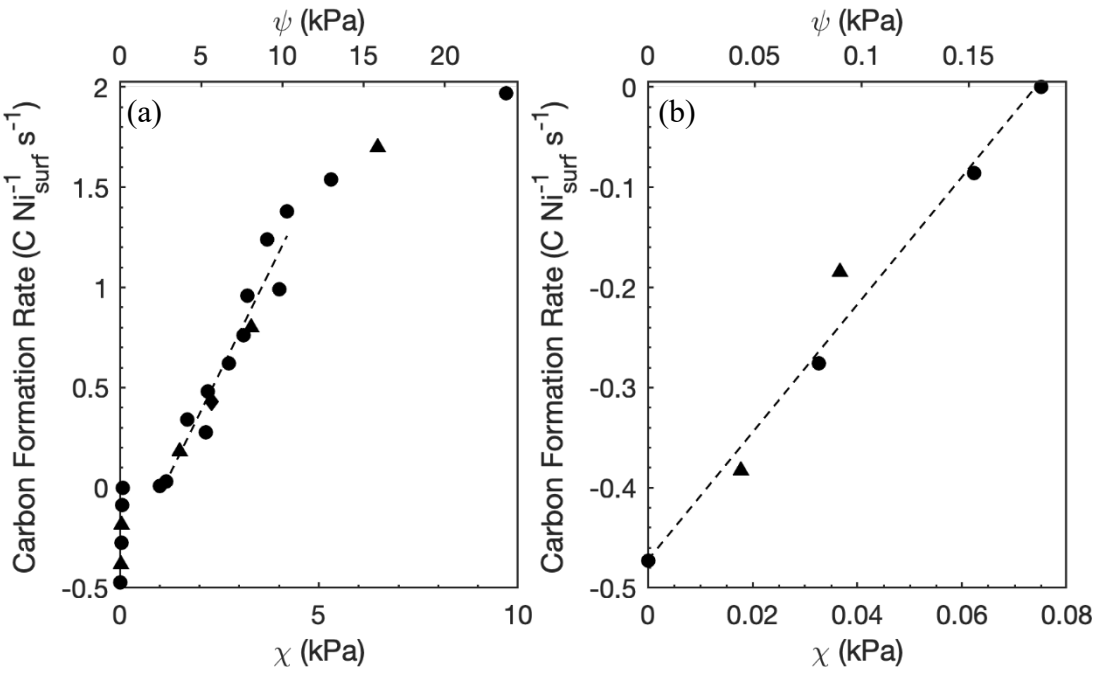

Figure 6. (a) Carbon formation rates vs. χ ($P_{CO}P_{CH4}/P_{CO2}$) or ψ ($P_{H2}P_{CH4}/P_{H2O}$) on 7% wt. Ni/MgO-A at 873 K with a magnified view (b) of carbon removal (regime IV). $P_{CO}P_{CH4}/P_{CO2}$ or $P_{H2}P_{CH4}/P_{H2O}$ ratios were changed by varying inlet CH_4, CO_2, CO, H_2, or H_2O partial pressures and/or space velocity during CH_4/CO_2 and CH_4/H_2O reactions. (●) CH_4/CO_2 reaction, (▲) CH_4/H_2O reaction, and (◆) CH_4/CO_2 reaction with addition of H_2. Dashed lines drawn to guide the eye and determined by linear best fit methods.

The linear dependence of carbon formation rates on χ (or ψ) in regime II can be used to obtain lumped parameters associated with the slope $\left(\frac{D_C^* c^0}{d_p}\alpha\right)$ and y-intercept $\left(\frac{D_C^* c^0}{d_{p(\mathrm{L})}}(a_{C^*})_{\mathrm{fil}}\right)$ (Eq. 22). This $\left(\frac{D_C^* c^0}{d_{p(\mathrm{L})}}(a_{C^*})_{\mathrm{fil}}\right)$ term represents the rate of carbon transport (per surface Ni) from the filament to a bare Ni surface. The product of ω ($\frac{D_C^* c^0}{d_{p(\mathrm{L})}}\frac{1}{\mathrm{k_1(CH_4)}}$; Eq. 19) and $(a_{C^*})_{\mathrm{fil}}$ in the numerator of Equations 16 and 21 therefore represents the ratio of this rate to that of carbon formation from CH_4 decomposition on sparsely covered Ni nanoparticle surfaces ($\mathrm{k_1(CH_4)}$; Scheme 1, step 1.1). These two rates were 0.41 ± 0.04 and 4.7 ± 0.1 C Ni_{surf}^{-1} s^{-1}, respectively, for χ (or ψ) values in regime II (χ = 1.1-4.2 kPa, ψ = 2.7-10.3 kPa; 25 kPa CH_4; 873 K); such values lead to $\omega(a_{C^*})_{\mathrm{fil}}$ values between 0.08 and 0.1. These small values influence only slightly the $(1+\omega(a_{C^*})_{\mathrm{fil}})$ term in the numerator of Equations 16 and 21, consistent with the single-valued dependence on χ (or ψ) observed in regime II (Fig. 6a).

The $\omega\alpha\chi(\mathrm{L})$ term in the denominator of Equations 16 and 21 represents the ratio of the rate of carbon diffusion from the Ni surface $\left(\frac{D_C^* c^0}{d_p}\alpha\chi\right)$, at conditions where such rates are insufficient to perturb the surface carbon activity $(a_{C^*})_s$, to that of C-H activation events ($\mathrm{k_1(CH_4)}$; Scheme

1, step 1.1). The linear trend in regime II (χ = 1.1-4.2 kPa, ψ = 2.7-10.3 kPa; 873 K; Fig. 6a) suggests that carbon transport rates in this regime are insufficient to perturb $(a_{C^*})_s$ and therefore obey the functional form of Equation 22, allowing $\left(\frac{D_C^* c^0}{d_p}\alpha\chi\right)$ to be extracted from these data (< 1.6 C Ni_{surf}^{-1} s^{-1}). CH_4 turnover rates were between 4.6 and 4.8 C Ni_{surf}^{-1} s^{-1} ($k_1(CH_4)$; Scheme 1, step 1.1; 25 kPa CH_4) for these conditions. These rates lead to $\omega\alpha\chi(L)$ values below 0.34, which lead, in turn, to small (but measurable) effects on $(1+\omega\alpha\chi(L))$ in the denominator of Equations 16 and 21 and to an expectation of some curvature in the trends of carbon formation rates with χ at the higher values of χ in regime II. The $(1+\omega\alpha\chi(L))$ term, however, is partially offset by the $(1+\omega(a_{C^*})_{fil})$ term (1.08-1.1) in the numerator (Eq. 16 and 21), which causes the linear trends to persist throughout regime II. These considerations illustrate the caution required in applying the model described by Equation 22 as carbon transport rates become similar to the rates of carbon formation (Scheme 1, step 1.1-1.4) or removal (Scheme 1, step 1.6), as in the case of regime III described below.

At even higher values of χ (or ψ) (regime III; χ > 4.2 kPa, ψ > 10.3 kPa; 873 K, 25 kPa CH_4), carbon formation rates, defined here as the maximum (and nearly constant) rates observed with time, do not increase linearly with the carbon activity. The carbon deposition rates in regime III (χ > 4.2 kPa, ψ > 10.3 kPa; 873 K) are below those predicted by extending the linear trends from regime II (Fig. 6a). This reflects, in part, the kinetically-detectable encapsulation of Ni nanoparticles by carbon adlayers, as shown by CH_4 reforming turnover rates that decreased with time (Fig. 5a). This trend also reflects the decrease in C* activity $(a_{C^*})_s$ caused by the high rates of C* removal by diffusion (1.6-2.0 C Ni_{surf}^{-1} s^{-1}, Fig. 6a) prevalent in regime III. This effect is captured by the $\omega\alpha\chi(L)$ term in the denominator of Equations 16 and 21, which represents the ratio of the rate of carbon diffusion away from the Ni surface $\left(\frac{D_C^* c^0}{d_p}\alpha\chi\right)$, when the surface carbon activity is unaffected by these diffusion processes, to the rate of CH_4 turnover on a bare surface ($k_1(CH_4)$; Scheme 1, step 1.1). The $\left(\frac{D_C^* c^0}{d_p}\alpha\chi\right)$ values can be estimated by extrapolating the linear trends from regime II (Fig. 6a), while the value of $k_1(CH_4)$ is given by CH_4 turnover rates (4.5-4.8 C Ni_{surf}^{-1} s^{-1}; 25 kPa CH_4; Fig. 5a), leading to $\omega\alpha\chi(L)$ values between 0.4 and 0.8, which lead, in turn, to lower carbon formation rates, as evident from Equation 21. Thus, the assumptions inherent in the derivation of Equation 22 are accurate only when the rates of carbon formation from CH_4 decomposition and removal by reaction between C* and O* are much higher than the rates of carbon transport into the Ni-C solid solution, conditions that are met in regimes I and II in this study.

2.3.5 Measured Effects of χ and ψ on Carbon Removal Rates

Previous studies have indicated that carbon removal processes occur when exposing Ni- or Fe-based catalysts to H_2O or H_2 environments.[35-36] The reversibility of filament formation processes was examined here by using low CH_4 pressures (and small χ values) (χ < 1.1 kPa, ψ < 2.7 kPa; 2.5 kPa CH_4; 873 K) on 7% Ni/MgO-A samples containing carbon filaments previously formed in regime II (χ = 2.16 kPa, ψ = 5.29 kPa; 25 kPa CH_4). These conditions were expected to consume such filaments via the reverse processes, as indicated by the form of Equation 22, and are denoted as regime IV. Gas compositions leading to χ values below 0.07 kPa (or ψ < 0.17 kPa;

2.5 kPa CH_4) at 873 K (after filament growth in regime II; χ = 2.16 kPa, ψ = 5.29 kPa) led to the removal of carbon at rates (Fig. 6b) that are linearly dependent on χ (and ψ) but which do not align with the linear trends in regime II (Fig. 6a), as would have been expected from Equation 22.

These results indicate that the low CH_4 pressure required to consume carbon filaments in regime IV leads to carbon diffusion rates from the filament that increase C* coverages over those present during steady-state catalysis in the absence of such filaments, thus requiring the functional form of Equation 21 to accurately describe carbon removal rates. Equation 21 allows estimates of the grouping of term associated with the y-intercept $\left(\frac{D_C^* c^0}{d_{p(\mathrm{L})}}(a_{C^*})_{\mathrm{fil}}\right)$, whose magnitude represents the rate of carbon diffusion from the filament to a bare Ni surface (0.47 ± 0.02 C Ni_{surf}^{-1} s^{-1}). This value is nearly identical to that obtained from the data in regime II (0.41 ± 0.04 C Ni_{surf}^{-1} s^{-1}; Section 2.3.4), as expected from carbon filament activities that are insensitive to the composition of the gas phase, and is similar to the CH_4 turnover rate expected at the CH_4 pressure used in regime IV ($k_1(CH_4)$; Scheme 1, step 1.1; 0.48 C Ni_{surf}^{-1} s^{-1}). These rates lead to a $(1 + \omega(a_{C^*})_{\mathrm{fil}})$ value of 2 in the numerator of Equations 16 and 21 and consequently an expectation of a two-fold larger slope in regime IV than in regime II. The observed slope for regime IV (6.4 ± 0.5; Fig. 6b) is 16-fold higher in regime IV than that in regime II (0.4 ± 0.03; Fig. 6a). Such a quantitative disagreement between the expected and observed slope may be caused by the formation of carbon patches that block active sites formed during the He purge that was used after the formation of the carbon filaments and before the carbon removal experiments.

The value of $\omega\alpha\chi(\mathrm{L})$ was estimated to be smaller than 0.07 at all conditions in regime IV by extrapolating the linear trends from regime II, described by the functional form of Equation 22, to determine the value of $\left(\frac{D_C^* c^0}{d_p}\alpha\chi\right)$; these small values of $\omega\alpha\chi(\mathrm{L})$ in the denominator of Equations 16 and 21 allow it to be neglected. Carbon removal rates in regime IV (χ < 1.1 kPa, ψ < 2.7 kPa; 2.5 kPa CH_4) therefore do not reflect the linear trends predicted by the functional form of Equation 22, but instead reflect an increase in the surface carbon activity caused by the diffusion of carbon from the filament to the free metal surface, which result in lower carbon removal rates than those predicted by extrapolating trends from regime II.

2.3.6 Electron Microscopy Evidence for the Morphology of Carbon Structures for Different Carbon Thermodynamic Activities

The morphologies of carbon deposits formed on Ni catalysts during CH_4-CO_2 and CH_4-H_2O reforming catalysis were determined by inspection of TEM images of samples exposed to conditions leading to regimes I, II, and III. The nature of the carbon structures (filamentous or encapsulating) was determined by the surface carbon activity $(a_{C^*})_s$, which led to distinct forms of carbon in regimes II and III and to the absence of detectable carbon structures in regime I (Section 2.3.4).

TEM images of 7% wt. Ni/MgO-A catalysts in regime I (Fig. 3a) do not show visible evidence of carbon deposits (χ = 1.01 kPa, ψ = 2.47 kPa, 873 K), consistent with CH_4 reforming rates that remained constant during contact with reacting mixtures (Fig. 2a) and with the small mass changes observed during steady-state reforming at these conditions (Fig. 2c). The absence of carbon filaments shows that the carbon activities $(a_{C^*})_s$ prevalent in regime I are too low to allow the widespread nucleation and growth of carbon filaments.

TEM images of 7% wt. Ni/MgO-A samples in regime II, (χ = 2.16 kPa, ψ = 5.29 kPa; 873 K; Fig. 3b) predominantly show multi-walled carbon filaments similar in diameter to the Ni nanoparticles affixed to their ends. These carbon filaments showed "fishbone"-like structures, with carbon layers angled relative to the axis of growth, but parallel to the crystallite surface. Such an ordered alignment of the carbon layers with the facets of the Ni particle on which they nucleate suggests that carbon atoms are systematically added to the filament; each carbon layer is completed before it is pushed away from the Ni surface and assembly of the next carbon layer begins. The interlayer spacing of approximately 0.35 nm at the filament walls (Fig. 7) is very similar to that expected for graphitic structures (0.34 nm) that are essentially free of residual H-atoms.[18]

Each filament formed in regime II contains a Ni nanoparticle affixed at one end and a part of each nanoparticle seemingly devoid of carbon deposits. Nanoparticles affixed at filament tips exhibit a "pear-shaped" nature (Fig. 3b and 7), which may reflect the significant restructuring required in order to accommodate the epitaxial growth of graphite-type layers that have been proposed to grow preferentially on Ni(111) and Ni(311) facets;[74-76] restructuring thus acts to preserve the other facets, such as the Ni(100) and Ni(110) surfaces that have been proposed to be favored for C-H activation.[11, 43, 77] Metal nanoparticles can exhibit liquid-like properties at reforming temperatures,[78-79] thus enabling the detachment of nanoparticle from the support and the adoption of these particle-filament arrangements. The clean surfaces, which may consist of (100) or (110) facets that are less likely to form epitaxial carbon layers,[11, 43, 77] can therefore continue to activate CH_4, leading to CH_4 reforming and carbon formation rates that remain essentially unchanged with time in regime II (Fig. 4a; Section 2.3.4), even as the extensive formation of filaments occurs (Fig. 4b and c; Section 2.3.4). The restructuring and reorienting of the metal crystallites due to interactions with hydrocarbons and subsequent filament growth are also conducive to the directional diffusion of carbon from the free metal surface to the carbon filament required to prevent the formation of encapsulating carbon adlayers, as reported in previous studies.[43, 63, 76, 80-83]

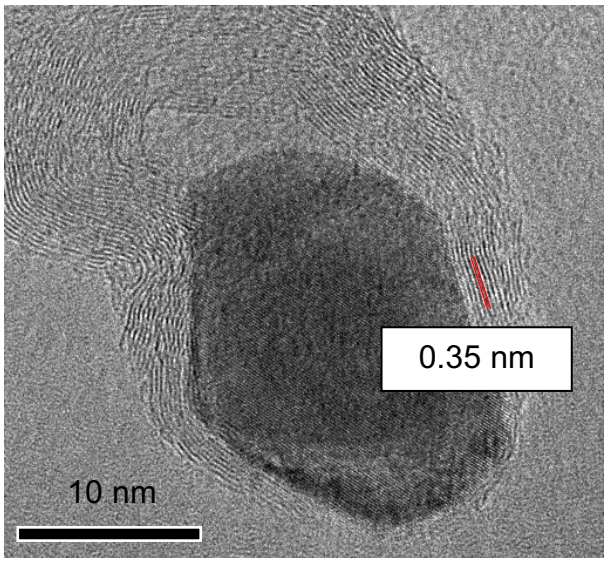

Figure 7. Transmission electron micrograph showing structure of carbon filament and interlayer spacing of graphite layers on 7 % wt. Ni/MgO-A after CH_4-CO_2 reaction at 873 K and χ = 2.16 kPa (ψ = 5.29 kPa).

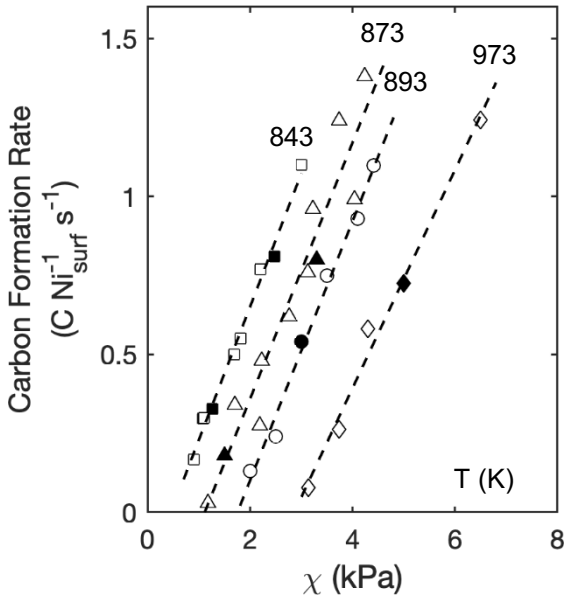

Figure 8. Carbon formation rates vs. χ ($P_{CO}P_{CH4}/P_{CO2}$) on 7 % wt. Ni/MgO-A during CH_4-CO_2 (open symbol) or CH_4-H_2O reactions (solid symbol) (□■ 843 K, △▲ 873 K, ○● 893 K, ◇◆ 973 K). Dashed lines determined by linear best fit models.

At 873 K and conditions of regime III (χ > 4.24 kPa; ψ > 10.4 kPa), TEM images show that CH_4 reforming on 7% wt. Ni/MgO-A causes the extensive encapsulation of Ni nanoparticles by onion-like carbon layers (Fig. 3c). Such structural motifs reflect the high carbon activity resulting from CH_4 reforming elementary steps at the conditions that lead to such large χ values. The resulting carbon supersaturation within Ni nanoparticles leads to the simultaneous nucleation of carbon patches as potential precursors to filament growth. These multiple carbon sinks lead, in turn, to a disruption of the unidirectional carbon activity gradient otherwise imposed by the presence of a single filament as the unique carbon sink. TEM images in regime III also show that Ni nanoparticles lack the "pear-shaped" character of those affixed to a filament (Fig. 3c vs. Fig. 3b). The formation of these encapsulating carbon structures causes a monotonic change in the fraction of the Ni nanoparticle surfaces that remain accessible for the activation of the C-H bonds in the step that limits CH_4 reforming rates and which form C* as products and, in doing so, sets the C* coverages that drive carbon diffusion and the rate of carbon deposition. Consequently, reforming and carbon deposition rates decrease monotonically with time in regime III (Fig. 6a and 6b; χ = 9.7 kPa, ψ = 23.8 kPa; Section 2.3.4). After complete encapsulation, Ni surfaces become inaccessible and cannot form active O* or H* species from gaseous reactants. As a result, exposure of these coated nanoparticles to low values of χ or ψ (χ < 1.1 kPa, ψ < 2.7 kPa; regime IV), which led to the removal of carbon from nanoparticles with affixed carbon filaments formed at the conditions of regime II (Fig. 6b; Section 2.3.5), did not lead to the removal of these carbon overlayers.

2.3.7 The Effects of CH_4 Reforming Reaction Temperature on Carbon Formation Rates

Carbon formation rates during CH_4-CO_2 and CH_4-H_2O reforming reactions were also measured on 7% wt. Ni/MgO-A at different temperatures (843-973 K) and χ (and ψ) values in

regime II, where carbon formation rates are strictly proportional to such χ (and ψ) values (Section 2.3.4). The data in Figure 8 show that carbon formation rates decreased with increasing temperature at each χ or ψ value. These temperature effects on carbon formation rates reflect the respective consequences of temperature for terms that account for the slope $\left(\frac{D_C^* c^0}{d_p}\alpha\right)$ and y-intercept $\left(\frac{D_C^* c^0}{d_{p(\mathrm{L})}}(a_{C^*})_{\mathrm{fil}}\right)$ in the functional form of Equation 22.

Figure 9 shows $\left(\frac{D_C^* c^0}{d_p}\alpha\right)$ values as a function of inverse temperature; all terms except the particle diameter (d_p) are expected to exhibit Arrhenius-like dependences. The data in Figure 9 give an effective energy barrier of -10 ± 2 kJ mol^{-1} for $\left(\frac{D_C^* c^0}{d_p}\alpha\right)$, which reflects the combined temperature effects on the diffusivity of carbon in Ni (D_C^*), its Henry's law constant (c^0), and the grouping of rate and equilibrium constants contained in α ($\frac{\mathrm{k_1}}{\mathrm{k_6 K_5 K_7}}$, Eq. 17; Scheme 1).

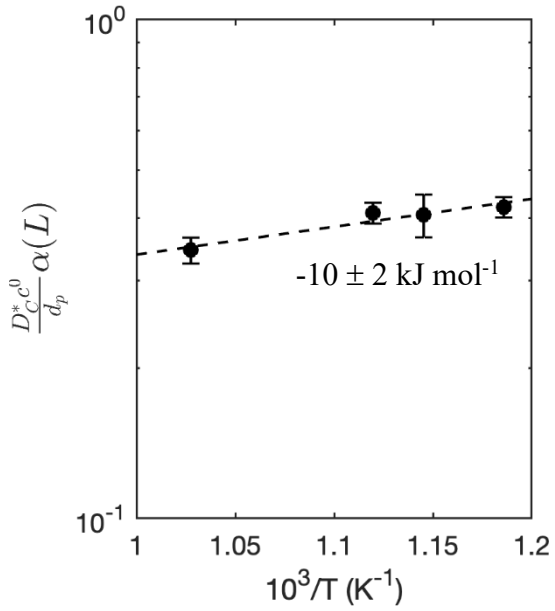

Figure 9. Arrhenius plot of $\frac{D_C^* c^0}{d_p}\alpha$(L). The carbon diffusivity in Ni D_C^*, Henry's Law constant c^0, and the group of kinetic and thermodynamic parameter α are expected to show temperature dependences. Dashed line was obtained through linear regression and reflects an effective energy barrier of -10 ± 2 kJ mol^{-1}.

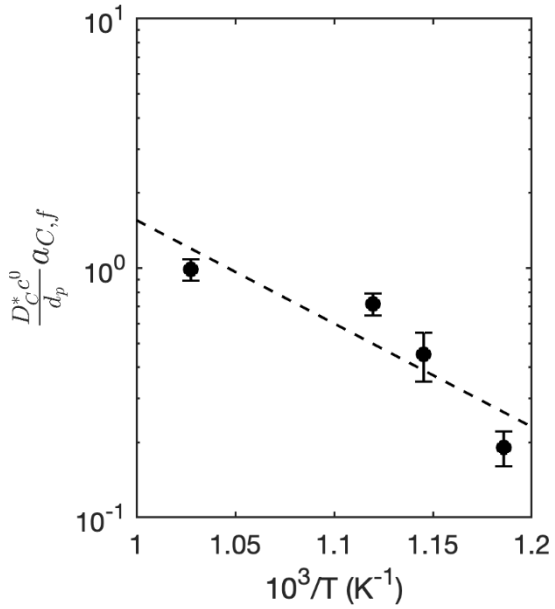

Figure 10. Arrhenius plot of $\frac{D_C^* c^0}{d_p}[(a_{C^*})_{\text{fil}}]$. The carbon diffusivity in Ni D_C^*, Henry's Law constant c^0, and the carbon filament activity $(a_{C^*})_{\text{fil}}$ are expected to show temperature dependences. Dashed line was obtained through linear regression and reflects an effective energy barrier of 95 ± 22 kJ mol^{-1}.

The activation energies and enthalpies for each of these terms can be obtained from the literature and used to evaluate the value reported here. Massaro and Petersen previously measured the diffusivity of carbon in Ni (D_C^*) using acetylene decomposition between 623 and 973 K and reported an activation energy barrier of 83 ± 5 kJ mol^{-1}.[84] Lander et al. measured the temperature dependence for the solubility of carbon in Ni, which is reflected in the Henry's law constant (c^0), and reported a dissolution enthalpy of -40 ± 1 kJ mol^{-1}.[85] The parameter α ($\frac{k_1}{k_6 K_5 K_7}$; Eq. 17) includes the rate constants for C-H activation (k_1; Scheme 1, step 1.1) and for C*-O* recombination (k_6, Scheme 1, step 1.6), and the equilibrium constants for CO_2 dissociative adsorption (K_5, Scheme 1, step 1.5) and molecular desorption of CO (K_7, Scheme 1, step 1.7). The temperature dependence of k_1 on these Ni-based catalysts, was previously found to be 105 ± 3 kJ mol^{-1}.[62] Snoeck et al. studied the gasification of carbon filaments on Ni-based catalysts using CO_2 at 773-848 K and used a mechanism-based rate equation to obtain k_6, K_5, and K_7 values.[86] They reported an activation energy of 244 ± 68 kJ mol^{-1} for k_6 along with the enthalpies associated with K_5 (-104 ± 85 kJ mol^{-1}) and K_7 (100 ± 61 kJ mol^{-1}).[86] The effective energy barrier calculated from the literature for $\left(\frac{D_C^* c^0}{d_p}\alpha\right)$, after rigorously propagating the respective uncertainties in the individual parameters, is therefore -12 ± 126 kJ mol^{-1}. This value is in agreement with that observed in this study (-10 ± 2 kJ mol^{-1}), though more precise measurements of the parameters k_6, K_5, and K_7 are needed to conclusively demonstrate this.

Figure 8 shows that $\left(\frac{D_C^* c^0}{d_{p(\mathrm{L})}}(a_{C^*})_{\mathrm{fil}}\right)$ values, reflected in the absolute value of the y-intercept in the carbon formation rates, increase with temperature. Figure 10 shows these $\left(\frac{D_C^* c^0}{d_{p(\mathrm{L})}}(a_{C^*})_{\mathrm{fil}}\right)$ values in a logarithmic scale as a function of inverse temperature, in which the slope corresponds to an effective energy barrier of 95 ± 22 kJ mol^{-1}.

This value can also be compared with literature values for the individual parameters in this term. The d_p and (L) terms are independent of temperature. The enthalpy of formation for carbon filaments was previously measured by de Bokx et al. (44 ± 4 kJ mol^{-1})[54] and accounts for the Arrhenius-like dependence of $(a_{C^*})_{\mathrm{fil}}$ term, which when combined with the temperature dependences of D_C^* and c^0 (83 ± 5 kJ mol^{-1} and 40 ± 1 kJ mol^{-1}, respectively; discussed above) gives an effective barrier of 79 ± 6 kJ mol^{-1} for $\left(\frac{D_C^* c^0}{d_{p(\mathrm{L})}}(a_{C^*})_{\mathrm{fil}}\right)$, in reasonable agreement with the value determined in the present study (95 ± 22 kJ mol^{-1}).

These data show that carbon formation rates decrease with increasing temperature, even though the diffusivity term $(D_C^* c^0)$ increases, because the coefficients that relate χ to $(a_{C^*})_{\mathrm{s}}$ (α; Eq. 17) show a compensating opposite trend, leading to similar values of $\left(\frac{D_C^* c^0}{d_p}\alpha\right)$ at different temperatures, as evident from the similar slopes in the data shown in Figure 8. The parameters reflected in the absolute value of the y-intercept $\left(\frac{D_C^* c^0}{d_{p(\mathrm{L})}}(a_{C^*})_{\mathrm{fil}}\right)$ become larger with increasing temperature. This trend reflects the temperature effects on the filament activity $(a_{C^*})_{\mathrm{fil}}$, which compensates for the increase in $(D_C^* c^0)$ values with increasing temperature. These combined temperature dependences for the parameters that define the $\left(\frac{D_C^* c^0}{d_p}\alpha\right)$ and $\left(\frac{D_C^* c^0}{d_{p(\mathrm{L})}}(a_{C^*})_{\mathrm{fil}}\right)$ terms lead to the observed lower carbon formation rates at higher temperatures for each given value of χ (Fig. 8).

The effects of temperature on $\left(\frac{D_C^* c^0}{d_p}\alpha\right)$ and $\left(\frac{D_C^* c^0}{d_{p(\mathrm{L})}}(a_{C^*})_{\mathrm{fil}}\right)$ also lead to a shift in the x-intercepts of the curves in Figure 8 toward higher values of χ as temperature increases. These intercepts represent the threshold value of χ (χ_{min}) required for the incipient growth of carbon filaments and the point at which $\alpha\chi(\mathrm{L})$ is equal to the activity of the filament $(a_{C^*})_{\mathrm{fil}}$. Higher reaction temperatures therefore broaden the range of χ values that preclude the detectable formation of carbon deposits, as observed in TEM images or mass changes during reforming catalysis (regime I; Sections 2.3.4 and 2.3.6) and enable the use of H_2O/CH_4 ratios closer to unity in practice, thereby improving process efficiencies.

2.3.8 Effect of Ni Nanoparticle Diameter on Carbon Morphology and Filament Formation Rates

TEM images of carbon filaments formed on 7% wt. Ni/MgO-B (11.0 nm mean diameter, Fig. 11a) and 15% wt. Ni/MgO-A (11.1 nm particles, Fig. 11b) after exposure to CH_4-CO_2 reaction conditions in regime II (873 K; χ = 2.6 kPa, ψ = 6.4 kPa) were used to compare Ni crystallite diameters to those of the carbon filament structures affixed to their ends for two different materials with similar mean nanoparticle size. In all cases, the diameters of the carbon filaments were similar

to those of the Ni nanoparticles to which they were attached. Filaments associated with larger particles in the size distribution typically exhibited thicker walls (Fig. 3b vs. Fig. 11), in agreement with previous reports[42, 50-51] and consistent with the larger carbon nucleating (Ni(111) and Ni(311)) facets prevalent on larger crystallites.

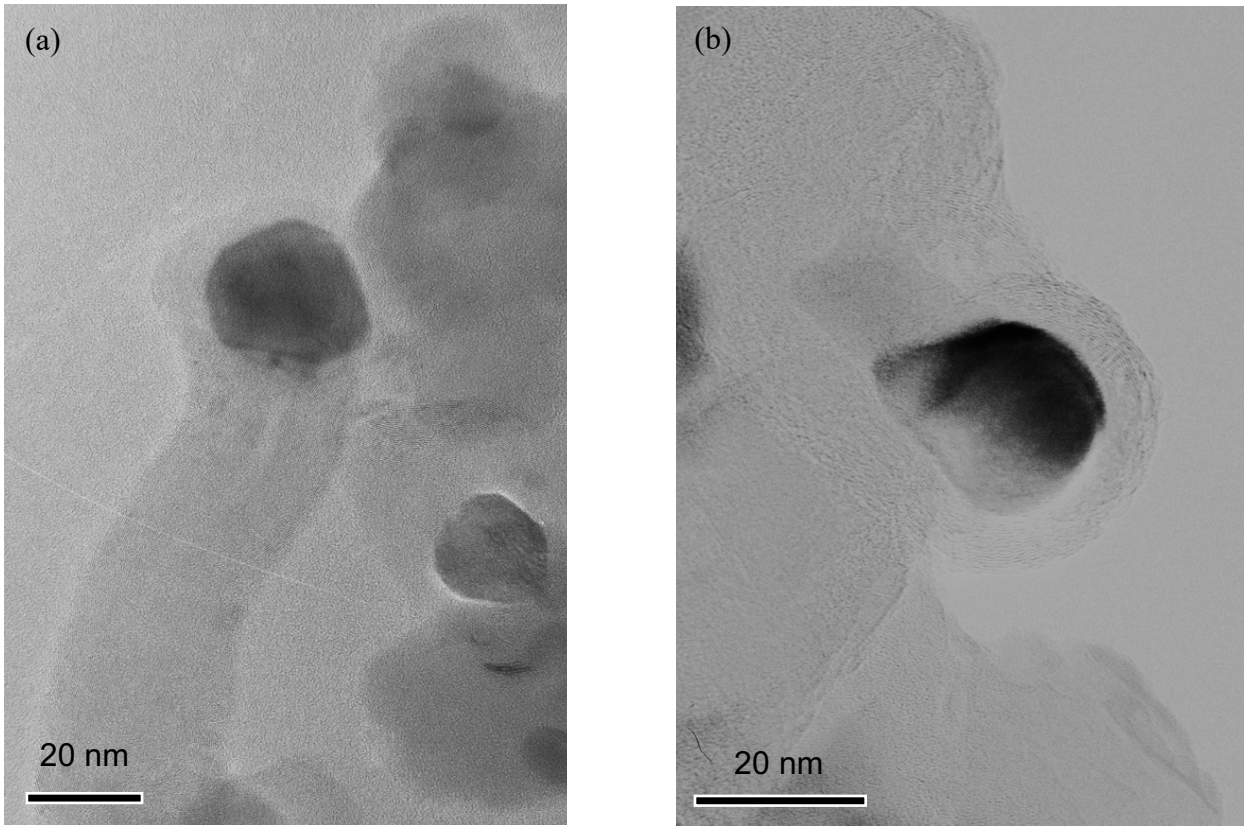

Figure 11. Transmission electron micrograph of carbon morphology after CH_4-CO_2 reaction on (a) 7 % wt. Ni/MgO-B and (b) 15 % wt. Ni/MgO-A at 873 K and χ = 2.60 kPa.

The role of Ni particle size on the dynamics of carbon deposition was investigated by comparing carbon deposition rates on 7% wt. Ni/MgO-A (5.4 nm particles) with those on 7% wt. Ni/MgO-B and 15% wt. Ni/MgO-A (11.0 and 11.1 nm particles, respectively) at χ (and ψ) values that led to proportional increases in carbon formation rates (873 K; regime II, Section 2.3.4). Carbon deposition rates were nearly identical on 7% wt. Ni/MgO-B and 15% wt. Ni/MgO-A (Fig. 12), in spite of their different MgO supports. Carbon deposition rates were larger on 7% wt. Ni/MgO-B and 15% wt. Ni/MgO-A (11.0 and 11.1 nm particles, respectively) than on 7% wt. Ni/MgO-A samples with smaller Ni particles (5.4 nm) at each given value of χ (or ψ) (Fig. 12). These trends with diameter are opposite to those reported previously, which attributed these their trends to the longer diffusion paths in larger Ni crystallites.[46-48, 87] These previous studies, however, measured carbon filament growth rates on larger catalyst particles (15-140 nm), where the diffusion length may be the dominant factor for these trends in carbon filament growth rates. The Ni crystallite diameter, however, affects terms other than this path length, specifically the rate and

equilibrium constants that determine the value of α ($\frac{k_1}{k_6 K_5 K_7}$; Eq. 17) and the activity of the carbon filament $(a_{C^*})_{fil}$. Such effects were probed by examining the expected effects of nanoparticle diameter particle size effects on the parameters included in the $\left(\frac{D_C^* c^0}{d_p}\alpha\right)$ and $\left(\frac{D_C^* c^0}{d_{p(L)}}(a_{C^*})_{fil}\right)$ values reflected by the slope and y-intercept, respectively, of the data in Figure 12.

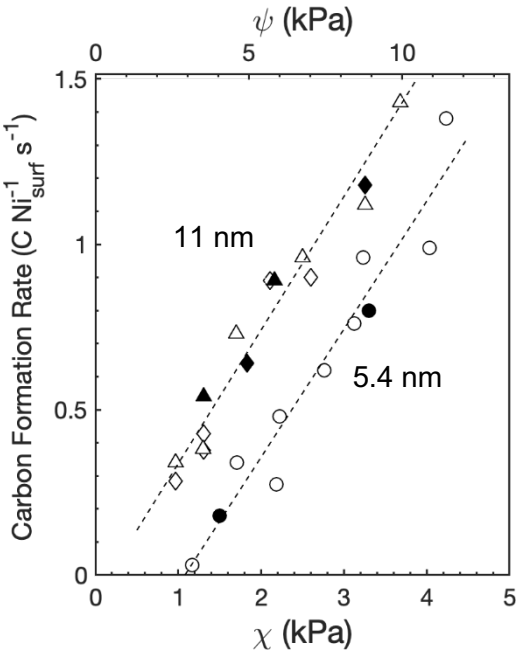

Figure 12. Carbon formation rates vs. χ ($P_{CO}P_{CH4}/P_{CO2}$) or ψ ($P_{H2}P_{CH4}/P_{H2O}$) on Ni/MgO at 873 K during CH_4-CO_2 (open symbol) or CH_4-H_2O reaction (solid symbol) (○● 7 % wt. Ni/MgO-A with 5.4 average nm Ni particles, △▲15 % wt. Ni/MgO-A with 11.1 nm average Ni particles, ◇◆ 7 % wt. Ni/MgO-B with 11.0 average nm Ni particles). Lines determined by linear best fit models.

The $\left(\frac{D_C^* c^0}{d_p}\alpha\right)$ values for 5.4 nm (7% wt. Ni/MgO-A; 0.39 ± 0.03) and 11 nm (7% wt. Ni/MgO-B and 15% wt. Ni/MgO-A; 0.40 ± 0.02) nanoparticles were nearly identical, in spite of a particle diameter (d_p) that differed by a factor of 2. The diffusivity of carbon (D_C^*) and the Henry's law constant (c^0) do not vary with particle size, suggesting that α must be two-fold larger on the larger particles to offset the longer diffusion length. This α term ($\frac{k_1}{k_6 K_5 K_7}$; Eq. 17) contains rate constants for C-H activation (k_1; Scheme 1, step 1.1) and C*-O* recombination (k_6, Scheme 1, step 1.6) and equilibrium constants for CO_2 dissociation (K_5, Scheme 1, step 1.5) and CO desorption (K_7, Scheme 1, step 1.7). CH_4 reforming turnover rates on these 11 nm nanoparticles (7% wt. Ni/MgO-B and 15% wt. Ni/MgO-A) were 1.3 times smaller than on the 5.4 nm particles (7% wt. Ni/MgO-A) at 873 K,[62] indicative of the difference in the values of k_1. Such differences reflect the lower average coordination at surfaces of smaller Ni crystallites,[62] which leads to lower C-H activation barriers.[88] The remaining parameters in α ($k_6K_5K_7$) must therefore be 2.6 times

larger on 5.4 nm particles (7% wt. Ni/MgO-A) than on 11 nm particles (7% wt. Ni/MgO-B and 15% wt. Ni/MgO-A) for α to be two-fold larger on the larger particles, as suggested by the nearly identical $\left(\frac{D_C^* c^0}{d_p}\alpha\right)$ values for 5.4 and 11 nm nanoparticles. The values of k_6, K_5, and K_7 cannot be determined from CH_4 reforming rates because the respective steps are not kinetically-relevant, thus rendering their sensitivity to nanoparticle diameters inaccessible from experiments. Energy estimates from density functional theory (DFT) for k_6 and K_7 on extended Rh surfaces have shown that stepped Rh(211) surfaces give lower activation barriers for C*-O* recombination (k_6; ~130 vs. ~185 kJ mol^{-1}) and more endothermic CO molecular desorption events (K_7; ~177 vs. ~160 kJ mol^{-1}) than close-packed Rh(111) surfaces,[89] which become more prevalent with increasing nanoparticle diameter. The smaller k_6 values (and likely K_5 values because more coordinatively saturated surfaces tend to exhibit lower molecular binding energies)[88] on larger particles may compensate, at least in part, for the smaller k_1 values and the larger diffusion lengths (d_p).

The $\left(\frac{D_C^* c^0}{d_p}(a_{C^*})_{\text{fil}}\right)$ term that accounts for the y-intercept for the data in Figure 12 contains terms that also depend on nanoparticle size. The data indicate that $\left(\frac{D_C^* c^0}{d_p}(a_{C^*})_{\text{fil}}\right)$ is 5.7 ± 4.3 times larger on the smaller (5.4 nm; 7% wt. Ni/MgO-A; -0.4 ± 0.1) than on the larger (11 nm; 7% wt. Ni/MgO-B and 15% wt. Ni/MgO-A; -0.07 ± 0.05) Ni particles. The carbon diffusivity (D_C^*) and solubility constant (c^0) are not likely to depend on size. Consequently, the larger $\left(\frac{D_C^* c^0}{d_p}(a_{C^*})_{\text{fil}}\right)$ values on smaller Ni nanoparticles must reflect the combined effects of a shorter diffusion path and a larger filament carbon activity for the smaller particles.

The diameters of the carbon filaments resembled those of the attached Ni particles (Fig. 3b and 11). Larger diameter filaments show less structural distortion of the sp^2 symmetry required for stable graphite layers[90] and are therefore thermodynamically more stable.[47] This change in carbon filament activity $(a_{C^*})_{\text{fil}}$ is reflected in the shift in the threshold value of χ (χ_{min}) required for carbon formation from 1.1 ± 0.3 to 0.2 ± 0.1 kPa for 5.4 nm (7% wt. Ni/MgO-A) and 11 nm particles (7% wt. Ni/MgO-B and 15% wt. Ni/MgO-A), respectively. These data indicate that the activity of carbon filaments on 5.4 nm particles is 5.5 ± 3.0 larger than on 11 nm particles, a value comparable to that derived from the y-intercept (2.8 ± 2.1).

The effects of particle size on $\left(\frac{D_C^* c^0}{d_p}\alpha\right)$ and $\left(\frac{D_C^* c^0}{d_{p(\text{L})}}(a_{C^*})_{\text{fil}}\right)$ values lead to a shift in χ_{min} required for the formation of carbon filaments towards higher values of χ with decreasing nanoparticle size. The synthesis and stabilization of small Ni particles therefore represents a potentially effective strategy in broadening the range of χ values that ensure the absence of detectable carbon deposits. Such strategies enable the use of H_2O/CH_4 ratios closer to unity for CH_4 reforming reactions in practice, thereby improving process efficiencies.

2.3.9 Implications of Approach to CH_4 Reforming Equilibrium for Carbon Formation Rates

The mechanism-based model described in Section 2.3.3 (Eq. 22) and used to describe measured filament formation rates in Sections 2.3.4-2.3.8 applies only when CH_4 decomposition (Scheme 1, steps 1.1-1.4) or C*-O* recombination (Scheme 1, step 1.6) steps are irreversible and CH_4 reforming reactions are far from equilibrium.

In this section, we extend these treatments to the general case in which these steps and the overall CH_4 reforming reaction approach equilibrium, as defined by their respective approach to equilibrium values. The approach to equilibrium parameter (η) relates the forward (r_f) and reverse (r_r) rate of a given reaction by:

$$\eta = \frac{r_r}{r_f} \tag{23}$$

Such formalisms are used here to derive an expression for the activity of surface carbon species in general, irrespective of the prevalent η value.

The catalytic sequence in Scheme 1 can be divided into two half-reactions, one including all the steps required to form C* and H_2 from CH_4 (reaction A) (Scheme 1, steps 1.1-1.4, 1.8) and the other involving the steps that remove C* via reactions with O* derived from CO_2 to form CO (reaction B) (Scheme 1, steps 1.5-1.7) or from H_2O to form H_2 and CO (reaction B') (Scheme 1, steps 1.6-1.10). The approaches to equilibrium (η) for reactions A and B (or B') are defined respectively as:

$$\eta_{\mathrm{A}} = \frac{(\mathrm{H_2})^2 (a_{C^*})_{\mathrm{s}}}{(\mathrm{L})(\mathrm{CH_4})\mathrm{K_A}} \tag{24}$$

$$\eta_{\mathrm{B}} = \eta_{\mathrm{B}'} = \frac{(\mathrm{CO})^2(\mathrm{L})}{(\mathrm{CO_2})(a_{C^*})_{\mathrm{s}}\mathrm{K_B}} = \frac{(\mathrm{H_2})(\mathrm{CO})(\mathrm{L})}{(\mathrm{H_2O})(a_{C^*})_{\mathrm{s}}\mathrm{K_{B'}}} \tag{25}$$

Here, K_A, K_B, and $K_{B'}$ are the equilibrium constants for their respective half-reactions. K_B, and $K_{B'}$ are also related to each other by the equilibrium constant for the water-gas shift reaction (K_{WGS}) because this reaction was found to be equilibrated for all experimental conditions:

$$\mathrm{K_B K_{WGS}} = \mathrm{K_{B'}} \tag{26}$$

The approaches to equilibrium for half-reactions A and B are also related to the overall approach to equilibrium parameters for CH_4-CO_2 (η_{DRM}) and CH_4-H_2O (η_{SRM}) reactions:

$$\eta_{\mathrm{A}}\eta_{\mathrm{B}} = \eta_{\mathrm{A}}\eta_{\mathrm{B}'} = \eta_{\mathrm{DRM}} = \eta_{\mathrm{SRM}} \tag{27}$$

The approach to equilibrium values for half-reactions A (η_{A}, Eq. 24) and B (or B'; η_{B}, Eq. 25) can be estimated for the conditions used here by using data available in the literature. K_A and K_B were previously reported for carbon filament growth on Ni-based catalysts using CH_4-H_2 and CO_2-CO mixtures (650-1000 K) to set the surface carbon activity (0.9 ± 0.3 and 0.16 ± 0.03, respectively);[54] the activity of the carbon filaments (10 nm diameter; $(a_{\mathrm{C}})_{\mathrm{fil,10\ nm}}$) formed under these conditions can also be derived from these data (1.8 ± 1, referenced to graphite).[54] The activity of carbon filaments $(a_{\mathrm{C}})_{\mathrm{fil}}$ is represented by the threshold value of χ required to form such carbon deposits (χ_{min}; Sections 2.3.7-2.3.8). The carbon activity $(a_{\mathrm{C}})_{\mathrm{s}}$ can therefore be calculated for a given value of χ using:

$$\frac{(a_{\mathrm{C}})_{\mathrm{s}}}{(a_{\mathrm{C}})_{\mathrm{fil,10nm}}} = \frac{\mathrm{c^0}\alpha\chi(\mathrm{L})}{\mathrm{c^0}\alpha\chi_{\mathrm{min,10nm}}(\mathrm{L})} = \frac{\chi}{\chi_{\mathrm{min,10nm}}} \tag{28}$$

Here, we approximate $\chi_{\mathrm{min,10nm}}$ as the value of χ required to nucleate filaments of similar diameter (11 nm) on Ni nanoparticles (0.2 ± 0.1 kPa; Section 2.3.8). This treatment of the data leads to values of η_{A} and η_{B} that are less than 0.04 and 0.001, respectively, calculated at the reactor exit. These values of η_{A} and η_{B} correspond with forward rates of CH_4 decomposition (reaction A) and C*-O* recombination (reaction B, or B') that are at least 25 and 1000 times faster throughout the CH_4 reforming reactor, respectively, indicating that both reactions are irreversible at the conditions of this study, thus corroborating the assumptions used to derive the models described by Equations 21 and 22.

The mechanism-based model that leads to Equation 22 requires that half-reactions A and B (or B') be irreversible, a condition met by the data reported in this study, but met only near the inlet region in practical CH_4 reforming reactors. An expression for the surface carbon activity $(a_{C^*})_{\mathrm{s}}$ that is valid for all CH_4 reforming conditions can be derived by including the approach to equilibrium for each of the half-reactions (details in Section 2.6.2):

$$\frac{(a_{C^*})_{\mathrm{s}}}{(\mathrm{L})} = \alpha\chi\frac{(1-\eta_{\mathrm{A}})}{(1-\eta_{\mathrm{B}})} = \alpha\chi\frac{(1+\eta_{\mathrm{B}}^*)}{(1+\eta_{\mathrm{A}}^*)} \tag{29}$$

$$\eta_{\mathrm{A}}^* = \frac{(\mathrm{H_2})^2\alpha\chi}{(\mathrm{CH_4})\mathrm{K_A}} \tag{30}$$

$$\eta_{\mathrm{B}}^* = \eta_{\mathrm{B}'}^* = \frac{(\mathrm{CO})^2}{(\mathrm{CO_2})\alpha\chi\mathrm{K_B}} = \frac{(\mathrm{H_2})(\mathrm{CO})}{(\mathrm{H_2O})\alpha\chi\mathrm{K_{B'}}} \tag{31}$$

The terms η_{A}^* and η_{B}^* (or $\eta_{\mathrm{B}'}^*$) are related to the approach to equilibrium for CH_4-CO_2 (η_{DRM}) and CH_4-H_2O (η_{SRM}) reactions by:

$$\eta_{\mathrm{A}}^*\eta_{\mathrm{B}}^* = \eta_{\mathrm{A}}^*\eta_{\mathrm{B}'}^* = \eta_{\mathrm{SRM}} = \eta_{\mathrm{DRM}} \tag{32}$$

Equation 29 was derived by assuming that the rate of diffusion of carbon is much smaller than the forward rates of reactions A and B (or B') and that there are no significant coverages of intermediates during steady-state CH_4 reforming catalysis, an assumption that will be relaxed later in this section.

Equation 29 indicates that surface carbon activities decrease as reaction A approaches equilibrium (while reaction B remains far from equilibrium; $\eta_{\mathrm{A}} \to 1$). The quasi-equililbration of reaction A before reaction B leads to η_{A}^* values significantly greater than unity, allowing Equation 29 to be simplified to:

$$\frac{(a_{C^*})_{\mathrm{s}}}{(\mathrm{L})} = \frac{(\mathrm{CH_4})\mathrm{K_A}}{(\mathrm{H_2})^2} \tag{33}$$

Conversely, when reaction B approaches equilibrium before reaction A ($\eta_{\mathrm{B}} \to 1$), the surface carbon activity increases. When reaction B achieves equilibrium before reaction A, η_{B}^* becomes significantly greater than unity, and Equation 29 can be simplified to:

$$\frac{(a_{C^*})_{\mathrm{s}}}{(\mathrm{L})} = \frac{\mathrm{K_B}(\mathrm{CO})^2}{(\mathrm{CO_2})} \tag{34}$$

Equations 33 and 34 are, in fact, the same as Equations 2 and 3, which describe the reactions of quasi-equilibrated binary mixtures of CO-CO_2 or CH_4-H_2, respectively. Thus, the quasi-equilibration of either half-reaction A or B, depending on which reaction reaches equilibrium more quickly, sets the surface carbon activity $(a_{C^*})_s$ as CH_4 reforming approaches equilibrium. The estimated maximum values of η_A and η_B for this study (0.04 and 0.001, respectively) indicate that the CH_4 decomposition half-reaction (reaction A; Scheme 1, steps 1.1-1.4) reaches equilibrium first for the conditions of this study. This is because the water-gas shift reaction favors the products (H_2 and CO_2) at these temperatures, causing a subsequent increase in η_A (Eq. 24) and decrease in η_B (Eq. 25).

Equation 29 was derived by assuming that there are no significant coverages of intermediates during steady-state CH_4 reforming catalysis. This assumption can be relaxed to give an expression for the surface carbon activity that is applicable even as C* coverages become significant (details in Section 2.6.2):

$$\frac{(a_{C^*})_s}{(L)} = \alpha\chi \frac{(1+\eta_B^*)}{\left(1+\frac{(CO)^2}{(CO_2)K_B}+\alpha\chi+\eta_A^*\right)} = \beta\psi \frac{\left(1+\eta_{B'}^*\right)}{\left(1+\frac{(CO)(H_2)}{(H_2O)K_{B'}}+\beta\psi+\eta_A^*\right)} \quad (35)$$

Equation 35 is able to describe and predict surface carbon activities for a wide range of CH_4 reforming reaction conditions, including those that may be encountered in practice. These derivations thus show that the mechanistic conclusions that lead to expressions for surface carbon activities and carbon formation rates at conditions far from CH_4 reforming equilibrium are general and provide a mathematical framework for the rigorous extension of the reaction-diffusion constructs to more practical conditions, including those corresponding with more moderate CH_4 reforming conversions and even equilibrium conditions for this reaction. The data reported and the kinetic parameters derived here are specific for Ni-based catalysts, but the mathematical framework is general for the analysis of other reactants and catalysts and demonstrates the requirement for the accurate details of catalytic mechanisms in describing the formation of chemisorbed carbon and its various solid forms during catalysis.

2.4 Conclusions

CH_4-CO_2 and CH_4-H_2O reactions on supported Ni catalysts tend to form carbon deposits that are detrimental to the catalytic process at stoichiometric reactant ratios. The dynamics of carbon formation on dispersed Ni nanoparticles of varying diameter (5-11 nm) were measured during steady-state CH_4 reforming reactions (843-973 K) in this study to understand the conditions under which these residues form. Carbon formation rates and morphologies (filamentous or encapsulating) were solely determined by the pressure ratio $P_{CH4}P_{CO}/P_{CO2}$ (χ) (or $P_{CH4}P_{H2}/P_{H2O}$ (ψ)), which sets the thermodynamic carbon activity at the metal surface $(a_{C^*})_s$ via the elementary steps that mediate CH_4 reforming at conditions far from equilibrium of this reaction. Carbon formation rates were proportional to χ (and ψ) at conditions leading to the formation of carbon filaments but without concurrent decreases in CH_4 reforming and carbon formation rates,

consistent with a filament growth mechanism limited by carbon diffusion. Higher values of χ and ψ (and values of $(a_{C^*})_s$) led to the simultaneous incipient nucleation of multiple carbon patches, ultimately leading to the encapsulation of Ni nanoparticles by carbon adlayers and loss of accessible surface for CH_4 turnovers. Carbon deposition rates decreased with increasing temperature because of the corresponding decrease in the value of the lumped kinetic and thermodynamic parameter that relates χ to $(a_{C^*})_s$. Carbon formation rates also decreased with decreasing Ni particle size because of the lower stability and concomitant increase in activity of the smaller diameter carbon filaments that formed on smaller Ni particles. The synthesis and stabilization of small Ni particles at high temperatures thus presents a potentially effective strategy in bringing H_2O/CH_4 ratios closer to that required by stoichiometry while ensuring the absence of detectable carbon deposits.

The results from this study are consistent with previously proposed bulk diffusion mechanisms for filament growth and expand on previous carbon formation studies by relating thermodynamic carbon activities to prevalent gas-phase compositions during the steady-state catalysis of multi-component CH_4 reforming mixtures. The study provides insight into the kinetic and thermodynamic parameters underlying the deposition and removal of carbon and provides guidance for avoiding carbon filament formation at conditions away from CH_4 reforming equilibrium. Carbon formation rates are accurately described by a mechanism-based reaction-transport model and demonstrate the need for accurate details of the catalytic mechanisms in describing the formation of chemisorbed carbon and its various solid forms during catalysis. Such mechanism-based relations are rigorous and general in their ability to relate surface carbon activities to prevalent gas-phase compositions and can therefore be extended, with additional parameters, to CH_4 reforming reactions that approach equilibrium, as in the case of reactions in practice.

2.5 Acknowledgements

Samuel Leung acknowledges Dr. Junmei Wei for the primary collection of the data in this chapter. This study was supported by BP as part of the Methane Conversion Cooperative Research Program at the University of California at Berkeley, by a MEXUS grant CN-02-76, by the Chevron technology Co., and by a Chevron Graduate Student Research Fellowship. The authors acknowledge Dr. John Collins and Dr. Theodore Fleisch (BP) for technical discussions and F. Ruiz and M. Dominguez for technical assistance in acquiring the electron micrograph images.

2.6 Supporting Information

2.6.1 Expression for $(a_{C^*})_s$ Derived from CH_4-H_2O and CH_4-CO_2 Reforming Mechanism at Conditions Far from Equilibrium

The surface concentration of carbon is derived by applying the pseudo-steady-state approximation (PSSA) on C*:

$$\frac{d(\mathrm{C}*)}{dt} = 0 = \mathrm{r}_4 - \mathrm{r}_{-4} - \mathrm{r}_6 + \mathrm{r}_{-6} - \mathrm{r}_\mathrm{C} \tag{SI-1}$$

Here, r_4 and r_{-4} are the forward and reverse rates of decomposition of CH* (Scheme 1, step 1.4), r_6 and r_{-6} are the forward and reverse rates of the reaction of C* and O* (Scheme 1, step 1.6), and r_C is the net rate of diffusion of carbon from the surface through the particle to the carbon filament, given by:

$$\mathrm{r}_\mathrm{C} = \frac{J_C}{(\mathrm{L})} = \frac{D_C^* c^0}{d_p}[(a_{C^*})_\mathrm{s} - (a_{C^*})_\mathrm{fil}] \tag{SI-2}$$

Here, (L) is the total concentration of surface sites. Applying the PSSA to the CH_x* intermediates results in:

$$\mathrm{r}_1 - \mathrm{r}_{-1} = \mathrm{r}_2 - \mathrm{r}_{-2} = \mathrm{r}_3 - \mathrm{r}_{-3} = \mathrm{r}_4 - \mathrm{r}_{-4} \tag{SI-3}$$

Equation SI-1 can therefore be written as:

$$\frac{d(\mathrm{C}*)}{dt} = 0 = \mathrm{r}_1 - \mathrm{r}_{-1} - \mathrm{r}_6 + \mathrm{r}_{-6} - \mathrm{r}_\mathrm{C} \tag{SI-4}$$

The formation of C* from methane (Scheme 1, step 1.1-1.4) and its removal by reaction with O* (Scheme 1, step 1.6) are irreversible (Section 2.3.9) at the conditions of this study. Equation SI-4 can therefore be simplified to:

$$\frac{d(\mathrm{C}*)}{dt} = 0 = \mathrm{r}_1 - \mathrm{r}_6 - \mathrm{r}_\mathrm{C} \tag{SI-5}$$

The activity of surface carbon is equivalent to the concentration of surface carbon here. Substituting the appropriate rate expressions in Equation SI-5 and solving for (C*) leads to:

$$(a_C)_\mathrm{s} = (\mathrm{C}*) = \frac{\mathrm{k}_1}{\mathrm{k}_6\mathrm{K}_5\mathrm{K}_7}\frac{(\mathrm{CH_4})(\mathrm{CO})}{(\mathrm{CO_2})}(*)\frac{\left(1 + \frac{D_C^* c^0(\mathrm{L})}{d_p}\frac{1}{\mathrm{k}_1(\mathrm{CH_4})(*)^2}(a_{C^*})_\mathrm{fil}\right)}{\left(1 + \frac{D_C^* c^0(\mathrm{L})}{d_p}\frac{1}{\mathrm{k}_1(\mathrm{CH_4})(*)}\frac{\mathrm{k}_1}{\mathrm{k}_6\mathrm{K}_5\mathrm{K}_7}\frac{(\mathrm{CH_4})(\mathrm{CO})}{(\mathrm{CO_2})}\right)}$$

$$= \frac{\mathrm{k}_1}{\mathrm{k}_6\mathrm{K}_8\mathrm{K}_9\mathrm{K}_{10}}\frac{(\mathrm{CH_4})(\mathrm{H_2})}{(\mathrm{H_2O})}(*)\frac{\left(1 + \frac{D_C^* c^0(\mathrm{L})}{d_p}\frac{1}{\mathrm{k}_1(\mathrm{CH_4})(*)^2}(a_{C^*})_\mathrm{fil}\right)}{\left(1 + \frac{D_C^* c^0(\mathrm{L})}{d_p}\frac{1}{\mathrm{k}_1(\mathrm{CH_4})(*)}\frac{\mathrm{k}_1}{\mathrm{k}_6\mathrm{K}_8\mathrm{K}_9\mathrm{K}_{10}}\frac{(\mathrm{CH_4})(\mathrm{H_2})}{(\mathrm{H_2O})}\right)} \tag{SI-6}$$

The catalyst surface remained clean throughout this study (i.e. (C*), (CH*), (CH_2*), (CH_3*), (H*), (OH*), (CO*), (O*) << (*) = (L)). Therefore, Equation SI-6 can be written as:

$$(a_C)_s = (C*) = \frac{k_1}{k_6 K_5 K_7}\frac{(CH_4)(CO)}{(CO_2)}(L)\frac{\left(1+\frac{D_C^* c^0}{d_p(L)}\frac{1}{k_1(CH_4)}(a_{C^*})_{fil}\right)}{\left(1+\frac{D_C^* c^0}{d_p(L)}\frac{1}{k_1(CH_4)}\frac{k_1}{k_6 K_5 K_7}\frac{(CH_4)(CO)}{(CO_2)}(L)\right)}$$

$$= \frac{k_1}{k_6 K_8 K_9 K_{10}}\frac{(CH_4)(H_2)}{(H_2O)}(L)\frac{\left(1+\frac{D_C^* c^0}{d_p(L)}\frac{1}{k_1(CH_4)}(a_{C^*})_{fil}\right)}{\left(1+\frac{D_C^* c^0}{d_p(L)}\frac{1}{k_1(CH_4)}\frac{k_1}{k_6 K_8 K_9 K_{10}}\frac{(CH_4)(H_2)}{(H_2O)}(L)\right)} \quad \text{(SI-7)}$$

The rate of carbon transport was small compared to the rates of carbon deposition from CH_4 decomposition (Scheme 1, step 1.1) and carbon removal by reaction with O* (Scheme 1, step 1.6) in regimes I and II. Under such conditions, the diffusive terms in Equation SI-7 can be neglected and the equation can be written as:

$$(a_C)_s = (C*) = \frac{k_1}{k_6 K_5 K_7}\frac{(CH_4)(CO)}{(CO_2)}(L) = \frac{k_1}{k_6 K_8 K_9 K_{10}}\frac{(CH_4)(H_2)}{(H_2O)}(L) \quad \text{(SI-8)}$$

2.6.2 Expression for $(a_{C^*})_s$ Derived from CH_4-H_2O and CH_4-CO_2 Reforming Mechanism at Conditions Approaching CH_4 Equilibrium When Carbon Formation Rates are Small

The approach to equilibrium (η) for a reaction relates the forward rate to the net rate:

$$r_f - r_r = r_f(1-\eta) \quad \text{(SI-9)}$$

Assuming the rate of diffusion of carbon (r_C) is small compared to the rates of carbon deposition from A) CH_4 decomposition (Scheme 1, steps 1.1-1.4) and carbon removal by reaction with O* derived from B) CO_2 (Scheme 1, steps 1.5-1.7) or B') H_2O (Scheme 1, steps 1.6-1.10), Equation SI-4 can be written as:

$$\frac{d(C*)}{dt} = 0 = r_1(1-\eta_A) - r_6(1-\eta_B) = r_1(1-\eta_A) - r_6(1-\eta_{B'}) \quad \text{(SI-10)}$$

$$\eta_A = \frac{(H_2)^2(a_{C^*})_s}{(*)(CH_4)K_A} \quad \text{(SI-11)}$$

$$\eta_{\mathrm{B}} = \eta_{\mathrm{B}'} = \frac{(\mathrm{CO})^2(*)}{(\mathrm{CO_2})(a_{C^*})_{\mathrm{s}}\mathrm{K_B}} = \frac{(\mathrm{H_2})(\mathrm{CO})(*)}{(\mathrm{H_2O})(a_{C^*})_{\mathrm{s}}\mathrm{K_{B'}}} \quad \text{(SI-12)}$$

Here, K_A, K_B and $K_{B'}$ are the equilibrium constants for the respective reactions. K_B, and $K_{B'}$ are related to each other by the equilibrium constant for the water-gas shift reaction (K_{WGS}) because this reaction was found to be equilibrated for all experimental conditions:

$$\mathrm{K_B K_{WGS}} = \mathrm{K_{B'}} \quad \text{(SI-13)}$$

The activity of surface carbon is equivalent to the concentration of surface carbon here. Substituting the appropriate rate expressions in Equation SI-10 and solving for (C*) leads to:

$$(a_{C^*})_{\mathrm{s}} = (\mathrm{C}*) = \alpha\chi\frac{(1+\eta_{\mathrm{B}}^*)}{(1+\eta_{\mathrm{A}}^*)}(*) = \beta\psi\frac{(1+\eta_{\mathrm{B}'}^*)}{(1+\eta_{\mathrm{A}}^*)}(*) \quad \text{(SI-14)}$$

$$\eta_{\mathrm{A}}^* = \frac{(\mathrm{H_2})^2\alpha\chi}{(\mathrm{CH_4})\mathrm{K_A}} \quad \text{(SI-15)}$$

$$\eta_{\mathrm{B}}^* = \eta_{\mathrm{B}'}^* = \frac{(\mathrm{CO})^2}{(\mathrm{CO_2})\alpha\chi\mathrm{K_B}} = \frac{(\mathrm{H_2})(\mathrm{CO})}{(\mathrm{H_2O})\beta\psi\mathrm{K_{B'}}} \quad \text{(SI-16)}$$

$$\alpha = \frac{\mathrm{k_1}}{\mathrm{k_6 K_5 K_7}} \quad \text{(SI-17)}$$

$$\beta = \frac{\mathrm{k_1 K_8}}{\mathrm{k_6 K_9 K_{10}}} \quad \text{(SI-18)}$$

Here, χ and ψ represent the $\frac{(\mathrm{CH_4})(\mathrm{CO})}{(\mathrm{CO_2})}$ and $\frac{(\mathrm{CH_4})(\mathrm{H_2})}{(\mathrm{H_2O})}$ pressure ratio. The catalyst surface remained clean throughout this study (i.e. (C*), (CH*), (CH_2*), (CH_3*), (H*), (OH*), (CO*), (O*) << (*) = (L)). Under such conditions, Equation SI-14 can be simplified to:

$$(a_{C^*})_{\mathrm{s}} = (\mathrm{C}*) = \alpha\chi\frac{(1+\eta_{\mathrm{B}}^*)}{(1+\eta_{\mathrm{A}}^*)}(\mathrm{L}) = \beta\psi\frac{(1+\eta_{\mathrm{B}'}^*)}{(1+\eta_{\mathrm{A}}^*)}(\mathrm{L}) \quad \text{(SI-19)}$$

For conditions where (C*) coverages become significant (i.e. (C*) + (*) = (L)), the following expression is obtained:

$$\begin{aligned}(a_{C^*})_{\mathrm{s}} = (\mathrm{C}*) &= \alpha\chi(\mathrm{L})\frac{(1+\eta_{\mathrm{B}}^*)}{\left(1+\frac{(\mathrm{CO})^2}{(\mathrm{CO_2})\mathrm{K_B}}+\alpha\chi+\eta_{\mathrm{A}}^*\right)} \\ &= \beta\psi(\mathrm{L})\frac{\left(1+\eta_{\mathrm{B}'}^*\right)}{\left(1+\frac{(\mathrm{CO})(\mathrm{H_2})}{(\mathrm{H_2O})\mathrm{K_{B'}}}+\beta\psi+\eta_{\mathrm{A}}^*\right)}\end{aligned} \quad \text{(SI-20)}$$

2.7 References

1. Rostrup-Nielsen, J. R., Catalytic Steam Reforming. In *Catalysis: Science and Technology*, Anderson, J. R.; Boudart, M., Eds. Springer Berlin Heidelberg: Berlin, Heidelberg, 1984; Vol. 5, pp 1-117.
2. Takanabe, K.; Nagaoka, K.; Aika, K., Improved Resistance Against Coke Deposition of Titania Supported Cobalt and Nickel Bimetallic Catalysts for Carbon Dioxide Reforming of Methane. *Catal. Lett.* **2005**, *102*, 153-157.
3. Horlyck, J.; Lawrey, C.; Lovell, E. C.; Amal, R.; Scott, J., Elucidating the impact of Ni and Co loading on the selectivity of bimetallic NiCo catalysts for dry reforming of methane. *Chem. Eng. J.* **2018**, *352*, 572-580.
4. Gonzalez-Delacruz, V. M.; Pereniguez, R.; Ternero, F.; Holgado, J. P.; Caballero, A., In Situ XAS Study of Synergic Effects on Ni-Co/ZrO2 Methane Reforming Catalysts. *Journal of Physical Chemistry C* **2012**, *116*, 2919-2926.
5. Wang, H. M.; Blaylock, D. W.; Dam, A. H.; Liland, S. E.; Rout, K. R.; Zhu, Y. A.; Green, W. H.; Holmen, A.; Chen, D., Steam Methane Reforming on a Ni-based Bimetallic Catalyst: Density Functional Theory and Experimental Studies of the Catalytic Consequence of Surface Alloying of Ni with Ag. *Catal. Sci. Technol.* **2017**, *7*, 1713-1725.
6. Zhang, J. G.; Wang, H.; Dalai, A. K., Development of Stable Bimetallic Catalysts for Carbon Dioxide Reforming of Methane. *J. Catal.* **2007**, *249*, 300-310.
7. Trimm, D. L., Formation and Removal of Coke from Nickel Catalyst. *Cat. Rev. - Sci. Eng.* **1977**, *16*, 155-189.
8. Rostrup-Nielsen, J. R.; Trimm, D. L., Mechanisms of Carbon Formation on Nickel-Containing Catalysts. *J. Catal.* **1977**, *48*, 155-165.
9. Baker, R. T. K.; Harris, P. S., The Formation of Filamentous Carbon. In *Chem. Phys. Carbon*, Walker, P. L.; Thrower, P. A., Eds. Dekker: New York, 1979; Vol. 14, pp 83-165.
10. Rodriguez, N. M., A Review of Catalytically Grown Carbon Nanofibers. *J. Mater. Res.* **1993**, *8*, 3233-3250.
11. De Jong, K. P.; Geus, J. W., Carbon Nanofibers: Catalytic Synthesis and Applications. *Cat. Rev. - Sci. Eng.* **2000**, *42*, 481-510.
12. Liu, C. J.; Ye, J. Y.; Jiang, J. J.; Pan, Y. X., Progresses in the Preparation of Coke Resistant Ni-based Catalyst for Steam and CO_2 Reforming of Methane. *Chemcatchem* **2011**, *3*, 529-541.
13. Lobo, L. S.; Figueiredo, J. L.; Bernardo, C. A., Carbon Formation and Gasification on Metals. Bulk Diffusion Mechanism: A Reassessment. *Catal. Today* **2011**, *178*, 110-116.
14. Sperle, T.; Chen, D.; Lodeng, R.; Holmen, A., Pre-reforming of Natural Gas on a Ni Catalyst - Criteria for Carbon Free Operation. *Appl. Catal., A* **2005**, *282*, 195-204.
15. Bonard, J. M.; Salvetat, J. P.; Stockli, T.; Forro, L.; Chatelain, A., Field Emission from Carbon Nanotubes: Perspectives for Applications and Clues to the Emission Mechanism. *Appl. Phys. A* **1999**, *69*, 245-254.
16. Robertson, S. D., Graphite Formation from Low Temperature Pyrolysis of Methane over Some Transition Metal Surfaces. *Nature* **1969**, *221*, 1044-1046.
17. Iijima, S., Helical Microtubules of Graphitic Carbon. *Nature* **1991**, *354*, 56-58.
18. Tavares, M. T.; Bernardo, C. A.; Alstrup, I.; Rostrup-Nielsen, J. R., Reactivity of Carbon Deposited on Nickel-Copper Alloy Catalysts from the Decomposition of Methane. *J. Catal.* **1986**, *100*, 545-548.

19. Hu, Y. H.; Ruckenstein, E., High-Resolution Transmission Electron Microscopy Study of Carbon Deposited on the NiO/MgO Solid Solution Catalysts. *J. Catal.* **1999**, *184*, 298-302.
20. Audier, M.; Oberlin, A.; Coulon, M., Crystallographic Orientations of Catalytic Particles in Filamentous Carbon; Case of Simple Conical Particles. *J. Cryst. Growth* **1981**, *55*, 549-556.
21. Alvarez, W. E.; Kitiyanan, B.; Borgna, A.; Resasco, D. E., Synergism of Co and Mo in the Catalytic Production of Single-wall Carbon Nanotubes by Decomposition of CO. *Carbon* **2001**, *39*, 547-558.
22. Kitiyanan, B.; Alvarez, W. E.; Harwell, J. H.; Resasco, D. E., Controlled Production of Single-wall Carbon Nanotubes by Catalytic Decomposition of CO on Bimetallic Co-Mo Catalysts. *Chem. Phys. Lett.* **2000**, *317*, 497-503.
23. Baker, R. T. K.; Harris, P. S.; Thomas, R. B.; Waite, R. J., Formation of Filamentous Carbon from Iron, Cobalt and Chromium Catalyzed Decomposition of Acetylene. *J. Catal.* **1973**, *30*, 86-95.
24. Baker, R. T. K.; Barber, M. A.; Waite, R. J.; Harris, P. S.; Feates, F. S., Nucleation and Growth of Carbon Deposits from Nickel Catalyzed Decomposition of Acetylene. *J. Catal.* **1972**, *26*, 51-62.
25. Holstein, W. L., The Roles of Ordinary and Soret Diffusion in the Metal-Catalyzed Formation of Filamentous Carbon. *J. Catal.* **1995**, *152*, 42-51.
26. Bianchini, E. C.; Lund, C. R. F., Kinetic Implications of Mechanisms Proposed for Catalytic Carbon-Filament Growth. *J. Catal.* **1989**, *117*, 455-466.
27. Nishiyama, Y.; Tamai, Y., Carbon Formation on Copper-Nickel Alloys from Benzene. *J. Catal.* **1974**, *33*, 98-107.
28. Keep, C. W.; Baker, R. T. K.; France, J. A., Origin of Filamentous Carbon Formation from Reaction of Propane over Nickel. *J. Catal.* **1977**, *47*, 232-238.
29. Tibbetts, G. G.; Devour, M. G.; Rodda, E. J., An Adsorption-Diffusion Isotherm and Its Application to the Growth of Carbon Filaments on Iron Catalyst Particles. *Carbon* **1987**, *25*, 367-375.
30. Lund, C. R. F.; Yang, R. T., Solid-State Diffusion during Carbon Gasification and Filament Growth. *Carbon* **1989**, *27*, 956-958.
31. Audier, M.; Coulon, M.; Bonnetain, L., Disproportionation of CO on Iron-Cobalt Alloys-III. Kinetic Laws of the Carbon Growth and Catalyst Fragmentation. *Carbon* **1983**, *21*, 105-110.
32. Lobo, L. S.; Trimm, D. L., Carbon Formation from Light Hydrocarbons on Nickel. *J. Catal.* **1973**, *29*, 15-19.
33. Alstrup, I.; Tavares, M. T., Kinetics of Carbon Formation from $CH_4 + H_2$ on Silica-Supported Nickel and Ni-Cu Catalysts. *J. Catal.* **1993**, *139*, 513-524.
34. Schneider, M.; Duff, D. G.; Mallat, T.; Wildberger, M.; Baiker, A., High Surface Area Platinum-Titania Aerogels: Preparation, Structural Properties, and Hydrogenation Activity. *J. Catal.* **1994**, *147*, 500-514.
35. Feng, X. F.; Chee, S. W.; Sharma, R.; Liu, K.; Xie, X.; Li, Q. Q.; Fan, S. S.; Jiang, K. L., In Situ TEM Observation of the Gasification and Growth of Carbon Nanotubes Using Iron Catalysts. *Nano Res.* **2011**, *4*, 767-779.
36. Figueiredo, J. L.; Bernardo, C. A.; Chludzinski, J. J.; Baker, R. T. K., The Reversibility of Filamentous Carbon Growth and Gasification. *J. Catal.* **1988**, *110*, 127-138.
37. Nolan, P. E.; Lynch, D. C.; Cutler, A. H., Carbon Deposition and Hydrocarbon Formation on Group VIII Metal Catalysts. *J. Phys. Chem. B* **1998**, *102*, 4165-4175.

38. Nolan, P. E.; Schabel, M. J.; Lynch, D. C.; Cutler, A. H., Hydrogen Control of Carbon Deposit Morphology. *Carbon* **1995**, *33*, 79-85.
39. Baughman, R. H.; Zakhidov, A. A.; de Heer, W. A., Carbon Nanotubes - the Route Toward Applications. *Science* **2002**, *297*, 787-792.
40. Tibbetts, G. G., Vapor Grown Carbon Fibers: Status and Prospects. *Carbon* **1989**, *27*, 745-747.
41. Tavares, M. T.; Alstrup, I.; Bernardo, C. A.; Rostrup-Nielsen, J. R., CO Disproportionation on Silica-Supported Nickel and Nickel-Copper Catalysts. *J. Catal.* **1994**, *147*, 525-534.
42. Zhu, Y. A.; Dai, Y. C.; Chen, D.; Yuan, W. K., First-principles Study of Carbon Diffusion in Bulk Nickel during the Growth of Fishbone-type Carbon Nanofibers. *Carbon* **2007**, *45*, 21-27.
43. Lobo, L. S., Nucleation and Growth of Carbon Nanotubes and Nanofibers: Mechanism and Catalytic Geometry Control. *Carbon* **2017**, *114*, 411-417.
44. Wang, P.; Tanabe, E.; Ito, K.; Jia, J.; Morioka, H.; Shishido, T.; Takehira, K., Filamentous Carbon Prepared by the Catalytic Pyrolysis of CH_4 on Ni/SiO_2. *Appl. Catal., A* **2002**, *231*, 35-44.
45. Demicheli, M. C.; Ponzi, E. N.; Ferretti, O. A.; Yeramian, A. A., Kinetics of Carbon Formation from CH_4-H_2 Mixtures on Nickel-alumina Catalyst. *Chem. Eng. J.* **1991**, *46*, 129-136.
46. Baker, R. T. K., Catalytic Growth of Carbon Filaments. *Carbon* **1989**, *27*, 315-323.
47. Chitrapu, P.; Lund, C. R. F.; Tsamopoulos, J. A., A Model for the Catalytic Growth of Carbon Filaments. *Carbon* **1992**, *30*, 285-293.
48. Patole, S. P.; Kim, H.; Choi, J.; Kim, Y.; Baik, S.; Yoo, J. B., Kinetics of Catalyst Size Dependent Carbon Nanotube Growth by Growth Interruption Studies. *Appl. Phys. Lett.* **2010**, *96*, 094101.
49. Tibbetts, G. G., Why Are Carbon Filaments Tubular. *J. Cryst. Growth* **1984**, *66*, 632-638.
50. Li, Y. M.; Kim, W.; Zhang, Y. G.; Rolandi, M.; Wang, D. W.; Dai, H. J., Growth of Single-Walled Carbon Nanotubes from Discrete Catalytic Nanoparticles of Various Sizes. *J. Phys. Chem. B* **2001**, *105*, 11424-11431.
51. Cheung, C. L.; Kurtz, A.; Park, H.; Lieber, C. M., Diameter-Controlled Synthesis of Carbon Nanotubes. *J. Phys. Chem. B* **2002**, *106*, 2429-2433.
52. Natesan, K.; Kassner, T. F., Thermodynamics of Carbon in Nickel, Iron-Nickel and Iron-Chromium-Nickel Alloys. *Metall. Trans.* **1973**, *4*, 2557-2566.
53. Audier, M.; Coulon, M., Kinetic and Microscopic Aspects of Catalytic Carbon Growth. *Carbon* **1985**, *23*, 317-323.
54. de Bokx, P. K.; Kock, A. J. H. M.; Boellaard, E.; Klop, W.; Geus, J. W., The Formation of Filamentous Carbon on Iron and Nickel Catalysts. I. Thermodynamics. *J. Catal.* **1985**, *96*, 454-467.
55. Safvi, S. A.; Bianchini, E. C.; Lund, C. R. F., The Dependence of Catalytic Carbon Filament Growth Kinetics Upon Gas-Phase Carbon Activity. *Carbon* **1991**, *29*, 1245-1250.
56. Snoeck, J. W.; Froment, G. F.; Fowles, M., Filamentous Carbon Formation and Gasification: Thermodynamics, Driving Force, Nucleation, and Steady-State Growth. *J. Catal.* **1997**, *169*, 240-249.
57. Rostrup-Nielsen, J. R.; Sehested, J.; Norskov, J. K., Hydrogen and Synthesis Gas by Steam- and CO_2 reforming. *Adv. Catal.* **2002**, *47*, 65-139.

58. Jablonski, G. A.; Geurts, F. W. A. H.; Sacco, A., Carbon Deposition over Fe, Ni, and Co Foils from CO-H_2-CH_4-CO_2-H_2O, CO-CO_2, CH_4-H_2, and CO-H_2-H_2O Gas-Mixtures: II. Kinetics. *Carbon* **1992**, *30*, 99-106.
59. Jablonski, G. A.; Geurts, F. W.; Sacco, A.; Biederman, R. R., Carbon Deposition over Fe, Ni, and Co Foils from CO-H_2-CH_4-CO_2-H_2O, CO-CO_2, CH_4-H_2, and CO-H_2-H_2O Gas-Mixtures: I. Morphology. *Carbon* **1992**, *30*, 87-98.
60. Sidjabat, O.; Trimm, D. L., Nickel-magnesia Catalysts for the Steam Reforming of Light Hydrocarbons. *Top. Catal.* **2000**, *11*, 279-282.
61. Borowiecki, T., Nickel Catalysts for Steam Reforming of Hydrocarbons - Size of Crystallites and Resistance to Coking. *Appl. Catal.* **1982**, *4*, 223-231.
62. Wei, J.; Iglesia, E., Isotopic and Kinetic Assessment of the Mechanism of Reactions of CH_4 with CO_2 or H_2O to Form Synthesis Gas and Carbon on Nickel Catalysts. *J. Catal.* **2004**, *224*, 370-383.
63. Tracz, E.; Scholz, R.; Borowiecki, T., High-resolution Electron Microscopy Study of the Carbon Deposit Morphology on Nickel Catalysts. *Appl. Catal.* **1990**, *66*, 133-147.
64. Kuznetsov, V. L.; Usoltseva, A. N.; Chuvilin, A. L.; Obraztsova, E. D.; Bonard, J. M., Thermodynamic Analysis of Nucleation of Carbon Deposits on Metal Particles and its Implications for the Growth of Carbon Nanotubes. *Phys. Rev. B* **2001**, *64*, 235401.
65. Bradford, M. C. J.; Vannice, M. A., Catalytic Reforming of Methane with Carbon Dioxide over Nickel Catalysts II. Reaction Kinetics. *Appl. Catal., A* **1996**, *142*, 97-122.
66. Stull, D. R.; Westrum, E. F.; Sinke, G. C., *The Chemical Thermodynamics of Organic Compounds*; J. Wiley: New York, 1969.
67. Parmaliana, A.; Arena, F.; Frusteri, F.; Giordano, N., Temperature-Programmed Reduction Study of NiO-MgO Interactions in Magnesia-Supported Ni Catalysts and NiO-MgO Physical Mixture. *J. Chem. Soc., Faraday Trans.* **1990**, *86*, 2663-2669.
68. Boudart, M.; Djéga-Mariadassou, G., *Kinetics of Heterogeneous Catalytic Reactions*; Princeton University Press: Princeton, NJ, 1984.
69. Wei, J.; Iglesia, E., Reaction Pathways and Site Requirements for the Activation and Chemical Conversion of Methane on Ru-Based Catalysts. *J. Phys. Chem. B* **2004**, *108*, 7253-7262.
70. Wei, J.; Iglesia, E., Structural requirements and reaction pathways in methane activation and chemical conversion catalyzed by rhodium. *J. Catal.* **2004**, *225*, 116-127.
71. Wei, J.; Iglesia, E., Isotopic and Kinetic Assessment of the Mechanism of Methane Reforming and Decomposition Reactions on Supported Iridium Catalysts. *Phys. Chem. Chem. Phys.* **2004**, *6*, 3754-3759.
72. Wei, J.; Iglesia, E., Structural and Mechanistic Requirements for Methane Activation and Chemical Conversion on Supported Iridium Clusters. *Angew. Chem. Int. Ed.* **2004**, *43*, 3685-3688.
73. Wei, J.; Iglesia, E., Mechanism and Site Requirements for Activation and Chemical Conversion of Methane on Supported Pt Clusters and Turnover Rate Comparisons among Noble Metals. *J. Phys. Chem. B* **2004**, *108*, 4094-4103.
74. Kim, M. S.; Rodriguez, N. M.; Baker, R. T. K., The Role of Interfacial Phenomena in the Structure of Carbon Deposits. *J. Catal.* **1992**, *134*, 253-268.
75. Kim, M. S.; Rodriguez, N. M.; Baker, R. T. K., The Interaction of Hydrocarbons with Copper-Nickel and Nickel in the Formation of Carbon Filaments. *J. Catal.* **1991**, *131*, 60-73.

76. Yang, R. T.; Chen, J. P., Mechanism of Carbon Filament Growth on Metal Catalysts. *J. Catal.* **1989**, *115*, 52-64.
77. Schouten, F. C.; Gijzeman, O. L. J.; Bootsma, G. A., Interaction of Methane with Ni(111) and Ni(100); Diffusion of Carbon into Nickel through the (100) Surface; An AES-LEED Study. *Surf. Sci.* **1979**, *87*, 1-12.
78. Wang, Z. L.; Ahmad, T. S.; ElSayed, M. A., Steps, Ledges and Kinks on the Surfaces of Platinum Nanoparticles of Different Shapes. *Surf. Sci.* **1997**, *380*, 302-310.
79. Wang, Z. L.; Petroski, J. M.; Green, T. C.; El-Sayed, M. A., Shape Transformation and Surface Melting of Cubic and Tetrahedral Platinum Nanocrystals. *J. Phys. Chem. B* **1998**, *102*, 6145-6151.
80. Rostrup-Nielsen, J. R., Sulfur-Passivated Nickel Catalysts for Carbon-Free Steam Reforming of Methane. *J. Catal.* **1984**, *85*, 31-43.
81. Helveg, S.; Lopez-Cartes, C.; Sehested, J.; Hansen, P. L.; Clausen, B. S.; Rostrup-Nielsen, J. R.; Abild-Pedersen, F.; Norskov, J. K., Atomic-scale Imaging of Carbon Nanofibre Growth. *Nature* **2004**, *427*, 426-429.
82. Rosei, R.; Decrescenzi, M.; Sette, F.; Quaresima, C.; Savoia, A.; Perfetti, P., Structure of Graphitic Carbon on Ni(111): a Surface Extended-Energy-Loss Fine-Structure Study. *Phys. Rev. B* **1983**, *28*, 1161-1164.
83. Yudasaka, M.; Kasuya, Y.; Kokai, F.; Takahashi, K.; Takizawa, M.; Bandow, S.; Iijima, S., Causes of Different Catalytic Activities of Metals in Formation of Single-wall Carbon Nanotubes. *Appl. Phys. A* **2002**, *74*, 377-385.
84. Massaro, T. A.; Petersen, E. E., Bulk Diffusion of Carbon-14 through Polycrystalline Nickel Foil between 350 and 700 Degrees C. *J. Appl. Phys.* **1971**, *42*, 5534-5539.
85. Lander, J. J.; Kern, H. E.; Beach, A. L., Solubility and Diffusion Coefficient of Carbon in Nickel: Reaction Rates of Nickel-Carbon Alloys with Barium Oxide. *J. Appl. Phys.* **1952**, *23*, 1305-1309.
86. Snoeck, J. W.; Froment, G. F.; Fowles, M., Steam/CO_2 Reforming of Methane. Carbon Filament Formation by the Boudouard Reaction and Gasification by CO_2, by H_2, and by Steam: Kinetic Study. *Ind. Eng. Chem. Res.* **2002**, *41*, 4252-4265.
87. Lobo, L. S., Intrinsic Kinetics in Carbon Gasification: Understanding Linearity, “Nanoworms" and Alloy Catalysts. *Appl. Catal., B* **2014**, *148*, 136-143.
88. Boudart, M., Catalysis by Supported Metals. In *Adv. Catal.*, Eley, D. D.; Pines, H.; Weisz, P. B., Eds. Academic Press: New York, NY, 1969; Vol. 20, pp 153-166.
89. Mavrikakis, M.; Baumer, M.; Freund, H. J.; Norskov, J. K., Structure Sensitivity of CO Dissociation on Rh Surfaces. *Catal. Lett.* **2002**, *81*, 153-156.
90. Georgakilas, V.; Perman, J. A.; Tucek, J.; Zboril, R., Broad Family of Carbon Nanoallotropes: Classification, Chemistry, and Applications of Fullerenes, Carbon Dots, Nanotubes, Graphene, Nanodiamonds, and Combined Superstructures. *Chem. Rev.* **2015**, *115*, 4744-4822.

Chapter 3

H_2-D_2 Isotopic Exchange Pathways and Thermodynamic Isotope Effects for Hydrogen Chemisorption on Pt Nanoparticles

Abstract

H_2 and D_2 chemisorption isotherms were obtained on Pt-based catalysts (0.1-30 kPa H_2 or D_2, 523-673 K) to measure thermodynamic isotope effects (TIE) for hydrogen dissociative adsorption. TIEs were near unity (0.7-1.0) and only weakly dependent on temperature and surface coverage. These results were extrapolated to assess H* and D* coverages at equilibrium at 383 K, where H_2-D_2 exchange kinetic experiments were carried out. H_2-D_2 isotopic exchange rates (5-80 kPa H_2, 5-80 kPa D_2; 383 K; H_2/D_2 = 0.0625-16) showed monotonic increases in rate with H_2 and D_2 pressures, in contrast with the kinetics expected from a recombinative desorption (H* + D*) mechanism or the extrapolated equilibrium compositions of H* and D*. The data implicate an alternative reaction pathway in which H_2 and D_2 reacts with D* and H* adatoms in a single-site mechanism. Exchange rates were nearly identical when H_2 and D_2 pressures were switched, indicating the absence of a kinetic isotope effect (KIE) for H_2-D* and D_2-H* reactions and a H*/D*-adlayer whose composition is controlled by the kinetics of exchange reactions rather than the thermodynamics (and TIE) for H_2 and D_2 adsorption. Recombinative desorption rates only became measurable at low combined H_2+D_2 pressures (<10 kPa) and at temperatures greater than 700 K. Density functional theory (DFT) shows that the reaction of H_2 and D* (or D_2 and H*) likely occurs via the dissociative adsorption of H_2 (or D_2) at vacancies that arise from fluctuations in mobile H*-adlayers. The results from this study demonstrate that H_2-D_2 isotopic exchange is mediated by reaction pathways that circumvent desorption/recombination reactions and therefore cannot be used to demonstrate reversibility of H_2 adsorption on catalytic surfaces at conditions of practice for hydrogenation/dehydrogenation reactions.

3.1 Introduction

Isotopic tracer experiments and analysis of kinetic effects of isotopic substitutions are essential tools in discerning among plausible mechanisms of chemical transformations. These methods can assess the identity, reversibility, and kinetic relevance of elementary steps without disturbing the nature of reactants and products or the chemical steady-state, thus providing direct mechanistic details, albeit often in difficult to interpret form. The isotopic identity of atoms can affect the chemical reactivity of the bonds being cleaved or formed; it can also change the thermodynamic properties of molecules and the equilibrium constants for their chemical interconversions.[1] The ratio of reaction rates or rate constants for a molecule with the most abundant isotope relative to those of its isotopologues is denoted as a kinetic isotope effect (KIE), while the corresponding ratio in their equilibrium constants is known as a thermodynamic isotope effect (TIE). These effects arise from the different mass of each isotopologue and the effects of the isotopic atom on the vibrational frequency in the bonds that contain them in reactants, products, and transition states.[2-3] As a result, these methods can be used to discern the involvement of specific bonds in kinetically-relevant and quasi-equilibrated steps within a sequence of elementary steps,[3-6] as shown previously for many catalytic reactions,[7-18] especially for hydrogen and deuterium atoms.

Isotopic labels can be used to "trace" the fate of atoms and the molecules that contain them through reaction networks, thus probing the reversibility of steps that form or cleave any chemical bonds that include the isotope;[19-20] these methods are broadly used in surface catalysis.[6-7, 21-24] H_2-D_2 isotopic exchange, in particular, is often used to assess the reversibility of H_2 dissociation and recombination steps on surfaces as such molecules react in catalytic hydrogenation-dehydrogenation events:

$$H_2 + 2^* \rightleftharpoons 2H^* \quad (1)$$

$$D_2 + 2^* \rightleftharpoons 2D^* \quad (2)$$

$$HD + 2^* \rightleftharpoons H^* + D^* \quad (3)$$

The equilibration of H_2-D_2 mixtures results in binomial distributions of H_2, HD, and D_2 molecules, as a result of the stochastic scrambling of all isotopic species.[19, 25] These experiments and interpretations, however, implicitly assume that isotopic scrambling events occur *only* via the dissociative adsorption and recombinative desorption reactions represented in Equations 1-3. Isotopic exchange between H_2 and D_2 and para-ortho hydrogen interconversion reactions were previously examined on Pt wires under high-vacuum conditions; these studies concluded that a single-site exchange between H_2 and bound D* adatoms (and D_2 and H* adatoms) may occur, without requiring the surface-mediated dissociation of the H-H bond in H_2, even below 200 K.[26] Similar pathways have been proposed on other metals (Ni, Cu, Ag, Au).[27-32] These studies, however, did not provide unequivocal kinetic evidence for such mechanisms at pressures and temperatures relevant for catalytic turnovers; as a result, such conclusions are seldom cited in later studies that exploited such methods to assess the reversibility of H_2 dissociation events during catalysis. These previous studies of H_2-D_2 exchange did not place the proposed exchange routes

firmly within the context of the thermodynamics of H_2 and D_2 chemisorption on surfaces, which have been the subject of several independent later studies (e.g., Pt[33-39]).

This study addresses the kinetics of H_2-D_2 isotopic exchange on Pt-based catalysts and the magnitude of H_2/D_2 thermodynamic isotope effects at conditions of catalytic relevance. H_2 and D_2 chemisorption isotherms obtained at 523-673 K (10^{-4}-10^{1} kPa H_2 or D_2; 0.1-0.8 monolayer coverages) are nearly identical at each temperature, reflecting TIE values near unity. The data reflect a very weak temperature dependence, consistent with dissociative chemisorption enthalpies for H_2 and D_2 on Pt surfaces that differ only by 4.2 ± 1.2 kJ mol^{-1}, and can be used to calculate equilibrium coverages of H* and D* (for a given mixture of H_2 and D_2) at other temperatures and conditions.

H_2-D_2 exchange rates on Pt catalysts at 383 K increase monotonically with H_2 and D_2 pressure (5-80 kPa H_2, 5-80 kPa D_2). Exchange rates are also nearly identical when H_2 and D_2 pressures are switched, in contrast with the difference expected with the TIE at 383 K (0.6 ± 0.2). These kinetic data are inconsistent with the involvement of dissociation/recombination events (Eq. 1-3) in isotopic exchange. An alternate exchange mechanism, in which H_2 reacts with D* (and D_2 reacts with H*),[26-32] is, however, consistent with all experimental and theoretical evidence. These reactions are shown to exhibit KIE values near unity (1.1 ± 0.33) (H_2-D* vs. D_2-H*). They provide an alternate reaction pathway that leads to H*/D* compositions that are determined by the kinetics of exchange reactions rather than the thermodynamics of H_2 and D_2 dissociation; such pathways are consistent with the absence of a maximum in rate at equimolar compositions. The data reported here indicate that these "associative" exchange reactions remain the dominant pathway at temperatures below 700 K (5-40 kPa, total H_2 + D_2 pressure). The kinetic behavior of H_2-D_2 exchange cannot distinguish various structurally distinct H_2-D* and D_2-H* reaction mechanisms. Density function theory calculations on Pt(111) surfaces and 201-atom Pt nanoparticles show that these exchange events likely involve the dissociation of H_2 or D_2 on Pt surfaces at vacancies that form from entropy-driven fluctuations in coverages within mobile H*/D* adlayers, without requiring the desorption of H* and D*. H_2-D_2 isotopic exchange is therefore mediated by reaction pathways that circumvent desorption/recombination. Consequently, exchange rates cannot be used to unequivocally demonstrate reversibility of H_2 adsorption at conditions of catalytic hydrogenation/dehydrogenation reactions.

3.2 Methods

3.2.1 Catalyst Synthesis Methods

Pt nanoparticles dispersed on SiO_2 (0.2% wt., Pt/SiO_2-A) were prepared using strong electrostatic adsorption methods[40] that exploit interactions between SiO_2 surfaces that are negatively-charged at the prevalent solution pH (11.4) and aqueous cationic Pt precursors ($Pt(NH_3)_4](NO_3)_2$; 99.99% metals basis; Alfa Aesar) to form well-dispersed strongly-bound precursors.

SiO_2 (Davisil, grade 62, Sigma-Aldrich) was treated in flowing air (0.83 cm^3 g^{-1} s^{-1}; zero grade, Praxair) while ramping from ambient temperature to 1073 K (0.083 K s^{-1}), holding for 5 h, and cooling to ambient temperature. $[Pt(NH_3)_4](NO_3)_2$ (0.0060 g) and SiO_2 (1.5 g) were then added to 25 cm^3 of a 0.4 M NH_4OH solution, prepared by diluting a 25% solution of NH_4OH (Sigma-Aldrich) with deionized (DI) water (>18.0 MΩ-cm resistivity) and stirring for 2 h. The solids were

filtered and rinsed three times with DI water (100 cm^3 g^{-1}) and treated overnight in ambient stagnant air at 368 K. Samples were then treated in flowing air (1.67 cm^3 g^{-1} s^{-1}; zero grade, Praxair) while heating from ambient temperature to 873 K (at 0.083 K s^{-1}) and holding for 3 h before again cooling to ambient temperature. This was followed by treatment in flowing H_2 (1.67 cm^3 g^{-1} s^{-1}; 99.999% UHP; Praxair) while ramping to 1073 K (at 0.083 K s^{-1}) and holding for 2 h. After cooling, the sample was exposed to flowing 2% mol O_2 (balance He) (1.67 cm^3 g^{-1} s^{-1}; certified grade, Praxair) for 0.5 h at ambient temperature. This O_2 treatment is intended to passivate the surfaces of Pt nanoparticles to avoid exothermic oxidation upon contact with ambient air. A second sample of Pt/SiO_2 (0.2% wt., Pt/SiO_2-B) was prepared using similar steps, but treated in flowing air and H_2 at 623 K instead of 873 K.

Pt nanoparticles dispersed on γ-Al_2O_3 (1% wt., Pt/γ-Al_2O_3-A) were prepared by incipient wetness impregnation. γ-Al_2O_3 (Sasol, CATALOX SBa 200) was treated in flowing air (0.83 cm^3 g^{-1} s^{-1}; zero grade, Praxair) while ramping to 1073 K (0.083 K s^{-1}) and holding for 5 h. An aqueous solution of H_2PtCl_6 (8% wt. in H_2O; Sigma-Aldrich) was added dropwise to γ-Al_2O_3 (0.26 cm^3 g^{-1} γ-Al_2O_3). The sample was treated in ambient air at 368 K overnight and then in flowing air (1.67 cm^3 g^{-1} s^{-1}; zero grade; Praxair) by heating from ambient temperature to 873 K (at 0.083 K s^{-1}) and holding for 3 h before cooling to ambient temperature. This procedure was followed by treatment in flowing H_2 (1.67 cm^3 g^{-1} s^{-1}; 99.999% UHP; Praxair) while heating to 1073 K (at 0.083 K s^{-1}) and holding for 2 h. After cooling, the sample was treated in 2% v/v O_2 (balance He; certified grade; Praxair) for 0.5 h at ambient temperature to passivate the Pt nanoparticles.

Pt/SiO_2 (5% wt., Pt/SiO_2-C) and Pt/γ-Al_2O_3 (1.6% wt., Pt/γ-Al_2O_3-B) samples were also prepared and used in H_2 and D_2 uptake experiments to measure thermodynamic isotope effects. Pt/γ-Al_2O_3-B was prepared as reported previously.[33] Pt/SiO_2-C was prepared by incipient wetness impregnation of SiO_2 (Cabosil, HS-5, 310 m^2 g^{-1}) with an aqueous solution of $Pt(NH_3)_4(NO_3)_2$ (Alfa Aesar, CAS 20634-12-2). The sample was treated in flowing dry air (99.99%, 0.8 cm^3 g^{-1} s^{-1}, Praxair) at 673 K (0.033 K s^{-1}) for 3 h and then treated in flowing 9 % v/v H_2 (balance He, Praxair, 1.67 cm^3 g^{-1} s^{-1}) by heating from ambient temperature to 773 K at 0.033 K s^{-1}, holding for 3 h. It was then passivated by exposure to flowing 0.5 % O_2/He (Praxair, certified grad, 0.05 cm^3 g^{-1} s^{-1}) at ambient temperature for 1 h before contact with ambient air.

Pt black (Strem Chemicals, 22.7 m^2 g^{-1} nominal surface area) was used as received and treated before H_2-D_2 kinetic experiments, as described below.

3.2.2 Measurement of H_2 and D_2 Chemisorption Isotherms

Pt dispersion values, defined as the ratio of the number of exposed Pt sites to the total number of Pt atoms, for Pt/SiO_2-A, Pt/SiO_2-B, and Pt/γ-Al_2O_3-A samples were measured from H_2 chemisorption uptakes. Samples (ca. 1 g) were treated in flowing H_2 (99.999% UHP; Praxair; 0.33 cm^3 g^{-1} s^{-1}) while at 673 K (0.083 K s^{-1}) for 1 h and then evacuated ($<10^{-5}$ Pa) at this temperature for 1 h. The sample was then cooled in vacuum to 373 K. H_2 chemisorption uptakes were measured at 1-40 kPa H_2 and 373 K. Saturation uptakes were determined by linear extrapolation of the uptakes to zero H_2 pressure. Nanoparticle diameters were calculated using the following relations:[41]

$$d = \frac{f_{shape} N_M}{2N_{H_2}} \frac{v_m}{a_m} \theta_{sat} \quad (4)$$

$$\theta_{sat} = \mathrm{H/Pt_s} = 1 + \alpha(d^{-1}) + \beta(d^{-2}) \quad (5)$$

Here, d is the diameter of the particle, f_{shape} is a shape factor (6 for a hemispherical particle), N_M is the total number of metal atoms, N_{H_2} is the number of H_2 molecules dissociated onto the surface, v_m and a_m are the volume and surface area of a Pt atom (from the bulk density of Pt, 21.45 g cm^{-3})[42], and α (0.0364) and β (0.735) are empirical parameters specific for Pt.[41] Pt_s denotes atoms on the metal surface. This system of equations (Eq. 4-5) can be solved iteratively to obtain the particle diameter (d) and saturation coverage (θ_{sat}) in a manner that corrects for suprastoichiometric coverages on small metal nanoparticles that arise from the binding of multiple H-atoms on corner and edge sites.[41]

H_2 and D_2 chemisorption uptakes (523-673 K at 0.1-30 kPa H_2 or D_2) were also measured on Pt/SiO_2-C and Pt/γ-Al_2O_3-B samples to determine thermodynamic isotope effects for dihydrogen dissociative adsorption. Samples (ca. 1 g) were treated at 723 K in flowing H_2 (1.33 cm^3 g^{-1} s^{-1}; UHP grade, Praxair; 0.083 K s^{-1} heating rate) for 1 h and then evacuated for 2 h. After evacuation, samples were brought to the target chemisorption temperature, and H_2 (or D_2) uptakes were measured by increasing the H_2 (or D_2) pressure from 0.1 to 30 kPa (H_2, Praxair, UHP; D_2, Spectra Gases Inc., UHP). The apparent cell volume was determined at each temperature using He as a non-adsorbing inert gas.

3.2.3 Measurement of Isotopic Exchange Rates

Isotopic exchange rates were measured on samples (0.0005-0.0500 g, <100 μm aggregate diameter) held on a quartz frit within a U-shaped quartz tube (6.35 mm O.D., 4 mm I.D.). H_2 (99.999% UHP; Praxair), D_2 (99.8% isotopic purity, Research Grade; Praxair), and N_2[1] (99.998%, Praxair) streams were treated using purifiers (VICI Metronics) designed to remove residual H_2O and O_2. Molar flow rates were controlled using electronic mass flow controllers (Parker Porter 200 series). Samples were treated in flowing H_2 (100 cm^3 g^{-1} s^{-1}) while heating from ambient temperature to 873 K (at 0.083 K s^{-1}) for 0.2% wt. Pt/SiO_2-A, 1% wt. Pt/γ-Al_2O_3-A, and Pt black samples and to 623 K for 1% wt. Pt/SiO_2-B samples and then holding for 2 h before isotopic exchange rate measurements.

Outlet streams were speciated using mass spectrometry (Leybold Inficon Transpector, TSP TH200). H_2-D_2 exchange rates were determined by correcting measured rates (r_n) for approach to isotopic equilibrium (η) to give forward rates (r_f) using:

$$r_n = r_f\,(1 - \eta) \quad (6)$$

The approach to equilibrium (η) for H_2-D_2 exchange:

$$H_2 + D_2 \rightarrow 2\,HD \quad (7)$$

is defined as:

$$\eta = \frac{(HD)^2}{(H_2)(D_2)}\frac{1}{K_{HD}} \quad (8)$$

[1] N_2 is used as the inert carrier and internal standard in place of He to avoid overlap with D_2 in mass spectrometry.

(i) denotes the pressure of species i. K_{HD} is the equilibrium constant for H_2-D_2 exchange; it equals 4 at all temperatures, corresponding to the binomial isotopologue distribution.[25] The thin catalyst beds used in these experiments exhibit hydrodynamics that resemble well-mixed systems; thus, exit concentrations were used in Equation 8. The absence of diffusional corruptions of measured exchange rates was confirmed by similar measured exchange rates as the size of the catalyst aggregates was varied (smaller particles, < 50 μm, were obtained by grinding the catalyst into a fine powder; Section 3.6.1).

3.2.4 Computational Methods

Periodic planewave density functional theory (DFT) calculations were performed using the Vienna ab initio simulation package (VASP)61,62 as implemented in the Computational Catalysis Interface (CCI). Planewaves were constructed using projector augmented waves (PAW)63-65 with an energy cutoff of 396 eV. The revised Perdew-Burke-Ernzerhof (RPBE) form of the generalized gradient approximation (GGA) was used to describe exchange and correlation energies.[43-44] Wavefunctions were converged until electronic energies varied by $<10^{-6}$ eV. Forces on all atoms were determined using a fast Fourier transform (FFT) grid with a cutoff equal to twice the planewave cutoff; the geometries of all structures were optimized until forces on all atoms were <0.05 eV $Å^{-1}$.

H_2 molecules in the gas phase were modeled by placing them within a 18 × 18 × 18 A˚ vacuum unit cell. Pt(111) surfaces were modeled as 4 × 4 closed-packed periodic lattices with four layers orthogonal to the surface and 1 nm of vacuum separating slabs; the bottom two layers were fixed at their bulk positions (fcc crystal with unit cell parameter of 0.39239 nm)[45], and the top two layers were relaxed. A 3 × 3 × 1 Monkhorst-pack sampling of the first Brillouin zone (k-point mesh)[46] was used during geometric convergence iterations; after convergence, a single-point calculation with a 6 × 6 × 1 k-point mesh was performed to determine electronic energies. Vibrational frequencies were calculated for bound species and transition states using a fixed displacement method (two displacements per mode), in which all metal atoms were fixed and all H atoms were allowed to vibrate (including spectator H* species). These frequency calculations were used, along with statistical mechanics formalisms and harmonic oscillator approximation models, to estimate vibrational zero-point energies, enthalpies, entropies, and Gibbs free energies. For H_2(g), the translational and rotational enthalpies and free energies were also computed instead of using experimental values. Symmetric cubooctahedral Pt nanoparticles (201 atoms, 1.4 nm diameter) with 1.4 nm of vacuum between metal atoms were also examined as model surfaces, as described in detail in previous reports.[7, 41, 47-48] The Brillouin zone was sampled only at the Γ-point in the case of nanoparticle model calculations.

3.3 Results and Discussion

3.3.1 Pt Dispersions and Nanoparticle Diameters

Fractional dispersions were measured for three Pt/SiO_2 samples and two Pt/γ-Al_2O_3 sample; these data were used to calculate nanoparticle diameters using Equations 4-5 (Table 1).

Table 1. Nominal metal contents, dispersions, and calculated particle diameters

Sample	Nominal Pt content (% wt.)	Pt Dispersion	Pt Nanoparticle Diameter (nm)[†]
Pt/SiO_2-A	0.2	0.38	3.2
Pt/SiO_2-B	0.2	1.0	1.5
Pt/SiO_2-C	5.0	0.32	3.8
Pt/γ-Al_2O_3-A	1.0	0.72	1.9
Pt/γ-Al_2O_3-B[*]	1.6	0.37	3.3

[*]Synthesis and characterization reported in a previous study.[33]
[†]Calculated by assuming hemispherical particle geometries and using the bulk density of Pt (21.45 g cm^{-3}).[42] H/Pt_s stoichiometries were estimated using Equations 4-5.

3.3.2 H_2 and D_2 Uptakes on Pt/SiO_2-C and Pt/γ-Al_2O_3-B and Thermodynamic Isotope Effects

H_2 and D_2 chemisorption uptakes (10^{-4}-10^{1} kPa) were measured on 5.0% wt. Pt/SiO_2-C and 1.6% wt. Pt/γ-Al_2O_3-B samples at 623 K. H_2 and D_2 uptake isotherms (Fig. 1) were very similar for each given sample; the uptakes (of both isotopes) differed between Pt/SiO_2-C and Pt/γ-Al_2O_3-B because of their different metal dispersion (Table 1).[33] These uptake data were used to determine dissociative adsorption equilibrium constants for H_2 (K_H) and D_2 (K_D):

$$K_H = \frac{\theta_H^2}{(H_2)\theta_s^2} \tag{9}$$

$$K_D = \frac{\theta_H^2}{(H_2)\theta_s^2} \tag{10}$$

θ_H and θ_D are the fractional surface coverages of H* and D* adatoms, defined as the number of H (or D) atoms adsorbed at a given pressure divided by the number of atoms adsorbed at saturation, and θ_s is fraction of unoccupied sites. The ratio of these adsorption equilibrium constants gives the thermodynamic isotope effect (TIE = K_H/K_D) for dissociative dihydrogen adsorption. These equilibrium constants and TIE ratios are shown as a function of fractional surface coverage in Figure 2. TIE ratios were only slightly influenced by coverage (slopes of 0.13 ± 0.13 and -0.25 ± 0.23 on Pt/SiO_2-C and Pt/γ-Al_2O_3-B, respectively). These ratios were near unity on Pt/SiO_2-C (0.90 ± 0.07) and Pt/γ-Al_2O_3-B (0.81 ± 0.1) at all H_2 and D_2 pressures and fractional coverages and agree well with DFT-derived values on Pt(111) surfaces (0.68, 0.87, and 0.91 for atop, fcc, and hcp binding modes; 1 ML, 623 K).[49]

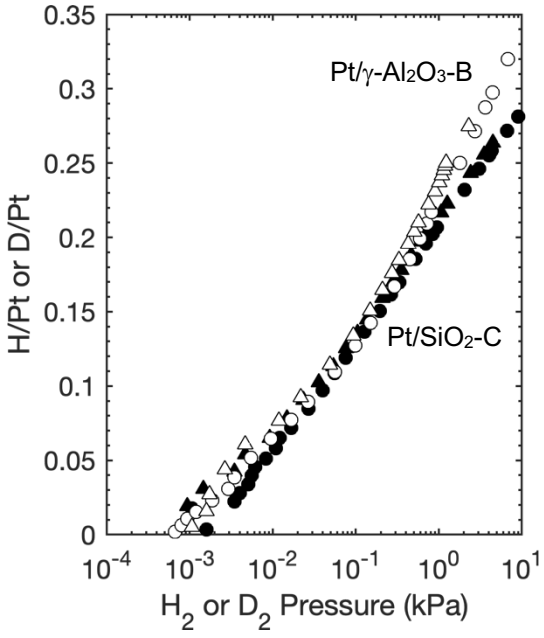

Figure 1. H_2 (●,○) and D_2 (▲,△) adsorption isotherms on Pt/SiO_2-C (closed symbols) and Pt/γ-Al_2O_3-B (open symbols) at 623 K.

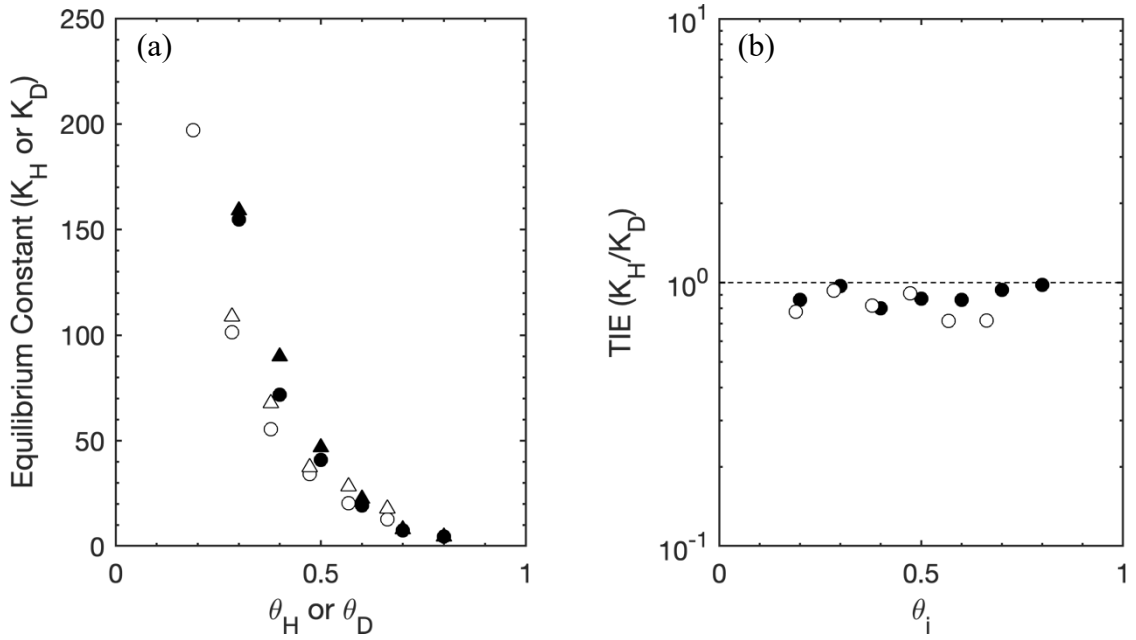

Figure 2. (a) Equilibrium constants for H_2 (K_H; ●,○) and D_2 (K_D; ▲,△) dissociative adsorption at different fractional surface coverages on Pt/SiO_2-C (closed symbols) and Pt/γ-Al_2O_3-B (open symbols). (b) Thermodynamic isotope effects (TIE = K_H/K_D) at different fractional surface coverages on Pt/SiO_2-C (●) and Pt/γ-Al_2O_3-B (○) at 623 K. Dashed line indicates the position of unity.

H_2 and D_2 adsorption isotherms were also measured at other temperatures (523-673 K; isotherms and equilibrium constants in Section 3.6.2) on 1.6% wt. Pt/γ-Al_2O_3-B to determine temperature effects on TIE values. Average TIE values, reflecting the mean over the range of fractional coverages (0.19-0.57) in view of their weak coverage dependence (Fig. 2), are shown in Figure 3 (523-673 K). These values are nearly independent of temperature, within experimental uncertainty, and thus reflect H_2 and D_2 adsorption enthalpies and entropies,

$$TIE = \frac{K_H}{K_D} = \exp\left(\left(\frac{\Delta H_{D_2,ads} - \Delta H_{H_2,ads}}{RT}\right) + \left(\frac{\Delta S_{D_2,ads} - \Delta S_{H_2,ads}}{R}\right)\right) \quad (11)$$

that are very similar. The small differences in enthalpy ($\Delta H_{D_2,ads} - \Delta H_{H_2,ads}$, -4.1 ± 1.4 kJ mol^{-1}) and entropy ($\Delta S_{D_2,ads} - \Delta S_{H_2,ads}$, 4.8 ± 2.3 kJ mol^{-1} K^{-1}) determined from the data in Figure 3 reflect a slightly more negative enthalpy of adsorption for D_2 compared to H_2. Equation 11 can be used to extrapolate TIE values to other temperature and to infer the relative coverages of H* and D* at the conditions of isotopic exchange (Eq. 9-10).

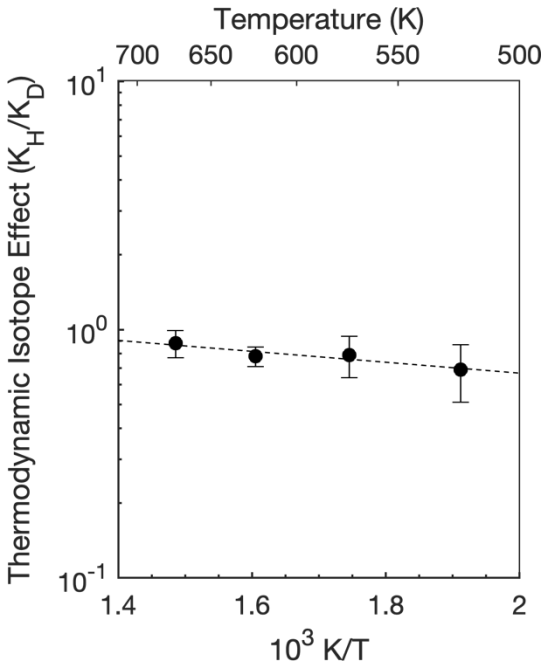

Figure 3. Mean thermodynamic isotope effect ratios (TIE = K_H/K_D) (averaged across H* or D* fractional coverages, 0.19-0.57) at different temperatures (523-673 K) on Pt/γ-Al_2O_3-B. Dashed line represents the line of best fit.

3.3.3 Effects of H_2 and D_2 Pressures on Exchange Rates and Implications for the Identity and Kinetic Relevance of Elementary Steps

H_2-D_2 isotopic exchange turnover rates were measured at 383 K over a range of H_2 and D_2 pressures (5-80 kPa) on 0.2% wt. Pt/SiO_2-A (3.2 nm, Table 1). HD formation rates were below detection limits on a Pt-free SiO_2 sample at these conditions. Figure 4 shows that exchange rates

increased monotonically with increasing H_2 or D_2 pressures (5-80 kPa; $\frac{(H_2)}{(D_2)}$ = 0.0625-16). HD formation rates were nearly identical when the H_2 and D_2 pressures were switched (as shown by significant overlap between the open and filled symbols of a given type in Fig. 4).

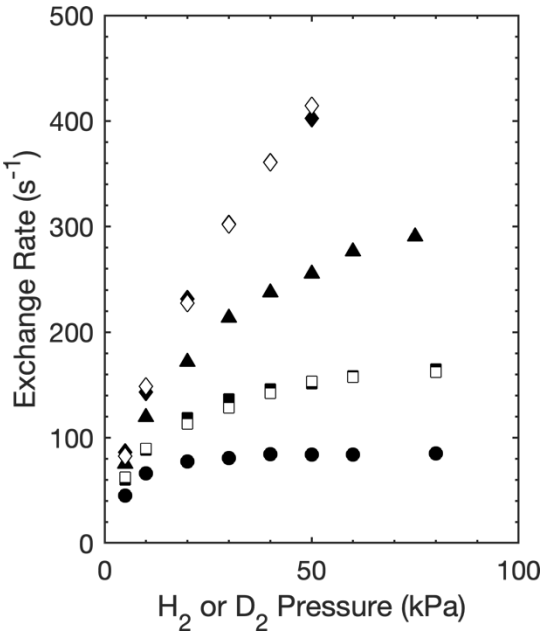

Figure 4. Isotopic exchange rates as a function of H_2 or D_2 pressure at 5 (●), 10 (■,□), 20 (▲), and 40 (◆,◇) kPa D_2 (closed symbol) or H_2 (open symbol) at 383 K on 0.2% wt. Pt/SiO_2-A. Overlapping black and white symbols indicate that exchange rates were nearly identical when H_2 and D_2 pressures were switched.

These kinetic trends are first examined in the context of the dissociation-recombination mechanism (Eq. 1-3) that they contradict. HD formation rates mediated by recombination of H* and D* (Eq. 2) would depend on the H* and D* coverages set by the thermodynamics of H_2 and D_2 dissociative adsorption and would reach maximum values when H* and D* become equal. The chemisorption data reported here (Section 3.3.2) and in previously studies[33] indicate that Pt surfaces are nearly saturated with H* or D* at all pressures used in these exchange experiments ($(H_2) + (D_2) > 10$ kPa). H* and D* coverages can be described by extrapolation of TIE ratios to 383 K from H_2/D_2 chemisorption data on Pt/γ-Al_2O_3-B (523-673 K, Fig. 3; Section 3.3.2), which gives a value of 0.6 ± 0.2. This TIE value (0.6, 383 K) indicates that H* and D* coverages become equal at H_2/D_2 ratios of about 1.3. This ratio was calculated assuming that only the desorption rate constants exhibit non-unity KIE values (Section 3.6.3.1). In the absence of a TIE, the rate of HD formation is given by (Section 3.6.3.1):

$$r_{HD,f} = k_{-1}\frac{(H_2)(D_2)}{\left((H_2)+(D_2)\right)^2} \tag{12}$$

and HD formation rates reach a maximum at $\frac{(H_2)}{(D_2)}$ ratios of unity. Measured HD formation rates, however, increased monotonically with increasing H_2 and D_2 pressure (Fig. 4), even for H_2/D_2 ratios as high as 16. Such trends are not consistent with the dissociation-recombination exchange routes depicted by Equations 1-3 and the rate equation consistent with such elementary steps (Eq. 12). These exchange rate data are also inconsistent with a two-site mechanism, in which H_2 and D_2 molecules adsorb and react in a concerted manner with H*-H*, H*-D*, or D*-D* pairs; this mechanism would give a rate equation (Section 3.6.3.2, assuming TIE value of unity):

$$r_{HD,f} = [64\, k_{-3}(H_2)(D_2)\big((H_2) + (D_2)\big)$$
$$\{(H_2)^6 + (D_2)^6 + 11(H_2)^2(D_2)^4 + 11(D_2)^2(H_2)^4 - \gamma((H_2)^4 + (D_2)^4 + 4(H_2)^2(D_2)^2)\}]$$
$$\div [(3(H_2)^2 + (D_2)^2 - \gamma)^2(3(D_2)^2 + (D_2)^2 - \gamma)^2] \quad (13)$$

$$\gamma = \sqrt{(H_2)^4 + 14(H_2)^2(D_2)^2 + (D_2)^4} \quad (14)$$

Equations 13-14 similarly predict a maximum in HD formation rate at $\frac{(H_2)}{(D_2)}$ ratios near unity, thus ruling out such exchange routes by contradicting the trends in Figure 4. Parity plots of measured and predicted HD formation rates confirm the inadequacy of these mechanisms in describing exchange rates (Fig. SI-4 in Section 3.6.4).

$H_2 + 2* \underset{k_{-1}}{\overset{k_1}{\rightleftharpoons}} 2H*$ [1.1]

$HD + 2* \xleftarrow[k_{-2}]{} H* + D*$ [1.2]

$D_2 + 2* \underset{k_{-3}}{\overset{k_3}{\rightleftharpoons}} 2D*$ [1.3]

$H_2 + D* \xrightarrow{k_4} HD + H*$ [1.4]

$D_2 + H* \xrightarrow{k_5} HD + D*$ [1.5]

Scheme 1. Dissociative (1.1-1.3) and associative (1.4-1.5) elementary steps for H_2-D_2 isotopic exchange.

Another plausible mechanism, as suggested in previous studies,[26-32] is the single-site associative routes in which H_2 and D_2 molecules react with single D* and H* adatoms to exchange their isotopes. These reactions are shown in Scheme 1 (steps 1.4-1.5), along with the dissociative-recombinative reactions (steps 1.1-1.3). HD formation rates mediated by the elementary steps in Scheme 1 are given by:

$$r_{HD,f} = k_{-2}\theta_H\theta_D + k_4(H_2)\theta_D + k_5(D_2)\theta_H \quad (15)$$

Equation 15 contains separate terms for H_2-D* and D_2-H* reactions, reflecting the possible presence of a kinetic isotope effect ($KIE_{ex} = \frac{k_4}{k_5}$).

The value of KIE_{ex} is inferred here from HD formation rates that were nearly identical when the magnitude of the H_2 and D_2 pressures were switched (Fig. 4, indicated by overlapping open and filled symbols of a given type). We define a parameter $\gamma_{i,j}$ as an inlet stream with H_2 pressure *i*, and D_2 pressure *j* (in kPa). Figure 5 shows that the ratios of rates defined as:

$$\chi_{i,j} = \frac{r_{HD}(\gamma_{i,j})}{r_{HD}(\gamma_{j,i})} \quad (16)$$

were near unity (1.01 ± 0.05) for all pairs of H_2 and D_2 pressures, contradicting H* and D* coverages calculated from the TIE at 383 K (0.6 ± 0.2). Such deviations from the expected H*/D* coverages suggest that H_2-D* and D_2-H* reactions (steps 1.4-1.5, Scheme 1), which provide an alternate pathway for exchanging hydrogen and deuterium atoms, occur much faster than dissociation and recombination events (steps 1.1-1.3, Scheme 1). These $\chi_{i,j}$ values were also calculated (Section 3.6.5) for various KIE_{ex} values (0.5-2), which led to significant deviations of $\chi_{i,j}$ values from unity (0.6-1.7; Fig. 5). The experimental values (Fig. 5) thus reflect KIE_{ex} $\left(\frac{k_4}{k_5}\right)$ values near unity (1.1 ± 0.33). H* and D* coverages in this limiting case (assuming a KIE_{ex} value of 1) are described by (derivation in Section 3.6.3.3):

$$\theta_H = \frac{(H_2)}{(H_2) + (D_2)} \quad (17)$$

$$\theta_D = \frac{(D_2)}{(H_2) + (D_2)} \quad (18)$$

H*/D* ratios, as described by Equation 17-18, are equal to the H_2/D_2 ratios in the contacting gas phase.

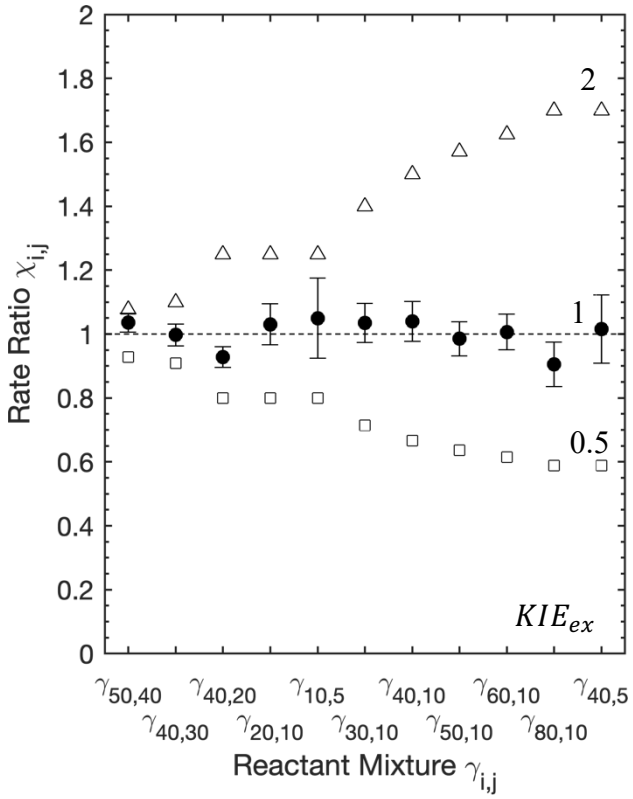

Figure 5. Rate ratios ($\chi_{i,j} = \frac{r_{HD}(\gamma_{i,j})}{r_{HD}(\gamma_{j,i})}$; ●) for reactant mixtures $\gamma_{i,j}$ (H_2 pressure *i*, and D_2 pressure *j*). Simulated ratios are included for KIE_{ex} $\left(\frac{k_4}{k_5}\right)$ values of 0.5 (□) and 2 (△) for comparison.

Equations 17 and 18 can be substituted into Equation 15 to give:

$$r_{HD,f} = k_{-2}\frac{(H_2)(D_2)}{\left((H_2)+(D_2)\right)^2} + 2k_4\frac{(H_2)(D_2)}{(H_2)+(D_2)} \tag{19}$$

for $\frac{k_4}{k_5}$ ratios of unity. This equation includes terms for dissociation-recombination reactions ($k_{-2}\frac{(H_2)(D_2)}{\left((H_2)+(D_2)\right)^2}$; steps 1.1-1.3, Scheme 1) and associative H_2-D* and D_2-H* reactions ($2k_4\frac{(H_2)(D_2)}{(H_2)+(D_2)}$; steps 1.4-1.5, Scheme 1). Equation 19 can also be expressed in a linear form that allows the rate constants k_{-2} and k_4 (normalized per surface site) to be regressed linearly from isotopic exchange rates:

$$\frac{r_{HD,f}\left((H_2)+(D_2)\right)^2}{(H_2)(D_2)} = k_{-2} + 2k_4\left((H_2)+(D_2)\right) \tag{20}$$

Figure 6 shows these rates at 383 K according to the functional form of Equation 20. The value of k_{-2} (-2.1 ± 20 s^{-1}) is given by the y-intercept of the data in Figure 6, while the value of k_4 (9.1 ± 0.2 kPa^{-1} s^{-1}) is reflected in the slope (uncertainties are defined as 95% confidence intervals). The near-zero value and large uncertainty of k_{-2} show that recombinative hydrogen desorption

reactions (steps 1.1-1.3 in Scheme 1) are much slower than H_2-D* and D_2-H* reactions (steps 1.4-1.5 in Scheme 1), as also indicated by $\chi_{i,j}$ values near unity (1.01 ± 0.05, Fig. 5); consequently, such routes contribute negligibly to measured exchange rates these reaction conditions (383 K, 5-80 kPa H_2 or D_2). Sensitivity analyses of k_{-2} further indicate that rates of recombination are too small to be measured. A parity plot of the HD formation rates modeled by Equation 20 and Scheme 1 is available in Section 3.6.4.

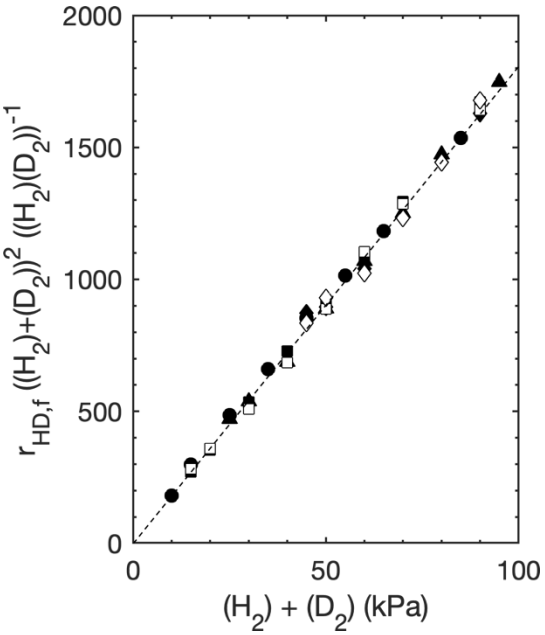

Figure 6. H_2-D_2 exchange rate data at 5 (●), 10 (■,□), 20 (▲), and 40 (◆,◇) kPa H_2 (open symbol) or D_2 (closed symbol) at 383 K on 0.2% wt. Pt/SiO_2-A, linearized in accordance with Equation 20. Dashed line represents linear regression of the data.

These data and analyses show that H_2-D_2 exchange occurs on surfaces saturated with a mixture of H* and D* adatoms at relative coverages dictated by the reactions of H_2 with D* and D_2 with H* (steps 1.4-1.5, Scheme 1) with KIE values near unity; these steps occur much faster than H_2/D_2 dissociation or H*-H*, H*-D*, D*-D* recombination reactions (steps 1.1-1.3 in Scheme 1) and lead to H*/D* ratios that equal the H_2/D_2 ratios in the contacting gas phase. Consequently, the specific value of the TIE for H_2 and D_2 dissociative adsorption does not influence H_2-D_2 isotopic exchange rates.

3.3.4 Effects of Temperature and H*/D* Coverage on Isotopic Exchange Rates

H_2-D_2 exchange rates were measured over a broad temperature range (303-1000 K) on Pt/SiO_2-A at several H_2 and D_2 pressures (2-20 kPa). HD formation rates for recombination reactions (step 1.2, Scheme 1) only depend on the relative ratio of H_2 and D_2 and do not increase with increasing pressure for a given ratio (Eq. 19), in contrast with H_2-D* and D_2-H* reactions. Decreasing the combined pressure of H_2 and D_2 therefore decreases the contribution of H_2-D* and

D_2-H* reactions (steps 1.4-1.5, Scheme 1), making dissociation-recombination reactions (steps 1.1-1.3, Scheme 1) easier to measure, as shown by rearranging Equation 19:

$$\frac{r_{HD,f}\left((H_2)+(D_2)\right)}{(H_2)(D_2)} = \frac{k_{-2}}{(H_2)+(D_2)} + 2k_4 \tag{21}$$

The value of k_{-2} and its temperature dependence can therefore only be measured at sufficiently low H_2 and D_2 pressures.

Figure 7 shows $\frac{r_{HD,f}\left((H_2)+(D_2)\right)}{(H_2)(D_2)}$ ratios (left-hand side; Eq. 21) at several H_2 and D_2 pressures (2-20 kPa) as a function of temperature in an Arrhenius-type plot. These data deviate from the linear trends only above 700 K (Fig. 7b); these deviations become more pronounced at low combined H_2 and D_2 pressures, as expected from greater relative contributions from dissociation-recombination routes (Eq. 21). The k_{-2} values can be obtained from the functional form of Eq. 21 by subtracting the contributions from the single-site associative routes (H_2 + D* and D_2 + H*, steps 1.4-1.5, Scheme 1) as given by their k_4 rate constants at each temperature (Eq. 21) from the rates measured at high temperature and low H_2 and D_2 pressures (750-1000 K, 2 kPa H_2, 2 kPa D_2; Fig. 7b, indicated by dashed line). These contributions from the associative routes ($2k_4$; Eq. 21) were calculated by extrapolating the data from temperatures at which $\frac{r_{HD,f}\left((H_2)+(D_2)\right)}{(H_2)(D_2)}$ values (left-hand side: Eq. 21) converged for different $(H_2)+(D_2)$ pressures (303-600 K) (Fig. 7a); this convergence indicates that these data primarily reflect contributions from the associative routes (steps 1.4-1.5, Scheme 1), which do not exhibit a dependence on the combined H_2 and D_2 pressure (Eq. 21). The temperature dependence of the resulting k_{-2} values gave an activation energy (78 ± 11 kJ mol^{-1}) that is significantly higher than for the low-temperature route and its k_4 rate parameter (32.1 ± 0.2 kJ mol^{-1}). The temperature dependences and the convergence of the $\frac{r_{HD,f}\left((H_2)+(D_2)\right)}{(H_2)(D_2)}$ values at temperatures below 700 K (Fig. 7a) indicate that H_2-D_2 isotopic exchange reactions at hydrogen pressures of practical relevance (>5 kPa H_2) occur almost exclusively via associative single-site routes (steps 1.4-1.5; Scheme 1) that do not require the endothermic desorption of H* or D* from saturated H*/D* adlayers for each isotopic exchange turnover. Consequently, the reversibility of dissociation-recombination steps during hydrogenation-dehydrogenation catalysis cannot be determined unequivocally from H_2-D_2 isotopic scrambling during catalysis.

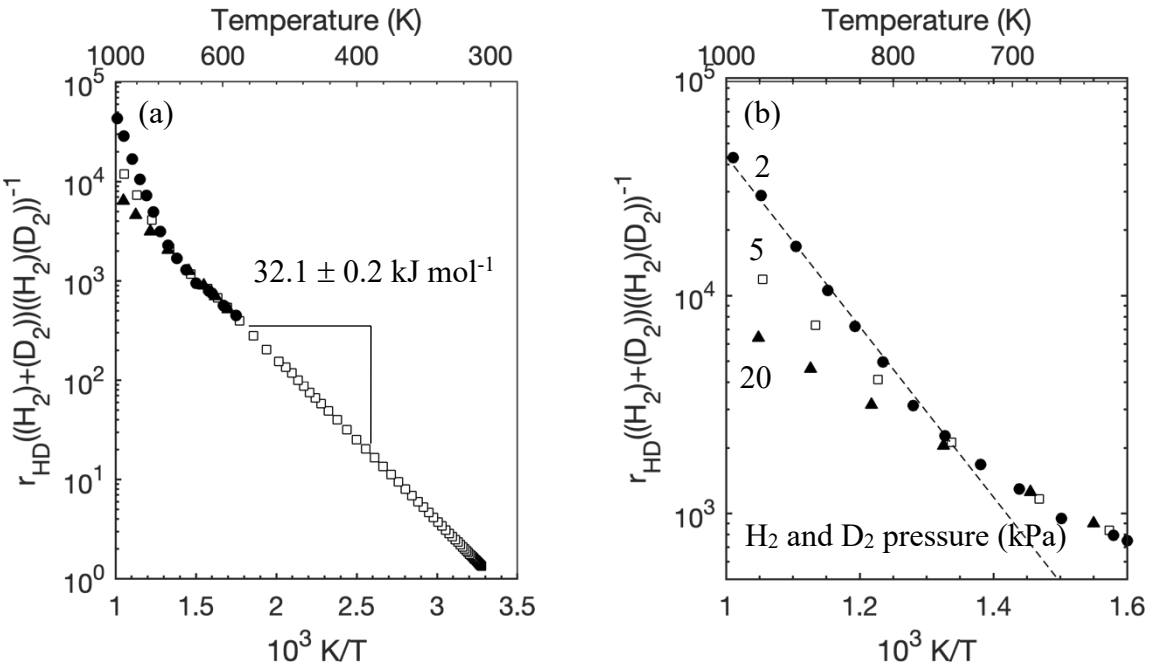

Figure 7. Arrhenius plot of H_2-D_2 exchange rates on 0.2% wt. Pt/SiO_2-A at 2 kPa H_2 and 2 kPa D_2 (●), 5 kPa H_2 and 5 kPa D_2 (□), and 20 kPa H_2 and 20 kPa D_2 (▲) between (a) 303 and 1000 K and (b) 625 and 1000 K. Dashed line in (b) represents data used to extract values of k_{-2}.

3.3.5 Effect of Catalyst Support and Particle Size on Isotopic Exchange Rates

H_2-D_2 isotopic exchange rates were measured on 0.2% wt. Pt/SiO_2-A, 0.2% wt. Pt/SiO_2-B, and 1% wt. Pt/γ-Al_2O_3-A at temperatures between 303 and 433 K to examine the effects of the supports and of the size of Pt nanoparticles (1.5-3.2 nm). Rates were also measured on Pt black samples, which sintered significantly during pretreatments at 873 K (Section 3.2.3); reported rates on Pt black were therefore calculated by assuming turnover rates on Pt black are identical to those on Pt/SiO_2-A at 383 K (171 ± 2 s^{-1}; 20 kPa H_2, 20 kPa D_2). Figure 8 shows $\frac{r_{HD,f}((H_2)+(D_2))}{(H_2)(D_2)}$ ratios (left-hand side; Eq. 21) as a function of temperature in an Arrhenius form (20 kPa H_2, 20 kPa D_2). These temperatures (300-430 K) were significantly lower than those where dissociation-recombination reactions (steps 1.1-1.3, Scheme 1) become significant (Fig. 7) and therefore reflect the temperature dependence of k_4 (Eq. 21). The activation energies derived from the rates (Table 2) are similar, consistent with the absence of significant effects of nanoparticle size (1.5-374 nm) on exchange rates (Table 2). These data indicate that the associative single-site events (H_2-D* and D_2-H*; steps 1.4-1.5, Scheme 1), responsible for exchange at these temperatures (303-433 K) and pressures (20 kPa H_2, 20 kPa D_2), are essentially insensitive to nanoparticle diameter or the identity of the support material (SiO_2, Al_2O_3).

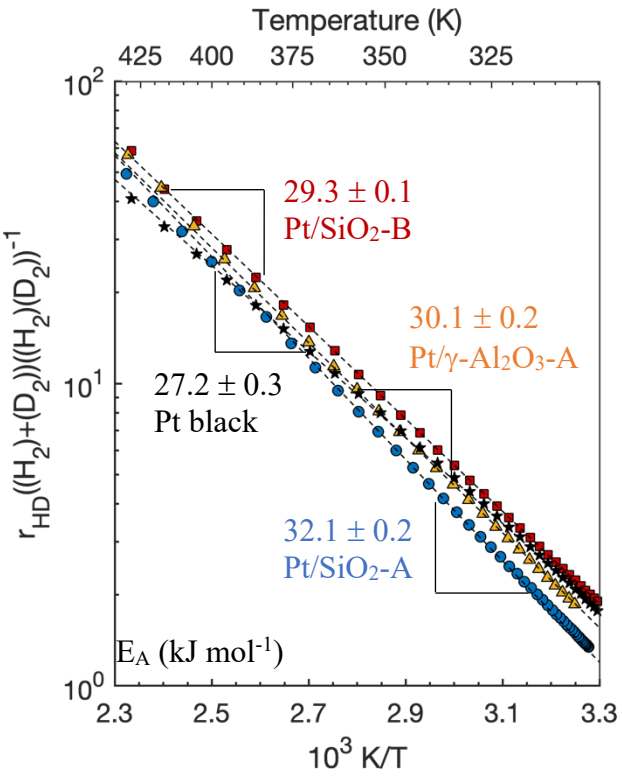

Figure 8. Arrhenius plot of H_2-D_2 exchange rates and activation energies on (●) 0.2% wt. Pt/SiO_2-A, (■) 0.2% wt. Pt/SiO_2-B, (▲) 1% wt. Pt/γ-Al_2O_3-A, and (★) Pt black at 20 kPa H_2 and 20 kPa D_2. Dashed lines represent linear regression of the data.

Table 2. Dispersion, mean nanoparticle diameter, H_2-D_2 exchange rate and activation energies on Pt/SiO_2-A, Pt/SiO_2-B, and Pt/γ-Al_2O_3-A.

Catalyst	Pt Dispersion	Nanoparticle Diameter (nm)†	H_2-D_2 Exchange Rate (s^{-1})†	H_2-D_2 Exchange Activation Energy (kJ mol^{-1})‡
Pt/SiO_2-A	0.38	3.2	171 ± 2	32.1 ± 0.2
Pt/SiO_2-B	1.0	1.5	183 ± 4	30.1 ± 0.2
Pt/γ-Al_2O_3-A	0.72	1.9	205 ± 11	29.3 ± 0.1
Pt black	~0.003§	374	171§	27.2 ± 0.3

*Calculated by assuming hemispherical particle geometries and using the bulk density of Pt (21.45 g cm^{-3}).[42] H/Pt_s stoichiometries were estimated using Equation 4-5.
†Measured at 383 K, 20 kPa H_2, 20 kPa D_2
‡Calculated for temperatures between 303 and 433 K (20 kPa H_2, 20 kPa D_2)
§Rates and dispersion of Pt black calculated by equating its activity with Pt/SiO_2-A at 383 K.

The kinetic dependence of H_2-D_2 isotopic exchange on H_2 and D_2 pressures was also measured on 1% wt. Pt/γ-Al_2O_3-A and Pt black. HD formation rates on Pt/γ-Al_2O_3-A and Pt black increased monotonically with H_2 and D_2 pressures at all pressures (Fig. 9) and, as in the case of Pt/SiO_2-A (Fig. 4), were essentially the same when H_2 and D_2 pressures were interchanged (Fig.

9). Isotopic exchange rates were accurately described by Equations 19-20, as in the case of Pt/SiO_2-A (Section 3.3.2; Fig. 10). The values of k_{-2} and k_4 on Pt/SiO_2-B and Pt black are summarized in Table 3. The k_{-2} values were essentially zero on Pt/γ-Al_2O_3-A (-5 ± 40 s^{-1}) and Pt black (-9 ± 49 s^{-1}), as for Pt/SiO_2 (-2.1 ± 20 s^{-1}), indicative of negligible contributions from dissociation-recombination routes (Scheme 1, step 1.1-1.3). The value of k_4 on Pt/γ-Al_2O_3-A (10.3 ± 0.6 kPa^{-1} s^{-1}; H_2 or D_2 reactions with D* and H* adatoms; Scheme 1, steps 1.4-1.5) is similar to that measured on Pt/SiO_2-A (9.1 ± 0.2 kPa^{-1} s^{-1}), within experimental uncertainty, reflecting the absence of significant effects of nanoparticle size (1.9 vs. 3.2 nm for Pt/γ-Al_2O_3-A and Pt/SiO_2-A, respectively; Table 2) on exchange turnover rates. (Absolute exchange rates and the value of k_4 on Pt black cannot be compared directly because rates on Pt black were normalized by rates on Pt/SiO_2-A at 383 K). These identical kinetic trends and activation energies even on Pt black (Fig. 4 and 9) indicate that these exchange events are not mediated (or affected) by hydrogen-spillover phenomena that could involve migration of H-atoms dissociated on Pt nanoparticles to exchange sites on supports.[50] The similar kinetic trends on Pt/SiO_2-A, Pt/γ-Al_2O_3-A, and Pt black samples (Fig. 4 and 9) reflect a similar single-site associative mechanism, involving the reaction of H_2 with D* or D_2 with H*, that is unaffected by the identity or presence of the support or by the size of the Pt nanoparticles (Table 3).

Table 3. Rate constants for H_2-D_2 exchange on Pt/SiO_2-A, Pt/γ-Al_2O_3-A, and Pt black

Catalyst	k_{-2} (s^{-1})	k_4 (kPa^{-1} s^{-1})
Pt/SiO_2-A	-2.1 ± 20	9.1 ± 0.2
Pt/γ-Al_2O_3-A	-5 ± 40	10.3 ± 0.6
Pt black	$-9 \pm 49^*$	$9.2 \pm 0.8^*$

*Rates on Pt black calculated by normalizing against Pt/SiO_2-A rates at 383 K. The absolute magnitudes of k_{-2} and k_4 on Pt black cannot be compared directly to those on other catalysts.

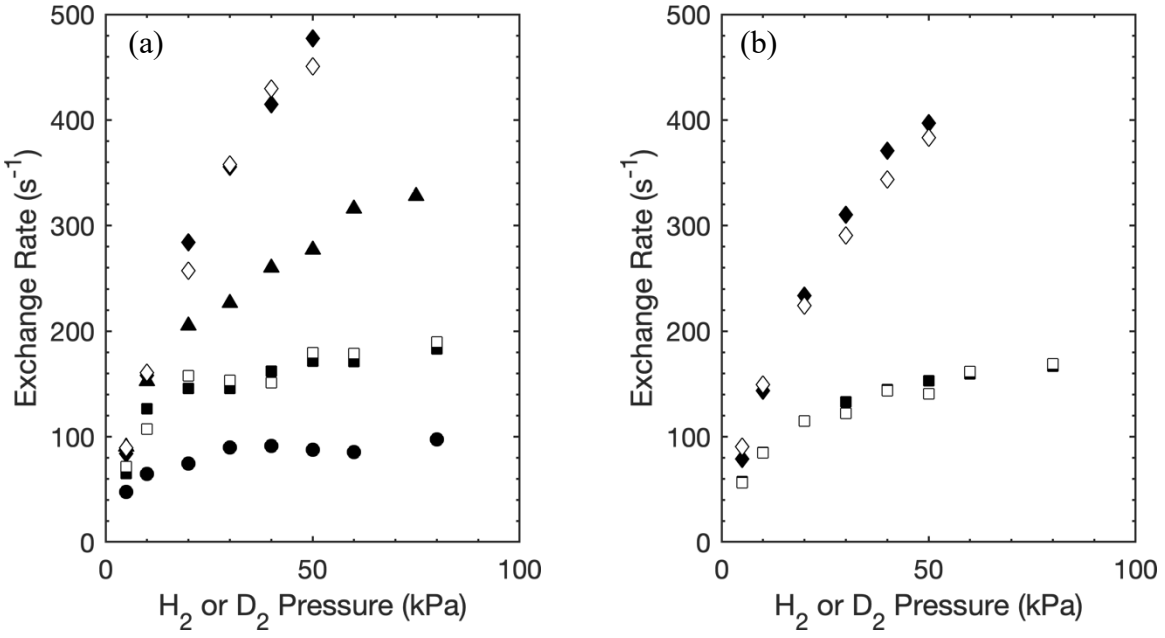

Figure 9. H_2-D_2 exchange rates as a function H_2 or D_2 pressure on (a) 1% wt. Pt/γ-Al_2O_3-A and (b) Pt black at 5 (●), 10 (■,□), 20 (▲), and 40 (◆,◇) kPa H_2 (open symbol) or D_2 (closed symbol) at 383 K.

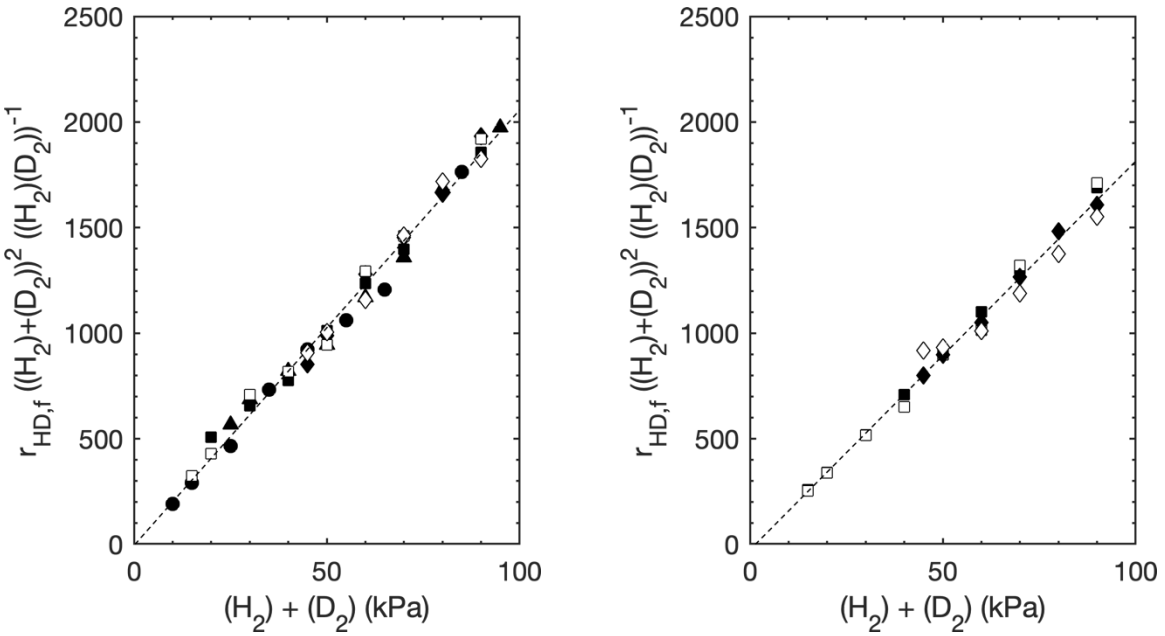

Figure 10. H_2-D_2 exchange rates linearized in the form of Equation 20 on (a) 1% wt. Pt/γ-Al_2O_3-A and (b) Pt black at 5 (●), 10 (■,□), 20 (▲), and 40 (◆,◇) kPa H_2 (open symbol) or D_2 (closed symbol) at 383 K. Dashed line represents the line of best fit of the data.

3.3.6 Theoretical Treatments of H_2-D_2 Exchange Elementary Steps on Saturated Pt Surfaces

Measured kinetic trends can guide the search for specific pathways and contradict specific mechanistic possibilities, as the previous sections demonstrate; such data, however, cannot precisely and unequivocally infer the nature of the interactions and geometries involved in H_2-D* and D_2-H* reactions on surfaces at near saturation H* and D* coverages. More specifically, the "non-competitive" nature of the H_2 "binding" at the transition state for H_2 reactions with D* may reflect reactions of (i) unbound gas phase H_2; (ii) weakly-held physisorbed H_2 molecules on top of a D* adlayer; or (iii) interactions of H_2 molecules with "spaces" made available within D* adlayers without requiring the desorption of D*. All of these events would be consistent with steps 1.4-1.5 (Scheme 1) and lead to the same rate equation (Equation 19, second term).

Theoretical methods (DFT) are used here to describe the formation of H*-adlayers on Pt surfaces, the interactions between H_2-derived species and these dense adlayers, and the plausible mechanism and transition states involved in the reactions of these species with H*/D*. The H* atoms formed by dissociation of H_2 can bind to atop, bridge, and two distinct (fcc and hcp) three-fold sites on Pt(111) surfaces. Atop and three-fold sites bind H* with similar adsorption enthalpies (-36 kJ mol^{-1} and -42 kJ mol^{-1} at 1 H*/Pt_s; $H_2 + 2^* \rightarrow 2$ H*). Such small differences between these two binding sites lie within the inaccuracies of DFT; consequently, H_2-H* exchange reactions were investigated on surfaces saturated in H* atoms in both configurations. Such exchange reactions can be studied using H_2 reactions with H* because individual species can be traced throughout the calculation. H_2-H* exchange reactions were also examined on a 201-atom Pt nanoparticle (Pt_{201}, 1.8 nm) because previous studies have shown that the structural model (flat extended surface vs. curved nanoparticle particle) can strongly impact activation barriers for ethane hydrogenolysis on H*-covered metal particles.[48] Pt_{201} nanoparticles bind H*-adatoms at atop or fcc sites within their (111) terraces and at a mixture of bridge and atop sites along edges, corners, and (100) terraces; such particles can achieve H*/Pt_s ratios above unity (Section 3.6.7 and previous studies[41, 51-54]). H_2-H* exchange reactions are therefore examined for a range of coverages (1-1.8 H*/Pt_s) on Pt_{201} surfaces.

DFT-derived enthalpy and free energy barriers for H_2-H* exchange are used to discern between various associative reactions that may correspond with the observed reaction route. Measured kinetic effects of H_2 and D_2 pressures on exchange rates (Section 3.3.3) below 700 K are consistent with single-site associative routes involving H_2 reactions with D* (or D_2 reactions with H*; steps 1.4-1.5, Scheme 1), but not with dissociation-recombination events (steps 1.1-1.3, Scheme 1), as the steps causing isotopic mixing. These single-site associative routes (steps 1.4-1.5, Scheme 1) involve an activation barrier of 29-32 kJ mol^{-1} (Table 2) for the rate constant k_4 on Pt nanoparticles saturated with H* and D*. The elementary steps in Scheme 1 implicates the involvement of a H_2 that does not compete with the surface site (*) that binds H* and the direct reaction of such species with H* (or D*).

One plausible route involves a metallocycle transition state (Fig. 11a). This route involves the formation of a transition state (TS) with an enthalpy of formation (from H_2(g) and a H* on a H*-covered Pt(111) surface) of 210 kJ mol^{-1} when H* is bound in atop configurations. This activation barrier is nearly 10-fold larger than measured values (29-32 kJ mol^{-1}; Table 2) and reflects the unstable nature of the H atoms in the metallocycle TS that do not interact with the surface. An alternate dual-site metallocycle-mediated exchange mechanism involving H-H dissociation across a H*-H* pair (atop binding to form a H*-H-H-H* TS (Fig. 11b) gave a barrier of 147 kJ mol^{-1}. This barrier is smaller than for the H-H-H* metallocycle (210 kJ mol^{-1}, Fig. 11a)

but still about five-fold larger than measured values (29-32 kJ mol^{-1}, Table 2); this dual-site metallocycle route also predicts kinetic trends contradicted by measured exchange rates (Section 3.6.3.2). For H* at fcc sites on Pt(111), the barrier for the dual-site metallocycle route (140 kJ mol^{-1}) was only slightly smaller. These high activation barriers for metallocycle-mediated routes indicate that the H_2 species that react with H* or D* must be perturbed through interactions with the surface for the exchange of its H-atoms with H*, but in a manner that does not require the desorption of H* or D* from the saturated surface to allow such interactions.

Such interactions may occur via the momentary displacement of a H* in the mobile adlayer[33] to a nearby location by H_2, so as to allow "space" for H_2 interactions with Pt surface atoms and potentially its dissociation. These routes involve sequential steps (Scheme 2) that displace H* to vicinal alternative regions that momentarily acquire higher local coverages. H (or D) atoms bound at atop and alternative (fcc or bridge) sites are denoted as H* and H' (or D* and D'), respectively. The proposed reaction (Scheme 2) proceeds with an enthalpy barrier (referenced to a H*(atop)-covered Pt surface; 1 H*/Pt_s) of 84 kJ mol^{-1} when H* moves to a vicinal bridge site (Fig. 11c and 12, denoted by ▲). Lower barriers were obtained when H* moves to a vicinal fcc site (70 kJ mol^{-1}, Fig. 11d and 12, denoted by ◆) or a farther fcc site (60 kJ mol^{-1}, Fig. 11e and 12, denoted by ●). These activation barriers include the enthalpy required to move H* from an atop site to an fcc site (step 2.1 Scheme 2) (16 kJ mol^{-1}) and the enthalpy required to dissociate H_2 at the spaces created by this displacement (43–67 kJ mol^{-1}; Fig. 12), which depends on the proximity between the H_2 dissociation transition state and the displaced H* atom. Displacing H* to a noninteracting distance (29 kJ mol^{-1}) followed by H_2 dissociation (36 kJ mol^{-1}) gives an overall barrier of 65 kJ mol^{-1} (Fig. 12, denoted by ■). Total activation barriers for H_2-H* exchange on H*-adlayers in the fcc binding mode varied from 101–116 kJ mol^{-1}. These barriers (> 60 kJ mol^{-1}) are still approximately 30 kJ mol^{-1} larger than those measured on Pt/SiO_2-A, Pt/SiO_2-B, and Pt/γ-Al_2O_3-A (29–32 kJ mol^{-1}, Table 2).

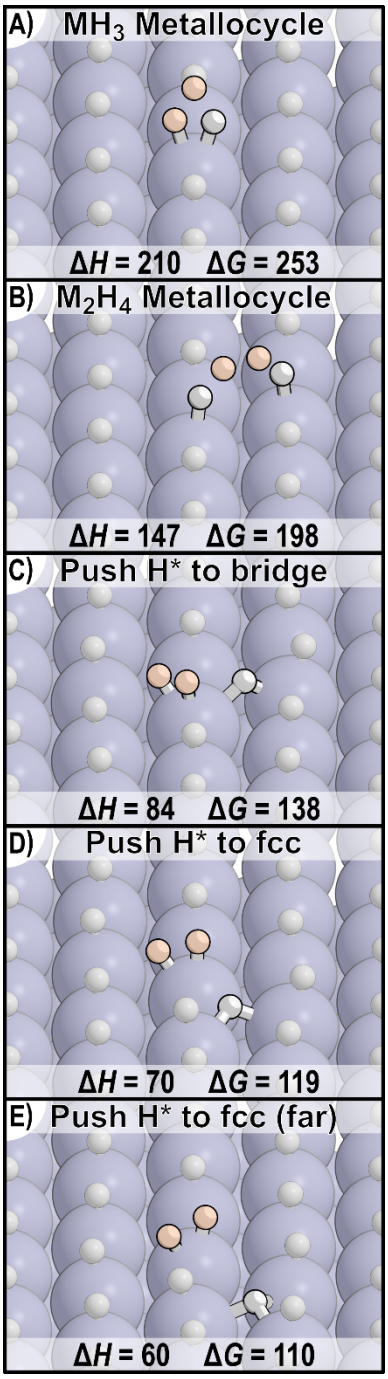

Figure 11. DFT-derived transition state structures for five H_2 activation mechanisms on Pt(111) surfaces at 1 ML H* coverages. DFT-derived enthalpy (ΔH) and free energy (ΔG) barriers are shown (383 K, 1 bar). Highlighted (red) atoms reflect those from gas-phase H_2.

$$H_2 + D^* \longrightarrow H_2 + * + D' \quad [2.1]$$

$$H_2 + * + D' \longrightarrow H^* + H' + D' \quad [2.2]$$

$$H^* + H' + D' \longrightarrow HD + * + H' \quad [2.3]$$

$$HD + * + H' \longrightarrow HD + H^* \quad [2.4]$$

Scheme 2. Proposed intermediate steps for H_2-D* reactions on Pt surfaces. DFT methods use H_2-H* reactions.

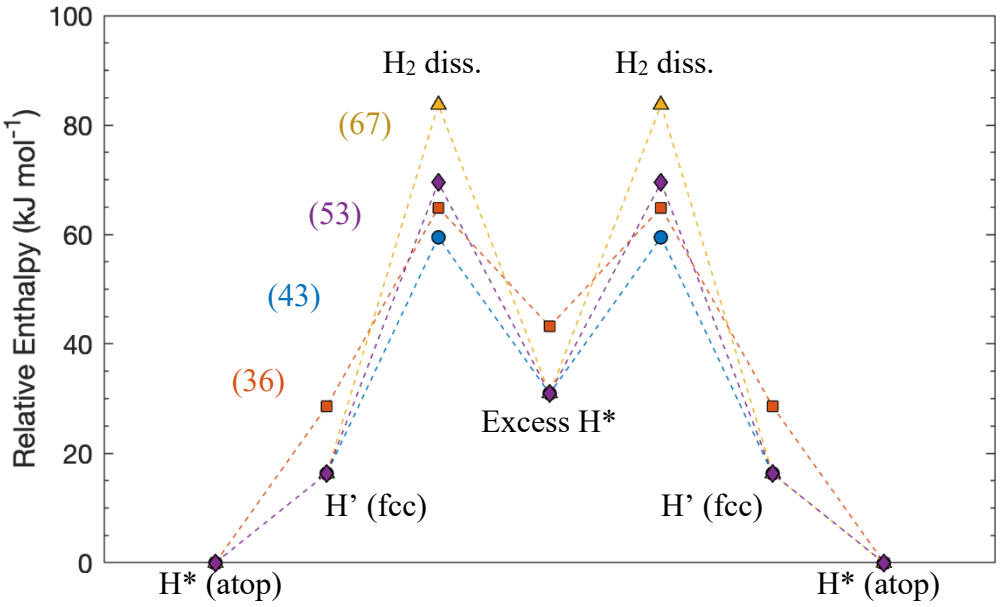

Figure 12. DFT-calculated enthalpies (383 K) for H_2-H* exchange through displacement mechanisms (Scheme 2) on Pt(111) surfaces at 1 H*(atop)/Pt_s. Reactions were examined via the displacement of H* to a vicinal bridge site (▲, Fig. 11c), vicinal fcc sites (◆, Fig. 11d), a "far" fcc site (●, Fig. 11e), and to a noninteracting distance (■). Dissociation barriers are shown in parentheses.

Overall H_2-H* exchange barriers were also examined on the close-packed (111) terraces of Pt_{201} particles. Measured H_2-D_2 exchange rates were insensitive to the size of Pt nanoparticles (Table 2), which leads, in turn, to differences in the average coordination of exposed Pt atoms; these observations indicate that exchange reactions do not occur preferentially at corner and edge Pt atoms that become more prevalent on smaller nanoparticles. H_2-H* on (111) terraces on Pt_{201}

(at 1 H*(atop)/Pt_s coverages) involves an overall enthalpic barrier of 39 kJ mol^{-1}, which is 21 kJ mol^{-1} smaller than for the same H* coverage on Pt(111) surface. This barrier includes the energy required to displace H* from an atop to a fcc site (20 kJ mol^{-1}), which is similar to the displacement energy of 16 kJ mol^{-1} on the Pt(111) surface (see above; Fig. 12). The enthalpic barrier for H_2 dissociation (at spaces created by H* displacement), however, was much lower on the Pt_{201} particle (19 kJ mol^{-1}) than on the Pt(111) surface (43 kJ mol^{-1}; ●, Fig. 12). Differential adsorption energies that become positive at H*/Pt_s ratios greater than 1.3 suggest that the Pt_{201} particle saturates at this value instead of at 1.0 H*/Pt_s (Section 3.6.7). This ratio was achieved by varying the number of H* bound to corner and edge atoms (1.0-1.8 H*/Pt_s) instead of on the (111) terrace on which the reaction is occurring. Overall enthalpy barriers in the suprastoichiometric regime (> 1.0 H*/Pt_s) varied from 39–41 kJ mol^{-1}, as coverages increased from 1–1.6 H*/Pt_s, and jumped to 64 kJ mol^{-1} at 1.8 H*/Pt_s (Fig. 13); dissociation barriers similarly increased gradually from 1–1.6 H*/Pt_s (19–28 kJ mol^{-1}) before jumping to 52 kJ mol^{-1} at 1.8 ML H* (Fig. 13). These trends demonstrate that the H* adlayers on the Pt_{201} particle are more able to accommodate the H_2 dissociation transition state than on Pt(111) surfaces.

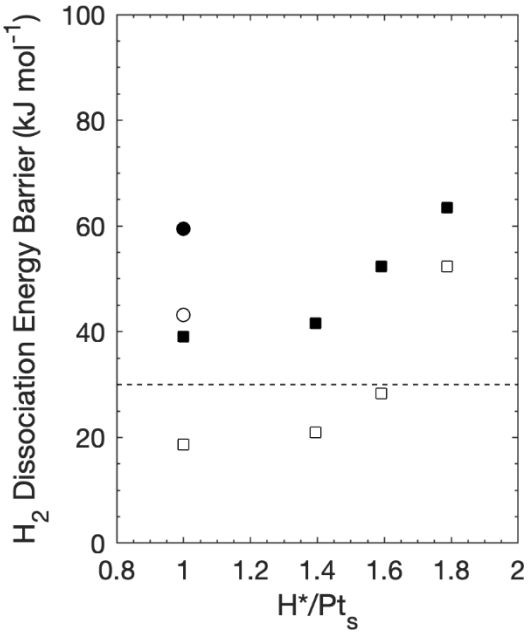

Figure 13. DFT-calculated activation energies for H_2 dissociation on Pt(111) surfaces (●,○) and on Pt_{201} particles (■,□) for H*-adlayers (atop) at varying coverages. Filled symbols represent total enthalpic barriers (including the energy required to displace a H* from an atop site to a fcc site). Hollow symbols represent only enthalpic barriers for H_2 dissociations (at spaces created by H* displacements). H_2-H* exchange barriers become similar for 1.0 H*/Pt_s on Pt(111) and 1.8 H*/Pt_s on Pt_{201}. A dashed gray line is drawn at 30 kJ mol^{-1}, corresponding to the measured activation enthalpy, and arrows at 1 and 1.3 ML indicate values at the saturation of the Pt(111) surface model and the Pt_{201} model.

The H_2 dissociation enthalpy barriers on Pt_{201} particles (19–28 kJ mol^{-1}, 1–1.6 H*/Pt_s) were similar to experimentally measured values (29–32 kJ mol^{-1}, Table 2). The total enthalpic barriers

were, however, still 11–29 kJ mol^{-1} higher and range from 39–70 kJ mol^{-1} (1–1.6 H*/Pt$_s$). This is similar to the conclusions from the Pt(111) surface models, in which the most facile paths had barriers that were approximately 30 kJ mol^{-1} too high (Fig. 12) compared to measured values. These barriers assume that the resting state of the H*-adlayer is ordered, such that all H*-adatoms on Pt(111) surfaces and (111) terraces of the Pt$_{201}$ particle occupy atop binding modes. There is an enthalpic penalty (11–29 kJ mol^{-1}) to shift H* from atop to fcc sites and disordering the H* adlayer. The selection of the resting state of the adlayer, however, is dictated by the free energy of the system and thus depends also on entropic effects that may naturally lead to disorder within the adlayer and create space for H_2 dissociation to occur. The configurational entropy from H* displacement from atop to fcc sites was therefore estimated for several model surfaces consisting of varying numbers of atoms (10-500 atoms, Section 3.6.8). These calculations reveal that the movement of one H-adatom from the atop site to the fcc site in a 122-atom system (corresponding with a 1 H*/Pt$_s$ adlayer on Pt$_{201}$) results in an entropy gain of 48 J mol^{-1} K^{-1} and thus lowers the free energy of the "single-defect" system by 18 kJ mol^{-1} at 383 K. As the particles grow or the H* coverage increases, the increase in configurational entropy upon defect formation also increases from 10 kJ mol^{-1} in a system of 10 H* to 23 kJ mol^{-1} in a system of 500 H* atoms (at 383 K). This 500-atom adlayer corresponds to a 3 nm 1289-atom Pt particle at 1.04 ML H*. The enthalpic penalty to displace a H* adatom is 21 kJ mol^{-1} on Pt$_{201}$ (122 H*, 1 H*/Pt$_s$), but a 48 J mol^{-1} K^{-1} increase in the entropy means that the free energy of the disordered system is just 3 kJ mol^{-1} higher than the ordered system. This small difference is well within the margin of error of DFT methods and these entropy estimates. Additional disorder in the surface arrangement of H adatoms is also entropically favorable, but the entropy gain for each additional defect results in less configurational entropy gain than the last. Similarly, the changes in enthalpy for H* shifting from atop to fcc sites will also depend on the total number of H* in each binding mode. The nonlinear nature of these entropic and enthalpic effects as more H* move from atop to fcc sites makes the exact prediction of the number of defect sites difficult without extensive DFT and molecular dynamic simulations. These assessments, along with the similarity of intrinsic energy barriers (19-28 kJ mol^{-1}) to experimental values (29-32 kJ mol^{-1}, Table 2), suggest that H_2-D_2 exchange reactions occur on disordered H*/D*-adlayers that allow for the dissociative adsorption of H_2 (or D_2) at "vacancies" that arise from entropically favorable fluctuations within these adlayers.

3.4 Conclusions

H_2-D_2 exchange reactions are frequently employed in mechanistic studies to probe the reversibility of H_2 dissociative adsorption reactions without considerations for the thermodynamics of H_2 vs. D_2 adsorption or the kinetics and mechanism by which isotopic exchange events occur. In this study, uptakes of H_2 and D_2 were measured on several Pt-based catalysts to determine TIEs at temperatures (523-673 K) relevant for catalytic hydrogenation/dehydrogenation reactions. These TIEs were near unity and depended only weakly on the temperature of adsorption, corresponding with a 4 kJ mol^{-1} difference in the dissociative adsorption enthalpy for H_2 and D_2. Such temperature dependences were used to calculate H* and D* equilibrium coverages at the temperatures of H_2-D_2 exchange kinetic studies. These coverages and the kinetic dependences of exchange on H_2 and D_2 pressures at 373 K were shown to be inconsistent with recombination/desorption reactions. H_2-D_2 exchange reactions instead occur predominantly via single-site reactions between H_2 and D* or D_2 and H* at temperatures below 700 K. Isotopic exchange rates were also nearly identical when H_2 and D_2 pressures were swapped,

reflecting the absence of a KIE and an adlayer whose composition is determined by H_2-D* or D_2-H* exchange reactions rather than the thermodynamics (and TIE) of H_2 and D_2 dissociative adsorption. Theoretical calculations showed that these exchange reactions are likely mediated by the dissociation of H_2 or D_2 onto the Pt surface at vacancies that arise from entropically-favorable fluctuations in the H*/D* mobile adlayer. The results from this study thus demonstrate that H_2-D_2 isotopic exchange are mediated by reaction pathways that bypass dissociation-recombination reactions and therefore cannot be used to conclusively demonstrate the reversibility of H_2 adsorption-desorption reactions on catalytic surfaces. They demonstrate the importance of having an accurate mechanistic understanding of exchange reactions.

3.5 Acknowledgements

Samuel Leung acknowledges Dr. Monica Garcia-Dieguez for the experimental collection of H_2 and D_2 isotherms and Dr. David Hibbitts for the theoretical investigations. This study was funded by Chevron Corporation and a Chevron Graduate Student Research Fellowship. We also thank Dr. Aaron Sattler for helpful technical discussions.

3.6 Supporting Information

3.6.1 Effect of Catalyst Pellet Size on Reaction Rates

H_2-D_2 isotopic exchange kinetics were obtained on 0.2% Pt/SiO_2-A catalyst powders sieved to retain particles smaller than 100 μm and on powders ground to a fine powder (<50 μm). These rates were compared to confirm the absence of mass transport limitations on these catalytic samples. Figure SI-1 shows exchange rates (2 kPa H_2, 2 kPa D_2) as a function of temperature in an Arrhenius plot for these samples and the ratio of these rates (r_{small}/r_{large}; r_{small}=rates on ground fine powders <50 μm, r_{large}=rates on the sieved particles <100 μm) for temperatures between 600 and 1000 K, which represents the conditions most likely to be mass-transport limited in this study. Rates were nearly identical for both samples, indicating the absence of mass-transport artifacts in this study.

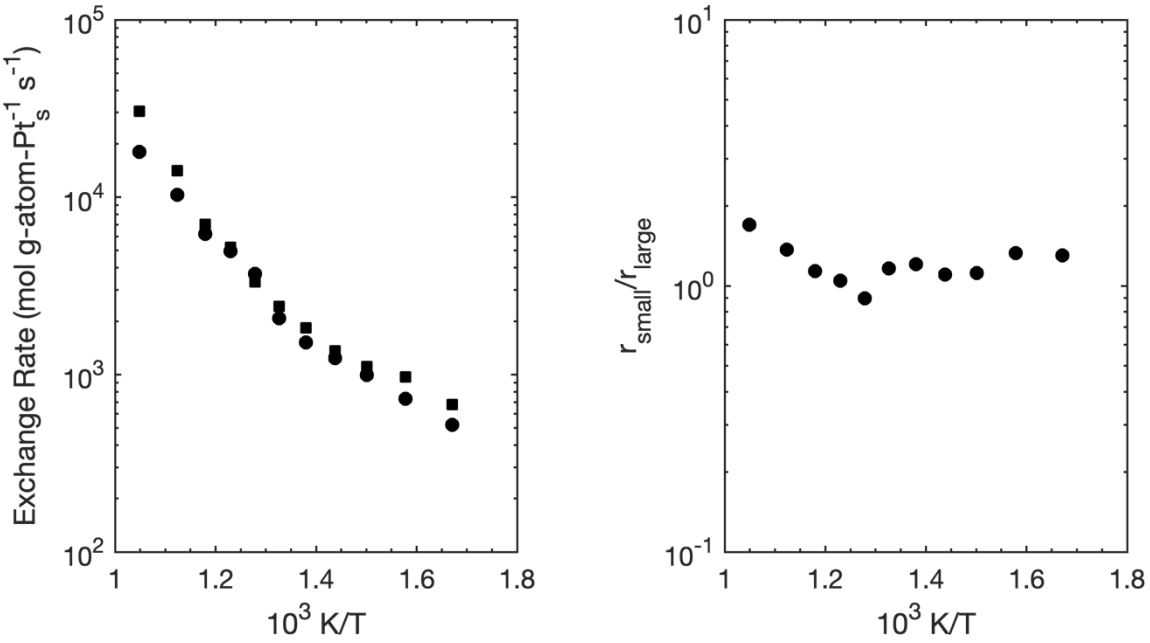

Figure SI-1. (a) Arrhenius plot of H_2-D_2 isotopic exchange rates (2 kPa H_2, 2 kPa D_2) on 0.2% Pt/SiO_2-A powders <100 μm (●) and <50 μm (■) (2 kPa H_2, 2 kPa D_2; 0.167 K s^{-1} heating rate). (b) Ratio of exchange rates obtained on fine, ground powders (<50 μm) to those on sieved powders (<100 μm).

3.6.2 H_2 and D_2 Chemisorption Isotherms on Pt/γ-Al_2O_3-B at 523-673 K

H_2 and D_2 adsorption isotherms were obtained for a range of temperatures (523-673 K) on 1.6% wt. Pt/γ-Al_2O_3-B (Fig. SI-2). These isotherms were used to extract the equilibrium constants for H_2 (K_H) and D_2 (K_D) adsorption (Fig. SI-3) as a function of temperature (at various fractional coverages of the Pt surface). The ratios of K_H/K_D (TIE) were only weakly dependent on fractional surface coverages and were thus averaged across these coverages at a given temperature (Fig. SI-3), as shown in Figure 3 (main text).

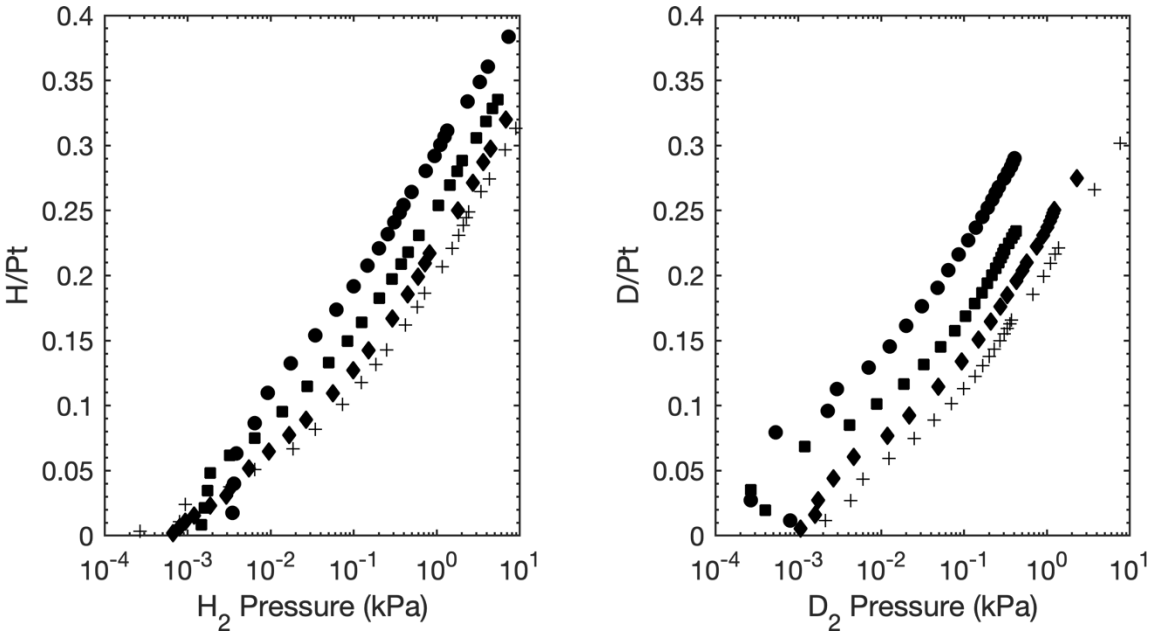

Figure SI-2. (a) H_2 and (b) D_2 dissociative adsorption isotherms on Pt/γ-Al_2O_3-B at (●) 523, (■) 573, (◆) 623, and (+) 673 K.

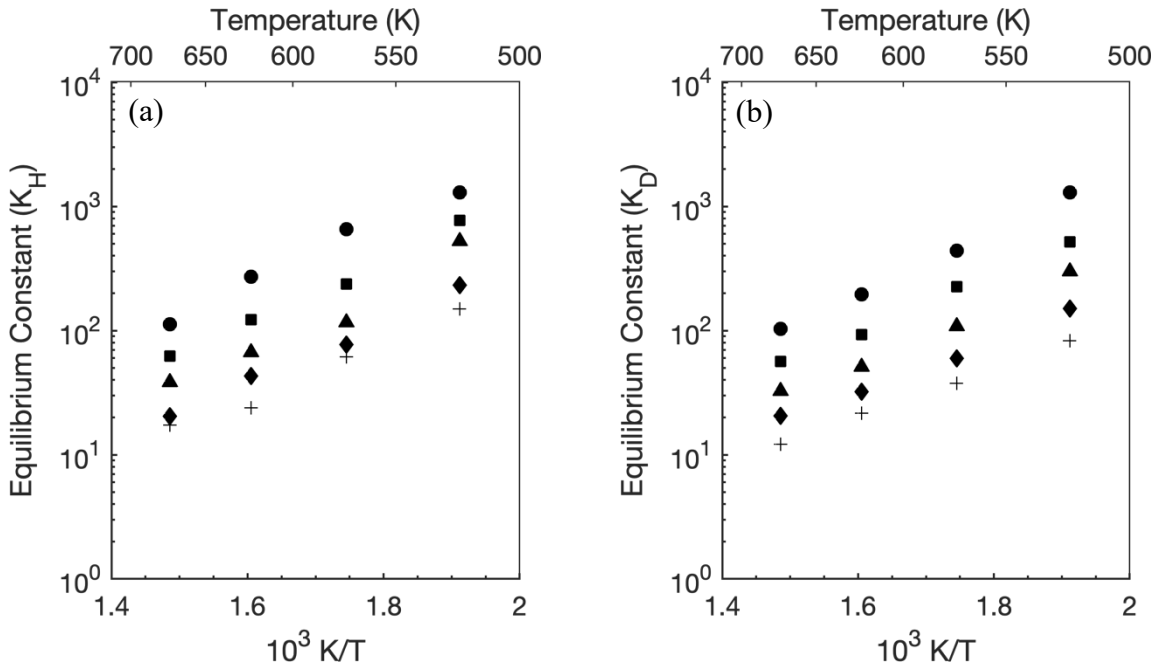

Figure SI-3. Equilibrium constants vs. temperature for the adsorption of (a) H_2 (K_H) and (b) D_2 (K_D) on Pt/γ-Al_2O_3-B at fractional surface coverages of 0.19 (●), 0.28 (■), 0.38 (▲), 0.47 (◆), and 0.57 (+).

3.6.3 Derivation of Rate Equations for H_2-D_2 Exchange Mechanisms

3.6.3.1 Derivation of Expressions for H* and D* Surface Coverages and the Rate Equation for HD Formation from the Reaction Between H* and D* Adatoms

$$H_2 + 2* \underset{k_{-1}}{\overset{k_1}{\rightleftharpoons}} 2H* \qquad \text{[SI-1.1]}$$

$$HD + 2* \xleftarrow[k_{-2}]{} H* + D* \qquad \text{[SI-1.2]}$$

$$D_2 + 2* \underset{k_{-3}}{\overset{k_3}{\rightleftharpoons}} 2D* \qquad \text{[SI-1.3]}$$

Scheme SI-1. Elementary steps for H_2 and D_2 dissociation and recombination

Scheme SI-1 shows the conventional representation of H_2-D_2 dissociation, recombination, and exchange. The rate of HD formation ($r_{HD,f}$) is given by:

$$r_{HD,f} = k_{-2}\theta_H\theta_D \qquad (SI-1)$$

Here, θ_H and θ_D are the fractional coverages of the metal surface by H* and D* adatoms, respectively. These fractional coverages can be found by first applying the pseudo-steady-state approximation (PSSA) to H*:

$$2r_{1.1} = 2r_{-1.1} + r_{-1.2} \qquad (SI-2)$$

$$2k_1(H_2)\theta_s^2 = k_{-1}\theta_H^2 + k_{-2}\theta_H\theta_D \qquad (SI-3)$$

and D*:

$$2r_{1.3} = r_{-1.2} + 2r_{-1.3} \qquad (SI-4)$$

$$2k_1(D_2)\theta_s^2 = k_{-2}\theta_H\theta_D + k_{-3}\theta_D^2 \qquad (SI-5)$$

Here, $r_{1.i}$ and $r_{-1.i}$ are the forward and reverse rates of reaction i in Scheme SI-1. We note that $r_{-1.1}$ and $r_{-1.3}$ are divided by 2 to avoid double-counting H*-H* and D*-D* reactions. H_2 and D_2 adsorption was shown to exhibit a mild TIE (denoted here as $TIE_{D2} = K_1/K_3$) in Section 3.3.2. For the dissociative adsorption of HD, the effect of the TIE was assumed to be halved, such that:

$$TIE_{HD} = \frac{TIE_{D2} + 1}{2} \qquad (SI-6)$$

The equilibrium constants for H_2, HD, and D_2 adsorption are related to the rate constants for steps 1.1-1.3 in Scheme SI-1 by:

$$K_i = \frac{k_i}{k_{-i}} \qquad (SI-7)$$

The TIE is therefore be reflected in the rate constants as a KIE, such that:

$$K_1 \equiv \frac{k_1}{k_{-1}} = TIE_{HD} K_2 \equiv TIE_{HD} \frac{k_2}{k_{-2}} = TIE_{D2} K_3 \equiv TIE_{D2} \frac{k_3}{k_{-3}} \qquad (SI-8)$$

Next, we assumed that the rate constant for adsorption is equal for H_2, HD, and D_2 ($k_1 = k_2 = k_3$). The relation between desorption rate constants is therefore given by:

$$k_{-1} = \frac{k_{-2}}{TIE_{HD}} = \frac{k_{-3}}{TIE_{D2}} \qquad (SI-9)$$

These equations (Eq. SI-2 – SI-9), along with the assumption that the surface is covered,

$$\theta_H + \theta_D = 1 \qquad (SI-10)$$

can be solved to give the following expressions for H* and D* coverage:

$$\theta_H = \frac{(D_2) - (H_2) + (D_2)TIE_{D2} + 3(H_2)TIE_{D2} - \beta}{2\big((H_2) + (D_2)\big)(TIE_{D2} - 1)} \qquad (SI-11)$$

$$\theta_D = \frac{-3(D_2) - (H_2) + (D_2)TIE_{D2} - (H_2)TIE_{D2} + \beta}{2\big((H_2) + (D_2)\big)(TIE_{D2} - 1)} \qquad (SI-12)$$

$$\beta = \sqrt{8(D_2)\big((H_2) + (D_2)\big)(TIE_{D2} - 1) + (3(D_2) + (H_2) - (D_2)TIE_{D2} + (H_2)TIE_{D2})^2} \qquad (SI-13)$$

In the absence of a TIE, Equations SI-2 – SI-5 and SI-10 can be solved to give:

$$\theta_H = \frac{(H_2)}{(H_2) + (D_2)} \qquad (SI-14)$$

$$\theta_D = \frac{(D_2)}{(H_2) + (D_2)} \qquad (SI-15)$$

and the equation for the formation rate of HD (Eq. SI-1) can be written as:

$$r_{HD,f} = k_{-1} \frac{(H_2)(D_2)}{\big((H_2) + (D_2)\big)^2} \qquad (SI-16)$$

3.6.3.2 Derivation of Rate Equation for HD Formation from the Reaction Between H_2 and D_2 with H*-H*, H*-D*, and D*-D* Pairs

The reaction between H_2 and D_2 with H*-H*, H*-D*, and D*-D* site pairs is considered here, as represented by the diagram and elementary steps in Scheme SI-2.

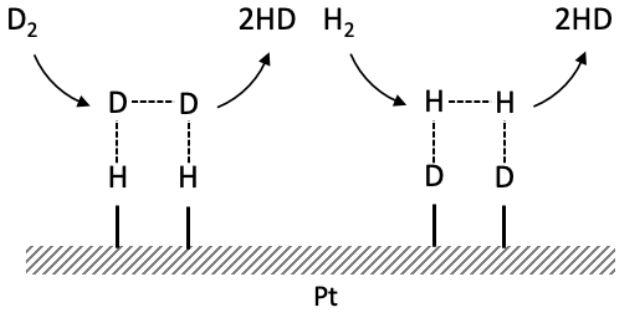

$$2\ H_2 + 2^* \underset{k_{-3}}{\overset{k_3}{\rightleftharpoons}} H_2 + 2H^* \qquad \text{[SI-2.1]}$$

$$H_2 + HD + 2^* \underset{k_{-3}}{\overset{k_3}{\rightleftharpoons}} H_2 + H^* + D^* \qquad \text{[SI-2.2]}$$

$$H_2 + HD + 2^* \underset{k_{-3}}{\overset{k_3}{\rightleftharpoons}} HD + 2H^* \qquad \text{[SI-2.3]}$$

$$HD + HD + 2^* \underset{k_{-3}}{\overset{k_3}{\rightleftharpoons}} H_2 + 2D^* \qquad \text{[SI-2.4]}$$

$$HD + HD + 2^* \underset{k_{-3}}{\overset{k_3}{\rightleftharpoons}} HD + H^* + D^* \qquad \text{[SI-2.5]}$$

$$HD + HD + 2^* \underset{k_{-3}}{\overset{k_3}{\rightleftharpoons}} D_2 + 2H^* \qquad \text{[SI-2.6]}$$

$$HD + D_2 + 2^* \underset{k_{-3}}{\overset{k_3}{\rightleftharpoons}} D_2 + H^* + D^* \qquad \text{[SI-2.7]}$$

$$HD + D_2 + 2^* \underset{k_{-3}}{\overset{k_3}{\rightleftharpoons}} HD + 2D^* \qquad \text{[SI-2.8]}$$

$$2\ D_2 + 2^* \underset{k_{-3}}{\overset{k_3}{\rightleftharpoons}} D_2 + 2D^* \qquad \text{[SI-2.9]}$$

Scheme SI-2. Elementary steps for H_2-D_2 isotopic exchange via the adsorption-assisted desorption of H*-H* and D*-D* site pairs.

The forward rate for HD formation ($r_{HD,f}$) from the elementary steps in Scheme SI-2 is given by:

$$r_{HD,f} = 2k_{-3}(H_2)\theta_D^2 + k_{-3}(H_2)\theta_H\theta_D + k_{-3}(D_2)\theta_H\theta_D + 2k_{-3}(D_2)\theta_H^2 \qquad (SI-17)$$

Here, θ_H and θ_D are the fractional coverage of the metal surface by H and D adatoms, respectively. Applying the pseudo-steady-state approximations (PSSA) on H* and D* and assuming that the reaction is far from equilibrium (the pressure of HD is small) gives the following expression for H*:

$$2r_{2.1} = 2r_{-2.1} + r_{-2.2} + 2r_{-2.6} + r_{-2.7} \qquad (SI-18)$$

$$2k_3(H_2)^2\theta_s^2 = 2k_{-3}(H_2)\theta_H^2 + k_{-3}(H_2)\theta_H\theta_D + 2k_{-3}(D_2)\theta_H^2 + k_{-3}(D_2)\theta_H\theta_D \qquad (SI-19)$$

and D*:

$$2r_{2.9} = r_{-2.2} + 2r_{-2.4} + r_{-2.7} + 2r_{-2.9} \qquad (SI-20)$$

$$2k_3(D_2)^2\theta_s^2 = k_{-3}(H_2)\theta_H\theta_D + 2k_{-3}(H_2)\theta_D^2 + k_{-3}(D_2)\theta_H\theta_D + 2k_{-3}(D_2)\theta_D^2 \qquad (SI-21)$$

$r_{2.i}$ and $r_{-2.i}$ are the forward and reverse rates of reaction i in Scheme SI-2. By assuming that the surface is covered by H* and D*, such that

$$\theta_H + \theta_D = 1 \qquad (SI-22)$$

expressions for θ_H and θ_D can be obtained:

$$\theta_H = -\frac{4(H_2)^2}{(D_2)^2 + 3(H_2)^2 - \gamma} \qquad (SI-23)$$

$$\theta_D = -\frac{4(D_2)^2}{(H_2)^2 + 3(D_2)^2 - \gamma} \qquad (SI-24)$$

$$\gamma = \sqrt{(H_2)^4 + 14(H_2)^2(D_2)^2 + (D_2)^4} \qquad (SI-25)$$

Equation SI-17 can therefore be written as:

$$r_{HD,f} = [64\, k_{-3}(H_2)(D_2)\big((H_2) + (D_2)\big)$$
$$\{(H_2)^6 + (D_2)^6 + 11(H_2)^2(D_2)^4 + 11(D_2)^2(H_2)^4 - \gamma((H_2)^4 + (D_2)^4 + 4(H_2)^2(D_2)^2)\}]$$
$$\div [(3(H_2)^2 + (D_2)^2 - \gamma)^2(3(D_2)^2 + (H_2)^2 - \gamma)^2] \qquad (SI-26)$$

This equation, as in the case of HD formation solely from the recombinative desorption of H* and D* (Section 3.6.3.1) gives a maximum in the rate at equimolar H_2 and D_2 feeds and thus contradicts the presented kinetic data.

3.6.3.3 Derivation of Rate Equation for HD Formation from H*-D*, H_2-D*, and D_2-H* Reactions

$$H_2 + 2* \underset{k_{-1}}{\overset{k_1}{\rightleftharpoons}} 2H* \qquad \text{[SI-3.1]}$$

$$HD + 2* \xleftarrow[k_{-2}]{} H* + D* \qquad \text{[SI-3.2]}$$

$$D_2 + 2* \underset{k_{-3}}{\overset{k_3}{\rightleftharpoons}} 2D* \qquad \text{[SI-3.3]}$$

$$H_2 + D* \xrightarrow{k_4} HD + H* \qquad \text{[SI-3.4]}$$

$$D_2 + H* \xrightarrow{k_5} HD + D* \qquad \text{[SI-3.5]}$$

Scheme SI-3. Elementary steps for H_2-D_2 isotopic exchange via the reaction between H_2 and D_2 with D* and H* adatoms.[2]

The rate for HD formation ($r_{HD,f}$) from the elementary steps in Scheme SI-3 is given by:

$$r_{HD,f} = k_{-2}\theta_H\theta_D + k_4(H_2)\theta_D + k_5(D_2)\theta_H \qquad (SI-27)$$

Here, θ_H and θ_D are the fractional coverage of the metal surface by H and D adatoms, respectively. We apply the pseudo-steady-state approximation (PSSA) to H*

$$2r_{3.1} + r_{3.4} = r_{-3.1} + r_{-3.2} + r_{3.5} \qquad (SI-28)$$

$$2k_1(H_2)\theta_s^2 + k_4(H_2)\theta_D = k_{-1}\theta_H^2 + k_{-2}\theta_H\theta_D + k_5(D_2)\theta_H \qquad (SI-29)$$

and D*

$$2r_{3.3} + r_{3.5} = r_{-3.2} + r_{-3.3} + r_{3.4} \qquad (SI-30)$$

$$2k_1(D_2)\theta_s^2 + k_5(D_2)\theta_H = k_{-2}\theta_H\theta_D + k_{-3}\theta_D^2 + k_4(H_2)\theta_D \qquad (SI-31)$$

These equations assume that the reaction is far from equilibrium, such that (HD) is small. HD formation rates were nearly identical when H_2 and D_2 pressures were interchanged, indicating that the rate constants k_4 and k_5 are equal. Exchange rates also increased monotonically with H_2 and D_2 pressures, even far above H_2/D_2 ratios that represent equal coverages of H* and D*, indicating that the rates of dissociation and recombination ($r_{3.1}, r_{-3.1}, r_{3.2}, r_{-3.2}, r_{3.3}, r_{-3.3}$) are much slower than the reaction between H_2 and D* (or D_2 and H*) ($r_{3.4}$, $r_{3.5}$). These interpretations allow Equations SI-29 and SI-31 to be simplified to:

$$k_4(H_2)\theta_D = k_4(D_2)\theta_H \qquad (SI-32)$$

[2] This scheme is the same as Scheme 1 in the main text.

The surface is fully saturated during all H_2-D_2 exchange experiments, such that:

$$\theta_H + \theta_D = 1 \qquad (SI-33)$$

The fractional coverage of H* and D* adatoms, θ_H and θ_D, is thus given by:

$$\theta_H = \frac{(H_2)}{(H_2)+(D_2)} \qquad (SI-34)$$

$$\theta_D = \frac{(D_2)}{(H_2)+(D_2)} \qquad (SI-35)$$

The equation for the formation rate of HD (Eq. SI-27) can therefore be written as:

$$r_{HD,f} = k_{-2}\frac{(H_2)(D_2)}{\left((H_2)+(D_2)\right)^2} + 2k_4\frac{(H_2)(D_2)}{(H_2)+(D_2)} \qquad (SI-36)$$

3.6.4 Parity Plots of H_2-D_2 Exchange Models

Figure SI-4 shows parity plots of H_2-D_2 exchange rates on Pt/SiO_2-A for each of the H_2-D_2 exchange models considered, including the recombination of H* and D* (Scheme SI-1), the reaction between H_2 and D_2 with H*-H*, H*-D*, and D*-D* pairs (Scheme SI-2), and the H_2-D* and D_2-H* reactions (Scheme SI-3).

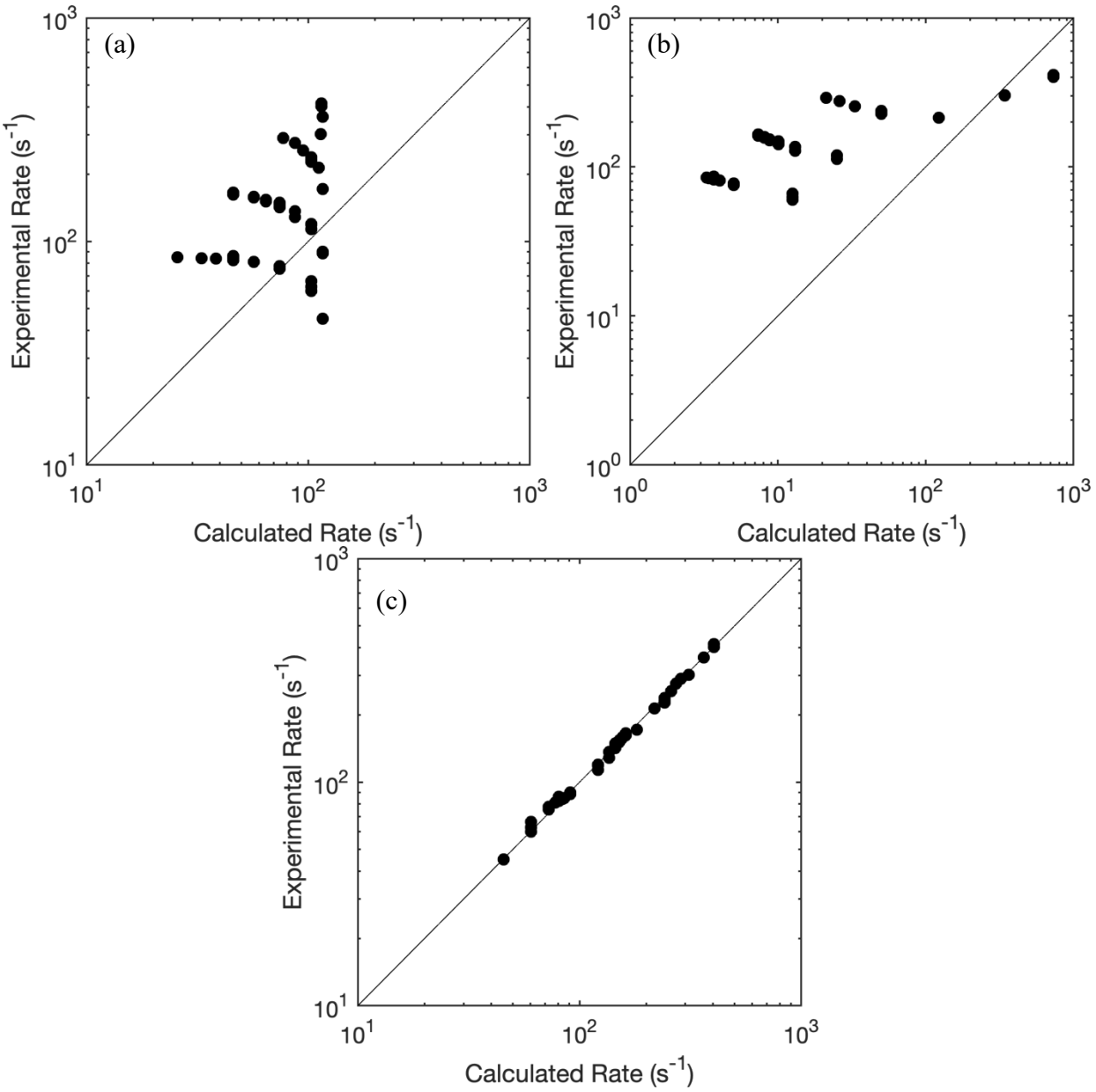

Figure SI-4. Parity plots of HD formation rates (a) H* and D* recombination reactions (Scheme SI-1) (b) H_2 and D_2 reactions with H*-H*, H*-D*, and D*-D* pairs (Scheme SI-2), and (c) H_2-D* and D_2-H* reactions (Scheme SI-3).

3.6.5 Simulations of Kinetic Isotope Effects for H_2-D_2 Exchange

H_2-D_2 isotopic exchange rates were simulated for various KIE values (for H_2-D* and D_2-H* reactions) to determine their effects on HD formation rates. Here, we define $\gamma_{i,j}$ as the gas-phase composition with H_2 pressure i and D_2 pressure j, and $\chi_{i,j}$ as the ratio of rates:

$$\chi_{i,j} = \frac{r_{HD}(\gamma_{i,j})}{r_{HD}(\gamma_{j,i})} \qquad (SI-37)$$

Figure SI-5 shows this rate ratio $\left(\chi_{i,j}\right)$ as a function of the simulated KIE (KIE_{ex}), defined as:

$$KIE_{ex} = \frac{k_4}{k_5} \qquad (SI-38)$$

for several compositions. k_4 and k_5 are the rate constants for reactions 1.4 and 1.5 in Scheme 1. Figure SI-5 shows that $\chi_{i,j}$ depends only on the ratio of H_2 and D_2 pressures $\left(\frac{(H_2)}{(D_2)}\right)$ and not on the individual pressures. The simulated data also demonstrate that any difference in the values of these rate constants would lead to clearly observable differences in the HD exchange rate when pressures are interchanged. The absence of such differences in the present work (Fig. 4-5) therefore reflects KIE_{ex} values near unity.

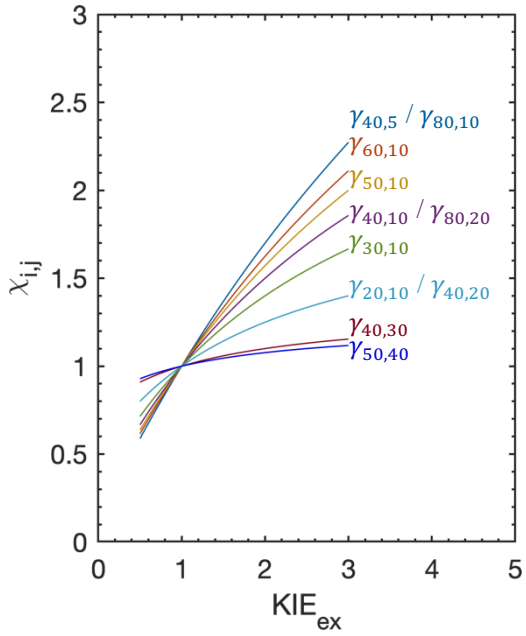

Figure SI-5. Simulated rate ratios $\left(\chi_{i,j} = \frac{r_{HD}(\gamma_{i,j})}{r_{HD}(\gamma_{j,i})}\right)$ as a function of a simulated kinetic isotope effect $\left(KIE_{ex} = \frac{k_4}{k_5}\right)$ for compositions of H_2 and D_2 $\left(\gamma_{i,j}\right)$ where i is the H_2 pressure and j is the D_2 pressure.

3.6.6 Sensitivity Analysis of k_{-2} and k_4

The sensitivity of the proposed mechanistic model for H_2-D_2 exchange (Scheme 1) towards the values of k_{-2} and k_4 was investigated by calculating the sum of squared residuals (SSR) while k_4 was varied over factor of 1.5 from its regressed value (9.1 ± 0.2 kPa^{-1} s^{-1}) and k_{-2} was varied between 0.01 and 100. This range was chosen for k_{-2} to represent positive values that are physical in nature. The SSR values are plotted in a contour plot in Figure SI-5. The SSR increases from its minimum value of 0.047 to 1.124 (at a constant value of k_4, 9.1 kPa^{-1} s^{-1}) as k_{-2} increases, indicating that the exchange reaction is dominated by the reaction of H_2 with D* (or D_2 with H*). The SSR increases to a maximum value of 3.251 as k_4 is increased by a factor of 1.5 (at a constant value of k_{-2}, 0.01 kPa^{-1} s^{-1}). These results show the SSR is insensitive to the value of k_{-2} until much larger values (>10 kPa^{-1} s^{-1}) and reflect the difficulty in measuring H*+D* recombination rates, as shown also by the large uncertainty in the regressed value (-2.1 ± 20 s^{-1}).

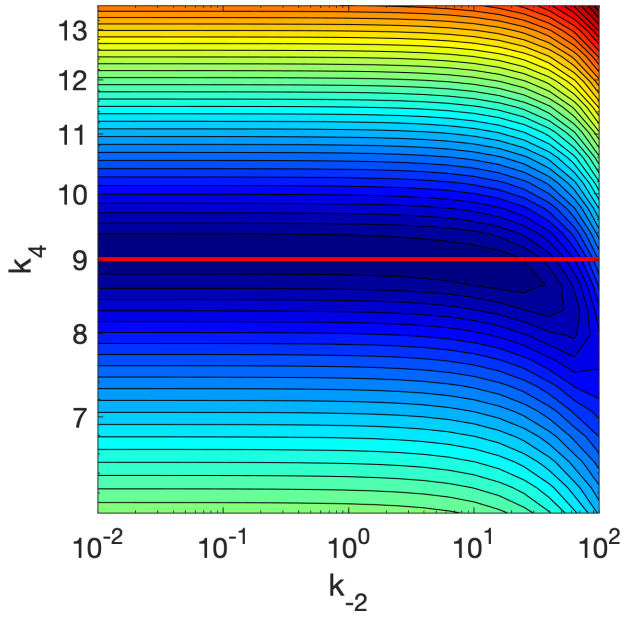

Figure SI-6. Contour plot of sum of squared residuals as k_4 is varied over factor of 1.5 from its regressed value (9.1 ± 0.2 kPa^{-1} s^{-1}, represented by red line) and k_{-2} is varied between 0.01 and 100.

3.6.7 Effect of Coverage on Adsorption Enthalpies

Adsorption enthalpies were calculated for a range of H*/Pt_s ratios on Pt(111) surfaces and Pt_{201} particles, as shown in Figure SI-7. These differential binding enthalpies from these data indicate that Pt(111) saturates at a H*/Pt_s ratio of 1, while Pt_{201} particles saturate at a H*/Pt_s ratio of 1.3.

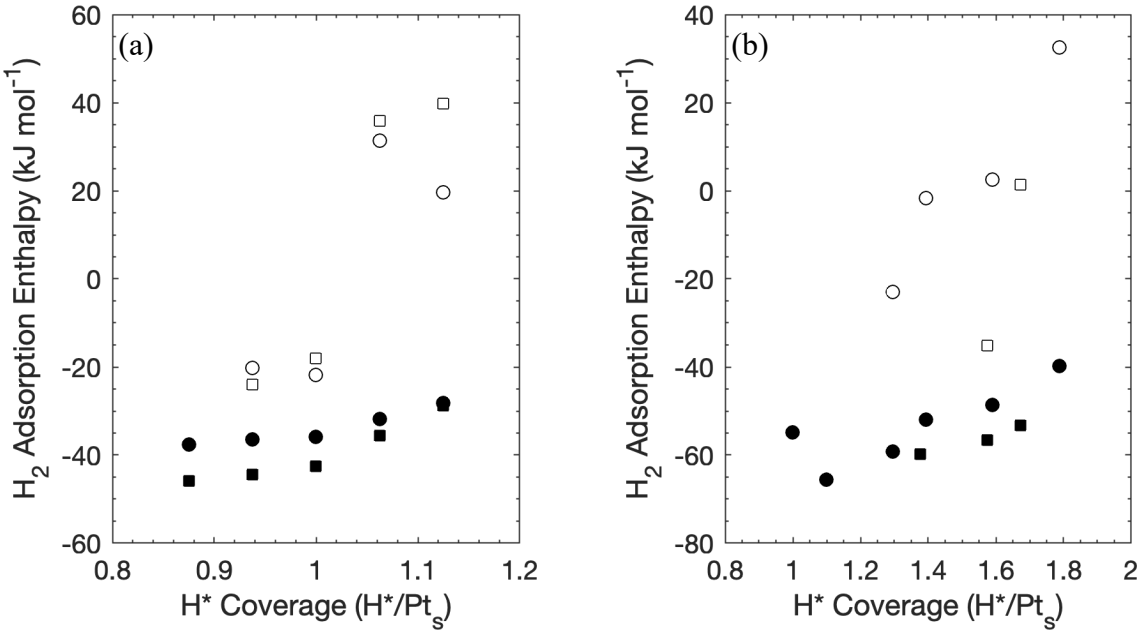

Figure SI-7. H_2 adsorption enthalpies (relative to H_2(g), 383 K; $H_2 + 2* \rightarrow 2$ H*) for H* on (a) Pt(111) surfaces and (b) Pt_{201} particles. Filled symbols represent adsorption enthalpies averaged across all H*-adatoms referenced to a bare Pt surface while hollow symbols denote differential adsorption enthalpies, representing the average adsorption enthalpy of H* added between states. H* adatoms can present in either (●,○) atop or (■,□) fcc positions on Pt(111). H* adatoms are also present in predominantly (●,○) atop or (■,□) fcc binding modes on Pt_{201}, but H* occupies a mixture of sites in both cases.

3.6.8 Configurational Entropies on Model Surfaces of Varying Size

Configurational entropies for H adsorption on alternative binding sites were estimated on model Pt surfaces varying from 10-500 atoms using Stirling's approximation:

$$\Delta S = k_B N(-\theta_{H'} \ln(\theta_{H'}) - (1-\theta_{H'}) \ln(1-\theta_{H'})) \qquad (SI-39)$$

where k_B is the Boltzmann constant, N is the number of atoms, and $\theta_{H'}$ is the fraction of H adatoms in the alternative binding mode (e.g. fcc site). The number of initial and alternative binding sites were both assumed to be equal to the number of Pt atoms. Figure SI-8 shows the entropy as a function of $\theta_{H'}$. These calculations show that the configurational entropy increases, as expected, as the size of the system (the number of Pt atoms) increases. The increase in configurational entropy is greatest when moving the first H adatom to the alternative binding mode. These entropies, specifically that for the first H adatom, can, in part, compensate for the enthalpic penalty (11–29 kJ mol^{-1}) of moving a H-adatom from the energetically preferred atop site to the alternative binding mode at the fcc site at the conditions of this study.

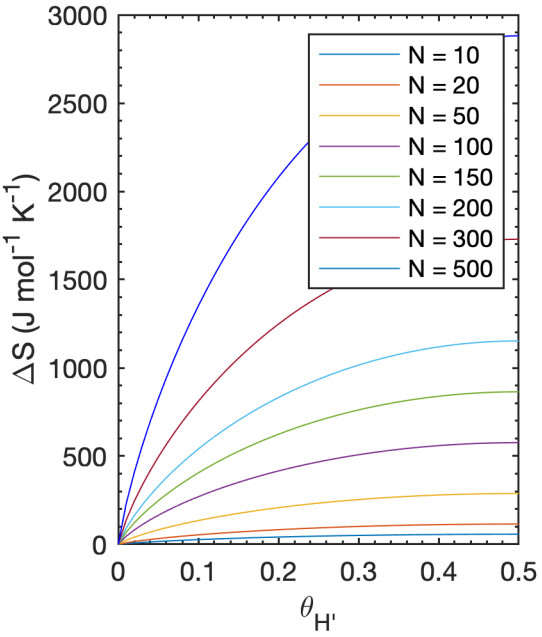

Figure SI-8. Configurational entropy as a function of the fraction of H adatoms in the alternative binding mode $\theta_{H'}$ for various model systems consisting of N Pt and H atoms.

3.7 References

1. Atkins, P. W.; De Paula, J., *Atkins' Physical chemistry*, 9th ed.; Oxford University Press: Oxford ; New York, 2010.
2. Bigeleisen, J.; Mayer, M. G., Calculation of Equilibrium Constants for Isotopic Exchange Reactions. *J. Chem. Phys.* **1947**, *15*, 261-267.
3. Bigeleisen, J.; Wolfsberg, M., Theoretical and Experimental Aspects of Isotope Effects in Chemical Kinetics. *Adv. Chem. Phys.* **1958**, *1*, 15-76.
4. Melander, L. C. S.; Saunders, W. H., *Reaction rates of isotopic molecules*; Wiley: New York, 1980.
5. Gonzalez-Lafont, A.; Lluch, J. M., Kinetic isotope effects in chemical and biochemical reactions: physical basis and theoretical methods of calculation. *Wiley Interdisciplinary Reviews-Computational Molecular Science* **2016**, *6*, 584-603.
6. Sattler, A., Hydrogen/Deuterium (H/D) Exchange Catalysis in Alkanes. *Acs Catalysis* **2018**, *8*, 2296-2312.
7. Loveless, B. T.; Buda, C.; Neurock, M.; Iglesia, E., CO Chemisorption and Dissociation at High Coverages during CO Hydrogenation on Ru Catalysts. *Journal of the American Chemical Society* **2013**, *135*, 6107-6121.
8. Panpranot, J.; Goodwin, J. G.; Sayari, A., Effect of H-2 partial pressure on surface reaction parameters during CO hydrogenation on Ru-promoted silica-supported Co catalysts. *J. Catal.* **2003**, *213*, 78-85.
9. Gnanamani, M. K.; Jacobs, G.; Shafer, W. D.; Sparks, D.; Davis, B. H., Fischer-Tropsch Synthesis: Deuterium Kinetic Isotope Study for Hydrogenation of Carbon Oxides Over Cobalt and Iron Catalysts. *Catal. Lett.* **2011**, *141*, 1420-1428.
10. Yang, J.; Tveten, E. Z.; Chen, D.; Holmen, A., Understanding the Effect of Cobalt Particle Size on Fischer-Tropsch Synthesis: Surface Species and Mechanistic Studies by SSITKA and Kinetic Isotope Effect. *Langmuir* **2010**, *26*, 16558-16567.
11. Burwell, R. L., Deuterium as a Tracer in Reactions of Hydrocarbons on Metallic Catalysts. *Acc. Chem. Res.* **1969**, *2*, 289-296.
12. Siegel, S.; Ohrt, D. W., Kinetic Hydrogen Isotope Effects in Catalytic Hydrogenation of Alkenes. *Journal of the Chemical Society D-Chemical Communications* **1971**, 1529-1530.
13. Osborn, J. A.; Jardine, F. H.; Young, J. F.; Wilkinso.G, Preparation and Properties of Tris(Triphenylphosphine)Halogenorhodium(1) and Some Reactions Thereof Including Catalytic Homogeneous Hydrogenation of Olefins and Acetylenes and Their Derivatives. *Journal of the Chemical Society a -Inorganic Physical Theoretical* **1966**, 1711-1732.
14. Montelatici, S.; van der Ent, A.; Osborn, J. A.; Wilkinson, G., Further Studies on Homogeneous Hydrogenation of Olefins by Use of Tris (Tertiary Phosphine)Chlororhodium(I) Complexes. *Journal of the Chemical Society a -Inorganic Physical Theoretical* **1968**, 1054-1058.
15. Jones, W. D.; Feher, F. J., Isotope Effects in Arene C-H Bond Activation by [(C5me5)Rh(Pme3)]. *Journal of the American Chemical Society* **1986**, *108*, 4814-4819.
16. Jones, W. D., Isotope effects in C-H bond activation reactions by transition metals. *Acc. Chem. Res.* **2003**, *36*, 140-146.
17. Logan, S. R.; Philp, J., Linetic Isotope Effects in Catalytic Synthesis of Ammonia. *J. Catal.* **1968**, *11*, 1-6.
18. Ozaki, A., *Isotopic Studies of Heterogeneous Catalysis*; Kodansha, 1977.
19. Emmett, P. H., Use of Isotopic Tracers in Studying Catalysts and Catalytic Reactions. *Catalysis Reviews* **1972**, *7*, 1-24.

20. Burwell, R. L., The Uses of Deuterium in the Study of Heterogeneous Catalysis. *Catalysis Reviews* **1972**, *7*, 25-49.
21. Yao, R.; Herrera, J. E.; Chen, L. H.; Chin, Y. H. C., Generalized Mechanistic Framework for Ethane Dehydrogenation and Oxidative Dehydrogenation on Molybdenum Oxide Catalysts. *Acs Catalysis* **2020**, *10*, 6952-6968.
22. Biscardi, J. A.; Iglesia, E., Reaction pathways and rate-determining steps in reactions of alkanes on H-ZSM5 and Zn/H-ZSM5 catalysts. *J. Catal.* **1999**, *182*, 117-128.
23. Cant, N. W.; Tonner, S. P.; Trimm, D. L.; Wainwright, M. S., Isotopic Labeling Studies of the Mechanism of Dehydrogenation of Methanol to Methyl Formate over Copper-Based Catalysts. *J. Catal.* **1985**, *91*, 197-207.
24. Joshi, R.; Zhang, G. H.; Miller, J. T.; Gounder, R., Evidence for the Coordination-Insertion Mechanism of Ethene Dimerization at Nickel Cations Exchanged onto Beta Molecular Sieves. *Acs Catalysis* **2018**, *8*, 11407-11422.
25. Hanson, R. M.; Green, S. M. E., *Introduction to molecular thermodynamics*; University Science Books: Sausalito, Calif., 2008.
26. Breakspere, R. J.; Norton, P. R.; Eley, D. D., Hydrogen Chemisorption and Exchange on Platinum. *J. Catal.* **1972**, *27*, 215-221.
27. Wachs, I. E.; Madix, R. J., On the H2-D2 Exchange on Stepped Platinum Surfaces. *Surf. Sci.* **1976**, *58*, 590-596.
28. Gillespie, R. D.; Burwell, R. L.; Marks, T. J., Isotopic Exchange between H2 and D2 by the Rideal-Eley Mechanism. *Catal. Lett.* **1991**, *9*, 363-368.
29. O'Brien, C. P.; Miller, J. B.; Morreale, B. D.; Gellman, A. J., The Kinetics of H-2-D-2 Exchange over Pd, Cu, and PdCu Surfaces. *J. Phys. Chem. C* **2011**, *115*, 24221-24230.
30. Rideal, E. K., On the hydrogen-deuterium exchange reaction. *Journal of the Research Institute for Catalysis Hokkaido University* **1968**, *16*, 45-51.
31. Eley, D. D.; Norton, P. R., Conversion and equilibration rates of hydrogen on nickel. *Discuss. Faraday Soc.* **1966**, *41*, 135-148.
32. Iida, I., Mechanism of Catalyzed Hydrogen-Deuterium Exchange on Gold Deposited over Poly(Tetrafluoroethylene). *Bull. Chem. Soc. Jpn.* **1979**, *52*, 2858-2862.
33. Garcia-Dieguez, M.; Hibbitts, D. D.; Iglesia, E., Hydrogen Chemisorption Isotherms on Platinum Particles at Catalytic Temperatures: Langmuir and Two-Dimensional Gas Models Revisited. *J. Phys. Chem. C* **2019**, *123*, 8447-8462.
34. Yang, G. J.; Akhade, S. A.; Chen, X.; Liu, Y.; Lee, M. S.; Glezakou, V. A.; Rousseau, R.; Lercher, J. A., The Nature of Hydrogen Adsorption on Platinum in the Aqueous Phase. *Angewandte Chemie-International Edition* **2019**, *58*, 3527-3532.
35. Vincent, J. K.; Olsen, R. A.; Kroes, G. J.; Baerends, E. J., Dissociative chemisorption of H-2 on Pt(111): isotope effect and effects of the rotational distribution and energy dispersion. *Surf. Sci.* **2004**, *573*, 433-445.
36. Nieuwenhuys, B. E., Influence of Surface-Structure on Adsorption of Hydrogen on Platinum, as Studied by Field-Emission Probe-Hole Microscopy. *Surf. Sci.* **1976**, *59*, 430-446.
37. Gomez, R.; Orts, J. M.; Alvarez-Ruiz, B.; Feliu, J. M., Effect of temperature on hydrogen adsorption on Pt(111), Pt(110), and Pt(100) electrodes in 0.1 M HClO4. *J. Phys. Chem. B* **2004**, *108*, 228-238.
38. Poelsema, B.; Lenz, K.; Comsa, G., The dissociative adsorption of hydrogen on defect-'free' Pt(111). *Journal of Physics-Condensed Matter* **2010**, *22*.

39. Rootsaert, W. J. M.; Vanreijen, L. L.; Sachtler, W. M. H., Field-Emission Study of Composite Adsorption Layers on Tungsten and Platinum. *J. Catal.* **1962**, *1*, 416-431.
40. de Jong, K. P., *Synthesis of solid catalysts*; Wiley-VCH: Weinheim, 2009.
41. Almithn, A. S.; Hibbitts, D. D., Supra-Monolayer Coverages on Small Metal Clusters and Their Effects on H-2 Chemisorption Particle Size Estimates. *AlChE J.* **2018**, *64*, 3109-3120.
42. Bergeret, G.; Gallezot, P., Particle Size and Dispersion Measurements. In *Handbook of Heterogeneous Catalysis*, Ertl, G.; Knözinger, H.; Schüth, F.; Weitkamp, J., Eds. Wiley: 2008; pp 738-765.
43. Kresse, G.; Joubert, D., From ultrasoft pseudopotentials to the projector augmented-wave method. *Phys. Rev. B* **1999**, *59*, 1758-1775.
44. Hammer, B.; Hansen, L. B.; Norskov, J. K., Improved adsorption energetics within density-functional theory using revised Perdew-Burke-Ernzerhof functionals. *Phys. Rev. B* **1999**, *59*, 7413-7421.
45. Kasper, J. S.; Lonsdale, K.; International Union of Crystallography., *International tables for X-ray crystallography*, 3rd ed.; Published for the International Union of Crystallography by D. Reidel Pub. Co.: Dordrecht ; Boston, 1985.
46. Pack, J. D.; Monkhorst, H. J., Special Points for Brillouin-Zone Integrations - Reply. *Phys. Rev. B* **1977**, *16*, 1748-1749.
47. Hibbitts, D. D.; Loveless, B. T.; Neurock, M.; Iglesia, E., Mechanistic Role of Water on the Rate and Selectivity of Fischer-Tropsch Synthesis on Ruthenium Catalysts. *Angewandte Chemie-International Edition* **2013**, *52*, 12273-12278.
48. Almithn, A.; Hibbitts, D., Effects of Catalyst Model and High Adsorbate Coverages in ab Initio Studies of Alkane Hydrogenolysis. *Acs Catalysis* **2018**, *8*, 6375-6387.
49. Chen, B. W. J.; Mavrikakis, M., How coverage influences thermodynamic and kinetic isotope effects for H-2/D-2 dissociative adsorption on transition metals. *Catal. Sci. Technol.* **2020**, *10*, 671-689.
50. Karim, W.; Spreafico, C.; Kleibert, A.; Gobrecht, J.; VandeVondele, J.; Ekinci, Y.; van Bokhoven, J. A., Catalyst support effects on hydrogen spillover. *Nature* **2017**, *541*, 68-71.
51. Sato, S., Photoelectrochemical Preparation of Pt/Tio2 Catalysts. *J. Catal.* **1985**, *92*, 11-16.
52. Kip, B. J.; Duivenvoorden, F. B. M.; Koningsberger, D. C.; Prins, R., Determination of Metal-Particle Size of Highly Dispersed Rh, Ir, and Pt Catalysts by Hydrogen Chemisorption and Exafs. *J. Catal.* **1987**, *105*, 26-38.
53. Wanke, S. E.; Doughart, N. A., Interaction of Hydrogen, Oxygen, and Carbon-Monoxide with Supported Rhodium. *J. Catal.* **1972**, *24*, 367-384.
54. Mcvicker, G. B.; Ziemiak, J. J., Chemisorption Properties of Platinum and Iridium Supported on Tio2-Al2o3 Mixed-Oxide Carriers - Evidence for Strong Metal Support Interaction Formation. *J. Catal.* **1985**, *95*, 473-481.

Chapter 4

H_2-D_2 and H_2O-D_2 Isotopic Exchange on Pt Crystallites: Dynamics, Thermodynamics and Elementary Steps

Abstract

H_2-D_2 exchange reactions (20 kPa H_2, 20 kPa D_2, 473 K) were used in the present study to probe the effects of H_2O adsorption on Pt surfaces. HD formation rates from H_2-D_2 exchange decreased irreversibly by a factor of 2 on Pt black and Pt/γ-Al_2O_3 following exposure to H_2O (20 kPa, 20 ks) and its subsequent removal. H_2-D_2 exchange rates recovered to their initial rates following treatments in H_2-D_2 mixtures (10 kPa H_2, 10 kPa D_2) at high temperatures (823 K), but not in equivalent thermal treatments in N_2. These results indicate that Pt surfaces become partially titrated by OH* or O* species that form from the dissociation of H_2O, leading to a decrease in the amount of dissociatively adsorbed hydrogen. H_2O-D_2 isotopic exchange rates (473 K) were measured on samples of Pt black over a range of broad range of H_2O and D_2 pressures (2.5-40 kPa H_2O, 5-80 kPa D_2). These exchange rates increased monotonically with H_2O and D_2 pressures, consistent with the reaction between D_2 and molecularly adsorbed H_2O*. This reaction pathway remains the dominant pathway for temperatures below 900 K; activation energy barriers above 900 K are consistent with the dissociation and recombination of H_2O. The kinetic model for H_2O-D_2 exchange was combined with that previously derived for H_2-D_2 exchange to obtain expressions that also accurately described exchange rates in H_2O-H_2-D_2 mixtures at 473 K. The effect of the formation of an extended liquid phase was investigated using H_2-D_2 exchange reactions (20 kPa H_2, 20 kPa D_2, 323 K) by condensing H_2O (0-12.3 kPa) within the mesopores of Pt/γ-Al_2O_3. H_2-D_2 exchange rates decreased with increasing H_2O pressure, consistent with the competitive adsorption of H_2O, but did not exhibit abrupt changes that would indicate the presence of H_2O solvation effects or mass transport effects. The results from this study provide alternative explanations for discrepancies in the literature and demonstrate the importance of having accurate understandings of the underlying mechanisms in the interpretation of isotopic exchange data.

4.1 Introduction

Surface catalysis requires adsorption of reactants, their chemical conversion, and the desorption of products.[1] Understanding the identity and kinetic relevance of bound species and the reversibility of elementary steps is essential for mechanistic interpretations of turnover rates. H_2 dissociation and the reactions of H adatoms are relevant in hydrogenation or hydrogenolysis[2-4] of alkanes,[5-7] alkenes,[8-10] arenes,[11-13] and CO.[14-17] H_2 chemisorption on metal catalysts has been extensively studied both with pure H_2[18-25] and with coadsorbed alkanes,[5, 26] CO,[27-28] and water.[14, 29-30] The effect of water on H_2 adsorption is of specific relevance in electrochemical systems.[29-35] Moreover, adsorption and reactions in the presence of a condensed H_2O phase, as in the case of fuel cells,[29, 36-39] require accurate assessments of mass transport and vapor-liquid equilibria.[40]

H_2 adsorption on catalytic surfaces has exploited techniques such as chemisorption uptakes,[18, 39] calorimetry,[24-25, 41] infrared spectroscopy,[14, 32, 37] electrochemical methods,[30-31, 33, 36] low-energy electron diffraction studies,[22-23] density functional theory (DFT),[42] and isotopic exchange experiments.[29, 43-44] D_2O-H_2 isotopic exchange was recently used to infer that liquid water significantly destabilizes H-adatoms at nanoparticle Pt surfaces (303-343 K), leading to much lower H* coverages.[29] Such inferences were based on kinetic isotope effects and on a proposed mechanism for reactions between H_2O(g) and D* that is contradicted by the evidence presented in the present study. Other studies[45-50] have proposed different exchange routes such as H_2O* reactions with D*[50] or H_2O* with D'[47] (H_2O* and D' bound at distinct non-competing sites). These studies did not place H_2O-D_2 (or D_2O-H_2) exchange mechanisms within the context of H_2-D_2 exchange steps that were recently revisited through theory and experiment (Chapter 3); H_2-D_2 exchange occurs predominantly via single-site associative H_2-D* and D_2-H* reactions below 700 K. Consequently, H_2-D_2 exchange rates cannot provide direct evidence for H_2/D_2 dissociation or H*/D* dynamics or thermodynamics.

The kinetics of H_2O-D_2 exchange reactions are interpreted here in the context of these findings by examining the effects of H_2O (in gaseous or liquid form) on H_2-D_2 exchange rates and the pressure dependences of isotopic exchange rates in H_2O-D_2 and H_2O-H_2-D_2 mixtures. Exchange rates before and after exposure to H_2O (and subsequent removal of H_2O from the reactant stream) are used to infer the reversibility of H_2O adsorption on Pt at 323-823 K. These rates show that exposure to 20 kPa H_2O at 473 K causes a significant decrease in H_2-D_2 exchange turnover rates, which cannot be reversed at exchange temperatures below 700 K. Exchange rates are shown to return to initial rates after H_2 treatments at 823 K but not upon treatment in N_2 at similar conditions. Such effects are evident on unsupported Pt and Pt nanoparticles dispersed on SiO_2 or γ-Al_2O_3. These effects reflect the formation of H_2O-derived species (OH* or O*) at low temperatures (473 K) and their removal by H_2 at significantly higher temperatures. These H_2O-derived species saturate Pt surfaces below monolayer coverages, leading to residual H_2-D_2 exchange rates even on surfaces exposed to H_2O. Such behavior may reflect significant differences in the thermodynamics of H_2O dissociation on different Pt facets, as previously reported by DFT studies (-16 kJ mol on Pt(100)[51] vs. 64 kJ mol^{-1} on Pt(111)[51-52]), thus preserving some reactive facets that remain unaffected by the dissociation of H_2O.

H_2O-D_2 isotopic exchange rates at 473 K are shown to increase monotonically with both H_2O (2.5-40 kPa) and D_2 pressures (5-80 kPa). The persistence of OH*/O* species during H_2-D_2 reactions below 700 K indicates that OH*+D* (or O*+2D*) recombination steps cannot be responsible for H_2O-D_2 (or D_2O-H_2) exchange events that occur readily at 323-700 K. The previously proposed reactions between H_2O* with D*[50] and H_2O* with D'[47] are also shown to be

inconsistent with the thermodynamic data reported in prior H_2 and D_2 chemisorption studies (Chapter 3). The dependence of H_2O-D_2 isotopic exchange rates on H_2O and D_2 pressures are instead consistent with reactions of D_2 molecules with bound molecular H_2O. Surface-bound H_2O species are present at significant coverages even at 473 K, as indicated by the ratio of equilibrium constants for D_2 (dissociative) and H_2O (molecular) adsorption regressed from the kinetic data. These temperatures are significantly higher than those in previous temperature programmed desorption (TPD) studies that showed the complete removal of bound molecular water at approximately 197 K.[53-54] Such H_2O coverages may therefore reflect extensive hydrogen-bonding interactions between H_2O and the OH*/O*-adlayer. Apparent activation energy barriers for H_2O-D_2 exchange are consistent for temperatures between 323 and 900 K; the apparent barrier increases significantly for temperatures higher than 900 K. These high temperature barriers (87 ± 8 kJ mol^{-1}) are similar to H_2O dissociation barriers reported by DFT (61 kJ mol^{-1} on Pt(111), 75 kJ mol^{-1} on Pt(100)),[51-52] indicating that H_2O dissociation-recombination reactions likely become the predominant exchange pathway at sufficiently high temperatures (> 900 K).

The formation of intrapore liquid H_2O (0-12.3 kPa H_2O; 323 K) through condensation in Pt/γ-Al_2O_3 mesopores does not lead to a detectable change in the kinetic effects of H_2O on HD formation rates (10 kPa H_2, 10 kPa D_2). These data show that neither diffusional nor solvation effects by an extended H_2O phase influence exchange rates or the state of the Pt surfaces and that rates reflect the prevalent pressure (and chemical potential) of H_2O in the contacting gas-phase. The formation of extended H_2O phases therefore does not influence the thermodynamics of H_2 and D_2 adsorption; the presence of H_2O does, however, lead to an apparent decrease in the amount of H_2 or D_2 adsorbed through the formation of OH*/O* titrating adlayers.

4.2. Methods

4.2.1 Catalyst Synthesis Methods

Pt/γ-Al_2O_3 (1% wt. Pt nominal) and Pt/SiO_2 (0.2% wt. Pt nominal) catalysts were prepared by incipient wetness impregnation and electrostatic adsorption methods, respectively, as reported previously (Chapter 3). Pt black (Strem Chemicals) was treated prior to kinetic experiments, as described below.

4.2.2 Measurement of Pt Dispersion on Pt/γ-Al_2O_3 and Pt/SiO_2

Pt dispersions, defined as the number of exposed Pt sites divided by the total number of Pt atoms, were measured using volumetric uptakes of H_2 for Pt/γ-Al_2O_3 and Pt/SiO_2. Samples (ca. 1 g) were heated from ambient temperature to 673 K (0.083 K s^{-1}) and held for 1 h in flowing H_2 (0.33 cm^3 g^{-1} s^{-1}; Praxair, UHP, 99.999% purity), then held under vacuum (<10^{-5} Pa) for 1 h at the same temperature before cooling to 373 K. H_2 uptakes were measured at 373 K and 1-40 kPa H_2. Saturation uptakes were determined by extrapolating the high-pressure linear portion of the isotherm to zero pressure. Particle diameters were calculated by assuming hemispherical particle geometries and the bulk density of Pt (21.45 g cm^{-3})[55]. Corner and edge sites on small metal nanoparticles can bind multiple H-atoms.[56] The following relations were thus used to calculate particle diameters (d):[56]

$$d = \frac{f_{shape} N_M}{2N_{H_2}} \frac{v_m}{a_m} \theta_{sat} \quad (1)$$

$$\theta_{sat} = \mathrm{H/Pt_s} = 1 + \alpha(d^{-1}) + \beta(d^{-2}) \quad (2)$$

in a way that corrects for the resulting suprastoichiometric coverages. Here, f_{shape} is a shape factor (6 for a hemispherical particle), N_M is the total number of metal atoms, N_{H_2} is the number of dissociatively adsorbed H_2 molecules, v_m and a_m are the volume and surface area of a Pt atom, Pt_s denotes atoms on the metal surface, and α (0.0364) and β (0.735) are empirical parameters specific for Pt.[56] The system of equations in Equations 1-2 are solved simultaneously to obtain the values of d and θ_{sat}.

4.2.3 Measurement of H_2-D_2, H_2O-D_2, and H_2O-H_2-D_2 Isotopic Exchange Rates

Isotopic exchange rates, normalized by the number of accessible Pt sites measured from chemisorption (Section 4.2.2), were measured on sieved (<100 μm) samples of unsupported Pt black (0.0001-0.0005 g), Pt/γ-Al_2O_3 (0.0005-0.0050 g), and Pt/SiO_2 powders (0.0050-0.0200 g) held on a quartz frit within a U-shaped quartz tube (6.35 mm O.D., 4 mm I.D.). H_2 (99.999% UHP; Praxair), D_2 (99.8% isotopic enrichment, research grade; Praxair), and N_2 (99.998%, Praxair) were treated using gas purifiers (VICI Metronics) to remove residual O_2 and H_2O. Gas flow rates were controlled using mass flow controllers (Parker Porter 200 series). Lines were heated to temperatures greater than 383 K to avoid condensation. Deionized H_2O (>18.0 MΩ-cm; degassed by bubbling N_2 for >24 h and then placing under vacuum for >24 h) was introduced into the gas stream at 423 K using a syringe pump (KD Scientific Legato 200). Samples were treated in flowing H_2 (100 $cm^3\ g^{-1}\ s^{-1}$) while heating from ambient temperature to 873 K at 0.083 $K\ s^{-1}$, holding for 2 h, and then cooling to the intended reaction temperature.

Effluent speciation was performed using a residual gas analyzer mass spectrometer (Leybold Inficon Transpector, TSP TH200). H_2-D_2 exchange rates (r_f) were calculated by correcting measured rates (r_n) for approach to equilibrium (η):

$$r_n = r_f\ (1 - \eta) \quad (3)$$

The approach to equilibrium for H_2-D_2 (η_{HD}) and H_2O-D_2 (η_{HDO}, η_{D_2O}) exchange reactions:

$$H_2 + D_2 \rightarrow 2\ HD \quad (4)$$

$$H_2O + D_2 \rightarrow HDO + HD \quad (5)$$

$$H_2O + 2\ D_2 \rightarrow D_2O + 2\ HD \quad (6)$$

are defined as:

$$\eta_{HD} = \frac{(HD)^2}{(H_2)(D_2)} \frac{1}{K_{HD}} \quad (7)$$

$$\eta_{HDO} = \frac{(HDO)^2(HD)}{(H_2O)(D_2)} \frac{1}{K_{HDO}} \quad (8)$$

$$\eta_{D_2O} = \frac{(D_2O)^2(HD)^2}{(H_2O)(D_2)^2} \frac{1}{K_{D_2O}} \quad (9)$$

Here, K_{HD}, K_{HDO}, and K_{D_2O} are equilibrium constants for Equations 4-6, corresponding with the binomial distribution of all isotopic species that results from stochastic scrambling.[57] (i) denotes the pressure of species i (in kPa). The pressure in the reactor effluent was used in Equations 7-9 because the hydrodynamics in the thin catalyst beds of these studies resemble those of well-mixed systems.

4.2.4 Textural Properties of γ-Al_2O_3

N_2 adsorption isotherms on γ-Al_2O_3 were obtained using volumetric uptakes at its normal boiling point (Micromeritics 3Flex Adsorption Analyzer). γ-Al_2O_3 samples (ca. 100 mg) were treated by heating from ambient temperature to 673 K at 0.17 K s^{-1} and holding for 3 h under vacuum prior to uptake measurements.

4.3. Results and Discussion

4.3.1 Pt Dispersion and Nanoparticle Diameters (Pt/γ-Al_2O_3 and Pt/SiO_2)

The dispersion of Pt in Pt/γ-Al_2O_3 and Pt/SiO_2 samples was measured using uptakes of H_2 at 373 K and found to be 0.72 and 0.38, respectively. These dispersions correspond with average crystallite diameters of 1.9 and 3.2 nm, calculated using Equations 1-2.

4.3.2 Effects of Contact with H_2O on H_2-D_2 Isotopic Exchange Rates on Pt powder, Pt/γ-Al_2O_3, and Pt/SiO_2

HD formation and H_2O conversion rates on Pt powder, Pt/γ-Al_2O_3, and Pt/SiO_2 in H_2-D_2 and H_2-D_2-H_2O mixtures were measured before, during, and after exposure to H_2O. Pt powders sintered during pretreatments (Section 4.2.2),[58-60] and the small mass of samples used (0.3 mg) did not allow surface area measurements after treatments and exchange measurements. Our previous study showed that H_2-D_2 exchange turnover rates were insensitive to nanoparticle diameter or support (1.5-3.2 nm; Pt/γ-Al_2O_3, and Pt/SiO_2) (Chapter 3); turnover rates on Pt black were calculated by assuming that initial H_2-D_2 exchange rates (10 kPa H_2, 10 kPa D_2, 473 K) on Pt black and Pt/γ-Al_2O_3 are equal.

H_2-D_2 exchange rates (10 kPa H_2, 10 kPa D_2; 473 K) under anhydrous conditions were stable with time. Catalyst samples were exposed to H_2O evaporated into the H_2-D_2-N_2 stream at 20 kPa, and exchange rates were measured as a function of time. Figure 1a shows that HD formation rates (normalized by those measured at the time of H_2O introduction; $r_{HD,f}/r^0_{HD,f}$) decreased with time on all samples and reached nearly constant values after 10 ks. H_2O exchange rates, measured by the sum of HDO and D_2O formation rates, also decreased with time in an identical manner during exposure to water, as indicated by $\frac{-r_{H_2O,f}}{r_{HD,f}}$ rate ratios that were constant with time (Fig. 1b). These data indicate that H_2O-D_2 and H_2-D_2 isotopic exchange events likely occur at the same active sites; both reactions were equally affected by an apparent titration of the catalyst surface during exposure to H_2O, reflected in the transients in Figure 1a.

The removal of H_2O led to an immediate increase in HD formation rates, indicating that water reversibly inhibits H_2-D_2 exchange rates (Fig. 1a, 20 ks); rates quickly reached stable values

but did not return to those measured before exposure to H_2O, even 20 ks after H_2O removal. The $r_{HD,f}/r^0_{HD,f}$ values after the removal of H_2O were similar for unsupported Pt and Pt/γ-Al_2O_3 (Fig. 1a; 0.52 ± 0.02 and 0.58 ± 0.03, respectively) but were much lower on Pt/SiO_2 (0.15 ± 0.01). Chemical conversions on catalytic surfaces can exhibit sensitivity towards the structure of particles and the prevalence of coordinatively unsaturated corner and edge atoms, which increase in proportion as particle sizes decrease.[61] The average Pt particle diameter for Pt/SiO_2 (3.2 nm), however, was between those for Pt/γ-Al_2O_3 (1.9 nm) and unsupported Pt (ca. 400 nm; estimated from a dispersion calculated using H_2-D_2 exchange rates on Pt powders); these differences in $r_{HD,f}/r^0_{HD,f}$ values following contact with H_2O thus cannot be attributed to particle size effects. Previous studies have shown that SiO_2-supported metal catalysts undergo rapid deactivation under hydrothermal conditions (573 K), caused by the migration of the silica onto and subsequent poisoning of metal surfaces.[62] Such processes have not been reported metal clusters supported on γ-Al_2O_3. These migratory processes are therefore likely responsible for the observed differences between Pt/SiO_2 and unsupported Pt or Pt/γ-Al_2O_3 catalysts (Fig. 1a). Pt powders, which do not have a support material that can poison the surface, still exhibited an irreversible effect of contact with H_2O; these data thus indicate that the titrant must be derived from H_2O molecules.

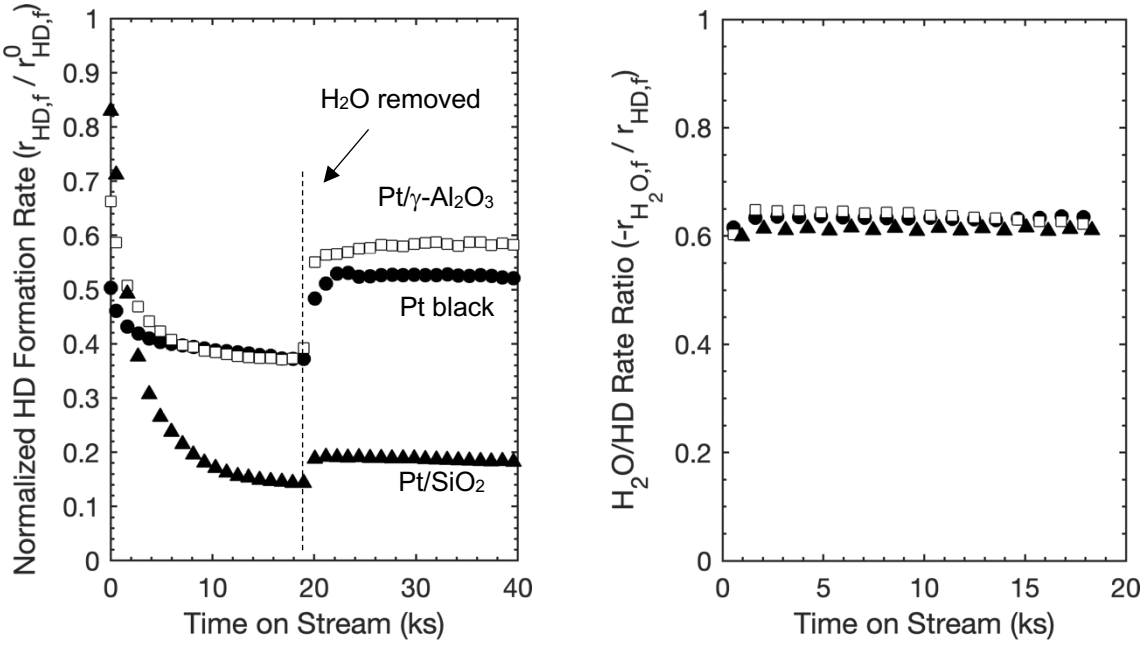

Figure 1. (a) HD formation rates, normalized by rates at the time of H_2O introduction $\left(\frac{r_{HD,f}}{r^0_{HD,f}}\right)$, and (b) the ratio of H_2O consumption and HD formation rates $\left(\frac{-r_{H_2O,f}}{r_{HD,f}}\right)$ as a function of time on stream in H_2-D_2-H_2O mixtures (10 kPa H_2, 10 kPa D_2, 20 kPa H_2O) on (●) Pt black, (□) Pt/γ-Al_2O_3, and (▲) Pt/SiO_2 at 473 K. H_2O is introduced at t = 0 and removed after 20 ks.

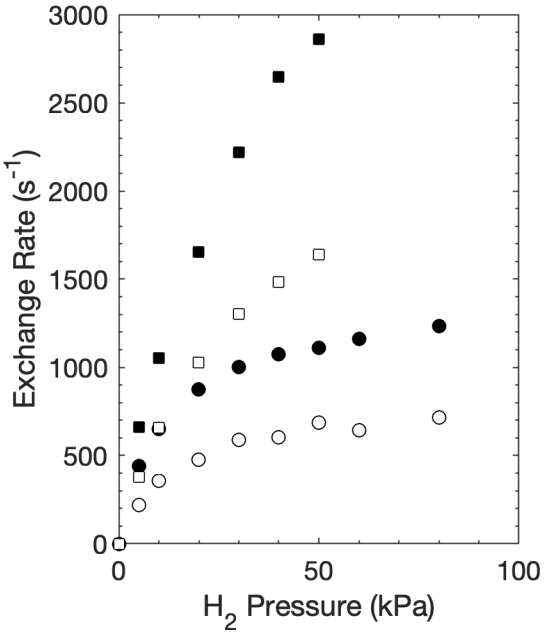

Figure 2. H_2-D_2 isotopic exchange rates as a function of H_2 pressure at 10 kPa D_2 (●,○) and 40 kPa D_2 (■,□) before (solid symbols) and after (hollow symbols) exposure to H_2O (20 kPa, 20 ks).

H_2-D_2 exchange rates on Pt black were measured under anhydrous conditions as a function of H_2 pressure (5-80 kPa H_2; 10 and 40 kPa D_2) at 473 K before and after exposure to H_2O (20 kPa, 20 ks; Fig. 2). Exchange rates increased monotonically with H_2 pressure in agreement with previous studies (Chapter 3), even after exposure to H_2O (Fig. 2). These kinetic dependences reflect H_2-D_2 exchange reactions (Scheme 1) that are mediated primarily by single-site routes involving H_2 reactions with D* (or D_2 with H*) (steps 1.4-1.5, Scheme 1). These kinetic trends are accurately described by the rate equation (Chapter 3):

$$r_{HD,f} = k_{-2}\frac{(H_2)(D_2)}{\left((H_2)+(D_2)\right)^2} + 2k_4\frac{(H_2)(D_2)}{(H_2)+(D_2)} \tag{10}$$

where k_{-2} is the rate constant for recombinative desorption of H* and D* (step 1.2, Scheme 1) and k_4 is the rate constant for reactions between H_2 and D* or D_2 and H* (steps 1.4-1.5, Scheme 1). Table 1 shows the rate constants regressed from the data in Figure 2. The value of k_4 after exposure to H_2O (39 ± 3 kPa^{-1} s^{-1}) was a factor of 0.58 ± 0.06 smaller than before exposure (66 ± 4 kPa^{-1} s^{-1}). The large uncertainties in regressed k_{-2} values (Table 1) reflect negligible contributions from H*-D* recombination reactions (step 1.2, Scheme 1) to measured exchange rates at the conditions of these experiments. These data indicate that the mechanism of H_2-D_2 exchange is unaffected by the titration of Pt nanoparticle surfaces by H_2O-derived species and involves the single-site associative mechanism previous demonstrated under anhydrous conditions (Chapter 3).

$$H_2 + 2^* \underset{k_{-1}}{\overset{k_1}{\rightleftharpoons}} 2H^* \quad [1.1]$$

$$HD + 2^* \underset{k_{-2}}{\longleftarrow} H^* + D^* \quad [1.2]$$

$$D_2 + 2^* \underset{k_{-3}}{\overset{k_3}{\rightleftharpoons}} 2D^* \quad [1.3]$$

$$H_2 + D^* \xrightarrow{k_4} HD + H^* \quad [1.4]$$

$$D_2 + H^* \xrightarrow{k_4} HD + D^* \quad [1.5]$$

Scheme 1. Elementary steps for H_2-D_2 isotopic exchange.

Table 1. Rate constants for H_2-D_2 exchange on Pt black before and after exposure to H_2O (20 kPa, 20 ks)

	k_{-2} (s^{-1})	k_4 (kPa^{-1} s^{-1})
Before	31 ± 495	66 ± 4
After	-17 ± 346	39 ± 3

*Rates on Pt black were calculated by normalizing against Pt/γ-Al_2O_3 rates at 473 K. The magnitudes of k_{-2} and k_4 on Pt black therefore cannot be compared directly to those on other catalysts.

4.3.3 Removal of H_2O-derived Titrants on Pt Surfaces by Thermal Treatments

H_2-D_2 exchange rates were measured on Pt powder samples used in H_2-D_2-H_2O exchange measurements (10 kPa H_2, 10 kPa D_2, 20 kPa H_2O, 20 ks, 473 K) under anhydrous conditions (10 kPa H_2, 10 kPa D_2) while increasing the sample temperature to 823 K (at 0.033 K s^{-1}). Figure 3 shows these exchange rates as the temperature was increased to 823 K and then decreased to 473 K at the same rate. The temperature effects on rates during the heating and cooling cycles were similar below 573 K (Fig. 3), as indicated by apparent activation barriers that are nearly identical (25.0 ± 0.8 kJ mol^{-1} and 26.0 ± 0.2 kJ mol^{-1} during heating and cooling, respectively), even though rates were two-fold higher (473 K) after the sample was heated to 823 K. H_2-D_2 exchange rates showed an increase in rate for temperatures between 573 and 700 K (Fig. 3) that appears to reflect the gradual removal of the H_2O-derived species (Fig. 3). Rates were nearly identical for temperatures greater than 700 K (Fig. 3), and the H_2-D_2 exchange rate (473 K) at the end of the thermal treatment (Fig. 3) was 645 ± 14 s^{-1} (Fig. 3) compared to 642 ± 29 s^{-1} before contact with H_2O, consistent with the complete removal of titrating species and recovery of initial H_2-D_2 exchange rates (Fig. 1a). The activation energy barrier for H_2-D_2 exchange (26.0 ± 0.2 kJ mol^{-1})

and exchange rates were also in agreement with those previously reported for H_2-D_2 exchange reactions on Pt black (27.2 ± 0.3 kJ mol^{-1}) (Chapter 3). These data indicate that the titrating species is completely removed by 700 K.

The same thermal treatment (heat to 823 K, 0.033 K s^{-1}; cool to 423 K, 0.033 K s^{-1}) in inert N_2 failed to remove the titrant (Fig. 3, indicated by star); the H_2-D_2 exchange rate at the end of this treatment (373 ± 6 s^{-1}) was similar to the rate before treatment (331 ± 5 s^{-1}) (Fig. 3). This N_2 thermal treatment temperature (823 K) is higher than the temperature required for atoms on Pt surfaces to exhibit mobility ($T_{Hüttig}$ = 608 K)[63] and is therefore sufficient to reverse any restructuring of the catalyst surface caused by exposure to H_2O. It is also significantly higher than those in temperature programmed desorption studies of H_2O on Pt surfaces, which showed the complete removal of bound molecular water at 197 K.[53-54] The requirement for a reductive environment to remove the titrant and recover initial rates implicates OH* or O* as the most likely titrant; these species form from the dissociation of H_2O but can become stranded on the catalyst surface in the absence of H_2 or another reductant. The asymptotic behaviors observed during H_2O exposure in Figure 1, may reflect the simultaneous formation H* species upon H_2O dissociation. These dissociation events lead to an equilibrium between H_2O (g), H_2 (g), H_2O*, OH* (or O*), and H* which limits the complete titration of Pt surfaces by OH* (or O*) species. These data (Fig. 1-3) cannot be used to discern between OH* or O*, but the unfavorable thermodynamics[64] of water splitting at 473 K suggest that OH* is more likely to be present.

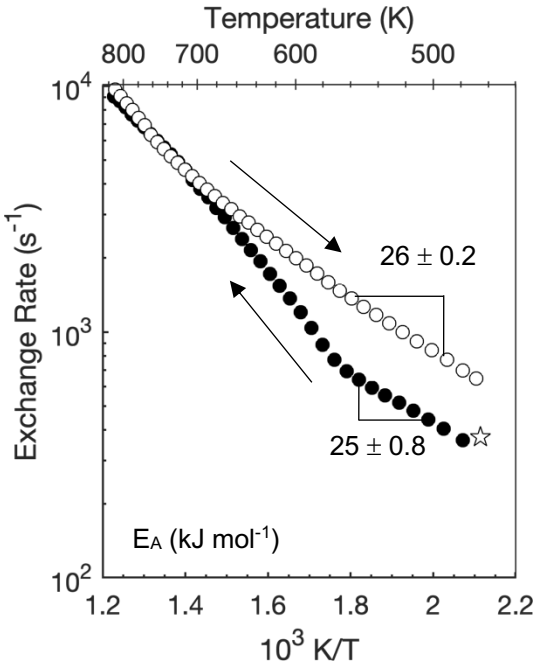

Figure 3. Arrhenius plot of HD formation rates (10 kPa H_2, 10 kPa D_2) on Pt black following exposure to H_2-D_2-H_2O mixtures (10 kPa H_2, 10 kPa D_2, 20 kPa H_2O, 20 ks) while the temperature was increased (●) to 823 K and decreased (○) to 473 K at 0.033 K s^{-1}. ☆ represents HD formation rates (10 kPa H_2, 10 kPa D_2) after identical thermal cycles in inert N_2.

The apparent irreversibility of H_2O dissociation events and subsequently titration at 473 K (Fig. 1a) suggest that activation energy barriers for recombination (OH*+H*) reactions are much greater than for H_2O dissociation reactions. These reactions have been previously probed by theoretical methods (density functional theory, DFT).[51] Calculations show that the dissociation of adsorbed H_2O on Pt(100) surfaces to form H* and OH* exhibits an energy barrier of 61 kJ mol^{-1}.[51] The reaction is thermodynamically favored with an energy of -16 kJ mol^{-1};[51] the recombinative reaction of H* and OH* to form H_2O* must therefore exhibit a higher energy barrier of 77 kJ mol^{-1}, consistent with the increased difficulty in removing the titrant at appreciable rates (Fig. 3). DFT calculations also suggest, however, that the converse is true on Pt(111) surfaces, where the reaction energy for H_2O dissociation is 64 kJ mol^{-1};[51-52] the activation energy barrier on such surfaces was found to be 75 kJ mol^{-1}, leading to barriers of only 11 kJ mol^{-1} for the reverse (OH* + H*) reaction. Such drastic differences in reaction energies on different Pt surfaces (Pt(100) vs. Pt(111)) lead to substantially different coverages of titrants on these facets. Pt(100) and Pt(111) surfaces are expected to be the most prominent faces on large nanoparticles (e.g. Pt black). These differences may therefore also explain the self-limiting titration behaviors observed in Figure 1a.

4.3.4 Kinetic Dependence of Isotopic Exchange Rates on H_2O and D_2 Pressures and Exchange Pathways During H_2O-D_2 Reactions on Pt

H_2O-D_2 exchange rates were measured on Pt black for a range of H_2O (2.5-40 kPa) and D_2 pressures (5-80 kPa) at 473 K. Samples were pretreated in a H_2O-H_2 mixture (40 kPa H_2O, 5 kPa H_2; 20 ks; 473 K) prior to kinetic studies; this mixture corresponds with the highest H_2O/H_2 ratio during these kinetic studies. This pretreatment was performed to allow for the formation of stable OH*/O* titrating adlayers (Section 4.3.2) to ensure that rates did not change with time. Figure 4 shows H_2O-D_2 exchange rates as functions of D_2 and H_2O pressure. These rates increased sublinearly with both H_2O and D_2 pressures (Fig. 4). The kinetic dependences shown here are inconsistent with the reactions of H_2O(g) and D*,[29] H_2O* and D*[50], and H_2O* and D'[47] (* and ' denote noncompeting sites) at the saturation coverages (of D*) expected at 473 K. Equilibrium constants for D_2 dissociative adsorption were regressed to the experimental data for each of these mechanistic models (Sections 4.6.1.1 – 4.6.1.3); the resulting values indicated that these pathways are best described on surfaces that are essentially bare (parity plots for these models can be found in Section 4.6.1.1 – 4.6.1.3). Previous H_2 and D_2 chemisorption uptake experiments (Chapter 3), however, indicate that surfaces are fully covered by H*/D* adlayers at this temperature (473 K) and these D_2 pressures (>5 kPa). These proposed reaction pathways are therefore inconsistent with extensive thermodynamic evidence from prior studies.

The dissociation of H_2O (to form OH* and H*) and subsequent recombination of OH* and D* is also inconsistent with the kinetic data. Such reactions are responsible for the formation of the OH*/O* refractory adlayer (Sections 4.3.2-4.3.3). The transients during exposure to H_2O (Fig. 1b, 0-20 ks) reflect dissociation rates, while the constant rates after the removal of H_2O (Fig. 1b, 20-40 ks) reflect undetectable recombination rates. These reactions therefore occur on much slower timescales (ca. 10 ks, Fig. 1) than those primarily responsible for exchange (0.001-0.02 s, inverse of rates in Fig. 4). Furthermore, regression analysis of this reaction pathway, as for the other proposed reaction mechanisms (Sections 4.6.1.1 – 4.6.1.3), similarly resulted in the prediction of a nearly bare surfaces (Section 4.6.1.4).

Another plausible reaction mechanism for H_2O-D_2 exchange reactions is proposed in Scheme 2. In this reaction scheme, the dissociative adsorption of D_2 to form D* is equilibrated (step 2.1, Scheme 2) and competes with the molecular adsorption of H_2O (step 2.2, Scheme 2). These adsorbed H_2O* molecules can desorb (step 2.3, Scheme 2) or exchange with D_2 molecules to form HDO* and HD (step 2.5, Scheme 2). HDO* can then similarly desorb (step 2.4, Scheme 2) or exchange again by reaction with additional D_2 to form D_2O* (step 2.6, Scheme 2).

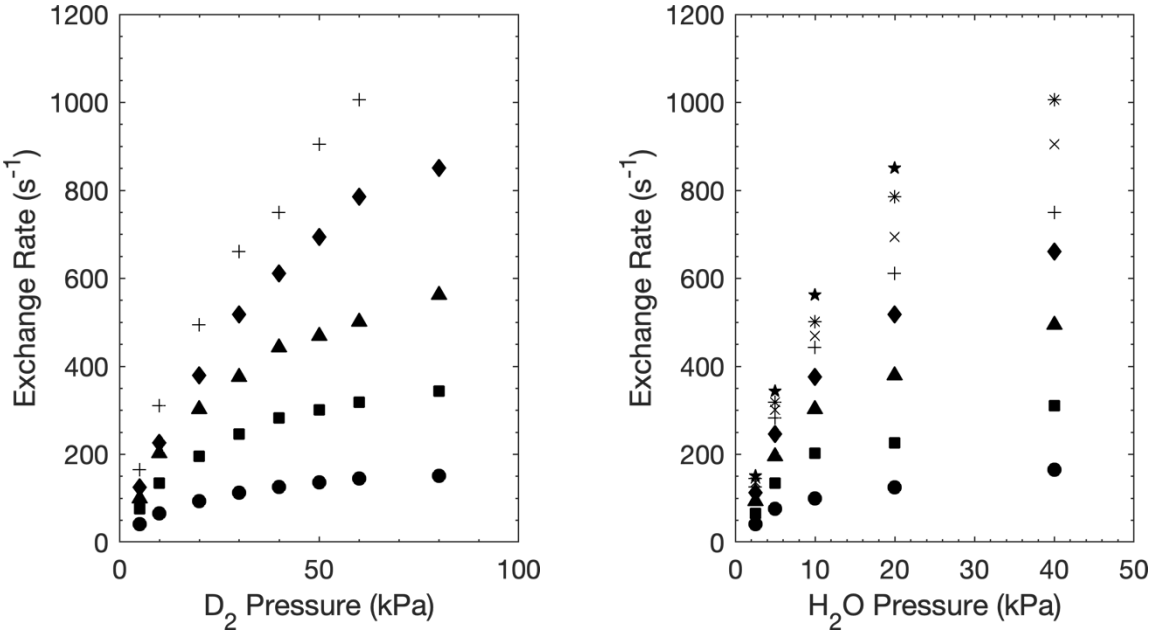

Figure 4. (a) H_2O-D_2 isotopic exchange rates as a function of D_2 pressure on Pt black at 2.5 (●), 5 (■), 10 (▲), 20 (◆) and 40 (+) kPa H_2O at 473 K. (b) H_2O-D_2 isotopic exchange rates as a function of D_2 pressure on Pt black at 2 (●), 5 (■), 10 (▲), and 20 (◆), 40 (+), 60 (×), and 80 (*) kPa D_2 at 473 K. Reported rates are calculated from total H_2O conversion.

H_2O-D_2 Exchange Elementary Steps

$$D_2 + 2* \underset{k_{-3}}{\overset{k_3}{\rightleftharpoons}} 2D* \quad [2.1]$$

$$H_2O + * \underset{k_{-5}}{\overset{k_5}{\rightleftharpoons}} H_2O* \quad [2.2]$$

$$HDO + * \underset{k_{-5}}{\overset{}{\leftarrow}} HDO* \quad [2.3]$$

$$D_2O + * \underset{k_{-5}}{\overset{}{\leftarrow}} D_2O* \quad [2.4]$$

$$D_2 + H_2O* \xrightarrow{k_6} HD + HDO* \quad [2.5]$$

$$D_2 + HDO* \xrightarrow{k_6} HD + D_2O* \quad [2.6]$$

Additional Steps for H_2O-H_2-D_2 Exchange

$$H_2 + 2* \underset{k_{-1}}{\overset{k_1}{\rightleftharpoons}} 2H* \quad [2.7]$$

$$HD + 2* \underset{k_{-2}}{\overset{}{\leftarrow}} H* + D* \quad [2.8]$$

$$H_2 + D* \xrightarrow{k_4} HD + H* \quad [2.9]$$

$$D_2 + H* \xrightarrow{k_4} HD + D* \quad [2.10]$$

$$H_2 + HDO* \xrightarrow{k_6} HD + H_2O* \quad [2.11]$$

$$H_2 + D_2O* \xrightarrow{k_6} HD + HDO* \quad [2.12]$$

Scheme 2. Elementary steps for H_2O-D_2 and H_2O-H_2-D_2 isotopic exchange reactions mediated by D_2-H_2O* reactions.

A rate equation was derived from Scheme 2 by assuming that kinetic isotopic effects for the desorption of molecular water (steps 2.2-2.4, Scheme 2) and the reactions between D_2 and adsorbed water (H_2O*, HDO*) (steps 2.5-2.6, Scheme 2) are negligible:

$$-r_{H_2O,f} = r_{HDO,f} + r_{D_2O,f} = \frac{k_6(H_2O)(D_2)}{\left((H_2O) + \frac{\sqrt{K_3}}{K_5}\sqrt{(D_2)}\right)\left(1 + \frac{k_6}{k_{-5}}(D_2)\right)} \quad (11)$$

k_i and K_i are rate and equilibrium constants corresponding to those shown in Scheme 2. The three parameters in this equation (k_6, $\frac{\sqrt{K_3}}{K_5}$, and $\frac{k_6}{k_{-5}}$) were regressed to the kinetic data at 473 K (Fig. 4); their values are summarized in Table 2. The value of $\frac{\sqrt{K_3}}{K_5}$ (2.46 ± 0.17 kPa$^{-0.5}$, Table 2) is consistent with the competitive adsorption of H_2O molecules at substantial coverages, even at temperatures far above ambient temperatures, in contrast with the prior H_2O TPD studies.[53-54] These coverages lead to the reversible inhibition of H_2-D_2 exchange reactions, as seen when H_2O was removed during earlier experiments (Fig. 1a). The adsorption of H_2O may be facilitated by hydrogen-bonding interactions with the OH*/O* adlayer (Section 4.3.2-4.3.3); such effects have been noted in previous studies, albeit at significantly lower temperature (< 200 K).[65] Sensitivity analyses of these parameters (Section 4.6.3) showed that model errors are strongly dependent on the values of all three parameters. They also showed that the regressed value of k_6 is correlated with the value of $\frac{\sqrt{K_3}}{K_5}$; these correlations reflect the relationship between the rate of reaction between H_2O* and D_2 (represented by k_6) and the concentration of H_2O* on the catalyst surface (represented by $\frac{\sqrt{K_3}}{K_5}$). Other pairs of parameters exhibited only weak correlations with each other (Section 4.6.3). Parity plots of the experimental and calculated rates (Eq. 11) are available in Section 4.6.3 (Fig. SI-6).

Table 2. Estimated values and confidence intervals of regressed parameters for H_2O-D_2 isotopic exchange at 473 K.

Parameter	Estimate	Lower limit (95% CI)	Upper limit (95% CI)
k_6 (kPa^{-1} s^{-1})	34.7	33.3	36.2
$\frac{\sqrt{K_3}}{K_5}$ (kPa$^{0.5}$)	2.46	2.29	2.64
$\frac{k_6}{k_{-5}}$ (kPa^{-1})	6.4 × 10^{-3}	5.4 × 10^{-3}	7.5 × 10^{-3}

The proposed mechanism (Scheme 2) indicates that D_2O can be formed as a primary product by the secondary deuteration of HDO* (step 2.6, Scheme 2) before it can desorb (step 2.3, Scheme 2). The ratio of D_2O to HDO was measured as a function of residence time during H_2O-D_2 exchange reactions (20 kPa H_2O, 20 kPa D_2, 473 K) on Pt black (Fig. 5). These data were used to extrapolate the D_2O/HDO ratio to zero residence time, giving a value of 0.056 ± 0.002 and reflecting the formation of D_2O as a primary product. This value can be compared to that derived from Scheme 2:

$$\frac{r_{D_2O}}{r_{HDO}} = \frac{k_6(D_2)}{2\,k_{-5}} \tag{12}$$

Equation 12 predicts an initial D_2O/HDO ratio of 0.064 ± 0.007 for these reaction conditions (20 kPa H_2O, 20 kPa D_2, 473 K), which is in close agreement with the experimental value (0.056 ± 0.002). These relative rates of HDO and D_2O formation (Eq. 12) reflect the steady-state concentrations of HDO* and D_2O* on Pt surfaces, which are in turn set by the relative rates of

H_2O*/HDO* conversion by reaction with D_2 (steps 2.5-2.6, Scheme 2) and H_2O*/HDO* desorption (steps 2.2-2.3, Scheme 2).

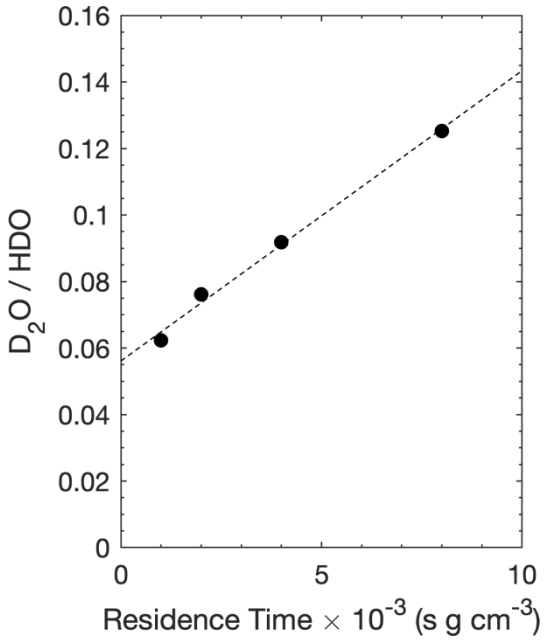

Figure 5. D_2O/HDO isotopic ratio as a function of residence time during H_2O-D_2 reactions on Pt black (20 kPa H_2O, 20 kPa D_2, 473 K). Dashed line is obtained by linear regression of the data.

4.3.5 Modelling HD Formation and H_2O Consumption Rates During H_2O-H_2-D_2 Exchange Reactions on Pt

The partial titration of Pt surfaces by OH*/O* did not lead to changes in kinetic behaviors (Fig. 2) or activation energy barriers (Fig. 3) for H_2-D_2 exchange reactions (Sections 4.3.2-4.3.3). H_2-D_2 exchange reactions are therefore proposed to occur via the same reaction pathways (H_2+D* and D_2+H*; steps 2.9-2.10, Scheme 2) in mixtures of H_2O, H_2, and D_2 as in anhydrous conditions. Here, HDO* and D_2O* can additionally undergo reaction with H_2 to form H_2O* (step 2.11, Scheme 2) and HDO* (step 2.12, Scheme 2), respectively. The rates of HD formation and H_2O conversion are given by (derivation in Section 4.6.2.2):

$$r_{HD} = \frac{2k_4(D_2)\left(\frac{\sqrt{K_3}}{K_5}\frac{(H_2)}{\sqrt{(H_2)+(D_2)}}\frac{k_6}{k_{-5}}(H_2) + \frac{k_6}{k_4}(H_2O) + \frac{k_6}{k_{-5}}(H_2)\frac{k_6}{k_4}(H_2O) + \frac{\sqrt{K_3}}{K_5}\frac{(H_2)}{\sqrt{(H_2)+(D_2)}}\left(2+\frac{k_6}{k_{-5}}\right)(D_2)\right)}{\left((H_2O)+\frac{\sqrt{K_3}}{K_5}\sqrt{(H_2)+(D_2)}\right)\left(2+\frac{k_6}{k_{-5}}((H_2)+(D_2))\right)} \quad (13)$$

$$r_{H_2O} = \frac{2k_6(H_2O)(D_2)\left(1+\frac{k_6}{k_{-5}}(H_2)\right) + \frac{k_6^2}{k_{-5}^2}(H_2O)(D_2)^2}{\left((H_2O)+\frac{\sqrt{K_3}}{K_5}\sqrt{(H_2)+(D_2)}\right)\left(2+3\frac{k_6}{k_{-5}}((H_2)+(D_2)) + \frac{k_6^2}{k_{-5}^2}((H_2)+(D_2))^2\right)} \quad (14)$$

Equations 13 and 14 were derived assuming H_2/D_2 dissociation and H*/D* recombination reactions (steps 2.1, 2.7, 2.8; Scheme 2) are slow compared to H_2-D* and D_2-H* reactions (steps

2.9-2.10, Scheme 2), as shown in our previous study (Chapter 3). They also assume that the thermodynamic isotope effect (TIE) for H_2 and D_2 adsorption $\left(TIE = \frac{K_1}{K_3}\right)$ is unity. TIE values for H_2 and D_2 dissociative adsorption were previously measured at 523-673 K and gave values that were near unity (0.7-1.0) (Chapter 3). These TIE values exhibited a weak temperature dependence and were used to calculate a TIE value at 473 K (0.63 ± 0.2). This value indicates that the assumption that H_2 and D_2 can be lumped together is not rigorously applicable. The assumption, however, leads to errors in the total combined surface coverage of H* and D* of less than 9% (calculated from simulations; Section 4.6.4). This error is within the experimental accuracy of the kinetic data and regression analyses. This assumption also allows for closed-form expressions for the rate equations (Eq. 13-14).

Equations 13 and 14 contain four parameters, three of which (k_6, $\frac{\sqrt{K_3}}{K_5}$, and $\frac{k_6}{k_{-5}}$) were previously regressed from H_2O-D_2 kinetic data (473 K, Table 2). The fourth parameter (k_4) represents the rate constant for H_2-D_2 exchange via the reaction of H_2 with D* and D_2 with H* (steps 2.9-2.10, Scheme 2) and can therefore be obtained from H_2-D_2 exchange rates in the absence of H_2O. The value of k_4 (39 ± 3 kPa^{-1} s^{-1}; Table 1) was previously measured on a sample of Pt black exposed to H_2O (Section 4.3.2). This value was used with the values of k_6, $\frac{\sqrt{K_3}}{K_5}$, and $\frac{k_6}{k_{-5}}$ (Table 2) to model HD formation and H_2O consumption rates in H_2O-H_2-D_2 mixtures (473 K) (Eq. 13-14). Figure 6 shows parity plots of these rates with the experimental data (raw data are available Section 4.6.5). The fit with the experimental data in these plots (Fig. 6) reflects a consistent mechanism for H_2-D_2 exchange (Scheme 1) under dry and wet conditions; it also reflects the flexibility and accuracy of the rate equations (Eq. 13-14) and proposed mechanism (Scheme 2) even after extensive assumptions and extrapolations.

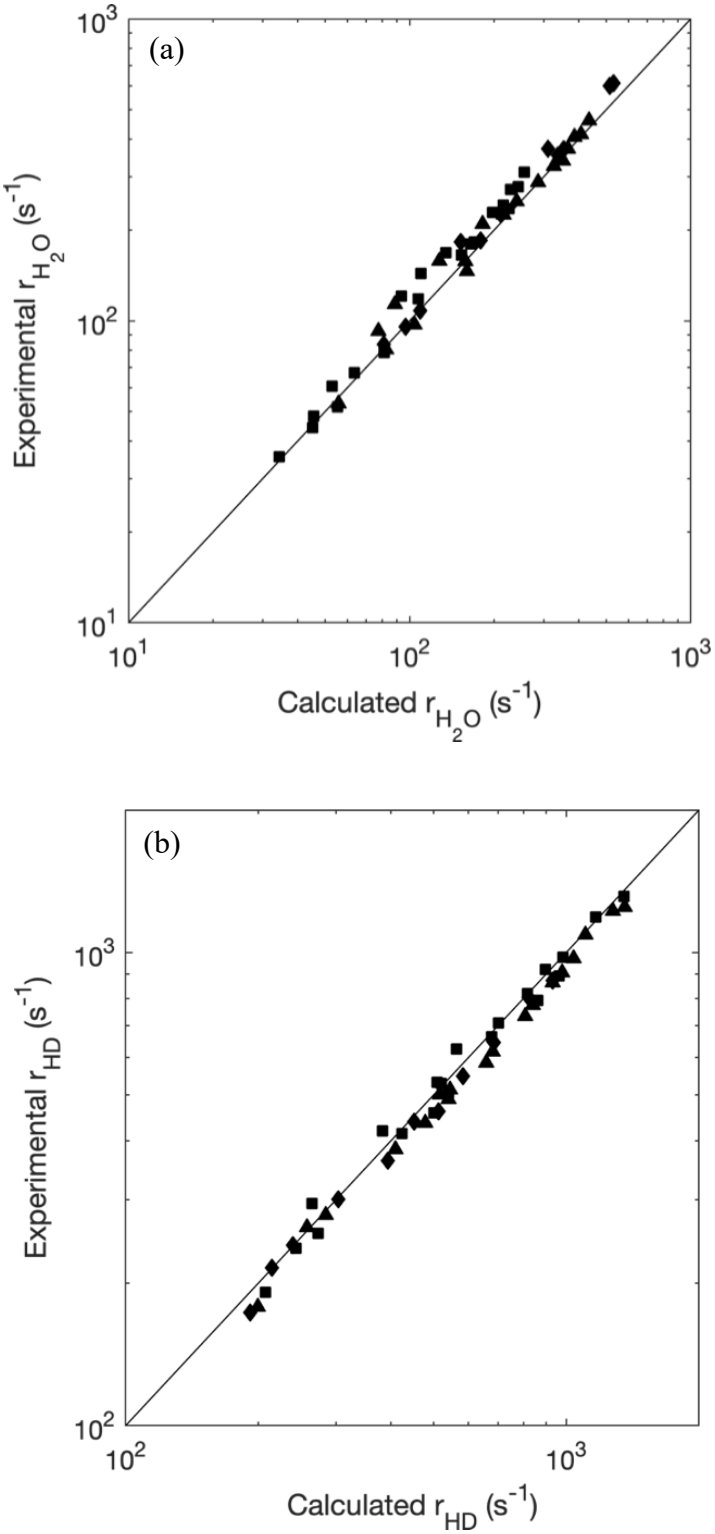

Figure 6. Parity plots of (a) H_2O conversion and (b) HD formation rates in H_2-D_2-H_2O mixtures at (■) 5, (▲) 10, and (◆) 20 kPa H_2O on Pt black (473 K). Rates are calculated using parameters regressed from H_2-D_2 and H_2O-D_2 isotopic exchange experiments.

4.3.6 Effect of Pore Condensation on HD Formation Rates in H_2O-H_2-D_2 Mixtures on Pt/γ-Al_2O_3

The presence of liquid water was previously claimed to destabilize the adsorption of H_2 on Pt surfaces,[29] but without considerations for the formation of titrating species on Pt or accurate mechanistic frameworks for H_2-D_2 and H_2O-D_2 (or D_2O-H_2) exchange reactions. Here, we probe the effects of the formation of condensed H_2O within the mesopores of Pt/γ-Al_2O_3. HD formation rates were measured in H_2-D_2-H_2O mixtures (20 kPa H_2, 20 kPa D_2) on Pt/γ-Al_2O_3 at 323 K as the H_2O pressure was varied between 0 kPa and its saturation pressure (P_0, 12.3 kPa).[66] Samples were pretreated in a H_2O-H_2 mixture (40 kPa H_2O, 2 kPa H_2) for 20 ks at 473 K prior to these measurements. H_2-D_2 exchange rates did not change with time at 323 K during any of these experiments, indicating that the surface coverage of titrating OH* or O* species (Section 4.3.2) remained stable with time.

Figure 7 shows HD formation rates and the fraction of filled pore volume as a function of H_2O pressure (expressed as P/P_0; P_0 = 12.3 kPa).[66] The H_2O isotherm was obtained using pore sizes derived from the Barrett-Joyner-Halenda equation[67] from N_2 desorption isotherms and conversion of these data using parameters for H_2O, as described in previous studies.[68] HD formation rates decreased smoothly with increasing H_2O pressure without any abrupt transitions in kinetic behavior even as significant amounts of H_2O condensed within the pores of the catalyst (~ 0.7 P/P_0, Fig. 7). This decrease in HD formation rates with increasing H_2O pressure is consistent with the competitive adsorption of molecular H_2O on Pt surfaces, which was shown to occur even at higher temperatures (473 K, Section 4.3.4). The formation of extended liquids within catalyst pores can lead to significant mass transport limitations, thereby decreasing apparent reaction rates. It can also lead to the stabilization or destabilization of adsorbed intermediates and transition states through van der Waals interactions,[68-69] resulting in significant changes in reaction rates. The absence of abrupt transitions in H_2-D_2 exchange rates as H_2O condensed within the pores of the support (Fig. 7) reflects the absence of both effects. This system demonstrates how reaction kinetics in multi-phase systems are controlled not by reactant and product concentrations, which change significantly between phases, but rather by thermodynamic properties, specifically reaction affinities and chemical potentials, which are equal in both phases (in the absence of mass transport restrictions).[40] H_2O does not influence the thermodynamics of H_2 and D_2 on Pt surfaces. It does, however, adsorb competitively, inhibiting H_2-D_2 exchange rates; H_2O also dissociates on Pt surfaces, forming a titrating OH*/O* adlayer that decreases the total available surface area for H_2/D_2 adsorption and catalytic turnovers.

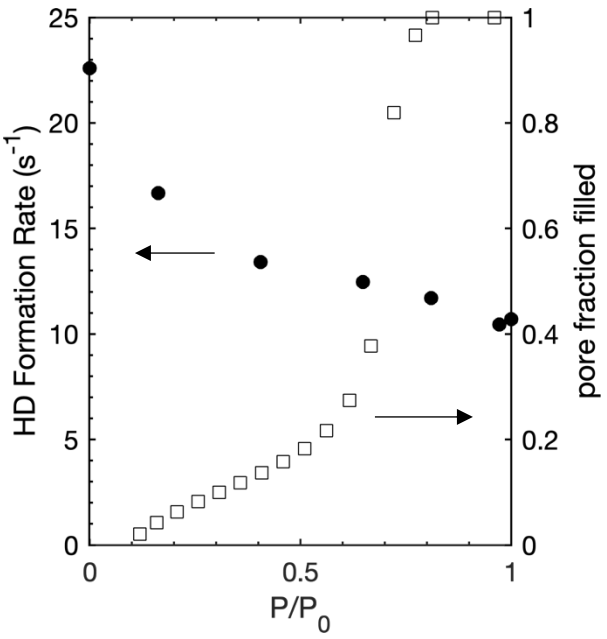

Figure 7. (●) HD formation rate and (□) pore fraction filled by H_2O (converted from N_2 desorption isotherm) vs. P/P_0 for H_2O (P_0 is the saturation pressure, 12.3 kPa) on Pt/γ-Al_2O_3 at 20 kPa H_2 and 20 kPa D_2 (323 K).

4.3.7 Effect of Temperature on H_2O-D_2 Exchange Rates

H_2O-D_2 isotopic exchange occurs primarily via the reaction between D_2 and molecularly adsorbed H_2O on Pt surfaces at 473 K (steps 2.5-2.6, Scheme 2; Section 4.3.4). H_2O and D_2 can, however, also exchange via dissociation and recombination reactions, albeit at very slow rates at this temperature; the former reaction leads to the formation of refractory OH*/O* adlayers, while the latter only occurs at temperatures above 523 K (Section 4.3.2). These slow rates are associated with the high activation energy barriers for H_2O dissociation reactions (61 kJ mol^{-1} on Pt(100) and 75 kJ mol^{-1} on Pt(111)).[51-52] These high barriers reflect a significant temperature dependence; contributions from these reactions are thus expected to become more pronounced at higher temperatures.

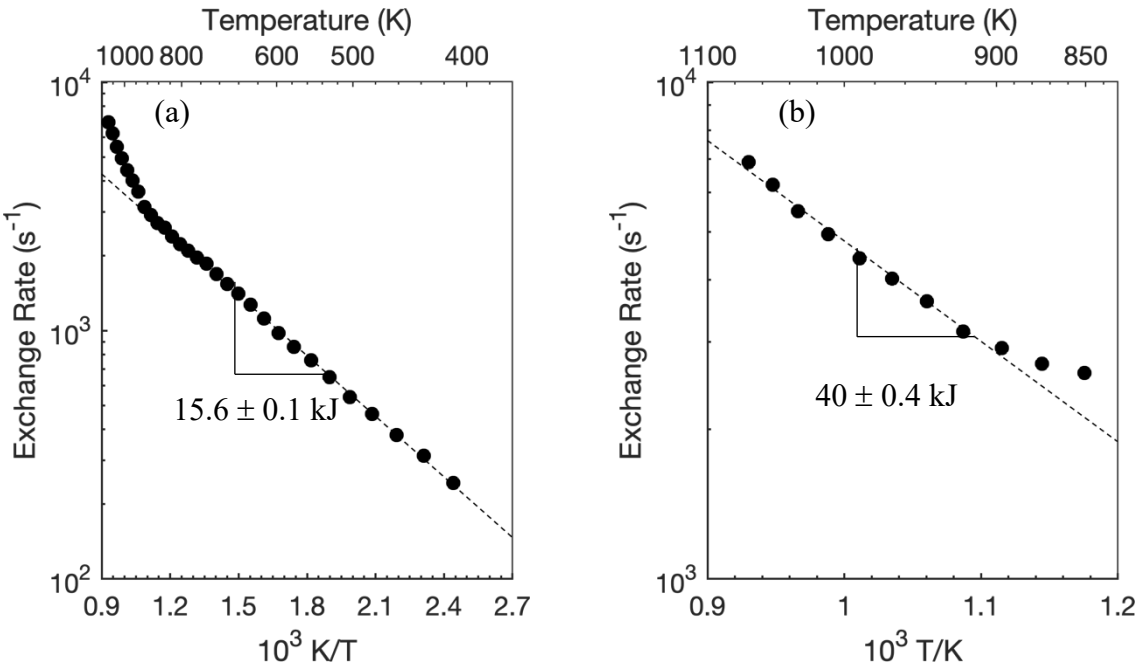

Figure 8. (a) Arrhenius plot of H_2O-D_2 isotopic exchange rates on Pt black at 5 kPa H_2O and 40 kPa D_2 between 423 and 1073 K. Dashed line represents linear regression of data between 423 and 873 K. (b) Arrhenius plot of H_2O-D_2 isotopic exchange rates on Pt black at 5 kPa H_2O and 40 kPa D_2 between 833 and 1073 K. Dashed line represents linear regression of data between 900 and 1073 K. Temperature ramped at 0.083 K s^{-1}.

H_2O-D_2 isotopic exchange rates (5 kPa H_2O, 40 kPa D_2) were measured as a function of temperature on Pt black for temperatures between 423 and 1073 K. These rates are shown as a function of temperature in Figure 8 in an Arrhenius form. The data in Figure 8 exhibit a nearly constant slope for temperatures between 423 K and 900 K, indicating a consistent mechanism for these temperatures; this slope corresponds with an apparent activation energy barrier of 15.6 ± 0.1 kJ. H_2O-D_2 exchange reactions occur via the reaction of D_2 and H_2O* (Scheme 2; Section 4.3.4) at these temperatures. The exchange rates in Figure 8 reflect the combined temperature dependences of k_6, $\frac{\sqrt{K_3}}{K_5}$, and $\frac{k_6}{k_{-5}}$ in Equation 11. The linearity of these data, however, suggest that Equation 11 can be further simplified under the prevalent reaction conditions (40 kPa D_2, 5 kPa H_2O). The value of $\frac{k_6}{k_{-5}}(D_2)$ at 473 K (0.26×10^{-1} ± 0.004; Eq. 11; Table 2) is small compared to 1, and the value of (H_2O) (5 kPa) is small compared to $\frac{\sqrt{K_3}}{K_5}\sqrt{(D_2)}$ at 473 K (98 ± 6 kPa; Eq. 11; Table 2). Equation 11 can therefore be simplified to:

$$-r_{H_2O,f} = r_{HDO,f} + r_{D_2O,f} = \frac{k_6 K_5}{\sqrt{K_3}}(H_2O)\sqrt{(D_2)} \qquad (15)$$

The apparent activation energy barrier for the data in Figure 8 (15.6 ± 0.1 kJ; 423-900 K) therefore reflects the temperature dependence of $\frac{k_6 K_5}{\sqrt{K_3}}$ (Eq. 15).

The exchange rate data at temperatures above approximately 900 K (Fig. 8b) exhibited a larger slope and corresponding activation energy barrier (40 ± 0.4 kJ) (Fig. 8). These data presumably reflect the added contributions from the dissociation and recombination pathway. A more accurate estimate of the energy barrier for the high temperature (> 900 K) reaction pathway was obtained by subtracting the contributions of the low temperature pathway (D_2-H_2O* and D_2-HDO*, steps 2.5-2.6, Scheme 2) toward measured H_2O-D_2 exchange rates at high temperature. These contributions were estimated by linearly extrapolating the exchange rates from low temperatures (423-873 K) and subtracting these rates from those observed at high temperatures (> 900 K). The resulting difference was regressed, giving an activation energy barrier of 87 ± 8 kJ mol^{-1}, a value that is similar to those previously reported for the dissociation of H_2O on (Pt(100): 61 kJ mol^{-1}, Pt(111): 75 kJ mol^{-1}).[51] These data therefore suggest that H_2O dissociation to form OH* (or O*) and D* and recombination with D* becomes the dominant pathway for H_2O-D_2 exchange at high temperatures, as predicted by theoretical insights.[51] These trends indicate that H_2O-D_2 exchange, as in the case of H_2-D_2 exchange, can take place via multiple reaction pathways depending on the prevalent reaction conditions and temperatures.

4.4 Conclusions

The adsorption and reaction of chemisorbed H_2 on metal surfaces and its interactions with co-adsorbed species have been the subject of numerous studies. This study addressed the role of H_2O adsorption and dissociation on H_2 adsorption at Pt surfaces and the kinetics of H_2O-D_2 exchange at temperatures and pressures of catalytic relevance. The results from this study showed that the presence of H_2O leads to the formation of refractory OH*/O* adlayers on Pt surfaces. These adlayers reduce the surface area available for catalytic turnovers and cannot be removed except by reaction with H_2 (or D_2) at temperatures greater than 700 K. The presence of H_2O (gas- or liquid-phase) did not lead to detectable changes in H_2-D_2 isotopic exchange pathways or the binding properties of H*/D* on Pt surfaces. The kinetics of H_2O-D_2 exchange were shown to be inconsistent with previously proposed reaction mechanisms; such mechanisms predicted exchange events on bare surfaces, contradicting extensive thermodynamic data for H_2/D_2 dissociative adsorption at these temperatures and pressures (473 K, > 5 kPa H_2). H_2O-D_2 exchange instead occurs via the reaction of D_2 and molecularly adsorbed H_2O*. This reaction pathway is reminiscent of H_2-D_2 exchange; the similarity of the rate constants for D_2-H_2O* and D_2-H* reactions may further reflect similarities in the intermediate steps and transition states, in which D_2 adsorbs dissociatively at vacancies that form in the mobile adlayers. The kinetic model proposed for H_2O-D_2 exchange reactions, in combination with the previously proposed H_2-D_2 exchange kinetic model, was able to accurately describe exchange rates in H_2O-H_2-D_2 mixtures. The results presented in this study suggest that the formation of OH*/O* from H_2O dissociation is problematic even at moderate reaction temperatures and may be a promising area of study for improvements in the efficient use of Pt-based catalytic materials within electrochemical systems.

4.5 Acknowledgments

This study was funded by Chevron Corporation and a Chevron Graduate Student Research Fellowship.

4.6 Supporting Information

4.6.1 Rate Equations and Regression Analysis for H_2O-D_2 Exchange Mechanisms Inconsistent with Kinetic and Thermodynamic Data

4.6.1.1 H_2O-D_2 Exchange via the Reaction of H_2O* and D*

The elementary steps for H_2O-D_2 exchange via the reaction between H_2O* and D* are given by Scheme SI-1.

$$H_2 + 2* \underset{k_{-3}}{\longleftarrow} 2H* \qquad \text{[SI-1.1]}$$

$$HD + 2* \underset{k_{-3}}{\longleftarrow} H* + D* \qquad \text{[SI-1.2]}$$

$$D_2 + 2* \underset{k_{-3}}{\overset{k_3}{\rightleftharpoons}} 2D* \qquad \text{[SI-1.3]}$$

$$D_2 + H* \xrightarrow{k_4} HD + D* \qquad \text{[SI-1.4]}$$

$$H_2O + * \underset{k_{-5}}{\overset{k_5}{\rightleftharpoons}} H_2O* \qquad \text{[SI-1.5]}$$

$$HDO + * \underset{k_{-5}}{\longleftarrow} HDO* \qquad \text{[SI-1.6]}$$

$$D_2O + * \underset{k_{-5}}{\longleftarrow} D_2O* \qquad \text{[SI-1.7]}$$

$$D* + H_2O* \xrightarrow{k_6} H* + HDO* \qquad \text{[SI-1.8]}$$

$$D* + HDO* \xrightarrow{k_6} H* + D_2O* \qquad \text{[SI-1.9]}$$

Scheme SI-1. Elementary steps for H_2O-D_2 isotopic exchange via the reaction of H_2O* and D*.

The rate of H_2O consumption during H_2O-D_2 exchange at conditions far from equilibrium, according to Scheme SI-1, is given by:

$$-r_{H_2O} = r_{HDO} + r_{D_2O} = k_{-5}\theta_{HDO} + k_{-5}\theta_{D_2O} \qquad (SI-1)$$

θ_i denotes the fractional coverages of the Pt surface by species *i*. The recombinative desorption of H* and D* is assumed to be slow (reverse of steps 1.1-1.3, Scheme SI-1), as shown in prior studies (Chapter 3). PSSA is applied to H*, H_2O*, HDO*, and D_2O* to give:

$$k_6\theta_{H_2O}\theta_D + \frac{1}{2}k_6\theta_{HDO}\theta_D = k_4(D_2)\theta_H + \frac{1}{2}k_6\theta_{HDO}\theta_H + k_6\theta_{D_2O}\theta_H \quad (SI-2)$$

$$k_5(H_2O)\theta_s + \frac{1}{2}k_6\theta_{HDO}\theta_H = k_{-5}\theta_{H_2O} + k_6\theta_{H_2O}\theta_D \quad (SI-3)$$

$$k_6\theta_{H_2O}\theta_D + k_6\theta_{D_2O}\theta_H = k_{-5}\theta_{HDO} + \frac{1}{2}k_6\theta_{HDO}\theta_H + \frac{1}{2}k_6\theta_{HDO}\theta_D \quad (SI-4)$$

$$k_6\theta_{HDO}\theta_D = k_{-5}\theta_{D_2O} + k_6\theta_{D_2O}\theta_H \quad (SI-5)$$

The total hydrogen adsorbed is assumed to be equilibrated:

$$K_3 = \frac{k_3}{k_{-3}} = \frac{(\theta_H + \theta_D)^2}{(D_2)\theta_s^2} \quad (SI-6)$$

Equations SI-2 – SI-6 are simplified by assuming that $\theta_H, \theta_{HDO}, \theta_{D_2O} \ll 1$:

$$k_6\theta_{H_2O}\theta_D = k_4(D_2)\theta_H \quad (SI-7)$$

$$k_5(H_2O)\theta_s = k_{-5}\theta_{H_2O} + k_6\theta_{H_2O}\theta_D \quad (SI-8)$$

$$k_6\theta_{H_2O}\theta_D = k_{-5}\theta_{HDO} + \frac{1}{2}k_6\theta_{HDO}\theta_D \quad (SI-9)$$

$$k_6\theta_{HDO}\theta_D = k_{-5}\theta_{D_2O} \quad (SI-10)$$

$$K_3 = \frac{k_3}{k_{-3}} = \frac{(\theta_H + \theta_D)^2}{(D_2)\theta_s^2} \quad (SI-11)$$

Equations SI-7 – SI-11 are solved to give:

$$\theta_H = \frac{(H_2O)\sqrt{K_3}k_5k_6\theta_s^2}{\sqrt{(D_2)}k_4k_{-5} + (D_2)\sqrt{K_3}k_4k_6\theta_s} \quad (SI-12)$$

$$\theta_D = \sqrt{(D_2)K_3}\theta_s \quad (SI-13)$$

$$\theta_{H_2O} = \frac{(H_2O)k_5\theta_s}{k_{-5} + \sqrt{(D_2)K_3}k_6\theta_s} \quad (SI-14)$$

$$\theta_{HDO} = \frac{2\sqrt{(D_2)K_3}(H_2O)k_5k_6\theta_s^2}{2k_{-5}^2 + 3\sqrt{(D_2)K_3}k_{-5}k_6\theta_s + (D_2)K_3k_6^2\theta_s^2} \quad (SI-15)$$

$$\theta_{D_2O} = \frac{2(D_2)(H_2O)K_3k_5k_6^2\theta_s^3}{2k_{-5}^3 + 3\sqrt{(D_2)K_3}k_{-5}^2k_6\theta_s + (D_2)K_3k_{-5}k_6^2\theta_s^2} \quad (SI-16)$$

Equation SI-1 can thus be written as:

$$-r_{H_2O} = k_{-5}\frac{2\sqrt{(D_2)K_3}(H_2O)k_5k_6\theta_s^2}{2k_{-5} + 3\sqrt{(D_2)K_3}k_{-5}k_6\theta_s + (D_2)K_3k_6^2\theta_s^2} + k_{-5}\frac{2(D_2)(H_2O)K_3k_5k_6^2\theta_s^3}{2k_{-5} + 3\sqrt{(D_2)K_3}k_{-5}^2k_6\theta_s + (D_2)K_3k_{-5}k_6^2\theta_s^2} \quad (SI-17)$$

θ_s is calculated separately by applying the condition of equilibrium across all water and hydrogen species and applying a site balance:

$$K_3 = \frac{\theta_D^2}{(D_2)\theta_s^2} \qquad (SI-18)$$

$$K_5 = \frac{\theta_{H_2O}}{(H_2O)\theta_s} \qquad (SI-19)$$

$$\theta_D + \theta_{H_2O} + \theta_s = 1 \qquad (SI-20)$$

to give:

$$\theta_s = \frac{1}{1 + \sqrt{(D_2)K_3} + (H_2O)K_5} \qquad (SI-21)$$

The model represented by Equations SI-17 and SI-21 was regressed to experimental H_2O-D_2 exchange rates with the regressed parameters shown in Table SI-1. The large errors in these parameters (Table SI-1) reflect the high covariance between these parameters. The accurate measurement of these parameters is therefore not possible without specifying one or more of the parameters. K_3 represents the equilibrium constant for hydrogen adsorption and was previously measured using H_2 chemisorption uptakes (of protium) at temperatures between 523-623 K.[70] These data gave enthalpies and entropies of adsorption of -35 to -65 kJ mol^{-1} and -20 to -80 J mol^{-1} K^{-1}, respectively (depending on the surface coverage).[70] The average of these values (ΔH_{ads} = -50 kJ mol^{-1}, ΔS_{ads} = -50 J mol^{-1} K^{-1}) can be used to obtain an order of magnitude approximation for the equilibrium constant for D_2 adsorption at 473 K (K_3 = 8 kPa^{-1}). This value is many orders of magnitude higher than even the upper limit (4.9×10^{-4} kPa^{-1}, 95% CI) of the regressed value (Table SI-1), indicating an inconsistency with experimental data. The extrapolated value of K_3 (8 kPa^{-1}) was therefore fixed while regressing all other parameters to check the fit of the data. These fits from regressing all parameters and from regressing parameters excluding K_3 are shown in parity plots in Figure SI-1. The poor fit of the data with the fixed value of K_3 and the inconsistency between the regressed value of K_3 ($1.1 \times 10^{-9} \pm 4.9 \times 10^{-4}$ kPa^{-1}, Table 1) and experimental K_3 values (~8 kPa^{-1}), indicate that this proposed mechanism is inconsistent with the kinetic and thermodynamic data.

Table SI-1. Regressed rate and equilibrium constants for H_2O-D_2 exchange reactions mediated by reactions between H_2O* and D* (Scheme SI-1).

Parameter	Estimate	Lower limit (95% CI)	Upper limit (95% CI)
K_3 (kPa^{-1})	1.3×10^{-7}	-6.3×10^{-3}	6.3×10^{-3}
	8 *	-	-
k_5 ($kPa^{-1}\ s^{-1}$)	3.7×10^{4}	-5.0×10^{9}	5.0×10^{9}
	8.1×10^{7} *	-1.3×10^{13}	1.3×10^{13}
k_{-5} (s^{-1})	2.0×10^{6}	-2.7×10^{11}	2.7×10^{11}
	1.3×10^{8} *	-2.1×10^{13}	2.1×10^{13}
k_6 (s^{-1})	1.4×10^{6}	-3.2×10^{10}	3.2×10^{11}
	2.3×10^{3} *	729	3.8×10^{4}

*Parameter regressed with fixed value of K_3 (8 kPa^{-1}), estimated by extrapolation of previous H_2 chemisorption data[70]

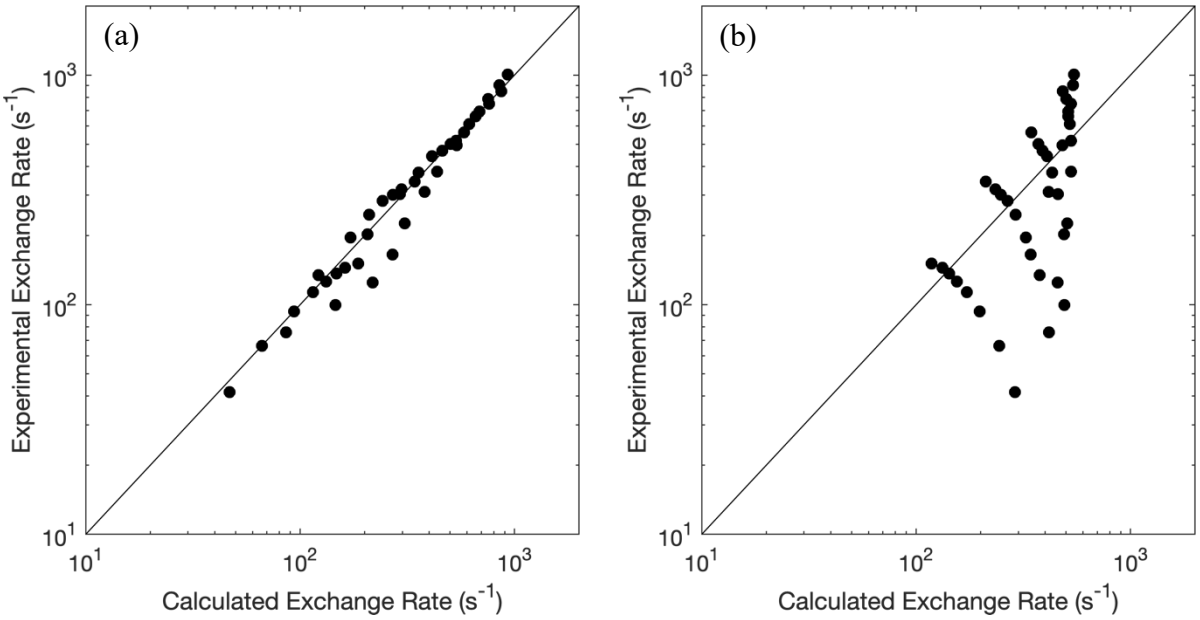

Figure SI-1. Parity plots of H_2O-D_2 exchange rates (Eq. SI-17) mediated by reactions between H_2O* and D* (Scheme SI-1) with (a) all parameters regressed and with (b) a fixed value for K_3 (8 kPa^{-1}) estimated by extrapolation of previous H_2 chemisorption data.[70]

4.6.1.2 H_2O-D_2 Exchange via the Reaction of H_2O (g) and D*

The elementary steps for H_2O-D_2 exchange via the reaction between H_2O (g) and D* are given by Scheme SI-2.

$$H_2 + 2* \underset{k_{-3}}{\longleftarrow} 2H* \quad \text{[SI-2.1]}$$

$$HD + 2* \underset{k_{-3}}{\longleftarrow} H* + D* \quad \text{[SI-2.2]}$$

$$D_2 + 2* \underset{k_{-3}}{\overset{k_3}{\rightleftharpoons}} 2D* \quad \text{[SI-2.3]}$$

$$D_2 + H* \xrightarrow{k_4} HD + D* \quad \text{[SI-2.4]}$$

$$H_2O + * \overset{K_5}{\rightleftharpoons} H_2O* \quad \text{[SI-2.5]}$$

$$D* + H_2O \xrightarrow{k_6} H* + HDO \quad \text{[SI-2.6]}$$

$$D* + HDO \xrightarrow{k_6} H* + D_2O \quad \text{[SI-2.7]}$$

Scheme SI-2. Elementary steps for H_2O-D_2 isotopic exchange via the reaction of H_2O (g) and D*. Circles on arrows denote quasi-equilibrated steps.

The rate of H_2O consumption during H_2O-D_2 exchange at conditions far from equilibrium, according to Scheme SI-2, is given by:

$$-r_{H_2O} = r_{HDO} = k_6(H_2O)\theta_D \qquad (SI-22)$$

The recombinative desorption of H* and D* is assumed to be slow (reverse of steps 2.1-2.3, Scheme SI-2), as shown in prior studies (Chapter 3). PSSA is applied to H*:

$$k_6(H_2O)\theta_D = k_4(D_2)\theta_H \qquad (SI-23)$$

The total amount of hydrogen adsorbed is assumed to be equilibrated:

$$K_3 = \frac{k_3}{k_{-3}} = \frac{(\theta_H + \theta_D)^2}{(D_2)\theta_s^2} \qquad (SI-24)$$

The adsorption of H_2O is also equilibrated (step 2.5, Scheme SI-2):

$$K_5 = \frac{\theta_{H_2O}}{(H_2O)\theta_s} \qquad (SI-25)$$

Equations SI-23 – SI-25 can be solved simultaneously to give:

$$\theta_H = \frac{\sqrt{(D_2)K_3}(H_2O)K_5k_6\theta_s^2}{(D_2)k_4 + (H_2O)K_5k_6\theta_s} \quad (SI-26)$$

$$\theta_D = \frac{\sqrt{(D_2)^3K_3}k_4\theta_s}{(D_2)k_4 + (H_2O)K_5k_6\theta_s} \quad (SI-27)$$

$$\theta_{H_2O} = \frac{(H_2O)K_5\theta_s}{k_{-5} + \sqrt{(D_2)K_3}k_6\theta_s} \quad (SI-28)$$

Equation SI-22 can thus be written as:

$$-r_{H_2O} = k_6(H_2O)\frac{\sqrt{(D_2)^3K_3}k_4\theta_s}{(D_2)k_4 + (H_2O)K_5k_6\theta_s} \quad (SI-29)$$

The model represented by Equations SI-21 and SI-29 was regressed to experimental H_2O-D_2 exchange rates with the regressed parameters shown in Table SI-2. K_3 represents the equilibrium constant for hydrogen adsorption and was previously measured using H_2 chemisorption uptakes (of protium) at temperatures between 523-623 K.[70] These data gave enthalpies and entropies of adsorption of -35 to -65 kJ mol^{-1} and -20 to -80 J mol^{-1} K^{-1}, respectively (depending on the surface coverage).[70] The average of these values (ΔH_{ads} = -50 kJ mol^{-1}, ΔS_{ads} = -50 J mol^{-1} K^{-1}) can be used to obtain an order of magnitude approximation for the equilibrium constant for D_2 adsorption at 473 K (K_3 = 8 kPa^{-1}). This value is several orders of magnitude higher than the regressed value ($6.7 \times 10^{-3} \pm 1.5 \times 10^{-3}$ kPa^{-1}) (Table SI-2), indicating an inconsistency with experimental data. The regressed value of k_4 (19.7 ± 2.1 kPa s^{-1}), which represents the rate constant for the reaction between D_2 and H* (step 1.4, Scheme SI-2) is also a factor of 2 ± 0.3 lower than the value regressed from H_2-D_2 isotopic exchange rates (39 ± 3 kPa^{-1} s^{-1}) on samples exposed to H_2O (Section 4.3.2). Thus, although the fit of the model with experimental data, shown by the parity plot in Figure SI-2, is quite good, the model is inconsistent with previous kinetic and thermodynamic data.

Table SI-2. Regressed rate and equilibrium constants for H_2O-D_2 exchange reactions mediated by reactions between H_2O (g) and D* (Scheme SI-2).

Parameter	Estimate	Lower limit (95% CI)	Upper limit (95% CI)
K_3 (kPa^{-1})	6.7×10^{-3}	5.2×10^{-3}	8.2×10^{-3}
k_4 (kPa^{-1} s^{-1})	19.7	17.6	21.8
K_5 (kPa^{-1})	7.4×10^{-2}	7.1×10^{-2}	7.7×10^{-2}
k_6 (s^{-1})	200	185	214

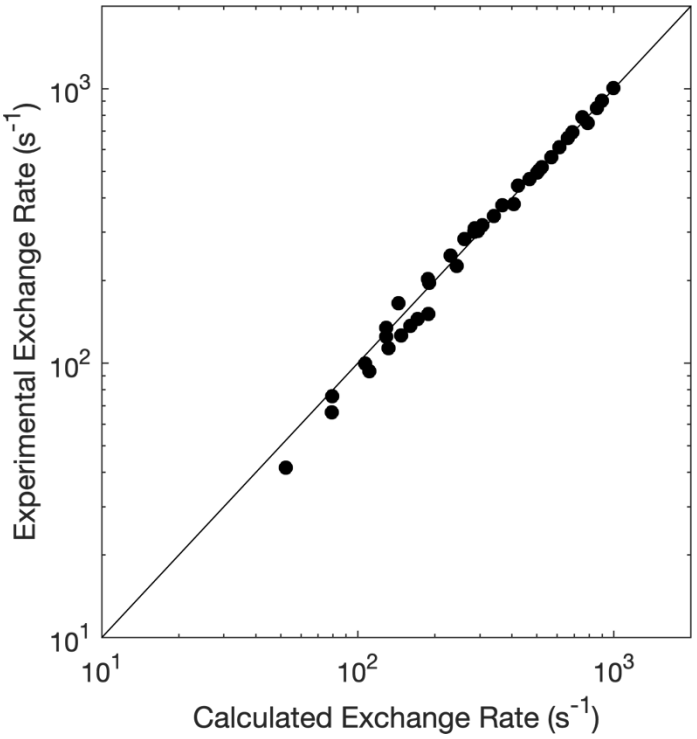

Figure SI-2. Parity plot of H_2O-D_2 exchange rates mediated by reactions between H_2O (g) and D* (Scheme SI-2).

4.6.1.3 H_2O-D_2 Exchange via the Reaction of H_2O' and D* (* and ' Denote Distinct Sites)

The elementary steps for the proposed mechanism are given by Scheme SI-3.

$$H_2 + 2* \underset{k_{-3}}{\longleftarrow} 2H* \quad [SI\text{-}3.1]$$

$$HD + 2* \underset{k_{-3}}{\longleftarrow} H* + D* \quad [SI\text{-}3.2]$$

$$D_2 + 2* \underset{k_{-3}}{\overset{k_3}{\rightleftharpoons}} 2D* \quad [SI\text{-}3.3]$$

$$D_2 + H* \xrightarrow{k_4} HD + D* \quad [SI\text{-}3.4]$$

$$H_2O + ' \underset{k_{-5}}{\overset{k_5}{\rightleftharpoons}} H_2O' \quad [SI\text{-}3.5]$$

$$HDO + ' \underset{k_{-5}}{\longleftarrow} HDO' \quad [SI\text{-}3.6]$$

$$D_2O + ' \underset{k_{-5}}{\longleftarrow} D_2O' \quad [SI\text{-}3.7]$$

$$D* + H_2O' \xrightarrow{k_6} H* + HDO' \quad [SI\text{-}3.8]$$

$$D* + HDO' \xrightarrow{k_6} H* + D_2O' \quad [SI\text{-}3.9]$$

Scheme SI-3. Elementary steps for H_2O-D_2 isotopic exchange via the reaction of H_2O' and D* (* and ' denote distinct sites)

The rate of H_2O consumption during H_2O-D_2 exchange at conditions far from equilibrium, according to Scheme SI-3, is given by:

$$-r_{H_2O} = r_{HDO} + r_{D_2O} = k_{-5}\theta_{HDO} + k_{-5}\theta_{D_2O} \qquad (SI-30)$$

The recombinative desorption of H* and D* is assumed to be slow (reverse of steps 3.1-3.3, Scheme SI-3), as shown in prior studies (Chapter 3). PSSA is applied to H*, D*, H_2O', HDO', and D_2O':

$$k_6\theta'_{H_2O}\theta_D + \frac{1}{2}k_6\theta'_{HDO}\theta_D = k_4(D_2)\theta_H + \frac{1}{2}k_6\theta'_{HDO}\theta_H + k_6\theta'_{D_2O}\theta_H \qquad (SI-31)$$

$$k_5(H_2O)\theta'_s + \frac{1}{2}k_6\theta'_{HDO}\theta_H = k_{-5}\theta'_{H_2O} + k_6\theta'_{H_2O}\theta_D \qquad (SI-32)$$

$$k_6\theta'_{H_2O}\theta_D + k_6\theta'_{D_2O}\theta_H = k_{-5}\theta'_{HDO} + \frac{1}{2}k_6\theta'_{HDO}\theta_H + \frac{1}{2}k_6\theta'_{HDO}\theta_D \qquad (SI-33)$$

$$k_6\theta'_{HDO}\theta_D = k_{-5}\theta'_{D_2O} + k_6\theta'_{D_2O}\theta_H \quad (SI-34)$$

Here, θ_i and θ'_i denote distinct non-interacting sites. The total hydrogen adsorbed is assumed to be equilibrated:

$$K_3 = \frac{k_3}{k_{-3}} = \frac{(\theta_H + \theta_D)^2}{(D_2)\theta_s^2} \quad (SI-35)$$

Equations SI-31 – SI-35 can be further simplified by also assuming that $\theta_H, \theta'_{HDO}, \theta'_{D_2O} \ll 1$:

$$k_6\theta'_{H_2O}\theta_D = k_4(D_2)\theta_H \quad (SI-36)$$

$$k_5(H_2O)\theta'_s = k_{-5}\theta'_{H_2O} + k_6\theta'_{H_2O}\theta_D \quad (SI-37)$$

$$k_6\theta'_{H_2O}\theta_D = k_{-5}\theta'_{HDO} + \frac{1}{2}k_6\theta'_{HDO}\theta_D \quad (SI-38)$$

$$k_6\theta'_{HDO}\theta_D = k_{-5}\theta'_{D_2O} \quad (SI-39)$$

$$K_3 = \frac{k_3}{k_{-3}} = \frac{(\theta_D)^2}{(D_2)\theta_s^2} \quad (SI-40)$$

Equations SI-36 – SI-40 can be solved simultaneously to give:

$$\theta_H = \frac{(H_2O)\sqrt{K_3}k_5k_6\theta_s\theta'_s}{\sqrt{(D_2)}k_4k_{-5} + (D_2)\sqrt{K_3}k_4k_6\theta_s} \quad (SI-41)$$

$$\theta_D = \sqrt{(D_2)K_3}\theta_s \quad (SI-42)$$

$$\theta_{H_2O} = \frac{(H_2O)k_5\theta'_s}{k_{-5} + \sqrt{(D_2)K_3}k_6\theta_s} \quad (SI-43)$$

$$\theta_{HDO} = \frac{2\sqrt{(D_2)K_3}(H_2O)k_5k_6\theta_s\theta'_s}{2k_{-5}^2 + 3\sqrt{(D_2)K_3}k_{-5}k_6\theta_s + (D_2)K_3k_6^2\theta_s^2} \quad (SI-44)$$

$$\theta_{D_2O} = \frac{2(D_2)(H_2O)K_3k_5k_6^2\theta_s^2\theta_p}{2k_{-5}^3 + 3\sqrt{(D_2)K_3}k_{-5}^2k_6\theta_s + (D_2)K_3k_{-5}k_6^2\theta_s^2} \quad (SI-45)$$

Equation SI-30 can thus be written as:

$$-r_{H_2O} = k_{-5}\frac{2\sqrt{(D_2)K_3}(H_2O)k_5k_6\theta_s\theta'_s}{2k_{-5}^2 + 3\sqrt{(D_2)K_3}k_{-5}k_6\theta_s + (D_2)K_3k_6^2\theta_s^2} + k_{-5}\frac{2(D_2)(H_2O)K_3k_5k_6^2\theta_s^2\theta_p}{2k_{-5}^3 + 3\sqrt{(D_2)K_3}k_{-5}^2k_6\theta_s + (D_2)K_3k_{-5}k_6^2\theta_s^2} \quad (SI-46)$$

θ_s is calculated separately by applying the condition of equilibrium on all hydrogen species and applying a site balance:

$$K_3 = \frac{\theta_D^2}{(D_2)\theta_s^2} \quad (SI-47)$$

$$\theta_D + \theta_s = 1 \quad (SI-48)$$

to give:

$$\theta_s = \frac{1}{1 + \sqrt{(D_2)K_3}} \qquad (SI-49)$$

θ_s' is calculated separately by applying the condition of equilibrium on all water species and applying a site balance:

$$K_5 = \frac{\theta_{H_2O}}{(H_2O)\theta_s'} \qquad (SI-50)$$

$$\theta_{H_2O} + \theta_s' = 1 \qquad (SI-51)$$

to give:

$$\theta_s' = \frac{1}{1 + K_5(H_2O)} \qquad (SI-52)$$

The model represented by Equations SI-46, SI-49, and SI-52 was regressed to experimental H_2O-D_2 exchange rates. The regressed parameters are shown in Table SI-3. The large errors in these parameters (Table SI-3) reflect the high covariance between these parameters. The accurate measurement of these parameters is therefore not possible without specifying one or more of the parameters or obtaining additional data at conditions difficult to access experimentally. K_3 represents the equilibrium constant for hydrogen adsorption and was previously measured using H_2 chemisorption uptakes (of protium) at temperatures between 523-623 K.[70] These data gave enthalpies and entropies of adsorption of -35 to -65 kJ mol^{-1} and -20 to -80 J mol^{-1} K^{-1}, respectively (depending on the surface coverage).[70] The average of these values (ΔH_{ads} = -50 kJ mol^{-1}, ΔS_{ads} = -50 J mol^{-1} K^{-1}) can be used to obtain an order of magnitude approximation for the equilibrium constant for D_2 adsorption at 473 K (K_3 = 8 kPa^{-1}). This value is many orders of magnitude higher than even the upper limit (7.5×10^{-5} kPa^{-1}, 95% CI) of the regressed value (Table SI-3), indicating an inconsistency with experimental data. The extrapolated value of K_3 (8 kPa^{-1}) was therefore fixed while regressing all other parameters to check the fit of the data. These fits from regressing all parameters and from regressing parameters excluding K_3 are shown in parity plots in Figure SI-3. The poor fit of the data with the fixed value of K_3 and the inconsistency between the regressed value of K_3 ($5.1 \times 10^{-10} \pm 7.5 \times 10^{-5}$ kPa^{-1}, Table 1) and experimental K_3 values (~8 kPa^{-1}), indicate that this proposed mechanism is inconsistent with the kinetic and thermodynamic data.

Table SI-3. Regressed rate and equilibrium constants for H_2O-D_2 exchange reactions mediated by reactions between H_2O' and D* (Scheme SI-3).

Parameter	Estimate	Lower limit (95% CI)	Upper limit (95% CI)
K_3 (kPa^{-1})	5.1×10^{-10}	-7.5×10^{-5}	7.5×10^{-5}
	8 *	-	-
k_5 ($kPa^{-1}\ s^{-1}$)	3.9×10^{5}	-5.0×10^{10}	5.0×10^{10}
	8.3×10^{5} *	-1.3×10^{10}	1.3×10^{10}
k_{-5} (s^{-1})	6.5×10^{6}	-8.2×10^{11}	8.2×10^{11}
	1.1×10^{7} *	-1.7×10^{11}	1.7×10^{11}
k_6 (s^{-1})	7.6×10^{6}	-5.6×10^{11}	-5.6×10^{11}
	905 *	330	1.5×10^{3}

*Parameter regressed with fixed value of K_3 (8 kPa^{-1}), estimated by extrapolation of previous H_2 chemisorption data[70]

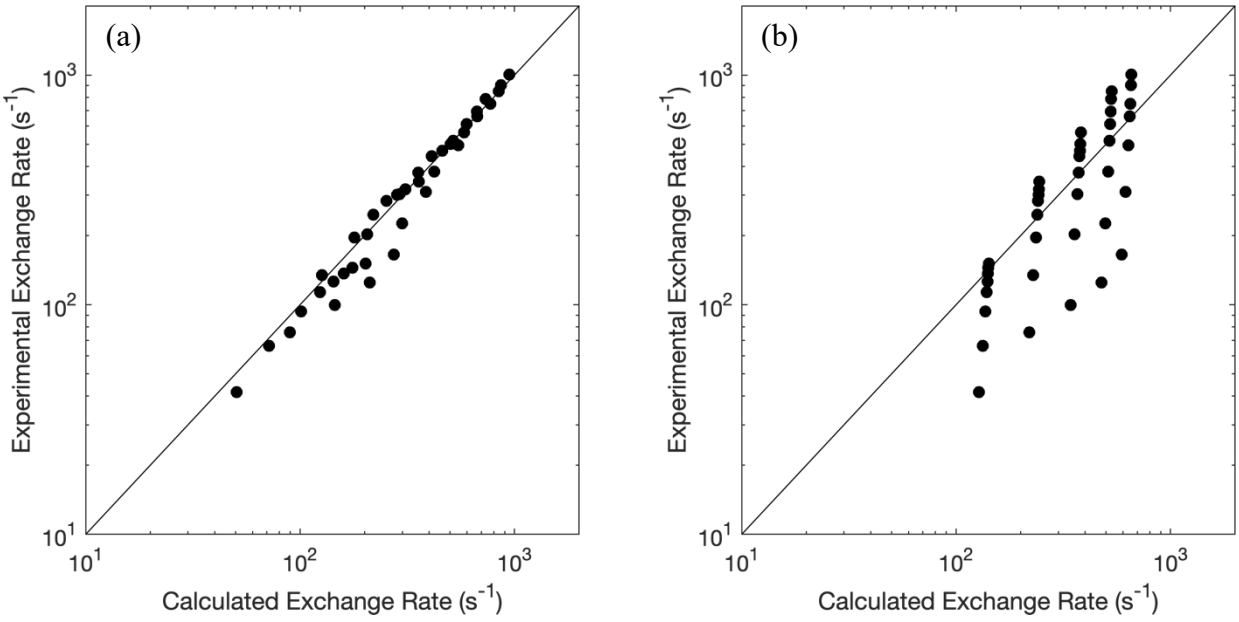

Figure SI-3. Parity plots of H_2O-D_2 exchange rates (Eq. SI-46) mediated by reactions between H_2O' and D* (Scheme SI-3) with (a) all parameters regressed and with (b) a fixed value for K_3 (8 kPa^{-1}) estimated by extrapolation of previous H_2 chemisorption data.[70]

4.6.1.4 H_2O-D_2 Exchange via the Dissociation and Recombination of Water

The elementary steps for H_2O-D_2 exchange reactions via the dissociation of H_2O to form OH* and H* and recombination between OH* and D* are given in Scheme SI-4.

$$H_2 + 2* \underset{k_{-1}}{\longleftarrow} 2H* \quad [SI\text{-}4.1]$$

$$HD + 2* \underset{k_{-2}}{\longleftarrow} H* + D* \quad [SI\text{-}4.2]$$

$$D_2 + 2* \underset{k_{-3}}{\overset{k_3}{\rightleftharpoons}} 2D* \quad [SI\text{-}4.3]$$

$$D_2 + H* \xrightarrow{k_4} HD + D* \quad [SI\text{-}4.4]$$

$$H_2O + * \underset{k_{-5}}{\overset{k_5}{\rightleftharpoons}} H_2O* \quad [SI\text{-}4.5]$$

$$HDO + * \underset{k_{-5}}{\longleftarrow} HDO* \quad [SI\text{-}4.6]$$

$$D_2O + * \underset{k_{-5}}{\longleftarrow} D_2O* \quad [SI\text{-}4.7]$$

$$H_2O* + * \underset{k_{-6}}{\overset{k_6}{\rightleftharpoons}} H* + OH* \quad [SI\text{-}4.8]$$

$$HDO* + * \underset{k_{-6}}{\overset{k_6}{\rightleftharpoons}} H* + OD* \quad [SI\text{-}4.9]$$

$$HDO* + * \underset{k_{-6}}{\overset{k_6}{\rightleftharpoons}} D* + OH* \quad [SI\text{-}4.10]$$

$$D_2O* + * \underset{k_{-6}}{\overset{k_6}{\rightleftharpoons}} D* + OD* \quad [SI\text{-}4.11]$$

Scheme SI-4. Elementary steps for H_2O-D_2 isotopic exchange via the dissociation and recombination of H_2O.

The rate of H_2O consumption during H_2O-D_2 exchange at conditions far from equilibrium, according to Scheme SI-4, is given by:

$$-r_{H_2O} = r_{HDO} + r_{D_2O} = k_{-5}\theta_{HDO} + k_{-5}\theta_{D_2O} \qquad (SI-53)$$

The recombinative desorption of H* and D* is assumed to be slow (reverse of steps 4.1-4.3, Scheme SI-4), as shown in prior studies (Chapter 3). PSSA is applied to H*, H_2O*, HDO*, D_2O*, OH*, and OD*:

$$k_6\theta_{H_2O}\theta_s + \frac{1}{2}k_6\theta_{HDO}\theta_s = k_4(D_2)\theta_H + k_{-6}\theta_H\theta_{OH} + k_{-6}\theta_H\theta_{OD} \quad (SI-54)$$

$$k_5(H_2O)\theta_s + k_{-6}\theta_H\theta_{OH} = k_{-5}\theta_{H_2O} + k_6\theta_{H_2O}\theta_s \quad (SI-55)$$

$$k_{-6}\theta_H\theta_{OD} + k_{-6}\theta_D\theta_{OH} = k_{-5}\theta_{HDO} + k_6\theta_{HDO}\theta_s \quad (SI-56)$$

$$k_{-6}\theta_D\theta_{OD} = k_{-5}\theta_{D_2O} + k_6\theta_{D_2O}\theta_s \quad (SI-57)$$

$$k_6\theta_{H_2O}\theta_s + \frac{1}{2}k_6\theta_{HDO}\theta_s = k_{-6}\theta_H\theta_{OD} + k_{-6}\theta_D\theta_{OH} \quad (SI-58)$$

$$\frac{1}{2}k_6\theta_{HDO}\theta_s + k_6\theta_{D_2O}\theta_s = k_{-6}\theta_H\theta_{OD} + k_{-6}\theta_D\theta_{OD} \quad (SI-59)$$

The total hydrogen adsorbed is assumed to be equilibrated:

$$K_3 = \frac{k_3}{k_{-3}} = \frac{(\theta_H + \theta_D)^2}{(D_2)\theta_s^2} \quad (SI-60)$$

Equations SI-54 – SI-59 can be simplified by assuming that the adsorption of H_2O (step 4.5, Scheme 4) is quasi-equilibrated and $\theta_H, \theta_{HDO}, \theta_{D_2O} \ll 1$:

$$k_6\theta_{H_2O}\theta_s = k_4(D_2)\theta_H + k_{-6}\theta_H\theta_{OH} \quad (SI-61)$$

$$k_5(H_2O)\theta_s = k_{-5}\theta_{H_2O} \quad (SI-62)$$

$$k_{-6}\theta_D\theta_{OH} = k_{-5}\theta_{HDO} + k_6\theta_{HDO}\theta_s \quad (SI-63)$$

$$k_{-6}\theta_D\theta_{OD} = k_{-5}\theta_{D_2O} + k_6\theta_{D_2O}\theta_s \quad (SI-64)$$

$$k_6\theta_{H_2O}\theta_s = k_{-6}\theta_D\theta_{OH} \quad (SI-65)$$

$$\frac{1}{2}k_6\theta_{HDO}\theta_s + k_6\theta_{D_2O}\theta_s = k_{-6}\theta_D\theta_{OD} \quad (SI-66)$$

$$K_3 = \frac{k_3}{k_{-3}} = \frac{(\theta_D)^2}{(D_2)\theta_s^2} \quad (SI-67)$$

Equations SI-61 – SI-67 can be solved simultaneously to give:

$$\theta_H = \frac{\sqrt{(D_2)K_3}(H_2O)k_5k_6\theta_s^2}{\sqrt{(D_2)^3K_3}k_4k_{-5} + (H_2O)k_5k_6\theta_s} \quad (SI-68)$$

$$\theta_D = \sqrt{(D_2)K_3}\theta_s \quad (SI-69)$$

$$\theta_{H_2O} = K_5(H_2O)\theta_s \quad (SI-70)$$

$$\theta_{HDO} = \frac{(H_2O)k_5k_6\theta_s^2}{k_{-5}^2 + k_{-5}k_6\theta_s} \quad (SI-71)$$

$$\theta_{D_2O} = \frac{(H_2O)k_5k_6^2\theta_s^3}{2k_{-5}^2(k_{-5} + k_6\theta_s)} \quad (SI-72)$$

$$\theta_{OH} = \frac{(H_2O)k_5k_6\theta_s}{\sqrt{(D_2)K_3}k_{-5}k_{-6}} \quad (SI-73)$$

$$\theta_{OD} = \frac{(H_2O)k_5k_6^2\theta_s^2}{2\sqrt{(D_2)K_3}k_{-5}^2k_{-6}} \quad (SI-74)$$

Equation SI-53 can thus be written as:

$$-r_{H_2O} = k_{-5}\frac{(H_2O)k_5k_6\theta_s^2}{k_{-5}^2 + k_{-5}k_6\theta_s} + k_{-5}\frac{(H_2O)k_5k_6^2\theta_s^3}{2k_{-5}^2(k_{-5} + k_6\theta_s)} \quad (SI-75)$$

θ_s is calculated separately by applying the condition of equilibrium across all water, hydrogen, and hydroxyl (OH*) species and applying a site balance:

$$K_3 = \frac{\theta_H^2}{(H_2)\theta_s^2} \quad (SI-76)$$

$$K_5 = \frac{\theta_{H_2O}}{(H_2O)\theta_s} \quad (SI-77)$$

$$K_6 = \frac{\theta_{OH}\theta_H}{\theta_{H_2O}\theta_s} \quad (SI-78)$$

$$\theta_H + \theta_{H_2O} + \theta_{OH} + \theta_s = 1 \quad (SI-79)$$

to give:

$$\theta_s = \frac{(H_2)(K_3 - (H_2O)K_3K_5) - \sqrt{(H_2)K_3\left((H_2)K_3 + (H_2O)K_5K_6\right)^2}}{(H_2)K_3\left(1 + (H_2O)^2K_5^2 - 2(H_2O)K_5(K_6 - 1)\right) - (H_2O)^2K_5^2K_6^2 - (H_2)^2K_3^2} \quad (SI-80)$$

Equation SI-54 applies for all dihydrogen and water species and can therefore be also written as:

$$\theta_s = \frac{(D_2)(K_3 - (H_2O)K_3K_5) - \sqrt{(D_2)K_3\left((D_2)K_3 + (H_2O)K_5K_6\right)^2}}{(D_2)K_3\left(1 + (H_2O)^2K_5^2 - 2(H_2O)K_5(K_6 - 1)\right) - (H_2O)^2K_5^2K_6^2 - (D_2)^2K_3^2} \quad (SI-81)$$

The model represented by Equations SI-75 and SI-81 was regressed to experimental H_2O-D_2 exchange rates. The regressed parameters are shown in Table SI-4. The large errors in these parameters (Table SI-4) reflect the high covariance between these parameters. The accurate measurement of these parameters is therefore not possible without specifying one or more of the parameters or obtaining additional data at conditions difficult to access experimentally. K_3 represents the equilibrium constant for hydrogen adsorption and was previously measured using H_2 chemisorption uptakes (of protium) at temperatures between 523-623 K.[70] These data gave enthalpies and entropies of adsorption of -35 to -65 kJ mol^{-1} and -20 to -80 J mol^{-1} K^{-1}, respectively (depending on the surface coverage).[70] The average of these values (ΔH_{ads} = -50 kJ mol^{-1}, ΔS_{ads} = -50 J mol^{-1} K^{-1}) can be used to obtain an order of magnitude approximation for the equilibrium constant for D_2 adsorption at 473 K (K_3 = 8 kPa^{-1}). This value is many orders of magnitude higher than even the upper limit (3.1×10^{-7} kPa^{-1}, 95% CI) of the regressed value (Table SI-4), indicating an inconsistency with experimental data. The extrapolated value of K_3 (8 kPa^{-1}) was therefore fixed while regressing all other parameters to check the fit of the data. These fits

from regressing all parameters and from regressing parameters excluding K_3 are shown in parity plots in Figure SI-4. The poor fit of the data with the fixed value of K_3 and the inconsistency between the regressed value of K_3 ($4.6 \times 10^{-11} \pm 3.1 \times 10^{-4}$ kPa^{-7}, Table SI-4) and experimental K_3 values (~8 kPa^{-1}), indicate that this proposed mechanism is inconsistent with the kinetic and thermodynamic data.

Table SI-4. Regressed rate and equilibrium constants for H_2O-D_2 exchange reactions mediated by H_2O dissociation and OH*-D* recombination (Scheme SI-4).

Parameter	Estimate	Lower limit (95% CI)	Upper limit (95% CI)
K_3 (kPa^{-1})	4.6×10^{-11}	-3.1×10^{-7}	3.1×10^{-7}
	8 *	-	-
k_5 (kPa^{-1} s^{-1})	0.34	-2.1	2.8
	1.2×10^{-4} *	-	-
k_{-5} (s^{-1})	6.7×10^{4}	-1.2×10^{8}	1.2×10^{8}
	1.9×10^{3} *	-	
k_6 (s^{-1})	3.3×10^{7}	-6.1×10^{10}	6.1×10^{10}
	6.8×10^{10} *	-	-
k_{-6} (s^{-1})	4.4×10^{7}	-1.5×10^{11}	1.5×10^{11}
	89 *	80	98

*Parameter regressed with fixed value of K_3 (8 kPa^{-1}), estimated by extrapolation of previous H_2 chemisorption data[70]

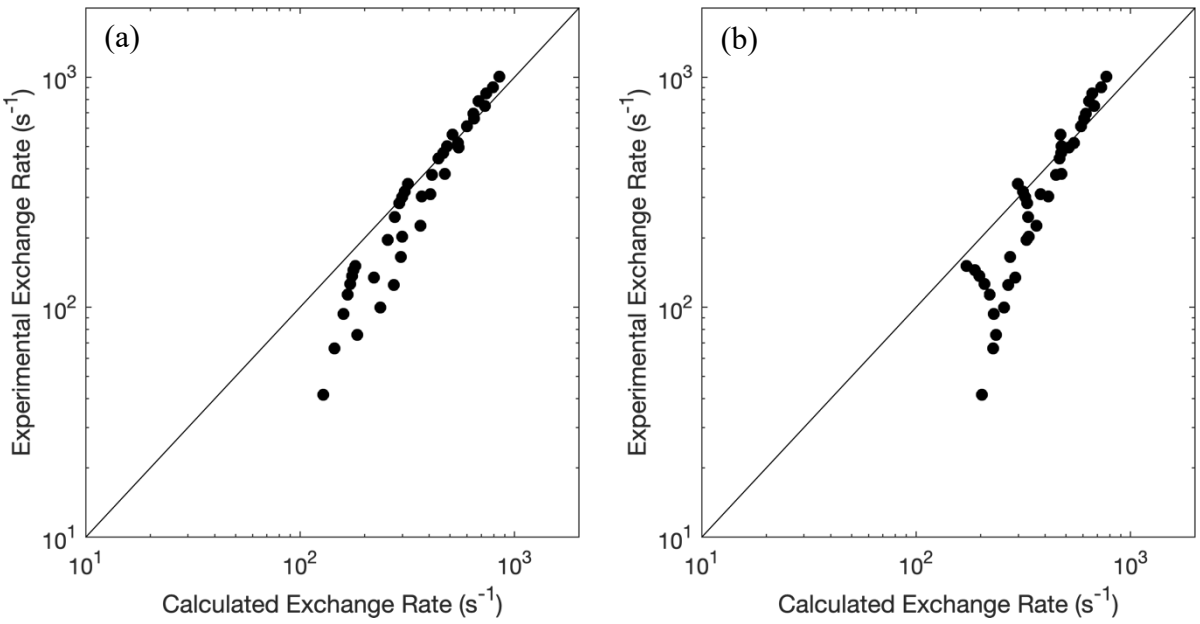

Figure SI-4. Parity plot of H_2O-D_2 exchange rates mediated by H_2O dissociation and recombination reactions (Scheme SI-4) with (a) all parameters regressed and with (b) a fixed value for K_3 (8 kPa^{-1}) estimated by extrapolation of previous H_2 chemisorption data.[70]

4.6.2 Derivation of Rate Equations for H_2O-D_2 and H_2O-H_2-D_2 Exchange Reactions Mediated by the Reaction of D_2 and H_2O*

4.6.2.1 Derivation of Rate Equation for HD Formation and H_2O Consumption in H_2O-D_2 Mixtures

H_2O-D_2 Exchange Elementary Steps

$$D_2 + 2* \underset{k_{-3}}{\overset{k_3}{\rightleftharpoons}} 2D* \quad \text{[SI-5.1]}$$

$$H_2O + * \underset{k_{-5}}{\overset{k_5}{\rightleftharpoons}} H_2O* \quad \text{[SI-5.2]}$$

$$HDO + * \underset{k_{-5}}{\overset{}{\leftarrow}} HDO* \quad \text{[SI-5.3]}$$

$$D_2O + * \underset{k_{-5}}{\overset{}{\leftarrow}} D_2O* \quad \text{[SI-5.4]}$$

$$D_2 + H_2O* \xrightarrow{k_6} HD + HDO* \quad \text{[SI-5.5]}$$

$$D_2 + HDO* \xrightarrow{k_6} HD + D_2O* \quad \text{[SI-5.6]}$$

Additional Steps for H_2O-H_2-D_2 Exchange

$$H_2 + 2* \underset{k_{-1}}{\overset{k_1}{\rightleftharpoons}} 2H* \quad \text{[SI-5.7]}$$

$$HD + 2* \underset{k_{-2}}{\overset{}{\leftarrow}} H* + D* \quad \text{[SI-5.8]}$$

$$H_2 + D* \xrightarrow{k_4} HD + H* \quad \text{[SI-5.9]}$$

$$D_2 + H* \xrightarrow{k_4} HD + D* \quad \text{[SI-5.10]}$$

$$H_2 + HDO* \xrightarrow{k_6} HD + H_2O* \quad \text{[SI-5.11]}$$

$$H_2 + D_2O* \xrightarrow{k_6} HD + HDO* \quad \text{[SI-5.12]}$$

Scheme SI-5. Elementary steps for H_2O-D_2 and H_2O-H_2-D_2 isotopic exchange.[3]

[3] Scheme SI-5 is identical to Scheme 2 in the main text.

Scheme SI-5 shows the elementary steps for H_2O-D_2 reactions mediated by the reaction of D_2 and H_2O*. The rate of H_2O consumption during H_2O-D_2 exchange at conditions far from equilibrium, according to Scheme SI-5, is given by:

$$-r_{H_2O} = r_{HDO} + r_{D_2O} = k_{-5}\theta_{HDO} + k_{-5}\theta_{D_2O} \qquad (SI-79)$$

θ_i denotes the fractional coverages of the Pt surface by species *i*. These fractional coverages are found by applying the pseudo-steady-state approximation to H_2O*, HDO*, D_2O*, and D*:

$$k_5(H_2O)\theta_s = k_{-5}\theta_{H_2O} + k_6(D_2)\theta_{H_2O} \qquad (SI-80)$$

$$k_6(D_2)\theta_{H_2O} = k_{-5}\theta_{HDO} + \frac{1}{2}k_6(D_2)\theta_{HDO} \qquad (SI-81)$$

$$\frac{1}{2}k_6(D_2)\theta_{HDO} = k_{-5}\theta_{D_2O} \qquad (SI-82)$$

$$k_3(D_2)\theta_s^2 = k_{-3}\theta_D^2 \qquad (SI-83)$$

Equations SI-80 – SI-83 can be solved simultaneously with the assumption that the surface is covered:

$$\theta_{H_2O} + \theta_{HDO} + \theta_{D_2O} + \theta_D = 1 \qquad (SI-84)$$

to give the following expressions:

$$\theta_{H_2O} = \frac{(H_2O)}{\left((H_2O) + \frac{\sqrt{K_1}}{K_3}\sqrt{(D_2)}\right)\left(1 + \frac{k_6}{k_{-5}}(D_2)\right)} \qquad (SI-85)$$

$$\theta_{HDO} = \frac{2\frac{k_6}{k_{-5}}(D_2)(H_2O)}{\left((H_2O) + \frac{\sqrt{K_3}}{K_5}\sqrt{(D_2)}\right)\left(2 + 3\frac{k_6}{k_{-5}}(D_2) + \frac{k_6^2}{k_{-5}^2}(D_2)^2\right)} \qquad (SI-86)$$

$$\theta_{D_2O} = \frac{\frac{k_6^2}{k_{-5}^2}(D_2)^2(H_2O)}{\left((H_2O) + \frac{\sqrt{K_3}}{K_5}\sqrt{(D_2)}\right)\left(2 + 3\frac{k_6}{k_{-5}}(D_2) + \frac{k_6^2}{k_{-5}^2}(D_2)^2\right)} \qquad (SI-87)$$

$$\theta_D = \frac{\sqrt{K_3}\sqrt{(D_2)}}{\left(K_5(H_2O) + \sqrt{K_3}\sqrt{(D_2)}\right)} \qquad (SI-88)$$

$$\theta_s = \frac{1}{\left(K_5(H_2O) + \sqrt{K_3}\sqrt{(D_2)}\right)} \qquad (SI-89)$$

Equation SI-79 can therefore be rewritten as:

$$-r_{H_2O,f} = r_{HDO,f} + r_{D_2O,f} = \frac{k_6(H_2O)(D_2)}{\left((H_2O) + \frac{\sqrt{K_3}}{K_5}\sqrt{(D_2)}\right)\left(1 + \frac{k_6}{k_{-5}}(D_2)\right)} \qquad (SI-90)$$

4.6.2.2 Derivation of Rate Equation for HD Formation and H_2O Consumption in H_2O-H_2-D_2 Mixtures

The rates of HD formation and H_2O consumption during H_2O-H_2-D_2 exchange reactions at conditions far from equilibrium, according to Scheme SI-5 are given by:

$$r_{HD} = k_4(D_2)\theta_H + k_4(H_2)\theta_D + k_6(D_2)\theta_{H_2O} + \frac{1}{2}k_6(D_2)\theta_{HDO} + \frac{1}{2}k_6(H_2)\theta_{HDO} + k_6(H_2)\theta_{D_2O} \quad (SI-91)$$

$$-r_{H_2O} = r_{HDO} + r_{D_2O} = k_{-5}\theta_{HDO} + k_{-5}\theta_{D_2O} \quad (SI-92)$$

The fractional coverages are found by applying the pseudo-steady-state approximation to H*, D*, H_2O*, HDO*, and D_2O*:

$$2k_1(H_2)\theta_s^2 + k_4(H_2)\theta_D = k_{-1}\theta_H^2 + k_{-2}\theta_H\theta_D + k_4(D_2)\theta_H \quad (SI-93)$$

$$2k_3(D_2)\theta_s^2 + k_4(D_2)\theta_H = k_{-2}\theta_H\theta_D + k_{-3}\theta_D^2 + k_4(H_2)\theta_D \quad (SI-94)$$

$$k_5(H_2O)\theta_s + \frac{1}{2}k_6(H_2)\theta_{HDO} = k_{-5}\theta_{H_2O} + k_6(D_2)\theta_{H_2O} \quad (SI-95)$$

$$k_6(D_2)\theta_{H_2O} + k_6(H_2)\theta_{D_2O} = k_{-5}\theta_{HDO} + \frac{1}{2}k_6(D_2)\theta_{HDO} + \frac{1}{2}k_6(H_2)\theta_{HDO} \quad (SI-96)$$

$$\frac{1}{2}k_6(D_2)\theta_{HDO} = k_{-5}\theta_{D_2O} + k_6(H_2)\theta_{D_2O} \quad (SI-97)$$

Equations SI-93 – SI-97 are solved simultaneously with the assumption that the surface is covered:

$$\theta_{H_2O} + \theta_{HDO} + \theta_{D_2O} + \theta_H + \theta_D = 1 \quad (SI-98)$$

and the assumption that the KIE for H_2/D_2 adsorption and desorption are negligible:

$$k_1 = k_2 = k_3 \quad (SI-98)$$

$$k_{-1} = k_{-2} = k_{-3} \quad (SI-99)$$

to give the following expressions:

$$\theta_{H_2O} = \frac{(H_2O)\left(2 + \frac{k_6}{k_{-5}}\left(3(H_2) + (D_2)\right) + \frac{k_6^2}{k_{-5}^2}(H_2)^2\right)}{\left((H_2O) + \frac{\sqrt{K_3}}{K_5}\sqrt{(H_2) + (D_2)}\right)\left(2 + 3\frac{k_6}{k_{-5}}\left((H_2) + (D_2)\right) + \frac{k_6^2}{k_{-5}^2}\left((H_2) + (D_2)\right)^2\right)} \quad (SI-100)$$

$$\theta_{HDO} = \frac{2\frac{k_6}{k_{-5}}(D_2)(H_2O)\left(1 + \frac{k_6}{k_{-5}}(H_2)\right)}{\left((H_2O) + \frac{\sqrt{K_3}}{K_5}\sqrt{(H_2) + (D_2)}\right)\left(2 + 3\frac{k_6}{k_{-5}}\left((H_2) + (D_2)\right) + \frac{k_6^2}{k_{-5}^2}\left((H_2) + (D_2)\right)^2\right)} \quad (SI-101)$$

$$\theta_{D_2O} = \frac{\frac{k_6}{k_{-5}}(D_2)^2(H_2O)}{\left((H_2O) + \frac{\sqrt{K_3}}{K_5}\sqrt{(H_2) + (D_2)}\right)\left(2 + 3\frac{k_6}{k_{-5}}\left((H_2) + (D_2)\right) + \frac{k_6^2}{k_{-5}^2}\left((H_2) + (D_2)\right)^2\right)} \quad (SI-102)$$

$$\theta_H = \frac{\sqrt{K_3}(H_2)}{\sqrt{(H_2)+(D_2)}\left(K_5(H_2O)+\sqrt{K_3}\sqrt{(H_2)+(D_2)}\right)} \quad (SI-103)$$

$$\theta_D = \frac{\sqrt{K_3}(H_2)}{\sqrt{(H_2)+(D_2)}\left(K_5(H_2O)+\sqrt{K_3}\sqrt{(H_2)+(D_2)}\right)} \quad (SI-104)$$

$$\theta_s = \frac{1}{\left(K_5(H_2O)+\sqrt{K_3}\sqrt{(H_2)+(D_2)}\right)} \quad (SI-105)$$

Equations SI-91 – SI-92 can therefore be written as:

$$r_{HD} = \frac{2k_4(D_2)\left(\frac{\sqrt{K_3}}{K_5}\frac{(H_2)}{\sqrt{(H_2)+(D_2)}}\frac{k_6}{k_{-5}}(H_2)+\frac{k_6}{k_4}(H_2O)+\frac{k_6}{k_{-5}}(H_2)\frac{k_6}{k_4}(H_2O)+\frac{\sqrt{K_3}}{K_5}\frac{(H_2)}{\sqrt{(H_2)+(D_2)}}\left(2+\frac{k_6}{k_{-5}}\right)(D_2)\right)}{\left((H_2O)+\frac{\sqrt{K_3}}{K_5}\sqrt{(H_2)+(D_2)}\right)\left(2+\frac{k_6}{k_{-5}}\left((H_2)+(D_2)\right)\right)} \quad (SI-106)$$

$$r_{H_2O} = \frac{2k_6(H_2O)(D_2)\left(1+\frac{k_6}{k_{-5}}(H_2)\right)+\frac{k_6^2}{k_{-5}^2}(H_2O)(D_2)^2}{\left((H_2O)+\frac{\sqrt{K_3}}{K_5}\sqrt{(H_2)+(D_2)}\right)\left(2+3\frac{k_6}{k_{-5}}\left((H_2)+(D_2)\right)+\frac{k_6^2}{k_{-5}^2}\left((H_2)+(D_2)\right)^2\right)} \quad (SI-107)$$

4.6.3 Sensitivity Analysis of k_6, $\frac{\sqrt{K_3}}{K_5}$, and $\frac{k_6}{k_{-5}}$ for H_2O-D_2 Exchange

H_2O-D_2 exchange rates were described by Equation 11 in the main text, which includes three regressed parameters (k_6, $\frac{\sqrt{K_3}}{K_5}$, and $\frac{k_6}{k_{-5}}$). A sensitivity analysis of each of these parameters was performed to determine how the quality of the fit, calculated from the sum of square residuals (SSR), varies with the values of k_6, $\frac{\sqrt{K_3}}{K_5}$, and $\frac{k_6}{k_{-5}}$. These analyses were performed by varying the value of each parameter (0.5-2 times the regressed value), while regressing all other parameters. The SSR from these calculations are shown in Table SI-5. The SSR increased sharply from the minimum of 0.078 to values as high as 2.296 as the value of k_6 deviated from 34.7 kPa^{-1} s^{-1} in either direction (17.4-69.5 kPa^{-1} s^{-1}; Table SI-5). The SSR increased to from 0.078 to 0.936 as $\frac{\sqrt{K_3}}{K_5}$ was decreased from 2.46 to 1.23 $kPa^{0.5}$ and increased to 0.815 as $\frac{\sqrt{K_3}}{K_5}$ was increased to 4.92 $kPa^{-0.5}$. The sensitivity towards $\frac{k_6}{k_{-5}}$ was comparatively weak, as decreasing the parameter from 6.44 × 10^{-3} kPa^{-1} to 3.23 × 10^{-3} kPa^{-1} only increased the SSR from 0.078 to 0.178; increasing $\frac{k_6}{k_{-5}}$ to .813 increased the SSR to only 0.098.

The correlation between parameters was also investigated by fixing each parameter at the minimum while varying the other two parameters over a factor of 2. Figure SI-5 shows contour plots of SSR values for each pair of parameters. These results (Fig. SI-5) show that the value of k_6 strongly correlates with the value that of $\frac{\sqrt{K_3}}{K_5}$. These parameters are therefore difficult to measure individually and accurately. These correlations reflect the relationship between the concentration of H_2O* on the catalyst surface and the rate of reaction between H_2O* and D_2. The other parameters exhibit only weak correlations with each other (Fig. SI-5). Figure SI-6 shows a parity plot of H_2O-D_2 exchange rates modelled by Equation SI-90 and these parameters (k_6, $\frac{\sqrt{K_3}}{K_5}$, and $\frac{k_6}{k_{-5}}$), showing a good fit of the experimental data with the proposed reaction scheme (Scheme SI-5).

Table SI-5. Sensitivity Analysis of k_6, $\frac{\sqrt{K_3}}{K_5}$, and $\frac{k_6}{k_{-5}}$ for H_2O-D_2 exchange. Bolded parameters were fixed, while the other parameters were regressed. Highlighted row represents the regressed minimum.

$\boldsymbol{k_6}$ ($kPa^{-1}\ s^{-1}$)	$\frac{\sqrt{\boldsymbol{K_3}}}{\boldsymbol{K_5}}$ ($kPa^{0.5}$)	$\frac{\boldsymbol{k_6}}{\boldsymbol{k_{-5}}}$ (kPa^{-1})	**SSR**
17.4	1.21	7.30×10^{-4}	2.296
21.9	1.51	2.54×10^{-3}	1.103
27.6	1.91	4.51×10^{-3}	0.341
34.7	2.46	6.44×10^{-3}	0.078
43.8	3.29	8.01×10^{-3}	0.344
55.2	4.66	8.38×10^{-3}	1.104
69.5	7.20	6.51×10^{-3}	2.198
26.6	1.23	1.07×10^{-3}	0.936
29.0	1.55	9.19×10^{-3}	0.461
31.7	1.95	7.79×10^{-3}	0.173
38.2	3.10	5.17×10^{-3}	0.168
42.2	3.91	3.94×10^{-3}	0.423
46.7	4.92	2.76×10^{-3}	0.815
33.3	2.70	3.23×10^{-3}	0.178
33.7	2.63	4.07×10^{-3}	0.130
34.2	2.55	5.12×10^{-3}	0.093
35.5	2.36	8.13×10^{-3}	0.098
36.4	2.26	1.02×10^{-3}	0.173
37.4	2.14	1.29×10^{-3}	0.322

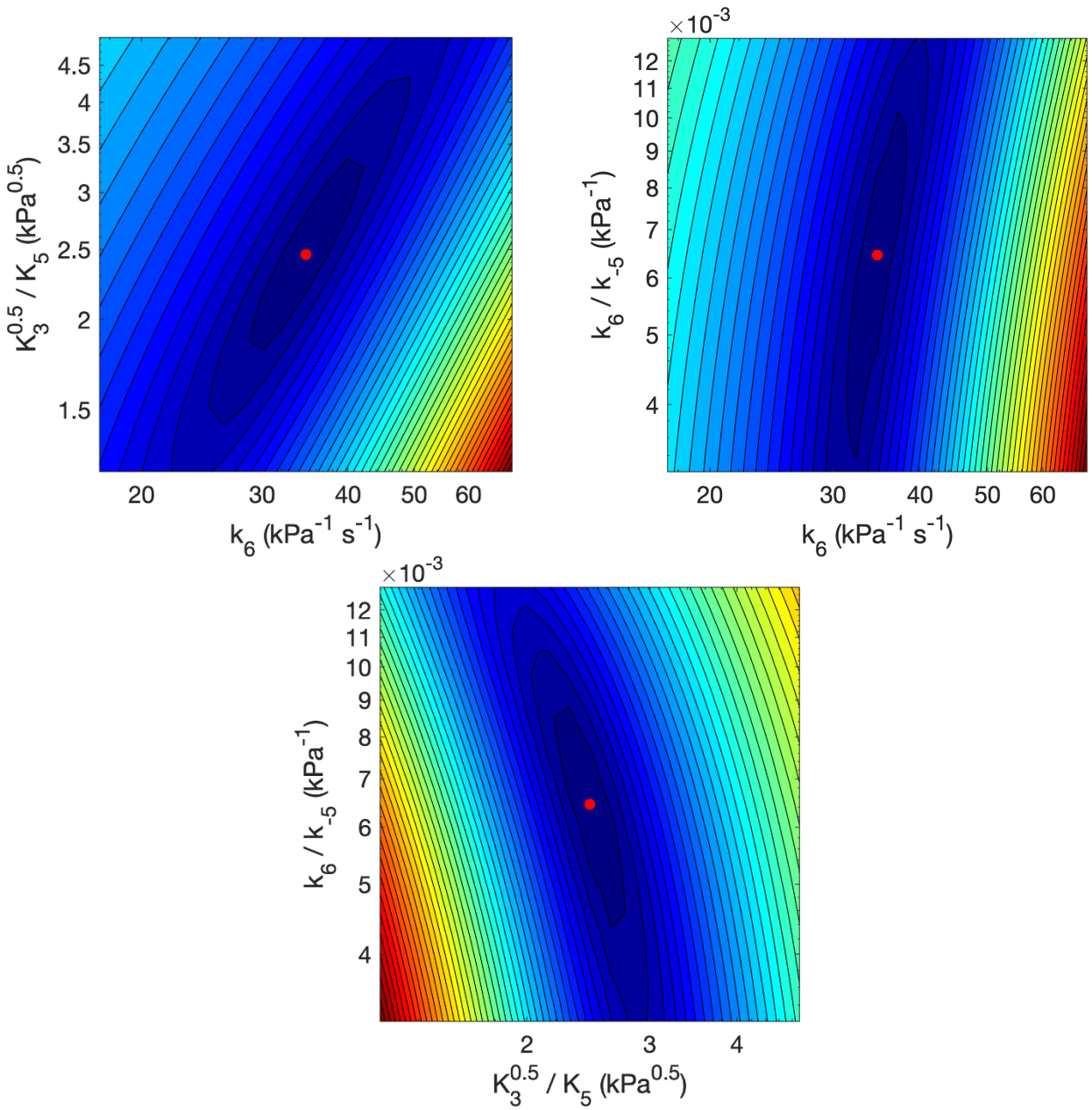

Figure SI-5. Contour plots of the SSR for each pair of parameters. The red point in the center represents the values corresponding with the regressed values.

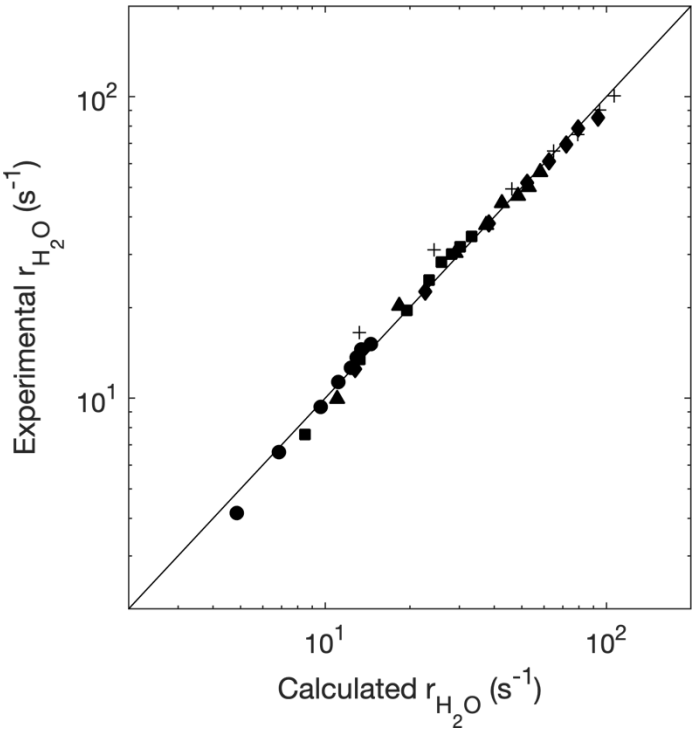

Figure SI-6. Parity plot of H_2O-D_2 isotopic exchange rates, calculated from the rate of H_2O conversion, at (●) 2.5, (■) 5, (▲) 10, (◆) 20, and (+) 40 kPa H_2O.

4.6.4 Simulating H*+D* Coverages for Various Gas-Phase Compositions and Adsorption Equilibrium Constants with a TIE for H_2/D_2 Adsorption

Combined coverages of H* and D* were simulated for several gas-phase (H_2O-H_2-D_2) compositions and equilibrium constants with and without a TIE (0.63 ± 0.2; 473 K) for H_2/D_2 adsorption. These values are shown in Table SI-6. The experimental $\frac{\sqrt{K_3}}{K_5}$ ratio (2.46 ± 0.17 $kPa^{0.5}$; Table 1) was used to calculate values of K_5. These data show the error in combined H* and D* coverage when assuming a TIE of 1.

Table SI-6. Combined H* and D* coverages for various H_2O-H_2-D_2 compositions and $\sqrt{K_3}$ values using a TIE $\left(\frac{K_1}{K_3}\right)$ of 0.63

$\sqrt{K_3}$ ($kPa^{-0.5}$)	$\sqrt{K_1}$ ($kPa^{-0.5}$)	K_5 (kPa^{-1})	(H_2) (kPa)	(D_2) (kPa)	(H_2O) (kPa)	$\theta_H + \theta_D$ (w/ TIE)	$\theta_H + \theta_D$ (w/o TIE)	Error (%)
1	0.79	0.41	5	40	5	0.73	0.74	1.5
1	0.79	0.41	40	5	5	0.71	0.74	4.7
1	0.79	0.41	5	40	20	0.47	0.48	2.9
1	0.79	0.41	40	5	20	0.44	0.48	9.3
10	7.94	4.07	5	40	5	0.79	0.80	1.1
10	7.94	4.07	40	5	5	0.77	0.80	3.6
10	7.94	4.07	5	40	20	0.50	0.51	2.8
10	7.94	4.07	40	5	20	0.47	0.51	8.8
100	79.37	40.65	5	40	5	0.80	0.81	1.1
100	79.37	40.65	40	5	5	0.78	0.81	3.5
100	79.37	40.65	5	40	20	0.50	0.51	2.8
100	79.37	40.65	40	5	20	0.47	0.51	8.8

4.6.5. H_2O Consumption and HD Formation Rates on Pt Black During H_2O-H_2-D_2 Reactions

Isotopic exchange (H_2O consumption and HD formation) rates in H_2O-H_2-D_2 reaction mixtures are shown in Table SI-7.

Table SI-7. H_2O consumption and HD formation rates on Pt black at 473 K during H_2O-H_2-D_2 reactions.

H_2 Feed Pressure (kPa)	D_2 Feed Pressure (kPa)	H_2O Feed Pressure (kPa)	$r_{HD,f}$ (s^{-1})	$-r_{H_2O,f}$ (s^{-1})
5	10	5	295	118
5	20	5	420	180
5	40	5	529	235
5	10	10	279	146
5	40	10	585	371
5	10	20	301	225
5	20	20	462	370
5	40	20	805	612
10	5	5	191	52
10	20	5	532	165
10	40	5	709	242
10	60	5	818	278
10	80	5	920	311
10	5	10	178	80
10	20	10	513	248
10	40	10	734	340
10	60	10	908	416
10	80	10	1090	461
10	5	20	173	108
10	20	20	548	354
10	40	20	873	599
20	5	5	237	44
20	10	5	414	79
20	20	5	663	168
20	40	5	977	228

20	60	5	1188	272
20	10	10	384	158
20	20	10	617	225
20	40	10	972	325
20	60	10	1224	406
20	5	20	216	96
20	10	20	363	185
20	20	20	645	371
40	5	5	255	35
40	10	5	458	67
40	20	5	793	143
40	40	5	1314	183
40	5	10	263	53
40	10	10	437	97
40	20	10	774	209
40	40	10	1248	288
40	5	20	241	84
40	10	20	439	183
60	10	5	504	61
60	20	5	892	121
60	10	10	501	113
60	20	10	864	158
80	10	5	625	48
80	10	10	490	92

4.7 References

1. Atkins, P. W.; De Paula, J., *Atkins' Physical Chemistry*, 9th ed.; Oxford University Press: Oxford ; New York, 2010.
2. Bigeleisen, J.; Mayer, M. G., Calculation of Equilibrium Constants for Isotopic Exchange Reactions. *J. Chem. Phys.* **1947**, *15*, 261-267.
3. Bigeleisen, J.; Wolfsberg, M., Theoretical and Experimental Aspects of Isotope Effects in Chemical Kinetics. *Adv. Chem. Phys.* **1958**, *1*, 15-76.
4. Melander, L. C. S.; Saunders, W. H., *Reaction Rates of Isotopic Molecules*; Wiley: New York, 1980.
5. Gonzalez-Lafont, A.; Lluch, J. M., Kinetic Isotope Effects in Chemical and Biochemical Reactions: Physical Basis and Theoretical Methods of Calculation. *Wiley Interdisciplinary Reviews-Computational Molecular Science* **2016**, *6*, 584-603.
6. Sattler, A., Hydrogen/Deuterium (H/D) Exchange Catalysis in Alkanes. *Acs Catalysis* **2018**, *8*, 2296-2312.
7. Loveless, B. T.; Buda, C.; Neurock, M.; Iglesia, E., Co Chemisorption and Dissociation at High Coverages During Co Hydrogenation on Ru Catalysts. *Journal of the American Chemical Society* **2013**, *135*, 6107-6121.
8. Panpranot, J.; Goodwin, J. G.; Sayari, A., Effect of H-2 Partial Pressure on Surface Reaction Parameters During Co Hydrogenation on Ru-Promoted Silica-Supported Co Catalysts. *J. Catal.* **2003**, *213*, 78-85.
9. Gnanamani, M. K.; Jacobs, G.; Shafer, W. D.; Sparks, D.; Davis, B. H., Fischer-Tropsch Synthesis: Deuterium Kinetic Isotope Study for Hydrogenation of Carbon Oxides over Cobalt and Iron Catalysts. *Catal. Lett.* **2011**, *141*, 1420-1428.
10. Yang, J.; Tveten, E. Z.; Chen, D.; Holmen, A., Understanding the Effect of Cobalt Particle Size on Fischer-Tropsch Synthesis: Surface Species and Mechanistic Studies by Ssitka and Kinetic Isotope Effect. *Langmuir* **2010**, *26*, 16558-16567.
11. Burwell, R. L., Deuterium as a Tracer in Reactions of Hydrocarbons on Metallic Catalysts. *Acc. Chem. Res.* **1969**, *2*, 289-296.
12. Siegel, S.; Ohrt, D. W., Kinetic Hydrogen Isotope Effects in Catalytic Hydrogenation of Alkenes. *Journal of the Chemical Society D-Chemical Communications* **1971**, 1529-1530.
13. Osborn, J. A.; Jardine, F. H.; Young, J. F.; Wilkinso.G, Preparation and Properties of Tris(Triphenylphosphine)Halogenorhodium(1) and Some Reactions Thereof Including Catalytic Homogeneous Hydrogenation of Olefins and Acetylenes and Their Derivatives. *Journal of the Chemical Society a -Inorganic Physical Theoretical* **1966**, 1711-1732.
14. Montelatici, S.; van der Ent, A.; Osborn, J. A.; Wilkinson, G., Further Studies on Homogeneous Hydrogenation of Olefins by Use of Tris (Tertiary Phosphine)Chlororhodium(I) Complexes. *Journal of the Chemical Society a -Inorganic Physical Theoretical* **1968**, 1054-1058.
15. Jones, W. D.; Feher, F. J., Isotope Effects in Arene C-H Bond Activation by [(C5me5)Rh(Pme3)]. *Journal of the American Chemical Society* **1986**, *108*, 4814-4819.
16. Jones, W. D., Isotope Effects in C-H Bond Activation Reactions by Transition Metals. *Acc. Chem. Res.* **2003**, *36*, 140-146.
17. Logan, S. R.; Philp, J., Linetic Isotope Effects in Catalytic Synthesis of Ammonia. *J. Catal.* **1968**, *11*, 1-6.
18. Ozaki, A., *Isotopic Studies of Heterogeneous Catalysis*; Kodansha, 1977.
19. Emmett, P. H., Use of Isotopic Tracers in Studying Catalysts and Catalytic Reactions. *Catalysis Reviews* **1972**, *7*, 1-24.

20. Burwell, R. L., The Uses of Deuterium in the Study of Heterogeneous Catalysis. *Catalysis Reviews* **1972**, *7*, 25-49.
21. Yao, R.; Herrera, J. E.; Chen, L. H.; Chin, Y. H. C., Generalized Mechanistic Framework for Ethane Dehydrogenation and Oxidative Dehydrogenation on Molybdenum Oxide Catalysts. *Acs Catalysis* **2020**, *10*, 6952-6968.
22. Biscardi, J. A.; Iglesia, E., Reaction Pathways and Rate-Determining Steps in Reactions of Alkanes on H-Zsm5 and Zn/H-Zsm5 Catalysts. *J. Catal.* **1999**, *182*, 117-128.
23. Cant, N. W.; Tonner, S. P.; Trimm, D. L.; Wainwright, M. S., Isotopic Labeling Studies of the Mechanism of Dehydrogenation of Methanol to Methyl Formate over Copper-Based Catalysts. *J. Catal.* **1985**, *91*, 197-207.
24. Joshi, R.; Zhang, G. H.; Miller, J. T.; Gounder, R., Evidence for the Coordination-Insertion Mechanism of Ethene Dimerization at Nickel Cations Exchanged onto Beta Molecular Sieves. *Acs Catalysis* **2018**, *8*, 11407-11422.
25. Hanson, R. M.; Green, S. M. E., *Introduction to Molecular Thermodynamics*; University Science Books: Sausalito, Calif., 2008.
26. Breakspere, R. J.; Norton, P. R.; Eley, D. D., Hydrogen Chemisorption and Exchange on Platinum. *J. Catal.* **1972**, *27*, 215-221.
27. Wachs, I. E.; Madix, R. J., On the H2-D2 Exchange on Stepped Platinum Surfaces. *Surf. Sci.* **1976**, *58*, 590-596.
28. Gillespie, R. D.; Burwell, R. L.; Marks, T. J., Isotopic Exchange between H2 and D2 by the Rideal-Eley Mechanism. *Catal. Lett.* **1991**, *9*, 363-368.
29. O'Brien, C. P.; Miller, J. B.; Morreale, B. D.; Gellman, A. J., The Kinetics of H-2-D-2 Exchange over Pd, Cu, and Pdcu Surfaces. *J. Phys. Chem. C* **2011**, *115*, 24221-24230.
30. Rideal, E. K., On the Hydrogen-Deuterium Exchange Reaction. *Journal of the Research Institute for Catalysis Hokkaido University* **1968**, *16*, 45-51.
31. Eley, D. D.; Norton, P. R., Conversion and Equilibration Rates of Hydrogen on Nickel. *Discuss. Faraday Soc.* **1966**, *41*, 135-148.
32. Iida, I., Mechanism of Catalyzed Hydrogen-Deuterium Exchange on Gold Deposited over Poly(Tetrafluoroethylene). *Bull. Chem. Soc. Jpn.* **1979**, *52*, 2858-2862.
33. Garcia-Dieguez, M.; Hibbitts, D. D.; Iglesia, E., Hydrogen Chemisorption Isotherms on Platinum Particles at Catalytic Temperatures: Langmuir and Two-Dimensional Gas Models Revisited. *J. Phys. Chem. C* **2019**, *123*, 8447-8462.
34. Yang, G. J.; Akhade, S. A.; Chen, X.; Liu, Y.; Lee, M. S.; Glezakou, V. A.; Rousseau, R.; Lercher, J. A., The Nature of Hydrogen Adsorption on Platinum in the Aqueous Phase. *Angewandte Chemie-International Edition* **2019**, *58*, 3527-3532.
35. Vincent, J. K.; Olsen, R. A.; Kroes, G. J.; Baerends, E. J., Dissociative Chemisorption of H-2 on Pt(111): Isotope Effect and Effects of the Rotational Distribution and Energy Dispersion. *Surf. Sci.* **2004**, *573*, 433-445.
36. Nieuwenhuys, B. E., Influence of Surface-Structure on Adsorption of Hydrogen on Platinum, as Studied by Field-Emission Probe-Hole Microscopy. *Surf. Sci.* **1976**, *59*, 430-446.
37. Gomez, R.; Orts, J. M.; Alvarez-Ruiz, B.; Feliu, J. M., Effect of Temperature on Hydrogen Adsorption on Pt(111), Pt(110), and Pt(100) Electrodes in 0.1 M Hclo4. *J. Phys. Chem. B* **2004**, *108*, 228-238.
38. Poelsema, B.; Lenz, K.; Comsa, G., The Dissociative Adsorption of Hydrogen on Defect-'Free' Pt(111). *Journal of Physics-Condensed Matter* **2010**, *22*.

39. Rootsaert, W. J. M.; Vanreijen, L. L.; Sachtler, W. M. H., Field-Emission Study of Composite Adsorption Layers on Tungsten and Platinum. *J. Catal.* **1962**, *1*, 416-431.
40. de Jong, K. P., *Synthesis of Solid Catalysts*; Wiley-VCH: Weinheim, 2009.
41. Almithn, A. S.; Hibbitts, D. D., Supra-Monolayer Coverages on Small Metal Clusters and Their Effects on H-2 Chemisorption Particle Size Estimates. *AlChE J.* **2018**, *64*, 3109-3120.
42. Bergeret, G.; Gallezot, P., Particle Size and Dispersion Measurements. In *Handbook of Heterogeneous Catalysis*, Ertl, G.; Knözinger, H.; Schüth, F.; Weitkamp, J., Eds. Wiley: 2008; pp 738-765.
43. Kresse, G.; Joubert, D., From Ultrasoft Pseudopotentials to the Projector Augmented-Wave Method. *Phys. Rev. B* **1999**, *59*, 1758-1775.
44. Hammer, B.; Hansen, L. B.; Norskov, J. K., Improved Adsorption Energetics within Density-Functional Theory Using Revised Perdew-Burke-Ernzerhof Functionals. *Phys. Rev. B* **1999**, *59*, 7413-7421.
45. Kasper, J. S.; Lonsdale, K.; International Union of Crystallography., *International Tables for X-Ray Crystallography*, 3rd ed.; Published for the International Union of Crystallography by D. Reidel Pub. Co.: Dordrecht ; Boston, 1985.
46. Pack, J. D.; Monkhorst, H. J., Special Points for Brillouin-Zone Integrations - Reply. *Phys. Rev. B* **1977**, *16*, 1748-1749.
47. Hibbitts, D. D.; Loveless, B. T.; Neurock, M.; Iglesia, E., Mechanistic Role of Water on the Rate and Selectivity of Fischer-Tropsch Synthesis on Ruthenium Catalysts. *Angewandte Chemie-International Edition* **2013**, *52*, 12273-12278.
48. Almithn, A.; Hibbitts, D., Effects of Catalyst Model and High Adsorbate Coverages in Ab Initio Studies of Alkane Hydrogenolysis. *Acs Catalysis* **2018**, *8*, 6375-6387.
49. Chen, B. W. J.; Mavrikakis, M., How Coverage Influences Thermodynamic and Kinetic Isotope Effects for H-2/D-2 Dissociative Adsorption on Transition Metals. *Catal. Sci. Technol.* **2020**, *10*, 671-689.
50. Karim, W.; Spreafico, C.; Kleibert, A.; Gobrecht, J.; VandeVondele, J.; Ekinci, Y.; van Bokhoven, J. A., Catalyst Support Effects on Hydrogen Spillover. *Nature* **2017**, *541*, 68-71.
51. Sato, S., Photoelectrochemical Preparation of Pt/Tio2 Catalysts. *J. Catal.* **1985**, *92*, 11-16.
52. Kip, B. J.; Duivenvoorden, F. B. M.; Koningsberger, D. C.; Prins, R., Determination of Metal-Particle Size of Highly Dispersed Rh, Ir, and Pt Catalysts by Hydrogen Chemisorption and Exafs. *J. Catal.* **1987**, *105*, 26-38.
53. Wanke, S. E.; Doughart.Na, Interaction of Hydrogen, Oxygen, and Carbon-Monoxide with Supported Rhodium. *J. Catal.* **1972**, *24*, 367-387.
54. Mcvicker, G. B.; Ziemiak, J. J., Chemisorption Properties of Platinum and Iridium Supported on Tio2-Al2o3 Mixed-Oxide Carriers - Evidence for Strong Metal Support Interaction Formation. *J. Catal.* **1985**, *95*, 473-481.

Chapter 5

Measurement of Characteristic Diffusion Times in Microporous Materials Using Effectiveness Factors Derived from Isotopic Exchange Reactions

Abstract

Microporous materials are widely used in heterogeneous catalysis because of their unique shape/size-selective properties, but often exhibit mass transport limitations leading to lower effective reaction rates. The measurement of diffusion time constants $\left(\frac{R^2}{D_e}\right)$ of relevant reactive molecules is useful for predicting and modelling these transport limitations. Conventional methods such as transient uptake measurements are often unable to accurately measure diffusion rates at or near reaction conditions. This study presents an alternative method for measuring diffusion time constants using effectiveness factors derived from isotopic exchange experiments. CH_4-D_2 (5-35 kPa CH_4, 5-30 kPa D_2) and H_2O-D_2 (5-30 kPa H_2O, 5-30 D_2) isotopic exchange rates were measured here on Pt/SiO_2, Pt/γ-Al_2O_3, Pt/Na-LTA, and Pt/Ca-LTA samples at temperatures (573-900 K) relevant for CH_4-H_2O reforming reactions. Effectiveness factors on Pt/Na-LTA and Pt/Ca-LTA were used to calculate diffusion time constants for CH_4 and H_2O using diffusion-reaction models. CH_4 exhibited significantly larger diffusion time constants (by factors of more than 10^2) than H_2O in both Pt/Na-LTA and Pt/Ca-LTA, indicating that H_2O diffuses more readily in these materials. These data indicate that CH_4 will exhibit steeper concentration gradients than H_2O in Pt/Na-LTA and Pt/Ca-LTA during CH_4-H_2O reactions. The methods for calculating $\frac{R^2}{D_e}$ values from isotopic exchange studies demonstrated in this study are general; they require only that intrinsic exchange rates of the molecule of interest at active sites located within the catalyst be sufficiently fast to cause significant mass transport limitations.

5.1 Introduction

Mass transport limitations in microporous materials are ubiquitous in catalytic applications.[1-4] Molecular motion within these host materials is severely hindered by constant interactions between guest molecules and the walls of the channels of molecular dimensions.[3] These interactions lead to concentration gradients and decreased catalytic productivity when the flux of molecules is insufficient to sustain the initial rate of their chemical conversion or production at active sites located within the micropores. The severity of these gradients depends on the concentration and reactivity of active sites, but also sensitively on the nature of the guest-host interactions. These interactions depend, in turn, on the geometry of the micropores, the prevalence and identity of charge-balancing ions, and the geometry and chemical properties of the diffusing molecule.[3-5] This sensitivity can lead to distinct concentration profiles for different molecules during chemical conversions inside of the micropores, leading not only to changes in effective reaction rates, but also reactant or product selectivities.[4] The accurate modelling of mass transport is therefore essential in the design of processes that use microporous media.

Effective reaction rates in mass transport limited systems can be estimated by calculating an effectiveness factor (λ), defined as the effective reaction rate (r_{eff}) divided by the reaction rate at equivalent conditions without mass transport limitations (r_{max}). This effectiveness factor is given by:[6-7]

$$\lambda \equiv \frac{r_{eff}}{r_{max}} = \frac{\sqrt{2}}{Lr(C_s)}\left[\int_{C_0}^{C_s} D_e(c)r(c)dc\right]^{\frac{1}{2}} \tag{1}$$

$$L = \frac{V_p}{S} \tag{2}$$

Here, $r(c)$ is the (volumetric) reaction rate at reactant concentration c, $D_e(c)$ is the effective diffusivity at c, C_s is the reactant composition at the surface of the catalytic pellet (or crystallite), C_0 is the (unknown) composition at the center of the catalytic pellet, V_p is the volume of the pellet, and S is the surface area of the pellet. C_0 can be implicitly obtained using:[6-7]

$$L = \int_{C_0}^{C_s} \frac{D_e(c')dc'}{\left[2\int_{C_0}^{C_s} D_e(c)r(c)dc\right]^{\frac{1}{2}}} \tag{3}$$

L in Equations 1-3 represents the relevant diffusion distance and in a quasi-spherical particle or crystallite is equal to the radius R. These equations provide a rigorous, albeit awkward, way to calculate an effective reaction rate r_{eff} provided that the intrinsic kinetics ($r(c)$) and maximum reaction rate (r_{max}) in the absence of mass transport limitations and the effective diffusivities $D_e(c)$ are known. Under strong transport limitations (λ < ~0.3),[6] the reactant concentration at the center of a pellet or crystallite is at equilibrium for a reversible reaction $\left(C_0 = C_{eq}\right)$ or zero for an irreversible one $(C_0 = 0)$. Thus, for an nth-order irreversible reaction in A described by the rate equation:

$$r(c) = k_v C_A^n \tag{4}$$

where C_A is the concentration of reactant A and k_v is the volumetric rate constant, Equation 1 can be integrated (assuming also that $D_e(c)$ is a constant) and simplified:

$$\lambda \equiv \frac{r_{eff}}{r_{max}} = \sqrt{\frac{2}{n+1}\frac{D_e}{k_v R^2 C_{A,s}^{n-1}}} = \frac{1}{\phi} \qquad n > -1 \tag{5}$$

$C_{A,s}$ represents the concentration of A at the particle surface. ϕ is commonly known as the Thiele modulus and represents the square root of the ratio of the maximum reaction rate (r_{max}) to the maximum diffusion rate.[8] Equation 5 thus provides a simple relation to calculate effective rates (r_{eff}) for reactions that can be described by a rate equation of the form described in Equation 4. Such calculations require knowledge of the effective diffusion coefficients (D_e) and particle radius (R).

A variety of methods can be used to measure diffusion in microporous materials, as reviewed by Ruthven;[9] they can be divided into microscopic and macroscopic methods. Microscopic methods measure molecular mobilities at the microscopic (< 1 nm) level[9] and include quasi-elastic neutron scattering (QENS)[10-11] and nuclear magnetic resonance (NMR)[12-13] studies. Estimating long-range diffusivities from these methods requires an estimation of the average jump length and the assumption that the processes controlling diffusion at the microscale level are identical to those at the macroscale level.[9] Such assumptions are not always valid and neglect the role of crystal defects and surface-skin effects on effective diffusivities (D_e).[14-15] Pulsed-field gradient NMR (PFG-NMR) methods offer significant improvements over traditional NMR-based measurements; they work across much longer length scales (up to tens of micrometers) but still notably fail for very slow diffusing systems (< 10^{-12}-10^{-13} m^2 s^{-1}).[2, 9, 16-18] These uncertainties in the direct measurement of diffusion coefficients (D_e) can compound with errors in estimating crystallite radii (R) from electron micrographs, which arise from the incomplete nature of two-dimensional projections of three-dimensional objects; the ratio of these values $\left(\frac{R^2}{D_e}\right)$ is the relevant parameter for describing diffusional constraints in a particle (Eq. 5) and is denoted as a diffusion time constant. Thus, while microscopic methods are able to provide information about intrinsic molecular mobilities in microporous materials, their use in describing systems at the laboratory or industrial scale is often limited.

Macroscopic methods,[9, 19-26] by their nature, do not directly measure diffusion coefficients (D_e) independently, as in microscopic methods, but instead report effective long-range diffusion time constants $\left(\frac{R^2}{D_e}\right)$, circumventing the need to extrapolate from the microscale level or separately estimate crystallite radii. Commonly utilized methods include transient uptake,[19-20] frequency response,[21-22] and chromatographic[27-31] measurements. These techniques, however, require that the diffusion time constant $\left(\frac{R^2}{D_e}\right)$ be greater than the time resolution of the measurement and any hydrodynamic delays to avoid inaccuracies. Intracrystalline diffusion is an activated process, with the activation energy arising primarily from steric hindrances.[9] The effective diffusion coefficient D_e is therefore sensitive to temperature and obeys an Arrhenius-like relationship:

$$D_e = D_0 \exp\left(-\frac{E_d}{R_{gas}T}\right) \tag{6}$$

where E_d is the energy barrier for diffusion, D_0 is a pre-exponential constant, R_{gas} is the gas constant, and T is the absolute temperature.[9, 32] The crystallite radius R is not a function of temperature. Measurements of $\left(\frac{R^2}{D_e}\right)$ are thus typically performed at temperatures much lower than

reaction conditions to ensure that diffusion time constants are accurately captured and then extrapolated to the relevant temperatures using Equation 6. The accuracy of such extrapolations is, however, highly dependent on estimates of E_d and can be considered reliable only for relatively small changes in temperature. The measurement of diffusion time constants at reaction conditions is desirable to avoid such extrapolations but often difficult to accomplish in practice using the techniques described above.

Equations 1-3 and 5 provide a relationship between effective and intrinsic rates and the diffusive properties ($\frac{R^2}{D_e}$ values) of relevant molecules. While these equations are commonly used to estimate effective reaction rates from $\frac{R^2}{D_e}$ values, they can also be used to back-calculate the $\frac{R^2}{D_e}$ values from the ratio of effective and intrinsic rates. This approach is naturally suited for measuring diffusion time constants at reaction temperature; it was first reported by Haag, et. al., who measured diffusion time constants of C_6 to C_9 hydrocarbons in ZSM-5 during catalytic cracking reactions.[24] It was later utilized by Post, et. al. to measure the diffusion of 2,2 dimethyl-butane during catalytic cracking on ZSM-5.[25] These studies used their reactions of interest to probe the value of $\frac{R^2}{D_e}$. Such an approach, however, is not always possible and limits measurements of $\frac{R^2}{D_e}$ values to species that appear in the rate equation of the reaction of interest; it may therefore fail to reveal the presence of concentration gradients in co-reactants and/or products that do not directly affect reaction rates, but which can affect reaction selectivities and even catalyst stability.

Here, we present a modified method for measuring $\frac{R^2}{D_e}$ values in microporous materials using effectiveness factors derived from isotopic (H-D) exchange rates rather than from rates of chemical conversions. The procedure for extracting these values is demonstrated for CH_4-D_2 and H_2O-D_2 isotopic exchange reactions at temperatures that are relevant for steam-methane reforming reactions (523-900 K) on Pt nanoparticles supported on SiO_2 or γ-Al_2O_3 (denoted as Pt/SiO_2 and γ-Al_2O_3, respectively) or encapsulated within Na-LTA and Ca-LTA (denoted as Pt/Na-LTA and Pt/Ca-LTA, respectively). CH_4 and H_2O both exhibit severe mass transport limitations during isotopic exchange reactions (523-900 K) on Pt/Na-LTA and Pt/Ca-LTA, leading to significantly lower effective exchange rates compared to reactions on Pt/SiO_2 or Pt/γ-Al_2O_3. These mass transport limitations allow for the extraction of $\frac{R^2}{D_e}$, but require careful considerations of the underlying kinetics of isotopic exchange. The mechanism by which H_2O-D_2 exchange reactions occur was addressed in a prior study (Chapter 4), while the mechanism for CH_4-D_2 exchange is shown here to be consistent with CH_4 decomposition (and recombination) reactions. The Thiele modulus and diffusion time constants $\frac{R^2}{D_e}$ are calculated here within the context of these mechanistic interpretations.

The results from this study show that the diffusion time constants $\left(\frac{R^2}{D_e}\right)$ for CH_4 and H_2O at high temperatures (523-900 K) are too fast to be accurately measured using conventional macroscopic methods (e.g., transient uptake). Effectiveness factors are therefore one of the only methods available to probe diffusion time constants at reaction conditions. The results also show that CH_4 exhibits significantly larger (by factors of more than 10^2) diffusion time constants than H_2O in both Pt/Na-LTA and Pt/Ca-LTA. These data indicate that concentration gradients in CH_4 are significantly steeper than those for H_2O during steam-methane reforming reactions on these

materials, thus altering intracrystalline reactant ratios. Such inferences would not be possible from effectiveness factors derived from steam-methane reforming rates because H_2O does not appear in the rate equation for these reactions.[33] Isotopic exchange reactions therefore represent a more flexible method for measuring diffusion time constants compared to prior studies that that were limited by their reaction of interest.[24-25] The isotopic exchange method presented here is applicable to a wide range of guest-host systems, with the only requirement being that the intrinsic reaction rate be sufficiently faster than the flux of molecules that the reaction is strongly mass transport limited and effectiveness factors are accurately measurable.

5.2 Experimental Methods

5.2.1 Catalyst Synthesis Methods

Pt nanoparticles supported on SiO_2 (0.2% wt., Pt/SiO_2) and on γ-Al_2O_3 (1% wt., Pt/γ-Al_2O_3) were prepared using electrostatic adsorption and incipient wetness impregnation methods, as described in our prior work (Chapter 3).

Pt clusters were encapsulated in LTA zeolites with Na^+ as the counterion (Pt/Na-LTA) by adding a Pt precursor and stabilizing ligand to a LTA zeolite synthesis gel prior to hydrothermal crystallization of the LTA framework, as reported previously.[34] The gel was prepared by adding 0.71 g of (3-mercaptopropyl)trimethoxysilane (95%; Sigma-Aldrich) and 4.80 g of NaOH (Certified ACS, Fisher Chemical) to 18.0 g of deionized (DI) H_2O (>18.0 MΩ-cm resistivity). A solution of 3.04 g of H_2PtCl_6 (8% wt. in H_2O, Sigma-Aldrich) diluted in 15.3 g of DI H_2O was then added dropwise into the NaOH solution under vigorous stirring. Colloidal SiO_2 (10.7 g; 30 wt. % suspension in H_2O; LUDOX HS-30; Sigma-Aldrich) was added to the mixture and heated to 353 K under stirring (300 s^{-1}) until transparent. A solution of 6.0 g of $NaAlO_2$ (53% Al_2O_3, 42.5% Na_2O; Riedel-de Haën) in 18.0 g of DI H_2O was added to this heated solution and stirred for 2 h at ambient temperature. The final synthesis gel molar ratios were 1.7 SiO_2/1.00 Al_2O_3/3.2 Na_2O/110 H_2O/0.019 Pt/0.12 (3-mercaptopropyl)trimethoxysilane. The gel was heated for 12 h at 373 K with stirring (300 s^{-1}) in a 1 L polypropylene bottle. The resulting mixture was filtered through a fine fritted funnel and washed with DI water until the rinse solution reached a pH of 7. The solids were treated overnight in ambient air at 368 K and then treated in flowing air (0.83 mL g^{-1} s^{-1}; zero grade; Praxair) while ramping from ambient temperature to 623 K (0.033 K/s) and holding for 3 h. The sample was then cooled and treated in flowing H_2 (0.83 mL g^{-1} s^{-1}; 99.999% UHP; Praxair) while ramping from ambient temperature to 623 K (0.083 K/s) and holding for 2 h. After cooling, the sample was treated in 2% O_2 v/v (balance He; certified grade; Praxair) for 0.5 h at ambient temperature to passivate the surfaces of Pt nanoparticles.

Ca^{2+}-exchanged LTA samples containing Pt nanoparticles (Pt/Ca-LTA) were prepared from the Pt/Na-LTA samples. Pt/Na-LTA (2 g) was added to a 2 M $CaCl_2$ (200 cm^3; ACS grade, VWR) solution and stirred for 8 h to allow for complete equilibration. The solids were then filtered out, and the process was repeated five times. After the final exchange, the solids were washed with deionized water (1.0 L g^{-1}) before treating in ambient air at 368 K overnight and then in flowing He (0.83 mL g^{-1} s^{-1}; 99.999%, UHP, Praxair) by ramping from ambient temperature to 473 K (0.083 K s^{-1}), holding for 2 h, and cooling to ambient temperature.

Na-LTA zeolites without Pt were synthesized by identical steps to Pt/Na-LTA, but without the addition of (3-mercaptopropyl)trimethoxysilane or H_2PtCl_6.

5.2.2 Catalyst Characterization

5.2.2.1 Pt Dispersion and Particle Size Estimations from H_2 Chemisorption

The dispersion of Pt on catalyst samples, defined as the number of exposed Pt sites divided by the total number of Pt atoms, was obtained using saturation uptakes of H_2 at 373 K. Samples (ca. 1 g) were treated in flowing H_2 by ramping at 0.083 K s^{-1} to 873 K and holding for 1 h. The sample chamber was then evacuated for 1 h at the same temperature before cooling to 373 K, also under vacuum. H_2 dissociative adsorption uptakes were measured at pressures between 1 and 40 kPa (373 K). Saturation uptakes were calculated by extrapolating the high-pressure portion of the isotherm to zero pressure. Particle diameters (d) were calculated from dispersions by assuming hemispherical particle geometries, the bulk density of Pt (21.45 g cm^{-3}),[35] and correcting for suprastoichiometric H/Pt_s (Pt_s = Pt atoms on nanoparticle surfaces) resulting from the binding of multiple H-atoms on corner and edge sites using:

$$d = \frac{f_{shape} N_M}{2N_{H_2}} \frac{v_m}{a_m} \theta_{sat} \tag{7}$$

$$\theta_{sat} = \mathrm{H/Pt_s} = 1 + \alpha(d^{-1}) + \beta(d^{-2}) \tag{8}$$

Here, f_{shape} is a shape factor (6 for a hemispherical particle), N_M is the total number of metal atoms in the sample, N_{H_2} is the number of dissociatively bound H_2 molecules on the catalyst surface, v_m and a_m are the volume and surface area of a Pt atom, and α (0.0364) and β (0.735) are empirical parameters specific for Pt.[36] These equations (Eq. 7-8) can be solved simultaneously for the particle diameter (d) and saturation coverage (θ_{sat}).

5.2.2.2. Transmission Electron Microscopy and Particle Size Estimations

Transmission electron micrographs of Pt/Na-LTA were obtained on a Philips/FEI Tecnai 12 microscope at 120 kV. Samples were prepared by suspending particles in acetone, sonicating the suspension for 0.5 h, and then placing drops of the suspension onto holey carbon films mounted on 400 mesh Cu grids (Ted Pella, #01824). Particle size distributions of metal clusters were obtained by counting at least 200 crystallites. Surface-averaged cluster diameters were calculated using:[35]

$$\langle d_{TEM} \rangle = \frac{\sum n_i d_i^3}{\sum n_i d_i^2} \tag{9}$$

where n_i is the number of clusters with diameter d_i.

5.2.2.3. X-ray Diffraction

X-ray diffractograms for Na-LTA, Pt/Na-LTA, and Pt/Ca-LTA samples were obtained using a Bruker D8 Discover GADDS Powder Diffractometer using Cu Kα radiation (40 kV, 40 mA). Sample powders were mixed with MgO (>99.99% trace metals basis; Sigma-Aldrich) in a 1:1 mass ratio (as an internal standard) and placed onto quartz slides and leveled. Diffractograms

were obtained for 2θ angles between 7.5° and 55° with a scan rate of 0.00625° s^{-1}. The crystallinities of Pt/Na-LTA and Pt/Ca-LTA samples were calculated as detailed in Section 5.6.1.1.

5.2.3 Measurement of Isotopic Exchange Rates and CH_4-H_2O Reaction Rates

Isotopic exchange rates and CH_4-H_2O reaction rates were measured over catalyst powders (0.0005-0.050 g; <100 μm) held on a quartz frit within a U-shaped quartz tube (6.35 mm O.D., 4 mm I.D.). Deionized H_2O was vaporized into flowing reactant streams at 423 K using a liquid syringe pump (Cole Parmer, 78-9100C). CH_4/Ar[4] (50% CH_4, balance Ar; certified grade; Praxair), D_2 (99.8% isotopic enrichment, research grade; Praxair), and N_2[5] (99.998%, Praxair) flow rates were controlled using mass flow controllers (Parker Porter 200 series). Samples were treated in flowing H_2 (100 cm^3 g^{-1} s^{-1}) while heating from ambient temperature to 873 K (ramping at 0.083 K s^{-1}) and then holding for 2 h prior to experiments. The composition of the effluent was analyzed by mass spectrometry (Leybold Inficon Transpector, TSP TH200).

The rate of CH_4-D_2 exchange was calculated by summing the rates of CH_3D, CH_2D_2, CHD_3, and CD_4 formation after correcting each observed rate (r_n) for its respective approach to equilibrium (η) to obtain forward rates (r_f) using:

$$r_n = r_f\,(1-\eta) \tag{10}$$

The approaches to equilibrium for these species are given by:

$$\eta_{CH_3D} = \frac{(CH_3D)(HD)}{(CH_4)(D_2)}\frac{1}{K_{eq,CH_3D}} \tag{11}$$

$$\eta_{CH_2D_2} = \frac{(CH_2D_2)(HD)^2}{(CH_4)(D_2)^2}\frac{1}{K_{eq,CH_2D_2}} \tag{12}$$

$$\eta_{CHD_3} = \frac{(CHD_3)(HD)^3}{(CH_4)(D_2)^3}\frac{1}{K_{eq,CHD_3}} \tag{13}$$

$$\eta_{CD_4} = \frac{(CD_4)(HD)^4}{(CH_4)(D_2)^4}\frac{1}{K_{eq,CD_4}} \tag{14}$$

where $K_{eq,i}$ is the equilibrium constant for the respective reactions, calculated from the binomial distribution of $CH_{4-x}D_x$ (x = 0-4) and $H_{2-y}D_y$ (y = 0-2) species at equilibrium.[37] The rate of H_2O-D_2 exchange was similarly calculated by summing the rates of HDO and D_2O formation after correcting for approach to equilibrium using Equation 10. The approaches to equilibrium for HDO and D_2O formation are given by:

$$\eta_{HDO} = \frac{(HDO)(HD)}{(H_2O)(D_2)}\frac{1}{K_{eq,HDO}} \tag{15}$$

$$\eta_{D_2O} = \frac{(D_2O)(HD)^2}{(H_2O)(D_2)^2}\frac{1}{K_{eq,D_2O}} \tag{16}$$

[4] Ar used as an internal standard in CH_4-D_2 isotopic exchange experiments.
[5] N_2 used as an internal standard in H_2O-D_2 isotopic exchange experiments.

Forward CH_4 turnover rates during CH_4-H_2O (SRM) reactions were also calculated by correcting measured rates for approach to equilibrium using Equation 10. The approach to equilibrium for CH_4-H_2O reactions is given by:

$$\eta_{SRM} = \frac{(CO)(H_2)^3}{(CH_4)(H_2O)} \frac{1}{K_{eq,SRM}} \tag{17}$$

The thin catalyst beds resulting from the small amounts of catalyst used in these experiments exhibit hydrodynamics that are similar to well-stirred systems. The pressures at the reactor exit were therefore used in Equations 11-17. The absence of mass transport limitations on Pt/SiO_2 and Pt/γ-Al_2O_3 samples was confirmed by identical rates on samples ground and sieved to retain particles smaller than 50 μm.

5.3 Results and Discussion

5.3.1 Catalyst Characterization

Pt dispersions in Pt/SiO_2, Pt/γ-Al_2O_3, and Pt/Na-LTA samples were measured using H_2 chemisorption uptakes at 373 K. These dispersions were used to calculate the average diameters of Pt nanoparticles (Table 1) after correcting for the binding of multiple H atoms at edge and corner sites (Eq. 7-8).[36] Average Pt nanoparticle diameters determined from TEM micrographs of Pt/Na-LTA samples (Section 5.6.1.2; 1.9 nm, Table 1) were in agreement with chemisorption values (2.4 nm; Table 1).

Table 1. Nominal metal content, dispersions, and calculated particle diameters for catalytic samples

Catalyst	Nominal Metal Content (% wt.)	Dispersion	Chemisorption Particle Diameter (nm)*	TEM Derived Particle Diameter (nm)
Pt/SiO_2	0.2	0.38	3.2	-
Pt/γ-Al_2O_3	1.0	0.72	1.9	-
Pt/Na-LTA	1.0	0.53	2.4	1.9

*Calculated by assuming hemispherical particle geometries and the bulk density of Pt (21.45 g cm^{-3})[35] after correcting for the binding of multiple H atoms at edge and corner sites.[36]

X-ray diffractograms of Na-LTA, Pt/Na-LTA, and Pt/Ca-LTA samples confirmed the synthesis of LTA crystallites and the absence of large Pt agglomerates (> 10 nm) (Section 5.6.1.1). Diffactograms of Pt/Na-LTA and Pt/Ca-LTA samples were quantitatively compared to measure differences in crystallinity (80 vs. 74%, respectively; details in 5.6.1.1). These values indicate that Ca^{2+} ion exchange procedures resulted in minimal loss of crystallinity.

5.3.2 Measurement of CH_4 Diffusion Time Constants $\left(\frac{R^2}{D_e}\right)$ in Pt/Na-LTA and Pt/Ca-LTA Samples

5.3.2.1 Kinetic Dependence of CH_4-D_2 Isotopic Exchange Rates on CH_4 and D_2 Pressure on Pt/SiO_2

CH_4-D_2 isotopic exchange rates were measured on Pt/SiO_2 as pressures of CH_4 (5-35 kPa) and D_2 (5-30 kPa) were varied (873 K; Fig. 1). Isotopic exchange rates increased proportionally with CH_4 pressure and did not depend on D_2 pressure (Fig. 1); these kinetic behaviors are accurately described by the rate equation:

$$r_{CH_4,f} = -k'_{CH_4}(CH_4) \tag{18}$$

where k'_{CH_4} (2.96 ± 0.06 kPa^{-1} s^{-1}; Fig. 1) denotes a pressure-based reaction rate constant normalized by the number of accessible Pt sites (Table 1, Section 5.3.1). The form of this rate equation (Eq. 18) is identical to that previously proposed for CH_4-H_2O reforming reactions;[33] CH_4-H_2O reaction rates (22 ± 3 s^{-1}; 10 kPa CH_4, 40 kPa H_2O, 873 K) measured on Pt/SiO_2 were very similar to exchange rates (30 ± 1.5 s^{-1}, 10 kPa CH_4, 20 kPa D_2, 873 K). These similarities indicate that the two reactions share a common rate limiting step, which was previously shown to be activation of the C-H bond.[33] The kinetic dependences in Figure 1 (873 K) reflect reactions on a nearly bare surface and are consistent with the dissociation of CH_4 to form CH_3*, CH_2*, CH*, and C* species and the recombination of these species with D* to form $CH_{4-x}D_x$ (x = 1-3).

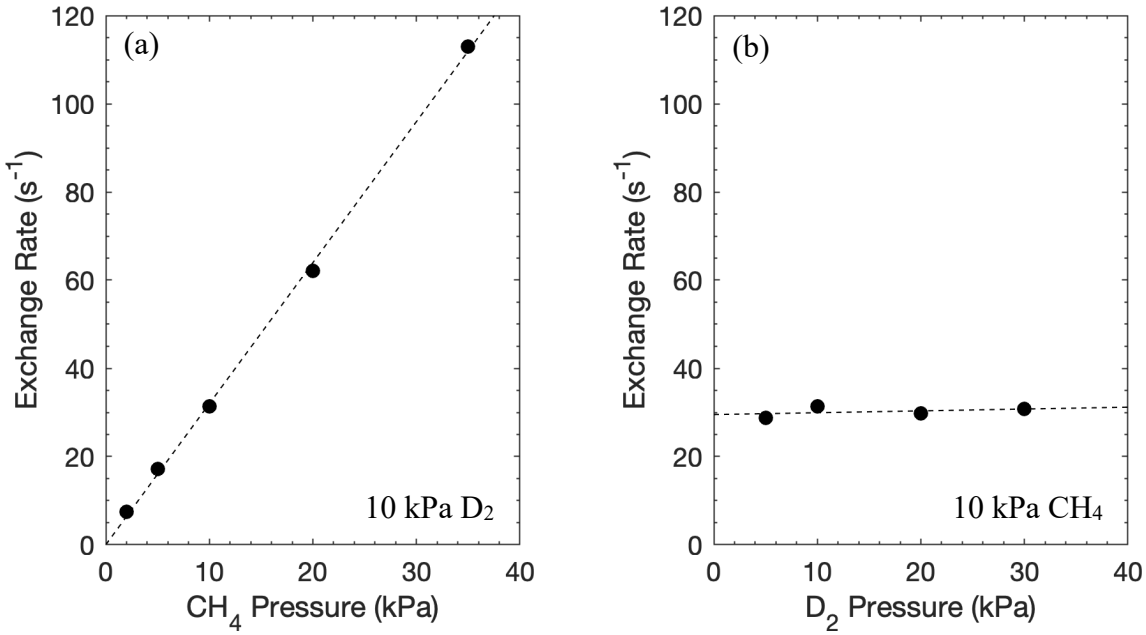

Figure 1. CH_4-D_2 isotopic exchange rates on Pt/SiO_2 as a function of (a) CH_4 pressure (10 kPa D_2) and (b) D_2 pressure (10 kPa CH_4) at 873 K. Dashed lines represent linear regression of the data.

The form of the rate equation describing CH_4-D_2 exchange (Eq. 18) corresponds with the form of Equation 4 (n = 1). The Thiele modulus and effective reaction rates can therefore be modelled accurately by Equation 5. The conventional usage of this equation is in estimating effectiveness factors for reactions in mesoporous materials; this would typically involve estimating the effective diffusion coefficient D_e from the Knudsen diffusivity (D_{Kn}),[38-39] estimating or measuring the pellet radius R, and converting k'_{CH_4} (normalized per Pt site) to a concentration-based volumetric rate constant k_{v,CH_4}, using:

$$k_{v,CH_4} = \frac{k'_{CH_4} D l_{Pt} \rho}{(MW_{Pt})} R_{gas} T \tag{19}$$

Here, D is the Pt dispersion, l_{Pt} is the metal content of Pt, (MW_{Pt}) is the molecular mass of Pt, and ρ is the solid density of the catalyst. These parameters are specific to the catalyst of interest; Equation 19 can therefore be used for a wide range of (Pt-based) catalytic materials. Our goal, however, is not in the estimation of effectiveness factors from a Thiele modulus, but rather in the estimation of the Thiele modulus from effectiveness factors. We measure such effectiveness factors from CH_4-D_2 isotopic exchange rates on Pt/SiO_2, Pt/Na-LTA, and Pt/Ca-LTA for a range of temperatures (673-900 K) in the following sections.

5.3.2.2 Effect of Temperature on CH_4-D_2 Isotopic Exchange Rates and k'_{CH_4} on Pt/SiO_2

CH_4-D_2 isotopic exchange rates (5 kPa CH_4, 10 kPa D_2) were measured on Pt/SiO_2 samples at temperatures between 673 and 900 K. Figure 2a shows these rates as a function of temperature in an Arrhenius plot. These data exhibit a constant slope (Fig. 2a) and thus reflect a consistent kinetically-relevant step throughout this temperature range (673-900 K). Equation 18 can therefore be used to calculate k'_{CH_4} values (shown in Fig. 2b) from these exchange rates. The activation energy associated with k'_{CH_4} (88.9 ± 0.3 kJ mol^{-1}; Fig. 2b) was similar to those previously measured for CH_4-H_2O (75 kJ mol^{-1}), CH_4-CO_2 (83 kJ mol^{-1}), and CH_4 decomposition (78 kJ mol^{-1}) reactions on Pt,[33] further indicating that the reactions share a common rate limiting step (C-H bond activation). The rates measured on Pt/SiO_2 (Fig. 2a) represent the maximum rate for a given condition (r_{max}, Eq. 5) and serve as the denominator for calculating effectiveness factors ($\lambda \equiv \frac{r_{eff}}{r_{max}}$, Eq. 5). The k'_{CH_4} values (Fig. 2b) will also be used in subsequent sections to extract diffusion time constants $\left(\frac{R^2}{D_e}\right)$ from effective rates for mass transport limited catalyst samples.

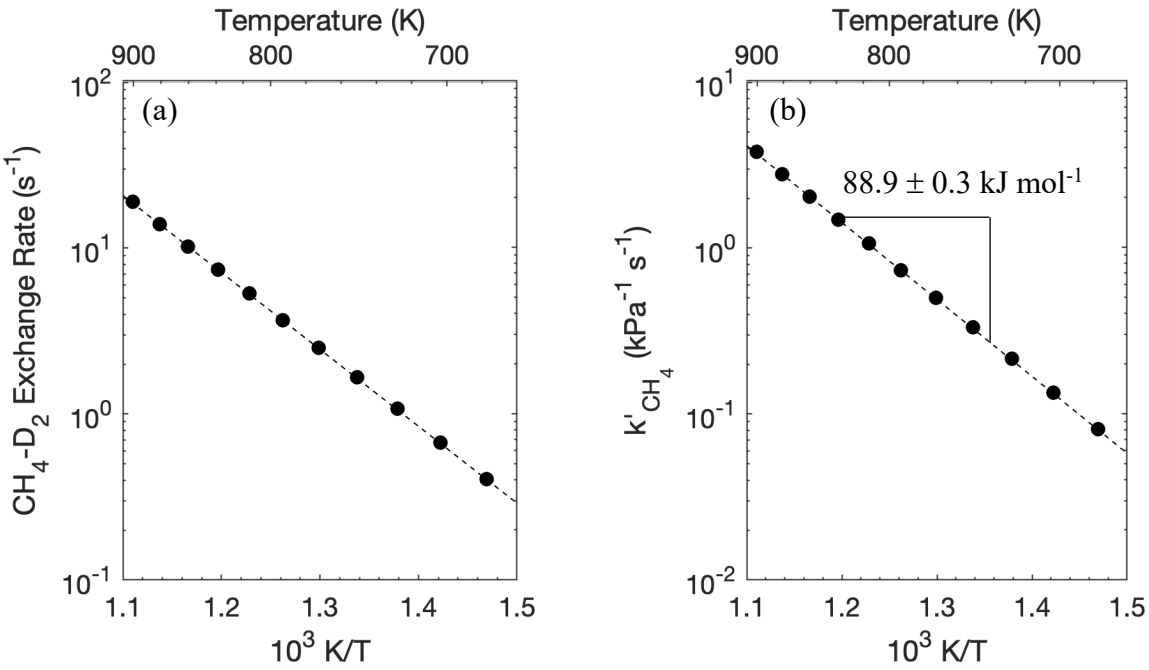

Figure 2. (a) CH_4-D_2 isotopic exchange rates and (b) k'_{CH_4} as a function of temperature for CH_4-D_2 reactions (5 kPa CH_4, 10 kPa D_2) on Pt/SiO_2. Dashed line represents linear regression of the data.

5.3.2.3 CH_4-D_2 Isotopic Exchange Rates on Pt/Na-LTA and Pt/Ca-LTA at Temperatures Between 673 and 900 K

CH_4-D_2 isotopic exchange rates were measured on Pt/Na-LTA and Pt/Ca-LTA at temperatures (673-900 K) and pressures (5 kPa CH_4, 10 kPa D_2) identical to those for Pt/SiO_2 experiments (Section 5.3.2.2). These rates (r_{eff}) (Fig. 3a) were significantly lower than those on Pt/SiO_2 at equivalent conditions (Fig. 2a), reflecting the presence of CH_4 mass transport limitations required for measurements of diffusion time constants. The temperature dependences of these data (Fig. 3a) correspond with apparent activation energies of 53 ± 1 kJ mol^{-1} and 48 ± 0.8 kJ mol^{-1} for Pt/Na-LTA and Pt/Ca-LTA, respectively. These energies represent the average of the diffusion (E_d) and reaction (E_A) energy barriers, as seen by writing Equation 5 (n = 1) in the following form:

$$r_{eff} = \sqrt{\frac{D_e}{k_v R^2 C_{A,s}^{n-1}}}\, r_{max} = \sqrt{\frac{D_0 \exp\left(-\frac{E_d}{RT}\right)}{k_{v,0} \exp\left(-\frac{E_A}{RT}\right) R^2}}\, k_{v,0} \exp\left(-\frac{E_A}{RT}\right)$$

$$= \sqrt{\frac{k_{v,0} D_0}{R^2}} \exp\left(-\frac{E_A + E_d}{2RT}\right) \qquad (20)$$

The isotopic exchange rates (r_{eff}) on Pt/Na-LTA and Pt/Ca-LTA were used to calculate effectiveness factors ($\lambda \equiv \frac{r_{eff}}{r_{max}}$, Eq. 5) by dividing by the rates on Pt/SiO_2 (r_{max}; Fig. 2a) at equivalent conditions; these values are shown in Figure 3b. Isotopic exchange rates and effectiveness factors (Fig. 3) on Pt/Na-LTA were smaller than for Pt/Ca-LTA by factors of 7.5-9.1

(Fig. 3). Pt/Ca-LTA catalysts were prepared by ion-exchange of Pt/Na-LTA catalysts and exhibited nearly identical crystallinities to the parent material (Section 5.6.1.1). These large differences in exchange rates are therefore unlikely to be caused by differences in textural properties. Instead, the exchange of monovalent Na^+ cations with divalent Ca^{2+} cations results in a decrease in the number of charge-balancing species within the micropores of LTA, thereby increasing the effective diffusivity D_e of CH_4 in such materials. These data (Fig. 3) thus reflect the lower resistances to molecular motion within the micropores of Pt/Ca-LTA compared to Pt/Na-LTA.

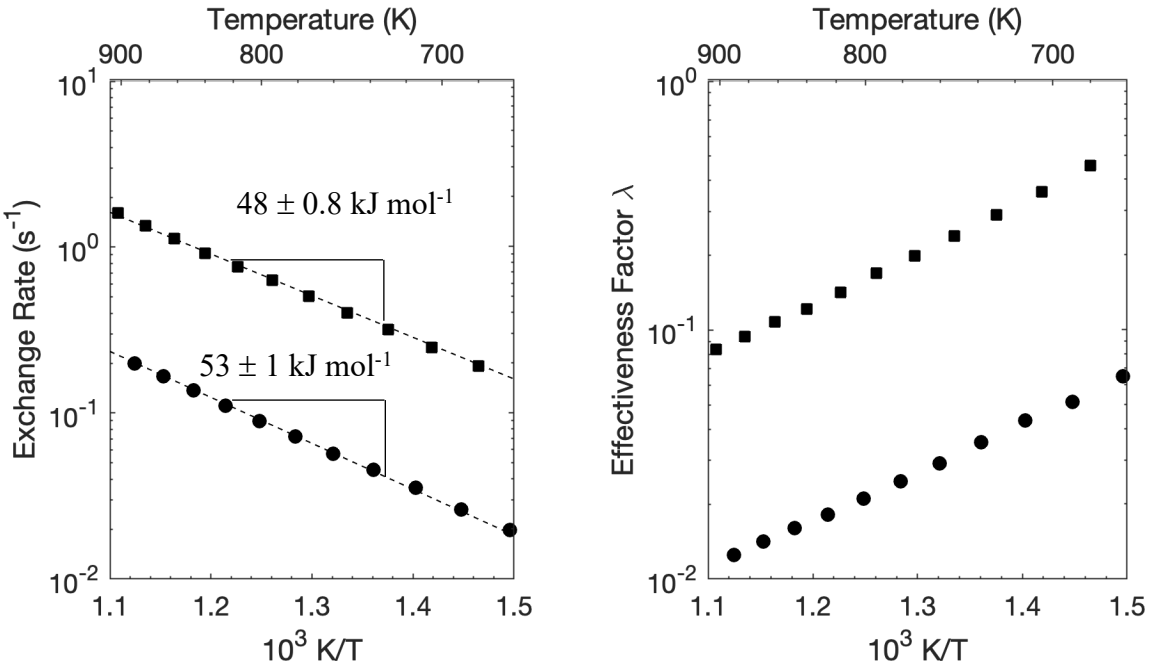

Figure 3. (a) CH_4-D_2 isotopic exchange rates and (b) effectiveness factors ($\lambda \equiv \frac{r_{eff}}{r_{max}}$) as a function of temperature (5 kPa CH_4, 10 kPa D_2) on (●) Pt/Na-LTA and (■) Pt/Ca-LTA samples. Effectiveness factors were calculated by dividing effective rates (r_{eff}) on Pt/Na-LTA and Pt/Ca-LTA by maximum rates (r_{max}) measured on Pt/SiO_2 at equivalent conditions.

5.3.2.4 Calculation of CH_4 Diffusion Time Constants in Pt/Na-LTA and Pt/Ca-LTA

The Thiele modulus for severely mass transport limited systems (λ < ~0.3)[6] is given by the inverse of the effectiveness factor (Eq. 5; Fig. 3b). These values for CH_4-D_2 isotopic exchange on Pt/Na-LTA and Pt/Ca-LTA are shown in Figure 4; they represent the square root of the product of the volumetric rate constant $\left(k_{v,CH_4}\right)$ for CH_4-D_2 isotopic exchange and the diffusion time constants $\left(\frac{R^2}{D_e}\right)$ for CH_4 in these materials (Eq. 5, n = 1). The values of k'_{CH_4} were previously measured as a function of temperature on Pt/SiO_2 (Fig. 2b). These values can be converted to a volumetric rate constant for Pt/Na-LTA and Pt/Ca-LTA samples using Equation 19 and parameters (D = 0.53, l_{Pt} = 0.01; Table 1) that are specific to Pt/Na-LTA and Pt/Ca-LTA. The solid density ρ of Pt/Na-LTA or Pt/Ca-LTA was calculated using the metal loading and the framework density

of Na-LTA (1.5174 g cm^3)[40] and Ca-LTA (1.4859 g cm^3, assuming complete Ca^{2+} exchange).[40] This treatment implicitly assumes that k'_{CH_4} is insensitive to particle size effects, which arise when reactions are more or less easily activated on coordinatively unsaturated edge and corner sites that become more prevalent as particle size decreases. C-H bond activation was shown to exhibit such structure sensitivity in previous studies;[33] these studies suggest that the smaller Pt particles in Pt/Na-LTA and Pt/Ca-LTA (2.4 nm) exhibit approximately 1.2 times higher activity than Pt particles on SiO_2 (3.2 nm). k_{v,CH_4} can therefore be corrected by multiplying the converted values by this factor of 1.2. These corrected values (k^*_{v,CH_4}) and the calculated Thiele moduli (ϕ; Fig. 4) were used to obtain $\left(\frac{R^2}{D_e}\right)$ values, as shown in Figure 5.

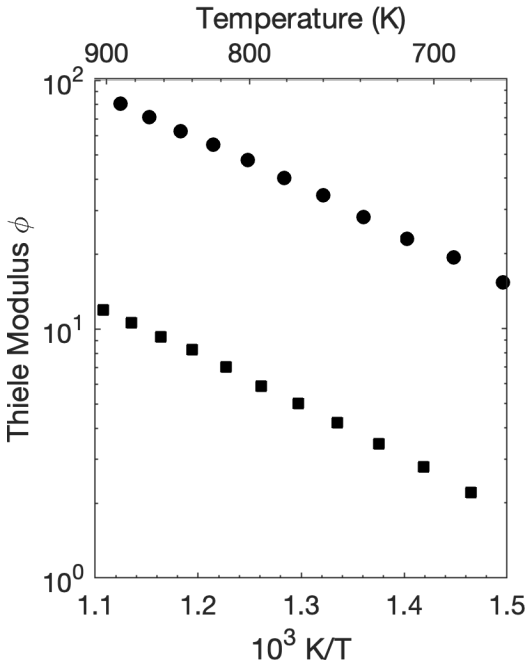

Figure 4. Thiele moduli for CH_4 in (●) Pt/Na-LTA and (■) Pt/Ca-LTA samples as a function of temperature calculated from CH_4-D_2 isotopic exchange effectiveness factors (λ) using Equation 5.

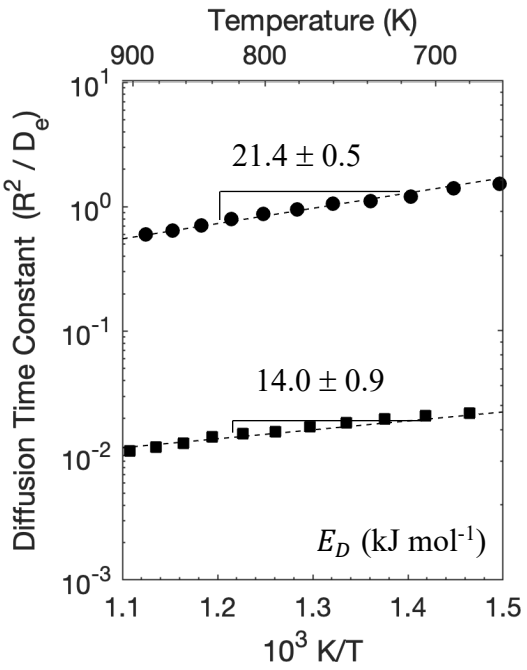

Figure 5. Diffusion time constants $\left(\frac{R^2}{D_e}\right)$ for CH_4 in (●) Pt/Na-LTA and (■) Pt/Ca-LTA samples as a function of temperature. Dashed lines represent linear regression of the data.

The data in Figure 5 reflect the temperature dependence of the diffusion coefficient (D_e) for CH_4 within the micropores of Pt/Na-LTA and Pt/Ca-LTA (Eq. 6). The slopes in Figure 5 therefore reflect the energy barriers (E_d) for CH_4 diffusion. These barriers are 21.4 ± 0.5 and 14.0 ± 0.9 kJ mol^{-1} in Pt/Na-LTA and Pt/Ca-LTA, respectively. The barrier for CH_4 diffusion in Pt/Na-LTA is in close agreement with values previously reported in the literature (18.9 ± 0.2 kJ mol^{-1}).[41] The energy barrier for diffusion in Pt/Ca-LTA (14.0 ± 0.9 kJ mol^{-1}) has not been documented in the literature, but the decrease in magnitude compared to Pt/Na-LTA (21.4 ± 0.5 kJ mol^{-1}) is consistent with a reduction in steric hindrances in Ca-LTA channels containing fewer charge-balancing cations.

The diffusion time constants in Figure 5 are on the order of 1 s for CH_4 in Pt/Na-LTA and 10^{-2} s in Pt/Ca-LTA. These diffusion timescales are too fast to be accurately measured by conventional macroscopic methods such as transient uptake measurements. The temperature dependence of the diffusion time constants $\left(\frac{R^2}{D_e}\right)$ in Figure 5 can be extrapolated to obtain diffusion time constants at other temperatures (Eq. 6). We can therefore assess the timescale of these diffusive processes at near-ambient conditions, assuming such extrapolations are accurate. These extrapolations gave values of 183 ± 41 and 0.48 ± 0.2 s for Pt/Na-LTA and Pt/Ca-LTA at 293 K, respectively. These diffusion time constants indicate that while the diffusion of CH_4 in these Pt/Na-LTA samples can be measured at ambient conditions, diffusion in Pt/Ca-LTA samples is still too fast be measured reliably using conventional uptake measurements. The isotopic exchange method presented here is thus not only able to measure diffusion time constants much closer to practical reaction temperatures, but is also one of the only methods that can be used even for extremely fast diffusing systems.

5.3.3 Measurement of H_2O Diffusion Time Constants $\left(\frac{R^2}{D_e}\right)$ in Pt/Na-LTA and Pt/Ca-LTA Using H_2O-D_2 Isotopic Exchange

5.3.3.1 Kinetic Dependence of H_2O-D_2 Isotopic Exchange Rates on H_2O and D_2 Pressure on Pt/γ-Al_2O_3 and Implications for Measuring H_2O Diffusion Time Constants

Diffusion time constants $\left(\frac{R^2}{D_e}\right)$ for H_2O in Pt/Na-LTA and Pt/Ca-LTA were obtained using isotopic exchange measurements and mathematical treatments analogous to those for CH_4 (Section 5.3.2). H_2O-D_2 isotopic exchange rates were measured on samples of Pt/γ-Al_2O_3 as H_2O and D_2 pressures were varied (2-30 kPa H_2O, 2-40 kPa D_2; 623 K). Pt/γ-Al_2O_3 was used in these kinetic measurements instead of Pt/SiO_2 because our prior work (Chapter 4) showed that Pt/SiO_2 exhibits lower rates after exposure to H_2O compared to Pt/γ-Al_2O_3 and Pt black, suggesting that SiO_2 may poison metal surfaces in hydrothermal conditions.[42] Isotopic exchange rates on Pt/γ-Al_2O_3 exhibited first-order dependences that transition to sublinear dependences as pressures increase for both H_2O (2-30 kPa) and D_2 (2-40 kPa) (Fig. 6; 623 K). These kinetic dependences are consistent with those reported in our previous work on H_2O-D_2 exchange pathways on Pt-based catalysts (Chapter 4); our studies showed that H_2O-D_2 exchange proceeds via the reaction of D_2 and molecularly adsorbed H_2O for temperatures lower than 900 K. The elementary steps for this reaction are shown in Scheme 1, and the rate of H_2O-D_2 exchange is given by (Chapter 4):

$$-r_{H_2O,f} = r_{HDO,f} + r_{D_2O,f} = \frac{k_6(H_2O)(D_2)}{\left((H_2O) + \frac{\sqrt{K_3}}{K_5}\sqrt{(D_2)}\right)\left(1 + \frac{k_6}{k_{-5}}(D_2)\right)} \quad (21)$$

where k_i and K_i are rate and equilibrium constants corresponding to those shown in Scheme 1.

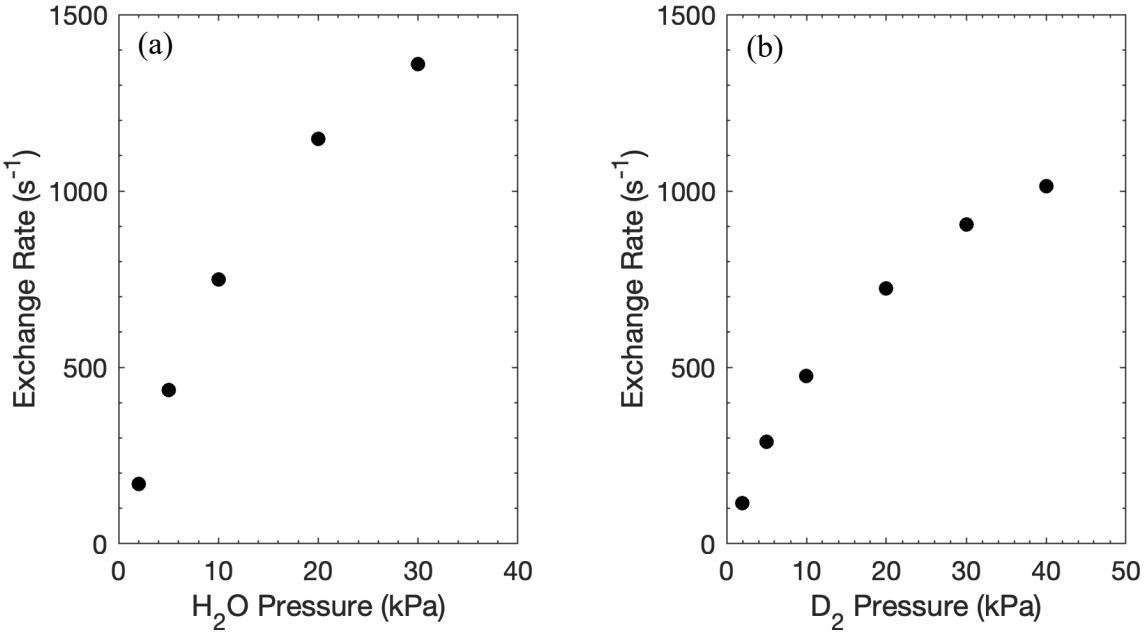

Figure 6. H_2O-D_2 isotopic exchange rates on Pt/γ-Al_2O_3 as a function of (a) H_2O pressure (40 kPa D_2) and (b) D_2 pressure (10 kPa H_2O) at 623 K.

$$D_2 + 2* \underset{k_{-3}}{\overset{k_3}{\rightleftharpoons}} 2D* \quad [1.1]$$

$$H_2O + * \underset{k_{-5}}{\overset{k_5}{\rightleftharpoons}} H_2O* \quad [1.2]$$

$$HDO + * \xleftarrow[k_{-5}]{} HDO* \quad [1.3]$$

$$D_2O + * \xleftarrow[k_{-5}]{} D_2O* \quad [1.4]$$

$$D_2 + H_2O* \xrightarrow{k_6} HD + HDO* \quad [1.5]$$

$$D_2 + HDO* \xrightarrow{k_6} HD + D_2O* \quad [1.6]$$

Scheme 1. Elementary steps for H_2O-D_2 isotopic exchange.

The form of Equation 21 does not correspond with the form of the rate equation described in Equation 4, so Equation 5 cannot be used to calculate the Thiele modulus from effectiveness factors for the general case. Isotopic exchange rates at H_2O pressures lower than 10 kPa, however,

exhibited near-first-order kinetics (Fig. 6a). These data reflect (H_2O) values that are much smaller than $\frac{\sqrt{K_3}}{K_5}\sqrt{(D_2)}$ (denominator of Eq. 21), allowing Equation 21 to be simplified to:

$$-r_{H_2O,f} = r_{HDO,f} + r_{D_2O,f} = \frac{k_6(H_2O)(D_2)}{\left(\frac{\sqrt{K_3}}{K_5}(D_2)^{\frac{1}{2}} + \frac{k_6}{k_{-5}}\frac{\sqrt{K_3}}{K_5}(D_2)^{\frac{3}{2}}\right)} \quad (22)$$

at low H_2O pressures. This equation still, however, contains a dependence on D_2 pressure. The diffusion rate of D_2 and its effect on H_2O-D_2 exchange rates must therefore also be considered when analyzing effective rates and effectiveness factors. The diffusion of D_2 can be handled separately from H_2O using H_2-D_2 exchange experiments and is addressed next.

5.3.3.2 H_2-D_2 Isotopic Exchange Rates on Pt/γ-Al_2O_3 and Pt/Na-LTA

H_2-D_2 exchange rates were measured on Pt/γ-Al_2O_3 and Pt/Na-LTA (10 kPa H_2, 10 kPa D_2) at temperatures between 573 and 900 K to probe for mass transport limitations in D_2 (and H_2) in Pt/Na-LTA and to determine effectiveness factors. H_2-D_2 exchange rates, however, were nearly identical for both samples (Fig. 7a), as shown by effectiveness factors ($\lambda = \frac{r_{Pt/Na-LTA}}{r_{Pt/SiO_2}}$; Fig. 7b) that were near unity at all temperatures (1.05 ± 0.08, 573-900 K). These data (Fig. 7b) indicate that there are no gradients in D_2 (or H_2), and therefore no mass transport limitations, within the micropores of Pt/Na-LTA during H_2-D_2 isotopic exchange reactions at these conditions. Pt/Ca-LTA, which contains fewer charge-balancing cations, is expected to exhibit even less mass transport resistance. H_2-D_2 isotopic exchange rates were at least a factor of 2 faster than H_2O-D_2 exchange rates at 623 K (Fig. 6 vs. Fig. 7). D_2 mass transport limitations are therefore not expected during H_2O-D_2 isotopic exchange experiments on Pt/Na-LTA and Pt/Ca-LTA, leading to a flat D_2 concentration profile within the micropores of the zeolites. The absence of concentration gradients in D_2 means that the dependence on D_2 in Equation 22 can be lumped into an effective rate constant (k'_{H_2O}):

$$-r_{H_2O,f} = r_{HDO,f} + r_{D_2O,f} = k'_{H_2O}(H_2O) \quad (23)$$

This equation matches the form of Equation 4 (n = 1); the Thiele modulus and diffusion time constants can therefore be calculated from effective H_2O-D_2 exchange rates on Pt/Na-LTA and Pt/Ca-LTA using Equation 5 as long as the D_2 pressure is kept constant and H_2O pressures are in first-order regime ((H_2O) < 10 kPa; Fig. 7a) throughout H_2O-D_2 isotopic exchange experiments.

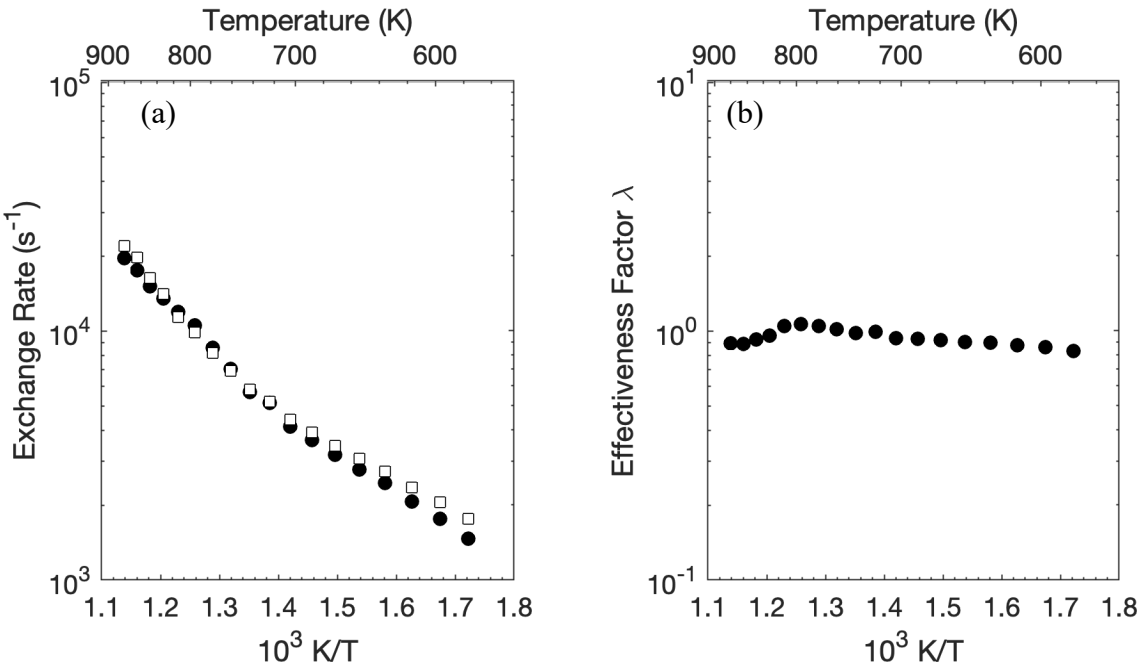

Figure 7. (a) H_2-D_2 isotopic exchange rates on (l) Pt/γ-Al_2O_3 and (□) Pt/Na-LTA (10 kPa H_2, 10 kPa D_2) and (b) effectiveness factors $\left(\lambda = \frac{r_{Pt/Na-LTA}}{r_{Pt/SiO_2}}\right)$ as a function of temperature.

5.3.3.3 Effect of Temperature on H_2O-D_2 Isotopic Exchange Rates and k'_{H_2O} on Pt/γ-Al_2O_3, Pt/Na-LTA, and Pt/Ca-LTA

H_2O-D_2 isotopic exchange rates (5 kPa H_2O, 40 kPa D_2, 573-823 K) were measured on Pt/γ-Al_2O_3, Pt/Na-LTA, and Pt/Ca-LTA to obtain the effective rate constant (k'_{H_2O}; Eq. 23) and effectiveness factors (λ; Eq. 5) as functions of temperature (Fig. 8). The temperature dependence of k'_{H_2O} (Fig. 8a) reflects an activation energy barrier of 15.4 ± 0.4 kJ mol^{-1}, in agreement with the value previously measured (15.6 ± 0.1 kJ mol^{-1}) for H_2O-D_2 reactions on Pt black (5 kPa H_2O, 40 kPa D_2; 423-900 K) (Chapter 4). H_2O-D_2 isotopic exchange rates were about a factor of 10 lower on Pt/Na-LTA and Pt/Ca-LTA than on Pt/γ-Al_2O_3 (Fig. 7b), confirming the presence of H_2O mass transport limitations. As was the case for CH_4, the rate constant k'_{H_2O} (Eq. 23) was converted into a volumetric rate constant k_{v,H_2O} using Equation 19 and used along with the measured effectiveness factors (Fig. 8b) to calculate $\left(\frac{R^2}{D_e}\right)$ values for H_2O in Pt/Na-LTA and Pt/Ca-LTA using Equation 5.

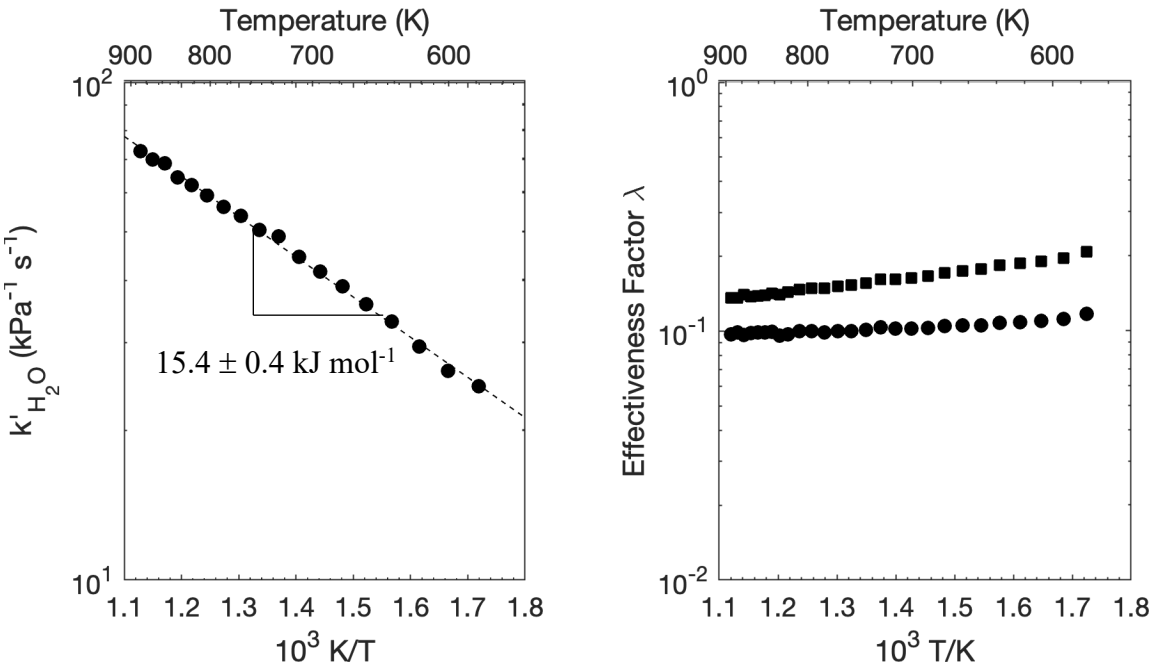

Figure 8. (a) k'_{H_2O} as a function of temperature (5 kPa H_2O, 40 kPa D_2) on Pt/γ-Al_2O_3. (b) H_2O-D_2 effectiveness factors on Pt/Na-LTA and Pt/Ca-LTA as a function of temperature, calculated by dividing exchange rates on Pt/Na-LTA and Pt/Ca-LTA by those measured on Pt/γ-Al_2O_3 (5 kPa H_2O, 40 kPa D_2)

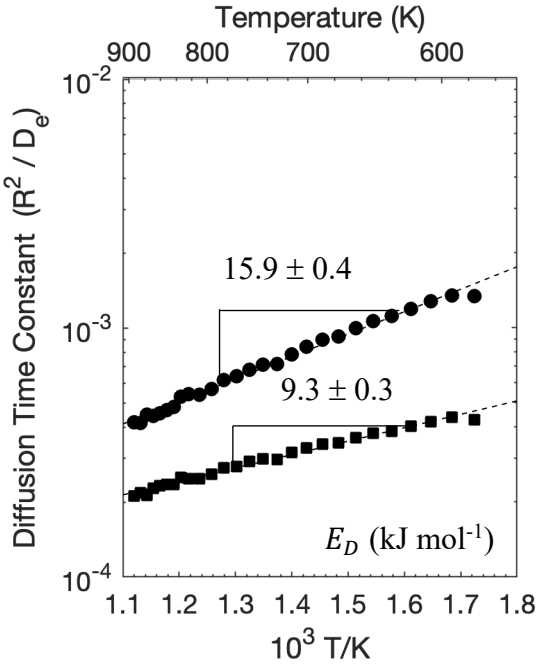

Figure 9. Diffusion time constants $\left(\frac{R^2}{D_e}\right)$ for H_2O in (●) Pt/Na-LTA and (■) Pt/Ca-LTA samples as a function of temperature. Dashed lines represent linear regression of the data.

H_2O exhibited smaller diffusion time constants $\left(\frac{R^2}{D_e}\right)$ than CH_4 (Fig. 5 and 9) in both Pt/Na-LTA and Pt/Ca-LTA, indicating that H_2O diffuses much more readily through LTA micropores. H_2O also exhibited lower energy barriers for diffusion (E_d, Eq. 6; 15.9 ± 0.4 and 9.3 ± 0.3 kJ mol^{-1} in Pt/Na-LTA and Pt/Ca-LTA, respectively) compared to CH_4 (21.4 ± 0.5 and 14.0 ± 0.9 kJ mol). These results are consistent with the smaller kinetic diameter of H_2O compared to CH_4 (0.264 vs. 0.376 nm), which leads to less molecular and framework distortion as H_2O molecules diffuse through the micropores of the zeolite.[5] The energy barrier for H_2O diffusion in Pt/Na-LTA (15.9 ± 0.4 kJ mol^{-1}) is higher than values previously reported from membrane permeation studies (3.23 ± 0.17 kJ mol^{-1})[43] but lower than those predicted from molecular dynamic simulations (19.5 kJ mol^{-1}).[44] Such large differences in reported energy barriers support the need to measure diffusion time constants at or near reaction conditions to avoid errors from extrapolation. These presented data demonstrate the generality of the isotopic exchange technique for measuring diffusion time constants and its applicability to a wide-range of molecules and reactive systems.

5.4 Conclusions

Predicting and modelling concentration gradients and effective reaction rates in microporous materials requires accurate diffusion time constants ($\frac{R^2}{D_e}$ values) at reaction conditions. Measuring these values at reaction temperatures, however, is often infeasible because the diffusive processes occur on timescales that are too fast to be accurately captured by conventional methods such as transient adsorption studies. Diffusion time constants are therefore often extrapolated from ambient or subambient conditions, which can lead to significant error. Here, we presented an alternative method for measuring $\frac{R^2}{D_e}$ values in microporous materials using effectiveness factors derived from isotopic exchange experiments rather than from chemical conversions. Such exchange reactions are more flexible in their application, as they can be used to probe, in theory, the diffusion of any molecule. The isotopic exchange methods were demonstrated here for CH_4 and H_2O molecules within Na^+-exchanged and Ca^{2+}-exchanged LTA samples at temperatures that are relevant for steam-methane reforming reactions (500-900 K). The energy barriers for diffusion obtained from the temperature dependences of CH_4 and H_2O diffusion time constants ($\frac{R^2}{D_e}$ values) were in agreement with those previously reported in the literature. The isotopic exchange technique presented here is applicable to a wide range of guest-host systems, with the only requirement being that the exchange rate be sufficiently fast to cause significant mass transport limitations within the material of interest at reaction conditions.

5.5 Acknowledgments

This study was funded by Chevron Corporation and a Chevron Graduate Student Research Fellowship.

5.6 Supporting Information

5.6.1 Catalyst Characterization

5.6.1.1 X-ray Diffractograms of LTA, Pt/Na-LTA, and Pt/Ca-LTA Samples and Zeolite Crystallinities

X-ray diffractograms of Na-LTA, Pt/Na-LTA, and Pt/Ca-LTA samples mixed in a 1:1 mass ratio with MgO, as an internal standard, were obtained to confirm the synthesis of LTA crystallites and the absence of large Pt agglomerates (> 10 nm). These diffractograms are shown in Figure SI-1. Reference patterns for LTA[45] and Pt[46] are also included. All synthesized LTA samples (Na-LTA, Pt/Na-LTA and Pt/Ca-LTA) showed reflections typical for LTA zeolites, indicating the successful synthesis of such crystallites. Pt/Na-LTA and Pt/Ca-LTA did not exhibit the reflections for bulk Pt, indicating the absence of large Pt agglomerates (> 10 nm) in these samples.

The crystallinity of 1% Pt/Na-LTA and 1% Pt/Ca-LTA samples were determined from the integration of the three most intense Bragg lines (at 27.12°, 30.13°, and 34.25°) in the diffractograms (Figure SI-1), using Na-LTA crystallites without encapsulated Pt as the standard. Pt/Na-LTA and Pt/Ca-LTA samples exhibited crystallinities of 80% and 74%, respectively. Samples containing Pt showed lower crystallinities than samples without Pt, likely reflecting local disruptions in the zeolite framework around Pt metal nanoparticles (~ 2 nm, Table 1) that are larger than size of LTA-cages (1.1 nm). The crystallinity of Pt/Na-LTA and Pt/Ca-LTA samples were similar within experimental error, indicating little to no loss in crystallinity following Ca^{2+} ion-exchange procedures (Section 5.2.1).

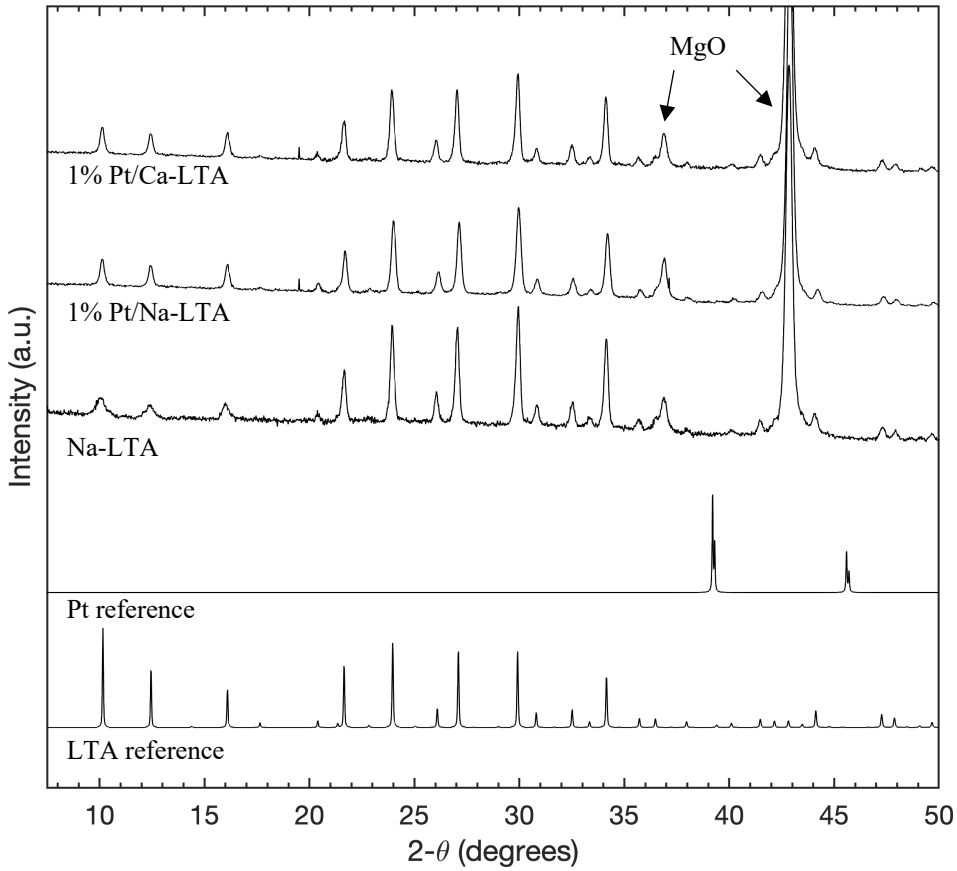

Figure SI-1. X-ray diffractograms for Na-LTA, 1% Pt/Na-LTA, and 1% Pt/Ca-LTA samples mixed in a 1:1 mass ratio with MgO, used as an internal standard.

5.6.2 Transmission Electron Micrographs of Pt/Na-LTA

Transmission electron micrographs of Pt/Na-LTA (Fig. SI-2) were used to characterize particle size distributions using Equation 9.

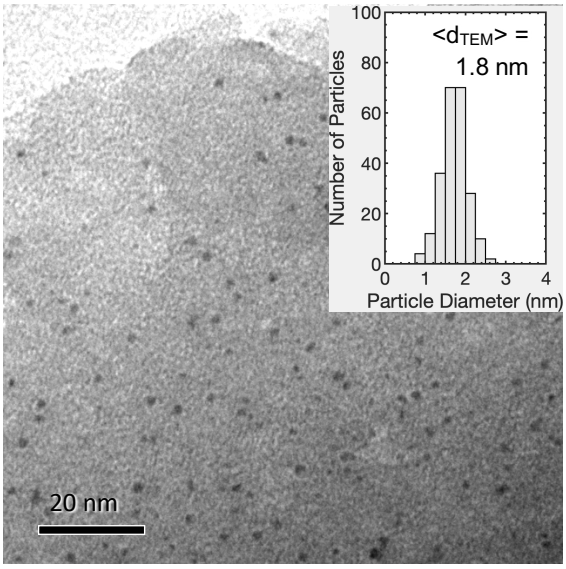

Figure SI-2. Transmission electron micrographs and Pt nanoparticle size distribution for Pt/Na-LTA samples.

5.7 References

1. Corma, A., From microporous to mesoporous molecular sieve materials and their use in catalysis. *Chem. Rev.* **1997**, *97*, 2373-2419.
2. Karger, J.; Valiullin, R.; Enke, D.; Glaser, R., Measuring Mass Transport in Hierarchical Pore Systems. *Mesoporous Zeolites: Preparation, Characterization and Applications* **2015**, 385-423.
3. Kärger, J.; Vasenkov, S.; Auerbach, S., Diffusion in Zeolites. In *Handbook of Zeolite Science and Technology*, CRC Press: 2003; pp 446-548.
4. Maxwell, I. E., Shape-Selective Catalysis and Process Technology Via Molecular Inclusion in Zeolites. *Journal of Inclusion Phenomena* **1986**, *4*, 1-29.
5. Sircar, S.; Myers, A., Gas Separation by Zeolites. In *Handbook of Zeolite Science and Technology*, CRC Press: 2003.
6. Froment, G. F.; Bischoff, K. B., *Chemical reactor analysis and design*; Wiley: New York, 1979.
7. Bischoff, K. B., Effectiveness Factors for General Reaction Rate Forms. *AlChE J.* **1965**, *11*, 351-355.
8. Thiele, E. W., Relation between Catalytic Activity and Size of Particle. *Industrial & Engineering Chemistry* **1939**, *31*, 916-920.
9. Ruthven, D. M.; Post, M. F. M., Diffusion in Zeolite Molecular Sieves. *Introduction to Zeolite Science and Practice* **2007**, *168*, 737-785.
10. Jobic, H.; Bee, M.; Caro, J.; Bulow, M.; Karger, J., Molecular Self-Diffusion of Methane in Zeolite Zsm-5 by Quasi-Elastic Neutron-Scattering and Nuclear Magnetic-Resonance Pulsed Field Gradient Technique. *Journal of the Chemical Society-Faraday Transactions I* **1989**, *85*, 4201-4209.
11. Delara, E. C.; Kahn, R.; Mezei, F., Determination of the Intracrystalline Diffusion-Coefficient of Methane in a-Zeolites by Means of Neutron Spin-Echo Experiments. *Journal of the Chemical Society-Faraday Transactions I* **1983**, *79*, 1911-1920.
12. Resing, H. A.; Murday, J. S., Nmr Relaxation and Molecular Motion in Zeolites. *Adv. Chem. Ser.* **1973**, 414-429.
13. Resing, H. A.; Thompson, J. K., Nmr Relaxation in Adsorbed Molecules .5. Sf6 on Faujasite - Dipolar Coupling of Fluorine Nuclei to Ferric-Ion Impurities. *J. Chem. Phys.* **1967**, *46*, 2876-2880.
14. Fritzsche, S., The influence of changes in the framework on the diffusion in zeolites. Molecular dynamics simulations. *Phase Transitions* **1994**, *52*, 169-190.
15. Suffritti, G. B.; Demontis, P., Molecular dynamics study of zeolites: The role of disorder. *Phase Transitions* **1994**, *52*, 191-211.
16. Pfeifer, H. In *Nuclear Magnetic Resonance and Relaxation of Molecules Adsorbed on Solids*, NMR Basic Principles and Progress / NMR Grundlagen und Fortschritte, Berlin, Heidelberg, 1972//; Diehl, P.; Fluck, E.; Kosfeld, R., Eds. Springer Berlin Heidelberg: Berlin, Heidelberg, 1972; pp 53-153.
17. Karger, J., Diffusion Study of Water on 13x, 4a and 5a Zeolites Using Pulsed Field Gradient Technique. *Zeitschrift Fur Physikalische Chemie-Leipzig* **1971**, *248*, 27-&.
18. Lechert, H.; Wittern, K. P.; Schweitzer, W., Nmr-Studies of Mobility of Aromatics in Faujasites. *Acta Physica Et Chemica* **1977**, *24*, 201-206.
19. Barrer, R. M., Migration in crystal lattices. *Trans. Faraday Society* **1941**, *37*, 0590-0599.

20. Barrer, R. M., Zeolites and clay minerals as sorbents and molecular sieves. *Chem. Ing. Tech.* **1980**, *52*, 366-366.
21. Yasuda, Y., Frequency-Response Method for Study of Kinetic-Behavior of a Gas-Surface System .1. Theoretical Treatment. *J. Phys. Chem.* **1976**, *80*, 1867-1869.
22. Vandenbegin, N. G.; Rees, L. V. C., Diffusion of Hydrocarbons in Silicalite Using a Frequency-Response Method. *Zeolites : Facts, Figures, Future, Pts a & B* **1989**, *49*, 915-924.
23. Wernick, D. L.; Osterhuber, E. J., *Diffusional transition in zeolite NaX: 1. single crystal gas permeation studies*; ; Corporate Research, Exxon Research and Engineering Company, Linden, NJ, 1984.
24. Haag, W. O.; Lago, R. M.; Weisz, P. B., Transport and Reactivity of Hydrocarbon Molecules in a Shape-Selective Zeolite. *Faraday Discuss.* **1981**, *72*, 317-330.
25. Post, M.; Van Amstel, J.; Kouwenhoven, H. In *Diffusion and catalytic reaction of 2, 2-dimethylbutane in ZSM-5 Zeolite*, Proc. 6th Int. Zeolite Conf, 1984.
26. Hufton, J. R.; Brandani, S.; Ruthven, D. M., Measurement of Intracrystalline Diffusion by Zero Length Column Tracer Exchange. *Zeolites and Related Microporous Materials: State of the Art 1994* **1994**, *84*, 1323-1330.
27. Ma, Y. H.; Mancel, C., Diffusion of Hydrocarbons in Mordenites by Gas-Chromatography. *Adv. Chem. Ser.* **1973**, 392-402.
28. Sarma, P. N.; Sarma, N.; Haynes, H. W., Application of Gas-Chromatography to Measurements of Diffusion in Zeolites. *Adv. Chem. Ser.* **1974**, 205-217.
29. Shah, D. B.; Ruthven, D. M., Measurement of Zeolitic Diffusivities and Equilibrium Isotherms by Chromatography. *AlChE J.* **1977**, *23*, 804-809.
30. Eic, M.; Ruthven, D. M., Diffusion of Linear Paraffins and Cyclohexane in Nax and 5a Zeolite Crystals. *Zeolites* **1988**, *8*, 472-479.
31. Ruthven, D. M.; Eic, M., Intracrystalline Diffusion in Zeolites. *ACS Symp. Ser.* **1988**, *368*, 362-375.
32. Fogler, H. S., *Elements of Chemical Reaction Engineering*; Prentice Hall PTR, 2006.
33. Wei, J.; Iglesia, E., Mechanism and Site Requirements for Activation and Chemical Conversion of Methane on Supported Pt Clusters and Turnover Rate Comparisons among Noble Metals. *J. Phys. Chem. B* **2004**, *108*, 4094-4103.
34. Choi, M.; Wu, Z. J.; Iglesia, E., Mercaptosilane-Assisted Synthesis of Metal Clusters within Zeolites and Catalytic Consequences of Encapsulation. *Journal of the American Chemical Society* **2010**, *132*, 9129-9137.
35. Bergeret, G.; Gallezot, P., Particle Size and Dispersion Measurements. In *Handbook of Heterogeneous Catalysis*, Ertl, G.; Knözinger, H.; Schüth, F.; Weitkamp, J., Eds. Wiley: 2008; pp 738-765.
36. Almithn, A. S.; Hibbitts, D. D., Supra-Monolayer Coverages on Small Metal Clusters and Their Effects on H-2 Chemisorption Particle Size Estimates. *AlChE J.* **2018**, *64*, 3109-3120.
37. Hanson, R. M.; Green, S. M. E., *Introduction to molecular thermodynamics*; University Science Books: Sausalito, Calif., 2008.
38. Satterfield, C. N., *Mass transfer in heterogeneous catalysis*; M.I.T. Press: Cambridge, Mass., 1969.
39. Welty, J. R.; Wicks, C. E.; Wilson, R. E., *Fundamentals of momentum, heat, and mass transfer*; J. Wiley: New York, 1969.
40. Wynnyk, K. G.; Hojjati, B.; Marriott, R. A., High-Pressure Sour Gas and Water Adsorption on Zeolite 13X. *Ind. Eng. Chem. Res.* **2018**, *57*, 15357-15365.

41. Haq, N.; Ruthven, D. M., Chromatographic Study of Sorption and Diffusion in 4a Zeolite. *J. Colloid Interface Sci.* **1986**, *112*, 154-163.
42. Huber, G. W.; Guymon, C. G.; Conrad, T. L.; Stephenson, B. C.; Bartholomew, C. H., Hydrothermal stability of Co/SiO2 Fischer-Tropsch synthesis catalysts. *Catalyst Deactivation 2001, Proceedings* **2001**, *139*, 423-430.
43. Zhu, W.; Gora, L.; van den Berg, A. W. C.; Kapteijn, F.; Jansen, J. C.; Moulijn, J. A., Water vapour separation from permanent gases by a zeolite-4A membrane. *J. Membr. Sci.* **2005**, *253*, 57-66.
44. Demontis, P.; Gulin-Gonzalez, J.; Jobic, H.; Suffritti, G. B., Diffusion of Water in Zeolites Na A and NaCa A: A Molecular Dynamics Simulation Study. *J. Phys. Chem. C* **2010**, *114*, 18612-18621.
45. Gramlich, V.; Meier, W. M., Crystal Structure of Hydrated Naa - Detailed Refinement of a Pseudosymmetric Zeolite Structure. *Zeitschrift Fur Kristallographie Kristallgeometrie Kristallphysik Kristallchemie* **1971**, *133*, 134-149.
46. Kasper, J. S.; Lonsdale, K.; International Union of Crystallography., *International tables for X-ray crystallography*, 3rd ed.; Published for the International Union of Crystallography by D. Reidel Pub. Co.: Dordrecht ; Boston, 1985.

Chapter 6

Exploiting Mass Transport Limitations in Pt/Na-LTA and Pt/Ca-LTA to Control Reactant Ratios During Methane Reforming Reactions

Abstract

Zeolites exhibit unique sieving properties that can be exploited to provide preferential access to active sites located within cages and channels of molecular dimensions, thereby altering intracrystalline reactant ratios from their prevalent values in the external fluid phase. These properties were exploited here for CH_4-H_2O reactions, which tend to form carbon deposits at stoichiometric and substoichiometric H_2O/CH_4 ratios. CH_4-H_2O reaction rates at 873 K were measured as a function of time on Pt nanoparticles supported on γ-Al_2O_3 or encapsulated within Na-LTA and Ca-LTA crystallites at several CH_4 (20, 40 kPa) and H_2O (5-40 kPa) pressures (873 K, 5 kPa H_2). Pt/Na-LTA and Pt/Ca-LTA exhibited initial reaction rates that were factors of 161 and 13 lower than on Pt/γ-Al_2O_3 at equivalent conditions, reflecting the presence of CH_4 concentration gradients required to alter intracrystalline reactant ratios. Deactivation rates on Pt/γ-Al_2O_3 were linearly dependent on a ratio of pressures $\left(\psi = \frac{(CH_4)(H_2)}{(H_2O)}\right)$ that uniquely determines the thermodynamic activity of carbon on the metal surface. Deactivation rates on Pt/Na-LTA and Pt/Ca-LTA were undetectable for ψ values below 10 and exhibited deactivation rates that were 3-8 times slower than on Pt/γ-Al_2O_3 for ψ values between 10 and 40. These improvements over the conventionally-supported catalyst reflect the high H_2O/CH_4 ratios within the zeolite pores, as indicated by extensive modelling of the CH_4 and H_2O concentration profiles. Simulations of deactivation behavior are used to provide additional insight into further optimizing these materials. The strategies for exploiting differences in diffusivity in zeolites, demonstrated here for CH_4 reforming reactions, are generally applicable to reactions where the selective access for smaller reactants is desirable.

6.1 Introduction

Zeolites and zeotypes are crystalline microporous materials with well-defined pore and cage structures unique to each framework type.[1] These materials have found wide use in separation and catalytic processes[1-11] because of their unique ability to selectively sieve and adsorb molecules. These sieving properties can be tuned by varying the chemical composition (e.g., Si/Al ratio) of the materials and by post-synthetic cation-exchange procedures.[12] Zeolites and zeotypes are frequently used as solid-acid catalysts for the cracking of carbon-carbon bonds, skeletal isomerizations, and polymerization reactions among other acid-catalyzed chemistries.[13] These microporous materials have also found increasing use in metal-catalyzed chemistries by encapsulating metal nanoparticles in voids within the framework.[14] The encapsulation of metal clusters provides many advantages over conventional metal-oxide supported metal nanoparticles,[14] including the protection of encapsulated metal nanoparticles from contact with bulky catalytic poisons,[11, 15] the selective retention of bulky products until they fragment or isomerize to form species that diffuse more readily through the pores of the framework,[16] and the stabilization of specific transition states via van der Waals interactions with intracrystalline pores and cages.[17] The framework structure surrounding metal nanoparticles also provides significant resistance against agglomeration of the nanoparticles, allowing them to retain their small size at temperatures that would otherwise lead to sintering and a concomitant loss in active surface area.[11, 15] The combination of metal-catalyzed chemistries with the sieving properties of zeolites (and zeotypes) represents an area of significant interest.

Zeolites and zeotypes sieve and select molecules based on their relative diffusivities. These diffusivities depend on the geometry of the zeolite framework, the prevalence of charge-balancing ions, and the size and shape of the diffusing molecule.[7, 9, 18] Differences in diffusivity can thus be exploited to alter reactant/product concentration ratios along zeolite channels. Such control can benefit CH_4-H_2O reactions, which are known to form carbonaceous deposits on metal surfaces at stoichiometric feed ratios ($CH_4/H_2O = 1$).[19] These reactions are mediated by a common series of elementary steps for Ru,[20] Rh,[21] Ir,[22] Pt,[23] and Ni[24] catalysts (Scheme 1). Application of the pseudo-steady-state approximation (PSSA) to C* gives an expression for the surface carbon activity $(a_{C^*})_s$ at conditions far from equilibrium (Chapter 2):

$$\frac{(a_{C^*})_s}{(L)} = \beta\psi \tag{1}$$

$$\beta = \frac{k_1 K_8}{k_6 K_9 K_{10}} \tag{2}$$

$$\psi = \frac{(CH_4)(H_2)}{(H_2O)} \tag{3}$$

Higher surface carbon activities $(a_{C^*})_s$ lead to greater carbon formation rates.[25] Industrial processes therefore typically utilize substoichiometric CH_4/H_2O feed ratios of 0.2-0.33 to decrease the surface carbon activity (Chapter 2), thereby suppressing carbon formation and deactivation. Such operations away from stoichiometry, however, requires the incorporation of energy-intensive recycle operations.[19] An alternative strategy that allows the utilization of stoichiometric feeds while also suppressing carbon formation is therefore desirable.

$$CH_4 + 2* \underset{k_{-1}}{\overset{k_1}{\rightleftharpoons}} CH_3* + H* \quad [1.1]$$

$$CH_3* + * \underset{k_{-2}}{\overset{k_2}{\rightleftharpoons}} CH_2* + H* \quad [1.2]$$

$$CH_2* + * \underset{k_{-3}}{\overset{k_3}{\rightleftharpoons}} CH* + H* \quad [1.3]$$

$$CH* + * \underset{k_{-4}}{\overset{k_4}{\rightleftharpoons}} C* + H* \quad [1.4]$$

$$CO_2 + 2* \overset{K_5}{\rightleftharpoons} CO* + O* \quad [1.5]$$

$$C* + O* \underset{k_{-6}}{\overset{k_6}{\rightleftharpoons}} CO* + * \quad [1.6]$$

$$CO* \overset{K_7}{\rightleftharpoons} CO + * \quad [1.7]$$

$$H_2 + 2* \overset{K_8}{\rightleftharpoons} 2H* \quad [1.8]$$

$$H_2O + 2* \overset{K_9}{\rightleftharpoons} OH* + H* \quad [1.9]$$

$$OH* + * \overset{K_{10}}{\rightleftharpoons} O* + H* \quad [1.10]$$

Scheme 1. Elementary steps for CH_4 reforming reactions on metal catalysts. Open circles on arrows denote quasi-equilibrated reactions.

Our prior measurements of diffusion time constants $\left(\frac{R^2}{D_e}\right)$ using isotopic exchange methods showed that the diffusion of H_2O in Na-LTA and Ca-LTA zeolites is much faster than CH_4 (Chapter 5). This difference in diffusivity can be exploited to decrease intracrystalline CH_4/H_2O ratios and surface carbon activities (Eq. 1-3), thereby suppressing carbon formation and deactivation. This control over CH_4/H_2O ratios at the catalyst level instead of at the process level also allows reactant feeds to be maintained at stoichiometric compositions. CH_4-H_2O reactions are carried out on Pt/γ-Al_2O_3, Pt/Na-LTA, and Pt/Ca-LTA catalyst samples in the present study at 873 K at various ψ (2.5-40 kPa, Eq. 3) ratios. CH_4-H_2O reaction rates on Pt/Na-LTA and Pt/Ca-LTA are significantly smaller than on Pt/γ-Al_2O_3, indicating the presence of the desired mass transport limitations in CH_4. These effective reaction rates are in agreement with CH_4 diffusion time constants previously measured using CH_4-D_2 isotopic exchange reactions on these same materials (Chapter 5). Deactivation rates on Pt/γ-Al_2O_3 are shown to increase proportionally with ψ, reflecting the dependence of carbon formation rates on surface carbon thermodynamic activities. Deactivation rates on Pt/Na-LTA and Pt/Ca-LTA samples, in contrast, are undetectable for stoichiometric (and substoichiometric) CH_4-H_2O feeds (873 K) (ψ < 10 kPa; Eq. 3). Deactivation

rates are also 3-8 times slower on Pt/Na-LTA and Pt/Ca-LTA than on Pt/γ-Al_2O_3 at higher CH_4/H_2O feed ratios (ψ = 10-40 kPa; Eq. 3). Deactivation rates are similar for Pt/Na-LTA and Pt/Ca-LTA catalysts, contrary to expectations that Pt/Na-LTA samples exhibiting greater mass transport limitations would lead to lower intracrystalline CH_4/H_2O ratios and thus slower deactivation rates. Numerical models are used to provide insight into these deactivation behaviors. These models utilize CH_4 and H_2O diffusion time constants $\left(\frac{R^2}{D_e}\right)$ measured by isotopic exchange methods (Chapter 5) to simulate CH_4 and H_2O concentration profiles over time as the catalyst deactivates. The simulations indicate that CH_4 concentrations decrease to zero near the surface of the crystallite for both Pt/Na-LTA and Pt/Ca-LTA; CH_4 turnovers therefore occur almost exclusively in a region where carbon activities remain high. Simulated deactivation rates are in close agreement with experimental values.

The strategies demonstrated here for CH_4-H_2O reactions for exploiting differences in diffusivity to control reactant ratios at the catalyst level rather than at the process level are widely applicable. Such strategies can be used to improve reactant selectivity in mixed feeds, scavenge products (e.g., H_2) to remove thermodynamic limits, and inhibit side reactions. The availability of a large library of microporous materials provides numerous tunable options for implementing these strategies.

6.2 Experimental Methods

6.2.1 Catalyst Synthesis Methods

Pt nanoparticles were dispersed on γ-Al_2O_3 (1% wt., Pt/γ-Al_2O_3) by employing incipient wetness impregnation techniques. γ-Al_2O_3 (Sasol, CATALOX SBa 200) was treated in flowing air (0.83 $cm^3\ g^{-1}\ s^{-1}$; zero grade; Praxair) while ramping from ambient temperature to 1073 K (0.083 K s^{-1}) and holding for 5 h. An aqueous solution of H_2PtCl_6 (8% wt. in H_2O; Sigma-Aldrich) was added dropwise to the treated γ-Al_2O_3 (0.26 $cm^3\ g^{-1}$ γ-Al_2O_3). The sample was then treated overnight in ambient air at 368 K, followed by treatment in flowing air (1.67 $cm^3\ g^{-1}\ s^{-1}$; zero grade; Praxair) by heating from ambient temperature to 873 K (at 0.083 K s^{-1}) and holding for 3 h before cooling to ambient temperature. The sample was next treated in flowing H_2 (1.67 $cm^3\ g^{-1}\ s^{-1}$; 99.999% UHP; Praxair) while heating to 1073 K (at 0.083 K s^{-1}) and holding for 2 h. After cooling to ambient temperature, the sample was held in 2% v/v O_2 (0.83 $cm^3\ g^{-1}\ s^{-1}$, balance He; certified grade; Praxair) for 0.5 h to passivate the surfaces of Pt nanoparticles.

Pt clusters were encapsulated in Na-LTA zeolites by previously reported strategies,[26] in which a Pt precursor and stabilizing ligand is added to the zeolite synthesis gel prior to hydrothermal crystallization of the LTA framework. The synthesis gel was prepared by adding 4.80 g NaOH (Certified ACS, Fisher Chemical) and 0.71 g (3-mercaptopropyl)trimethoxysilane (95%; Sigma-Aldrich) to 18.0 g of deionized (DI) H_2O (>18.0 MΩ-cm resistivity). A solution of 3.04 g of H_2PtCl_6 (8% wt. in H_2O, Sigma-Aldrich) was diluted in 15.3 g of DI H_2O and added dropwise into the solution while stirring. Colloidal SiO_2 (10.7 g; 30 wt. % suspension in H_2O; LUDOX HS-30; Sigma-Aldrich) was added, and then the mixture was heated to 353 K under stirring (300 s^{-1}) and held at this temperature until the mixture turned transparent. The mixture was removed from heat, and a solution of 6.0 g of $NaAlO_2$ (53% Al_2O_3, 42.5% Na_2O; Riedel-de Haën) in 18.0 g of DI H_2O was added. The mixture was stirred for 2 h at ambient temperature. The final synthesis gel molar ratios were 1.7 SiO_2/1.00 Al_2O_3/3.2 Na_2O/110 H_2O/0.019 Pt/0.12 (3-

mercaptopropyl)trimethoxysilane. The gel was heated for 12 h at 373 K with stirring (300 s^{-1}) in a 1 L polypropylene bottle. The resulting solid-liquid mixture was filtered through a fine fritted funnel and washed with DI water until the rinse solution reached a pH of 7. The solids were treated overnight in ambient air at 368 K and then in flowing air (0.83 mL g^{-1} s^{-1}; zero grade; Praxair) while ramping from ambient temperature to 623 K (0.033 K s^{-1}) and holding for 3 h. After cooling to ambient temperature, the sample was treated in flowing H_2 (0.83 cm^3 g^{-1} s^{-1}; 99.999% UHP; Praxair) while ramping to 623 K (0.083 K s^{-1}) and holding for 2 h before cooling back to ambient temperature. The sample was exposed to flowing 2% O_2 v/v (0.83 cm^3 g^{-1} s^{-1},nbalance He; certified grade; Praxair) for 0.5 h to passivate the surfaces of Pt nanoparticles.

Pt/Ca-LTA samples were prepared by ion exchange of Pt/Na-LTA samples using $CaCl_2$ solutions. A 2 M $CaCl_2$ solution (200 cm^3; ACS grade, VWR) was added to Pt/Na-LTA (2 g). The mixture was stirred for 8 h at ambient temperature to allow for complete equilibration. The solids were then filtered out, and the process was repeated four more times. The solids were washed with DI water (1.0 L g^{-1}) before treating in ambient air at 368 K overnight. The samples were then treated in flowing He (0.83 mL g^{-1} s^{-1}; 99.999%, UHP, Praxair) by ramping from ambient temperature to 473 K (0.083 K s^{-1}) and holding for 2 h.

6.2.2 Catalyst Characterization

6.2.2.1 Pt Dispersion and Particle Size Estimations from H_2 Chemisorption

The dispersion of Pt, defined as the ratio of exposed Pt sites to the total number of Pt atoms, was measured using uptakes of H_2 at 373 K. Samples (ca. 1 g) were first treated by heating from ambient temperature to 873 K at 0.083 K s^{-1} in flowing H_2 and then held at this temperature for 1 h. The sample was then evacuated for 1 h at the same temperature before cooling under vacuum to 373 K. H_2 uptakes were measured at pressures between 1 and 40 kPa. Saturation uptakes were calculated by extrapolating the high-pressure linear portion of the isotherm to zero pressure. Particle diameters (d) were calculated from dispersions by using:[27]

$$d = \frac{f_{shape} N_M}{2N_{H_2}} \frac{v_m}{a_m} \theta_{sat} \tag{4}$$

$$\theta_{sat} = \mathrm{H/Pt_s} = 1 + \alpha(d^{-1}) + \beta(d^{-2}) \tag{5}$$

Here, d is the diameter of the particle, f_{shape} is a shape factor (6 for a hemispherical particle), N_M is the total number of metal atoms, N_{H_2} is the number of adsorbed H_2 molecules, and v_m and a_m are the volume and surface area of a Pt atom (calculated using the bulk density of Pt, 21.45 g cm^{-3}).[28] α (0.0364) and β (0.735) are empirical parameters specific to Pt.[27] These equations (Eq.4-5) can be solved iteratively; they correct for the binding of multiple H atoms to corner and edge atoms on small Pt nanoparticles.[27]

6.2.2.2 X-ray Diffraction of Zeolite Samples (Pt/Na-LTA and Pt/Ca-LTA)

X-ray diffraction patterns of Pt/Na-LTA and Pt/Ca-LTA samples were obtained on a Bruker D8 Discover GADDS Powder Diffractometer using Cu Kα radiation (40 kV, 40 mA). Samples were prepared by mixing with MgO (>99.99% trace metals basis; Sigma-Aldrich) in a

1:1 mass ratio (internal standard) and placed onto quartz slides. Diffractograms were obtained for 2θ angles between 7.5° and 55° with a scan rate of 0.00625° s^{-1}.

6.2.3 Measurement of CH_4-H_2O Reaction Rates

CH_4-H_2O reforming turnover rates were measured on Pt/γ-Al_2O_3, Pt/Na-LTA, and Pt/Ca-LTA samples diluted 1:10 by mass in γ-Al_2O_3, pressed into pellets, then sieved to retain particles with diameters between 177 and 250 μm. These samples (0.0003-0.0020 g Pt/γ-Al_2O_3, 0.05-0.15 g Pt/Na-LTA, 0.010-0.030 g Pt/Ca-LTA) were then further diluted in 0.8 g of acid-purified quartz (Sigma-Aldrich). The samples were held on quartz wool plugs (Hereaus Quartz, 4-8 μm diameter wool) within a quartz tube (9.5 mm outer diameter, 7 mm inner diameter). Samples were treated by heating from ambient temperature to 873 K (0.083 K s^{-1}) in flowing He (1.67 cm^3 g^{-1} s^{-1}; Praxair, UHP, 99.999%), then switching to flowing H_2 for 2 h (1.67 cm^3 g^{-1} s^{-1}; Praxair, UHP, 99.999%), then back to flowing He before catalytic measurements. Methane (Praxair, 99.99%), H_2 (Praxair, UHP, 99.999%), and He (Praxair, UHP, 99.999%) flow rates were adjusted with mass flow controllers (Porter Instrument) to achieve desired pressures. H_2O was vaporized into flowing gas streams at 473 K using a liquid syringe pump (Isco Teledyne, 500D). All transfer lines were maintained above 393 K to avoid condensation. Effluent concentrations of reactants and products were measured by gas chromatography (Shimadzu GC-2014; equipped with Porapak Q column and a thermal conductivity detector). Methane conversions were kept below 5% in all experiments. Measured turnover rates (r_n) were corrected for approach to equilibrium (η) to obtain forward rates (r_f) using:

$$r_n = r_f\,(1-\eta) \tag{6}$$

$$\eta = \frac{(CO)(H_2)^3}{(CH_4)(H_2O)}\frac{1}{K_{SRM}} \tag{7}$$

where (i) denotes the pressure of species i (in kPa), and K_{SRM} is the equilibrium constant for the steam reforming (CH_4-H_2O) reaction at the reaction temperature (873 K). The pressures used in Equation 7 were the average pressures within the catalyst bed. The absence of *intrapellet* mass transport limitations was confirmed by identical rates when varying the extent of dilution (1:65 by mass) or pellet size (125-149 μm).

6.3 Results and Discussion

6.3.1 Catalyst Characterization

Pt dispersions on Pt/SiO_2 and Pt/Na-LTA were measured by H_2 chemisorption uptake measurements at 373 K. The Pt dispersion of Pt/Ca-LTA samples was assumed to be identical to that of Pt/Na-LTA since these samples were synthesized by ion-exchange of Pt/Na-LTA samples. These dispersions were used to calculate the average diameter of Pt nanoparticles contained within the samples (Eq. 4-5). The dispersions and chemisorption-derived diameters are summarized in Table 1.

Table 1. Nominal metal contents, dispersions, and particle diameters for catalytic samples

Catalyst	Nominal Metal Content (% wt.)	Dispersion	Nanoparticle Diameter (nm)†
Pt/γ-Al_2O_3	1.0	0.72	1.9
Pt/Na-LTA	1.0	0.53	2.4
Pt/Ca-LTA*	1.0	0.53	2.4

†Calculated by assuming hemispherical particle geometries and using the bulk density of Pt (21.45 g cm^{-3}).[28] H/Pt_s stoichiometries were estimated using Equation 5.
*Pt/Ca-LTA samples assumed to exhibit identical properties as its parent material Pt/Na-LTA

X-ray diffractograms of Pt/Na-LTA and Pt/Ca-LTA samples confirmed the synthesis of LTA crystallites (Section 6.6.1).

6.3.2 Measurement of CH_4-H_2O Reaction Rates on Pt/γ-Al_2O_3, Pt/Na-LTA, and Pt/Ca-LTA and Assessments of Mass Transport Limitations of CH_4 at 873 K

CH_4-H_2O turnover rates were measured on Pt/γ-Al_2O_3, Pt/Na-LTA, and Pt/Ca-LTA samples (10 kPa CH_4, 40 kPa H_2O, 5 kPa H_2; 873 K) to compare the magnitudes of their initial rates (Fig. 1). CH_4-H_2O turnover rates were lower on Pt/Na-LTA and Pt/Ca-LTA than on Pt/γ-Al_2O_3 by factors of 0.0093 ± 0.0011 and 0.073 ± 0.006, respectively. These values reflect significant *intracrystalline* mass transport limitations in Pt/Na-LTA and Pt/Ca-LTA and represent effectiveness factors, defined by:

$$\lambda \equiv \frac{r_{eff}}{r_{max}} \tag{8}$$

where r_{eff} is the effective rate of reaction (on Pt/Na-LTA and Pt/Ca-LTA), and r_{max} is the rate of reaction in the absence of mass transport limitations (given by rates on Pt/γ-Al_2O_3).

Effectiveness factors can also be estimated using Thiele formalisms.[29] CH_4-H_2O reforming rates on Pt are described by a first-order dependence in CH_4:[23]

$$r_{CH_4} = k'_{CH_4}(CH_4) \tag{9}$$

where k'_{CH_4} ([=] kPa^{-1} s^{-1}) represents the rate constant for CH_4-H_2O reactions normalized by the number of Pt sites. For a first-order reaction in a quasi-spherical particle with severe mass transport limitations ($\lambda < \sim 0.3$) [30], the Thiele modulus (ϕ)[29] can be related to the effectiveness factor by:[30]

$$\phi = \sqrt{\frac{k_v R^2}{D_e}} = \frac{1}{\lambda} \tag{10}$$

where the ratio of the square of the radius to the effective diffusivity $\left(\frac{R^2}{D_e}\right)$ is denoted as a diffusion time constant and k_v is the volumetric rate constant. The diffusion time constant $\left(\frac{R^2}{D_e}\right)$ for CH_4 in Pt/Na-LTA and Pt/Ca-LTA was measured previously at 873 K using CH_4-D_2 isotopic exchange experiments (0.64 ± 0.07 and 0.013 ± 0.002 s, respectively). The volumetric rate constant can be

estimated by converting the per-site rate constant k'_{CH_4} (Eq. 9) to a volumetric rate constant k_{v,CH_4} using:

$$k_{v,CH_4} = \frac{k'_{CH_4} D l_{Pt} \rho}{(MW_{Pt})} RT = f k'_{CH_4} \tag{11}$$

Here, D is the Pt dispersion in Pt/Na-LTA and Pt/Ca-LTA (0.53, Table 1), (MW_{Pt}) is the molecular mass of Pt, l_{Pt} is the Pt content in Na-LTA and Ca-LTA (1% wt., Table 1), and ρ is the solid density of Pt/Na-LTA or Pt/Ca-LTA, calculated using the bulk densities of Na-LTA (1.5174 g cm^3)[31] and Ca-LTA (1.4859 g cm^3, assuming complete Ca^{2+} exchange).[31] Equations 10 and 11 were used to calculate effectiveness factors for CH_4-H_2O reactions on Pt/Na-LTA and Pt/Ca-LTA, giving values of 0.012 ± 0.002 and 0.085 ± 0.003, respectively; the experimental and calculated effective reaction rates are shown in Figure 1. These effectiveness factors were in close agreement with the experimental values (0.0093 ± 0.0011 and 0.073 ± 0.006, for Pt/Na-LTA and Pt/Ca-LTA, respectively), validating the CH_4 diffusion time constants previously measured on these materials and demonstrating the presence of the desired intracrystalline mass transport limitations.

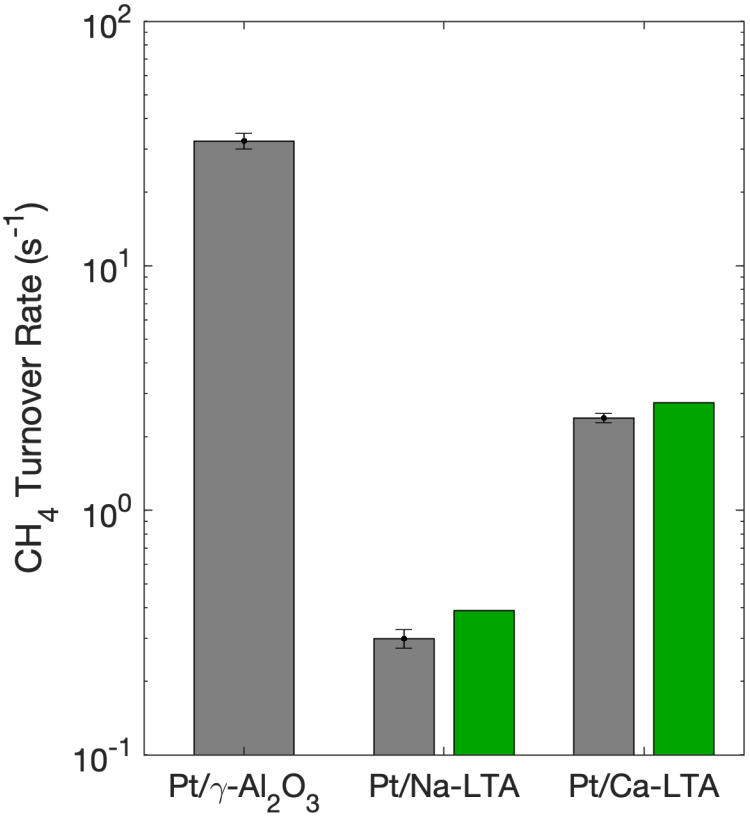

Figure 1. Initial CH_4 turnover rates measured on Pt/γ-Al_2O_3, Pt/Na-LTA, and Pt/Ca-LTA catalytic pellets (diluted 1:10 in γ-Al_2O_3) (177-250 μm) at 873 K (10 kPa CH_4, 40 kPa H_2O, 5 kPa H_2). Gray bars represent measured rates while green bars denote rates calculated using Thiele formalisms and CH_4 diffusion time constants derived from previous isotopic exchange studies (Chapter 5).

6.3.3 Effects of CH_4/H_2O Feed Ratios on Deactivation Rates on Pt/γ-Al_2O_3, Pt/Na-LTA, and Pt/Ca-LTA at 873 K

Previous investigations on carbon formation during CH_4-H_2O reactions on Ni showed that the rate of carbon deposition during these reactions is linearly dependent on the surface carbon activity and on $\psi\left(\frac{(CH_4)(H_2)}{(H_2O)}\right)$ (Eq. 1-3) (Chapter 2). The morphology of these carbon deposits typically assumes the form of filaments for Ni-based catalysts; these filaments continuously deplete the surface of carbon atoms during reactions, thereby allowing continued access to the surface for catalytic turnovers.[25, 32] The formation of these filaments occurs via the dissolution of carbon at the reactive surface, diffusion through the Ni nanoparticle, and finally nucleation at the filament.[33] Carbon deposits on Pt, conversely, tend to form graphite-like layers that block access to the surface over time, leading to deactivation of the catalyst;[32] these behaviors reflect the much lower solubility of carbon in Pt (4×10^{-12} wt. %, 873 K; extrapolated from measurements at 1473-1773 K)[34] than in Ni (0.04 wt. %, 873 K).[35] Thus, deactivation rates on Pt are expected to depend on the surface carbon activity and on $\psi\left(\frac{(CH_4)(H_2)}{(H_2O)}\right)$.

CH_4-H_2O reforming rates were measured as a function of time on Pt/γ-Al_2O_3, Pt/Na-LTA, and Pt/Ca-LTA samples as ψ was varied between 2.5 and 40 kPa (873 K). Figure 2 shows first-order rate constants (Eq. 9) normalized by their values at the start of these experiments $\left(\frac{k'_{CH_4}(t)}{k'_{CH_4}(0)}\right)$ as a function of time for each catalyst. $\psi\left(\frac{(CH_4)(H_2)}{(H_2O)}\right)$ values were increased over time by varying H_2O (2.5-40 kPa) and CH_4 (20, 40 kPa) pressures while maintaining constant H_2 pressures (5 kPa; Fig. 2). Reaction rates exhibited first-order deactivation kinetics at each value of ψ (Fig. 2), as indicated by the linear trends in Figure 2. Such behaviors can be modelled using:[36]

$$\frac{k'(t)}{k'(0)} = \frac{k_v(t)}{k_v(0)} = \exp(-k_d t) \tag{12}$$

where k_d is the first-order deactivation rate constant, corresponding with the slope of the data in Figure 2. k_d values were regressed for each experimental condition and catalyst in order to compare deactivation rates on Pt/γ-Al_2O_3, Pt/Na-LTA, and Pt/Ca-LTA (Fig. 3).

P_{CH4} (kPa)	20	20	20	20	40
P_{H2O} (kPa)	40	20	10	5	5
P_{H2} (kPa)	5	5	5	5	5
ψ (kPa)	2.5	5	10	20	40

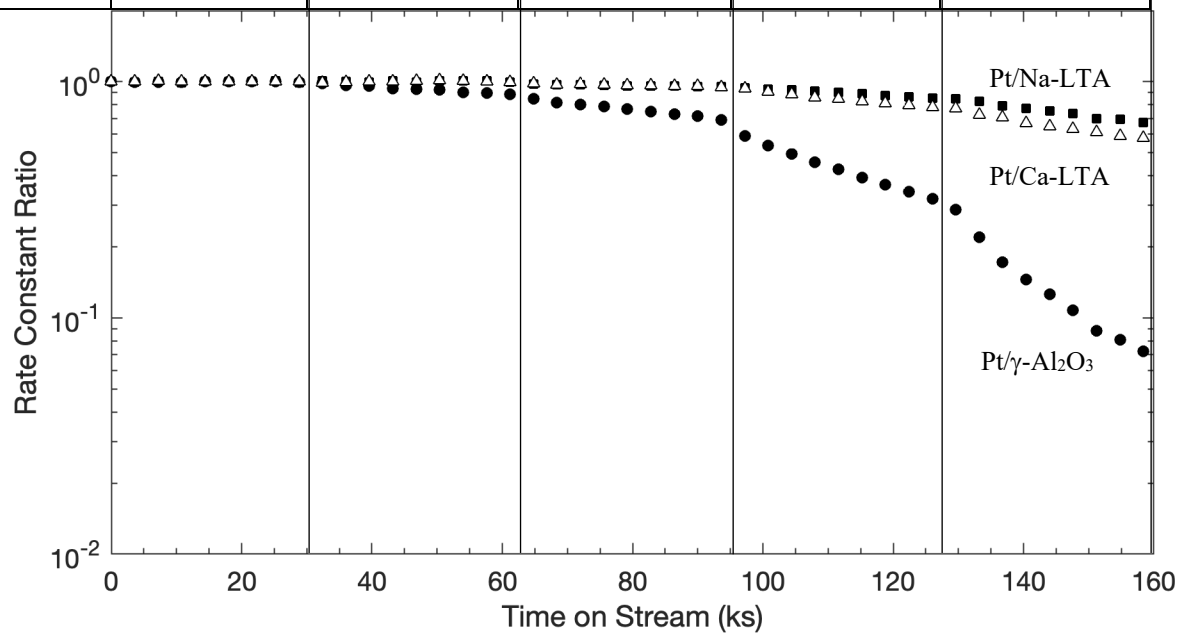

Figure 2. CH_4-H_2O first-order rate constants normalized by initial values $\left(\frac{k'_{CH_4}(t)}{k'_{CH_4}(0)}\right)$ on (●) Pt/γ-Al_2O_3, (■) Pt/Na-LTA, and (△) Pt/Ca-LTA, as a function of time (873 K). ψ $\left(\frac{(CH_4)(H_2)}{(H_2O)}\right)$ ratios were varied by changing H_2O (2.5-40 kPa) and CH_4 (20, 40 kPa) pressures while keeping H_2 pressures constant (5 kPa).

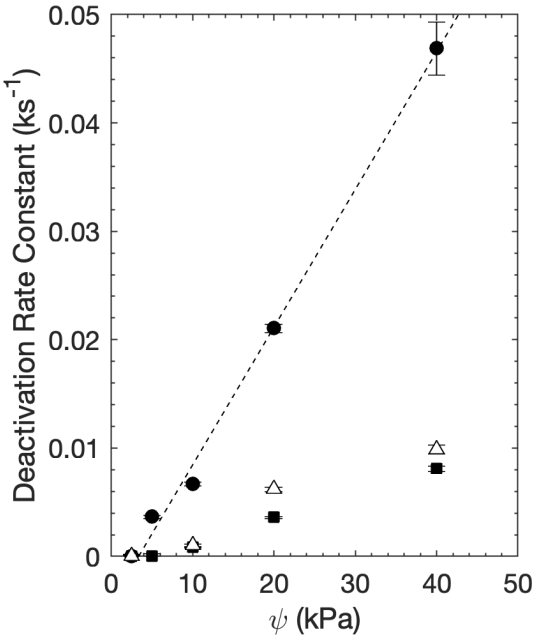

Figure 3. First-order deactivation rate constants (k_d; Eq. 12) during CH_4-H_2O reactions as a function of the pressure ratio ψ $\left(\frac{(CH_4)(H_2)}{(H_2O)}\right)$ at 873 K. ψ ratios were varied by changing H_2O (2.5-40 kPa) and CH_4 (20, 40 kPa CH_4) pressures while keeping H_2 pressures constant (5 kPa). Dashed line represents linear regression of deactivation rate constants on Pt/γ-Al_2O_3 for ψ values between 5 and 40 kPa.

Figure 3 shows that deactivation constants (k_d; Eq. 12) on Pt/γ-Al_2O_3 were proportional to ψ $\left(\frac{(CH_4)(H_2)}{(H_2O)}\right)$ values, reflecting dependence of deactivation rates on the surface carbon activity. Such trends with ψ are similar to those previously reported for carbon filament formation rates on Ni-based catalysts (Chapter 2). Deactivation rate constants (k_d) were smaller on Pt/Na-LTA and Pt/Ca-LTA than on Pt/γ-Al_2O_3 (Fig. 2-3) by factors of 5.9-8.3 and 3.4-6.4, respectively, for ψ values between 10 and 40. These lower deactivation rates reflect in part the effects of mass transport limitations on apparent deactivation rates; such effects can be modelled analytically when intracrystalline CH_4/H_2O ratios are constant.

The rate of CH_4-H_2O reaction in a mass transport limited particle is given by:

$$r = \lambda k'_{CH_4}(CH_4) = \lambda f k_{v,CH_4}(CH_4) \tag{13}$$

Substitution of Equation 10 into Equation 13 gives:

$$r = \sqrt{\frac{D_e}{k_{v,CH_4}R^2}} f k_{v,CH_4}(CH_4) \tag{14}$$

k_{v,CH_4} varies with time but not position, assuming that the CH_4/H_2O ratio and ψ are constant (Eq. 12). Equation 12 can be substituted into Equation 14 to give:

$$r(t) = \sqrt{\frac{D_e k_{v,CH_4}(0)}{R^2}} f \exp(-0.5 k_d t)(CH_4) \quad (15)$$

The form of Equation 15 and the factor of 0.5 appearing the exponential term indicates that even at constant CH_4/H_2O ratios, the presence of mass transport limitations leads to an apparent decrease in deactivation rates by a factor of 2. This analysis indicates that decreasing intracrystalline CH_4/H_2O ratios must lead to decreases in deactivation rate constants (k_d) by more than factors of 2, which was demonstrated by both Pt/Na-LTA (factors of 5.9-8.3) and Pt/Ca-LTA (factors of 3.4-6.4) (ψ = 10-40 kPa; Fig. 3). The significantly lower deactivation rate constants exhibited by Pt/Na-LTA and Pt/Ca-LTA (Fig. 3) therefore reflect the faster diffusion of H_2O compared to CH_4 in the micropores of Pt/Na-LTA and Pt/Ca-LTA, resulting in the suppression of carbon formation on Pt nanoparticles located within the zeolite crystallites. These deactivation behaviors cannot be modelled analytically; modelling deactivation rates with diffusion-reaction models using CH_4 and H_2O diffusion time constants $\left(\frac{R^2}{D_e}\right)$ previously derived from isotopic exchange experiments is therefore addressed using numerical methods in the following section.

6.3.4 Deactivation Rates and Insights from Numerical Modeling on Pt/Na-LTA and Pt/Ca-LTA

CH_4 and H_2O exhibit distinct concentration gradients in Pt/Na-LTA and Pt/Ca-LTA crystallites during CH_4-H_2O reactions because of their significantly different diffusivities.[9] These concentration gradients lead to CH_4/H_2O (and $\psi = \frac{(CH_4)(H_2)}{(H_2O)}$) ratios that also vary along the channels of the zeolite, which lead in turn to deactivation rates that depend on position. The prediction of observed deactivation rates therefore requires the use of reaction-diffusion models along with finite difference methods to predict concentration profiles and ψ ratios within Pt/Na-LTA and Pt/Ca-LTA crystallites at a given time and position. Such methods were used to simulate the deactivation of Pt/Na-LTA and Pt/Ca-LTA catalyst particles over time.

Pt/Na-LTA and Pt/Ca-LTA crystallites were modelled as isotropic quasi-spherical particles. A shell balance on a reactive particle gives the following equations (derivation in Section 6.6.2):

$$\frac{\partial^2 \xi_i(\theta,t)}{\partial \theta^2} + \frac{2}{\theta}\frac{\partial \xi_i(\theta,t)}{\partial \theta} + \nu_i \phi_i^2(\theta,t)\xi_{CH_4}(\theta,t) = 0 \quad (16)$$

$$\phi_i(\theta,t) = \sqrt{k_{v,CH_4}(\theta,t)\left(\frac{R^2}{D_e}\right)_i} \quad (17)$$

$$k_{v,CH_4}(\theta,t) = k_{v,CH_4}(\theta,0)\exp(-k_d(\theta,t) \times t) \quad (18)$$

where ξ_i is a dimensionless concentration of species i (normalized by the external CH_4 concentration), θ is a dimensionless radius $\left(\frac{r}{R}\right)$, ν_i is the stoichiometric number for species i (negative for reactants and positive for products), and $\left(\frac{R^2}{D_e}\right)_i$ is the diffusion time constant for species i. Here, $k_{v,CH_4}(\theta,0)$ was calculated from the initial rates on Pt/γ-Al_2O_3 using Equation 11,

as above (Section 6.3.2). Diffusion time constants $\left(\frac{R^2}{D_e}\right)_i$ for CH_4 and H_2O were previously measured on these samples at 873 K using CH_4-D_2 and H_2O-D_2 exchange reactions (Chapter 5); these values are reported in Table 2. H_2 does not exhibit concentration gradients, as indicated by our previous H_2-D_2 isotopic exchange experiments on these materials (Chapter 5). To solve these equations (Eq. 16-18), the model particle was divided into 5000 shells, each with its own reaction rate constant $k_{v,CH_4}(\theta, t)$ (Eq. 18) that was updated with each time step. The deactivation rate constant was modelled by:

$$k_d(\theta, t) = 0.00127\,\psi(\theta, t) - 0.00424 \tag{19}$$

This equation was obtained by regressing the deactivation rate constants in Figure 3 for ψ values between 5 and 40 kPa. The time step was chosen such that the change in $k_{v,CH_4}(\theta, t)$ (Eq. 18) from the previous time step was less than 0.05%.

Table 1. Diffusion time constants $\left(\frac{R^2}{D_e}\right)_i$ (873 K) used in numerical simulations of reaction-diffusion within Pt/Na-LTA and Pt/Ca-LTA

Molecule	Catalyst	$\frac{R^2}{D_e}$ (s) at 873 K
CH_4*	Pt/Na-LTA	0.64 ± 0.07
	Pt/Ca-LTA	0.013 ± 0.0025
H_2O*	Pt/Na-LTA	$4.5 \times 10^{-4} \pm 2.7 \times 10^{-5}$
	Pt/Ca-LTA	$2.3 \times 10^{-4} \pm 9.2 \times 10^{-6}$
H_2	Pt/Na-LTA	1×10^{-12}†
	Pt/Ca-LTA	1×10^{-12}†

*Measured previously using CH_4-D_2 and H_2O-D_2 isotopic exchange reactions (Chapter 5)
†Values used for the absence of mass transport limitations

The set of partial differential equations given by Equation 16 (for CH_4, H_2O, and H_2) requires 6 boundary conditions to solve. Three of these boundary conditions are Neumann conditions, corresponding with the no flux condition at the $\theta = 0$:

$$\frac{\partial \xi_i}{\partial \theta}|_{\theta=0} = 0 \tag{20}$$

The other three boundary conditions are Dirichlet conditions, set by the external concentrations $(i)_0$ of CH_4, H_2O, and H_2:

$$\xi_i = \frac{(i)_0}{(CH_4)_0} \tag{21}$$

Equation 16 was solved at each time step to give concentration profiles for CH_4, H_2O, CO, and H_2. The composition of reactants and products within each differential slice was used in the calculation

of $k_d(\theta, t)$ (Eq. 19) and $k_{v,CH_4}(\theta, t)$ (Eq. 18) in the next time step. The effective rate was calculated from the integral average rate within the model particle.

P_{CH4} (kPa)	20	20	20	20	40
P_{H2O} (kPa)	40	20	10	5	5
P_{H2} (kPa)	5	5	5	5	5
ψ (kPa)	2.5	5	10	20	40

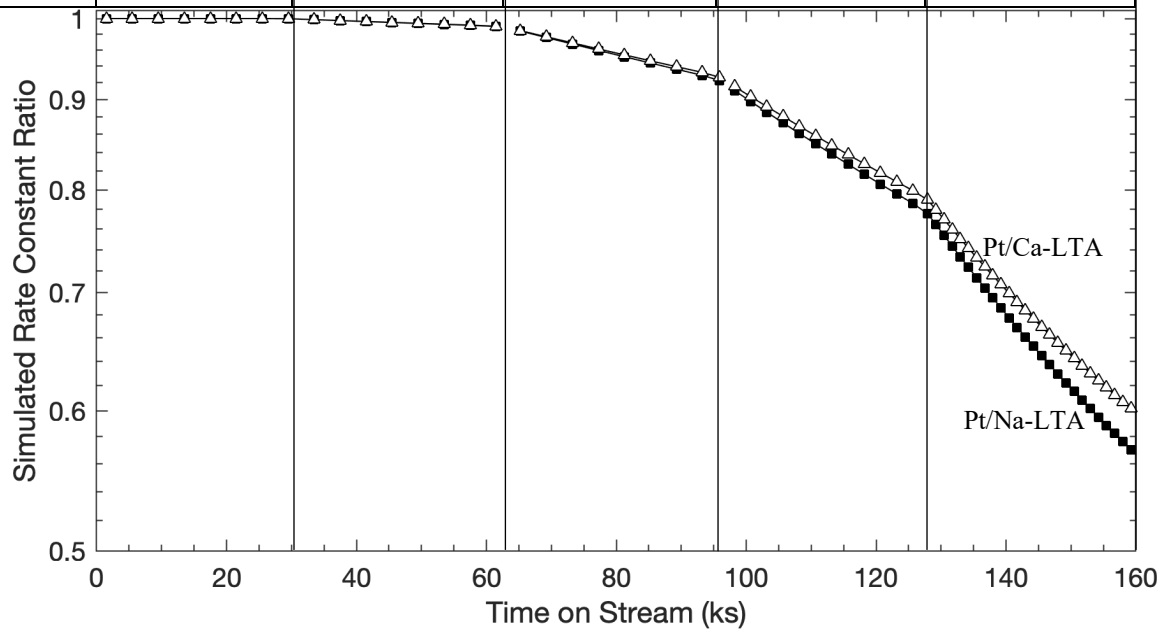

Figure 4. Simulated CH_4-H_2O rate constant ratios $\left(\frac{k'_{CH_4}(t)}{k'_{CH_4}(0)}\right)$ on (■) Pt/Na-LTA and (△) Pt/Ca-LTA, as a function of time at 873 K.

Table 2. Simulated and experimental deactivation rate constants on Pt/γ-Al_2O_3, Pt/Na-LTA, and Pt/Ca-LTA

ψ (kPa)	Catalyst	Experimental k_d (ks^{-1})	Simulated k_d (ks^{-1})
5	Pt/Na-LTA	$5.5 \times 10^{-5} \pm 1.8 \times 10^{-4}$	3.1×10^{-4}
	Pt/Ca-LTA	$-2.3 \times 10^{-4} \pm 2.5 \times 10^{-4}$	3.0×10^{-4}
10	Pt/Na-LTA	$8.4 \times 10^{-4} \pm 4.1 \times 10^{-5}$	2.1×10^{-3}
	Pt/Ca-LTA	$1.0 \times 10^{-3} \pm 1.2 \times 10^{-4}$	2.0×10^{-4}
20	Pt/Na-LTA	$3.6 \times 10^{-3} \pm 1.0 \times 10^{-4}$	5.4×10^{-3}
	Pt/Ca-LTA	$6.2 \times 10^{-3} \pm 2.0 \times 10^{-4}$	5.0×10^{-4}
40	Pt/Na-LTA	$8.1 \times 10^{-3} \pm 2.7 \times 10^{-4}$	9.7×10^{-3}
	Pt/Ca-LTA	$9.9 \times 10^{-3} \pm 4.2 \times 10^{-4}$	8.8×10^{-4}

Figure 4 shows the simulated effective rate constant ratios $\left(\frac{k'_{CH_4}(t)}{k'_{CH_4}(0)}\right)$ on Pt/Na-LTA and Pt/Ca-LTA versus time at 873 K as ψ values (2.5-40 kPa) were sequentially increased over time, as in the experiments in Figure 2. The data in Figure 4 also show first-order deactivation trends (on these timescales) on Pt/Na-LTA and Pt/Ca-LTA samples, in agreement with the experimental deactivation trends, allowing for the extraction of first-order deactivation rate constants k_d. The values of deactivation rate constants k_d from simulations and from experiments (Fig. 3) are tabulated in Table 2.

The simulated deactivation rate constants were in good agreement with experimental values (Table 2). The simulated data (Table 2), however, predicted that Pt/Na-LTA samples deactivate more quickly than Pt/Ca-LTA samples, contrary to the experimental data and expectations that greater mass transport limitations in CH_4 would lead to lower CH_4/H_2O ratios and thus lower deactivation rates. Simulated concentration profiles in Pt/Na-LTA crystallites, however, were nearly vertical; such concentration gradients are so severe that the majority of CH_4 conversion occurs also where deactivation is most likely, near the surface of the crystallite. The simulated data (Table 2, Fig. 4) therefore reflect concentration gradients that are unable to fully exploit the internal volume of Pt/Na-LTA and Pt/Ca-LTA where most Pt active sites are located.

Figure 5 shows simulated initial deactivation rate constants k_d as a function of the Thiele modulus ϕ (Eq. 17) for ψ values between 5 kPa and 40 kPa, assuming the absence of H_2O gradients. These data show that deactivation rate constants initially decrease with increasing values of the Thiele modulus, representing increasing mass transport limitations in CH_4, but then exhibit an inflection and slightly increase before approaching an asymptotic limit. These latter trends correspond with the higher simulated deactivation rate constants for Pt/Na-LTA than for Pt/Ca-LTA (Table 2). The Thiele moduli, calculated from the experimental effectiveness factors using Equation 10 (107 ± 13 and 14 ± 1 for Pt/Na-LTA and Pt/Ca-LTA, respectively), indicate that the deactivation experiments in this study (Fig. 2) were performed in the asymptotic regime (indicated by arrows in Fig. 10). These asymptotic limits (Fig. 5) were, however, all lower than the factor of

0.5 improvement expected from mass transport limitations without changes in intracrystalline CH_4/H_2O ratios (Eq. 15). Thus, while Pt/Na-LTA and Pt/Ca-LTA exhibited deactivation rates well below those on Pt/γ-Al_2O_3 (Fig. 2), reflecting the preferential access provided to H_2O molecules, the catalyst can be further optimized by choosing or synthesizing a material with less severe mass transport limitations (i.e., lower $\frac{R^2}{D_e}$ values, Eq. 17) that aligns with the minima in Figure 5.

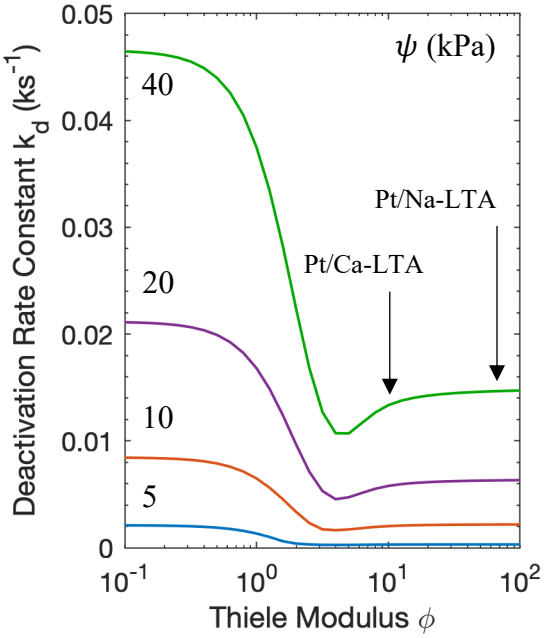

Figure 5. Deactivation rate constants k_d as a function of the Thiele modulus for CH_4 at ψ values of (●) 5 , (■) 10, (▲) 20, and (◆) 40 kPa. All other molecules (H_2O, H_2) are assumed to be constant throughout the crystallite.

CH_4-H_2O reactions on Pt/Na-LTA and Pt/Ca-LTA were carried out at each value of ψ for approximately 32 ks (Fig. 2). These data showed first-order deactivation behaviors that were consistent with numerical simulations (Fig. 4) over similar timescales. Numerical models, however, showed that deactivation deviates from this first-order behavior over longer timescales. Figure 6 shows simulated effective rate constant ratios $\left(\frac{k'_{CH_4}(t)}{k'_{CH_4}(0)}\right)$ as a function of time on Pt/Na-LTA crystallites for a ψ value of 40 kPa over a period of 500 ks. These data (Fig. 6) show that deactivation rates decrease with time and appear to approach an asymptotic value. Such trends reflect the gradual formation of a deactivated shell near the particle surface; this shell contributes less reactivity over time but continues to limit the diffusion of CH_4 molecules. This "core-shell" structure protects internal active sites from contact with the high CH_4/H_2O ratios and carbon activities closer to the surface. These data (Fig. 6) therefore indicate that Pt/Na-LTA and Pt/Ca-LTA materials not only show improved deactivation rates at early times but are also expected to exhibit long-term stability after an initial deactivation period. They also suggest that synthesizing a material with a reactive core but an inactive shell structure that retains its sieving capabilities can

provide improved catalytic stability even at the onset of such reactions. Such properties make these materials a promising alternative to current Ni-based catalysts.

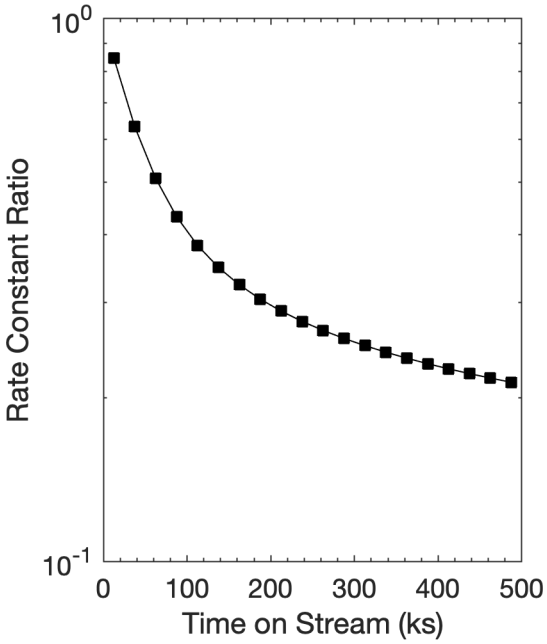

Figure 6. Simulated CH_4-H_2O rate constant ratios $\left(\frac{k'_{CH_4}(t)}{k'_{CH_4}(0)}\right)$ on Pt/Na-LTA as a function of time (ψ = 40 kPa; 873 K).

6.4 Conclusions

Zeolites and zeotypes have found wide use in separations and catalytic processes because of their ability to selectively sieve and adsorb molecules. These microporous materials provide preferential access to smaller, faster diffusing molecules, leading to distinct concentration profiles for each reactant during steady-state catalysis that can be exploited to control reactant/product concentration ratios along zeolite channels. Such strategies were demonstrated here for CH_4-H_2O reactions on Pt/Na-LTA and Pt/Ca-LTA catalysts. H_2O diffuses more quickly than CH_4 molecules in the pores of LTA, leading to substoichiometric intracrystalline CH_4/H_2O ratios, thereby decreasing the carbon activity and suppressing the formation of carbon deposits and deactivation. Pt/Na-LTA and Pt/Ca-LTA exhibited deactivation rate constants significantly lower than on Pt/γ-Al_2O_3. These deactivation rates were in agreement with those obtained by numerical simulations using CH_4-H_2O diffusion time constants $\left(\frac{R^2}{D_e}\right)$ previously measured on the same Pt/Na-LTA and Pt/Ca-LTA samples. Numerical simulations also showed that Pt/Na-LTA and Pt/Ca-LTA samples become more stable with time, reflecting the formation of a core-shell structure that protects internal sites from further deactivation. The strategies demonstrated here for exploiting differences in diffusivity are applicable to a variety of reactions where granting preferential access to the active site for a specific reactant is desirable.

6.5 Acknowledgements

This study was funded by Chevron Corporation and a Chevron Graduate Student Research Fellowship.

6.6 Supporting Information

6.6.1 X-ray Diffraction Patterns of Pt/Na-LTA and Pt/Ca-LTA Samples

X-ray diffraction patterns of Pt/Na-LTA and Pt/Ca-LTA samples mixed in a 1:1 mass ratio with MgO (internal standard) were obtained to confirm the synthesis of LTA crystallites. These diffractograms are shown in Figure SI-1. Reference patterns for LTA[37] are also included. All synthesized LTA samples showed reflections typical for LTA zeolites, indicating the successful synthesis of such crystallites.

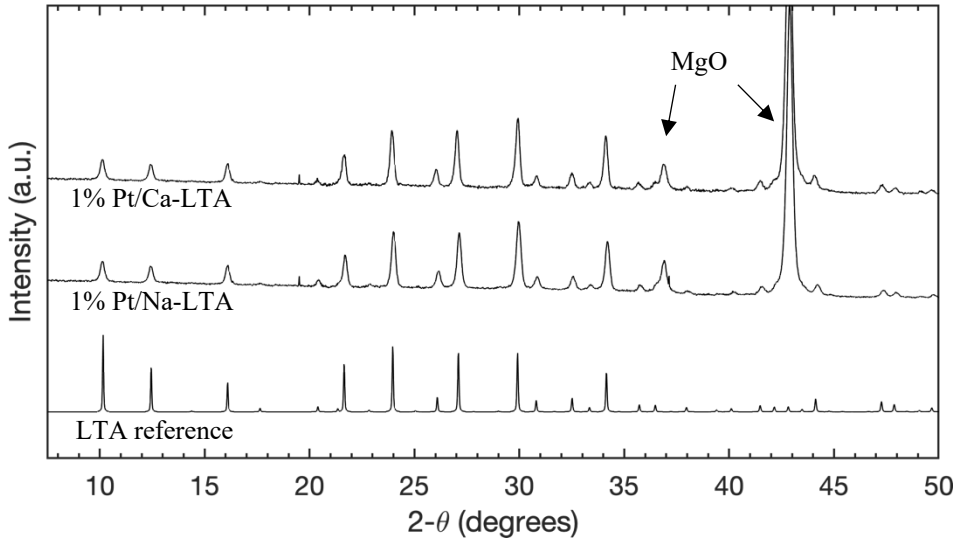

Figure SI-1. X-ray diffraction patterns of 1% Pt/Na-LTA, and 1% Pt/Ca-LTA samples mixed in a 1:1 mass ratio with MgO.

6.6.2 Shell Balance for Reaction in Quasi-Spherical Particle with Deactivation

The mass balance over a spherical shell with thickness Δr is given by:

$$(In\ at\ r) - (Out\ at\ r + \Delta r) + (Generation\ in\ \Delta r) = 0 \qquad (SI-1)$$

$$(W_i \times 4\pi r^2|_r) - (W_i \times 4\pi r^2|_{r+\Delta r}) + (r_i \times 4\pi r^2 \Delta r) = 0 \qquad (SI-2)$$

Here, r is the radial position, W_i is the flux of molecule i, and r_i is the rate of generation of species i. Dividing by $(-4\pi\Delta r)$ and taking the limit $\Delta r \to 0$ gives:

$$\frac{d(W_i r^2)}{dr} - r_i r^2 = 0 \qquad (SI-3)$$

The flux of molecule i is proportional to the gradient in concentration, such that:

$$W_i = -D_e \frac{dC_i}{dr} \qquad (SI-4)$$

This equation can be substituted into Equation SI-3:

$$\frac{d^2C_i}{dr^2} + \frac{2}{r}\frac{dC_i}{dr} + \frac{r_i}{D_e} = 0 \qquad (SI-5)$$

The rate of generation of species i during CH_4-H_2O reactions is:

$$r_i = \nu_i k_{v,CH_4} C_{CH_4} \qquad (SI-6)$$

where ν_i is the stoichiometric number for species i (CH_4 = -1, H_2O = -1, CO = 1, H_2 = 3). Equation SI-5 can therefore be rewritten as:

$$\frac{d^2C_i}{dr^2} + \frac{2}{r}\frac{dC_i}{dr} + \frac{\nu_i k_{v,CH_4} C_{CH_4}}{D_e} = 0 \qquad (SI-7)$$

Equations SI-7 can be nondimensionalized using:

$$\xi_i = \frac{C_i}{C_{CH_4,0}} \qquad (SI-8)$$

$$\theta = \frac{r}{R} \qquad (SI-9)$$

where $C_{CH_4,0}$ is the external pressure of CH_4, to obtain:

$$\frac{d^2\xi_i}{d\theta^2} + \frac{2}{\theta}\frac{d\xi_i}{d\theta} + \nu_i \phi_i^2 \xi_{CH_4} = 0 \qquad (SI-10)$$

$$\phi_i = \sqrt{k_{v,CH_4}\left(\frac{R^2}{D_e}\right)_i} \qquad (SI-11)$$

Equations SI-10 – SI-11 can be used to obtain concentration gradients of each species in a catalytic particle in the absence of deactivation. When deactivation does occur, Equation SI-10 becomes a partial differential equation and k_{v,CH_4} becomes a function of position and time, such that:

$$\frac{\partial^2\xi_i(\theta,t)}{\partial\theta^2} + \frac{2}{\theta}\frac{\partial\xi_i(\theta,t)}{\partial\theta} + \nu_i \phi_i^2(\theta,t)\xi_{CH_4}(\theta,t) = 0 \qquad (SI-12)$$

$$\phi_i(\theta,t) = \sqrt{k_{v,CH_4}(\theta,t)\left(\frac{R^2}{D_e}\right)_i} \qquad (SI-13)$$

$$k_{v,CH_4}(\theta,t) = k_{v,CH_4}(\theta,0)\exp(-k_d t) \qquad (SI-14)$$

6.7 References

1. Breck, D. W., *Zeolite molecular sieves: structure, chemistry, and use*; New York, Wiley [1973, c1974], 1973.
2. Gallezot, P., Preparation of Metal Clusters in Zeolites. In *Post-Synthesis Modification I*, Springer Berlin Heidelberg: Berlin, Heidelberg, 2002; pp 257-305.
3. Sachtler, W. M. H., Zeolite-Supported Transition-Metal Catalysts by Design. *Catal. Today* **1992**, *15*, 419-429.
4. Barrer, R. M., Zeolites and clay minerals as sorbents and molecular sieves. *Chem. Ing. Tech.* **1980**, *52*, 366-366.
5. Chen, N. Y., Molecular transport and reaction in zeolites : design and application of shape selective catalysts. Degnan, T. F.; Smith, C. M., Eds. VCH: New York :, 1994.
6. Csicsery, S. M., Shape-selective catalysis in zeolites. *Zeolites* **1984**, *4*, 202-213.
7. Maxwell, I. E., Shape-Selective Catalysis and Process Technology Via Molecular Inclusion in Zeolites. *Journal of Inclusion Phenomena* **1986**, *4*, 1-29.
8. Rabo, J. A.; Bezman, R. D.; Poutsma, M. L., Zeolites in Industrial Catalysis. *Acta Physica Et Chemica* **1977**, *24*, 39-52.
9. Sircar, S.; Myers, A., Gas Separation by Zeolites. In *Handbook of Zeolite Science and Technology*, CRC Press: 2003.
10. Vermeiren, W.; Gilson, J. P., Impact of Zeolites on the Petroleum and Petrochemical Industry. *Top. Catal.* **2009**, *52*, 1131-1161.
11. Sachtler, W. M. H., Metal-Clusters in Zeolites - an Intriguing Class of Catalysts. *Acc. Chem. Res.* **1993**, *26*, 383-387.
12. Arcoya, A.; Gonzalez, J. A.; Llabre, G.; Seoane, X. L.; Travieso, N., Role of the countercations on the molecular sieve properties of a clinoptilolite. *Microporous Mater.* **1996**, *7*, 1-13.
13. Corma, A., From microporous to mesoporous molecular sieve materials and their use in catalysis. *Chem. Rev.* **1997**, *97*, 2373-2419.
14. Farrusseng, D.; Tuel, A., Perspectives on zeolite-encapsulated metal nanoparticles and their applications in catalysis. *New J. Chem.* **2016**, *40*, 3933-3949.
15. Goel, S.; Wu, Z. J.; Zones, S. I.; Iglesia, E., Synthesis and Catalytic Properties of Metal Clusters Encapsulated within Small-Pore (SOD, GIS, ANA) Zeolites. *Journal of the American Chemical Society* **2012**, *134*, 17688-17695.
16. Teketel, S.; Erichsen, M. W.; Bleken, F. L.; Svelle, S.; Lillerud, K. P.; Olsbye, U., Shape selectivity in zeolite catalysis. The Methanol to Hydrocarbons (MTH) reaction. *Catalysis, Vol 26* **2014**, *26*, 179-217.
17. Csicsery, S. M., Catalysis by Shape Selective Zeolites - Science and Technology. *Pure Appl. Chem.* **1986**, *58*, 841-856.
18. Kärger, J.; Vasenkov, S.; Auerbach, S., Diffusion in Zeolites. In *Handbook of Zeolite Science and Technology*, CRC Press: 2003; pp 446-548.
19. Koehle, M.; Mhadeshwar, A., Chapter 3 - Nanoparticle Catalysis for Reforming of Biomass-Derived Fuels A2 - Suib, Steven L. In *New and Future Developments in Catalysis*, Elsevier: Amsterdam, 2013; pp 63-93.
20. Wei, J.; Iglesia, E., Reaction Pathways and Site Requirements for the Activation and Chemical Conversion of Methane on Ru-Based Catalysts. *J. Phys. Chem. B* **2004**, *108*, 7253-7262.

21. Wei, J.; Iglesia, E., Structural requirements and reaction pathways in methane activation and chemical conversion catalyzed by rhodium. *J. Catal.* **2004**, *225*, 116-127.
22. Wei, J.; Iglesia, E., Structural and Mechanistic Requirements for Methane Activation and Chemical Conversion on Supported Iridium Clusters. *Angew. Chem. Int. Ed.* **2004**, *43*, 3685-3688.
23. Wei, J.; Iglesia, E., Mechanism and Site Requirements for Activation and Chemical Conversion of Methane on Supported Pt Clusters and Turnover Rate Comparisons among Noble Metals. *J. Phys. Chem. B* **2004**, *108*, 4094-4103.
24. Wei, J.; Iglesia, E., Isotopic and Kinetic Assessment of the Mechanism of Reactions of CH_4 with CO_2 or H_2O to Form Synthesis Gas and Carbon on Nickel Catalysts. *J. Catal.* **2004**, *224*, 370-383.
25. Leung, S. L.; Wei, J. M.; Holstein, W. L.; Avalos-Borja, M.; Iglesia, E., Dynamics and Mechanism of Carbon Filament Formation during Methane Reforming on Supported Nickel Clusters. *J. Phys. Chem. C* **2020**, *124*, 20143-20160.
26. Choi, M.; Wu, Z. J.; Iglesia, E., Mercaptosilane-Assisted Synthesis of Metal Clusters within Zeolites and Catalytic Consequences of Encapsulation. *Journal of the American Chemical Society* **2010**, *132*, 9129-9137.
27. Almithn, A. S.; Hibbitts, D. D., Supra-Monolayer Coverages on Small Metal Clusters and Their Effects on H-2 Chemisorption Particle Size Estimates. *AlChE J.* **2018**, *64*, 3109-3120.
28. Bergeret, G.; Gallezot, P., Particle Size and Dispersion Measurements. In *Handbook of Heterogeneous Catalysis*, Ertl, G.; Knözinger, H.; Schüth, F.; Weitkamp, J., Eds. Wiley: 2008; pp 738-765.
29. Thiele, E. W., Relation between Catalytic Activity and Size of Particle. *Industrial & Engineering Chemistry* **1939**, *31*, 916-920.
30. Froment, G. F.; Bischoff, K. B., *Chemical reactor analysis and design*; Wiley: New York, 1979.
31. Wynnyk, K. G.; Hojjati, B.; Marriott, R. A., High-Pressure Sour Gas and Water Adsorption on Zeolite 13X. *Ind. Eng. Chem. Res.* **2018**, *57*, 15357-15365.
32. Schulz, L. A.; Kahle, L. C. S.; Delgado, K. H.; Schunk, S. A.; Jentys, A.; Deutschmann, O.; Lercher, J. A., On the coke deposition in dry reforming of methane at elevated pressures. *Appl. Catal., A* **2015**, *504*, 599-607.
33. Holstein, W. L., The Roles of Ordinary and Soret Diffusion in the Metal-Catalyzed Formation of Filamentous Carbon. *J. Catal.* **1995**, *152*, 42-51.
34. Watson, E. B., Diffusion and Solubility of C in Pt. *Am. Mineral.* **1987**, *72*, 487-490.
35. Lander, J. J.; Kern, H. E.; Beach, A. L., Solubility and Diffusion Coefficient of Carbon in Nickel: Reaction Rates of Nickel-Carbon Alloys with Barium Oxide. *J. Appl. Phys.* **1952**, *23*, 1305-1309.
36. Fogler, H. S., *Elements of Chemical Reaction Engineering*; Prentice Hall PTR, 2006.
37. Gramlich, V.; Meier, W. M., Crystal Structure of Hydrated Naa - Detailed Refinement of a Pseudosymmetric Zeolite Structure. *Zeitschrift Fur Kristallographie Kristallgeometrie Kristallphysik Kristallchemie* **1971**, *133*, 134-149.